



Supersymmetry Searches Involving Multiple b-Jets and Missing Energy at the ATLAS Experiment

Probing an extreme phase space with the LHC Run 2
dataset

Evangelos Kourlitis

A dissertation submitted for the degree of
Doctor of Philosophy
at The University of Sheffield

2019

Supersymmetry Searches Involving Multiple b-Jets and Missing Energy at the ATLAS Experiment

Probing an extreme phase space with the LHC Run 2
dataset

Evangelos Kourlitis

Supervisor: Davide Costanzo

Department of Physics and Astronomy

The University of Sheffield

A dissertation submitted for the degree of
Doctor of Philosophy

September 2019

Dedicated to the memory of Charalambos Papadopoulos,
who did not have the time to appreciate this work.

Abstract

Supersymmetry is an extension of space-time symmetries that predicts new bosonic partners for the Standard Model (SM) fermions and vice versa. The main subject of this dissertation is the search for these partners in final states involving multiple jets originating from the hadronisation of bottom quarks (b-jets) and missing energy, at the LHC $\sqrt{s} = 13$ TeV proton-proton collision data collected by the ATLAS detector during the Run 2 period (2015 to 2018).

Moreover, in light of the Phase-II upgrade of the ATLAS detector, radiation tolerance studies of future silicon microstrip sensors are also presented. In particular, a sensor performance characterisation facility was developed at the University of Sheffield. A description of the facility along with initial benchmark measurements of microstrip sensors, before and after irradiation are presented. The results support the successful commissioning of the facility and are found to be in agreement with what is expected from the literature and similar measurements conducted at other facilities.

Regarding the Supersymmetry searches, first, a search concerning the pair production of gluinos decaying via third generation squarks into the lightest neutralino ($\tilde{\chi}_1^0$) is presented. The data used constitute a partial Run 2 dataset collected during 2015 and 2016, corresponding to an integrated luminosity of 36.1 fb^{-1} . The final state studied comprise of multiple energetic jets, at least three of which must be identified as b-jets, and large missing energy. The dataset is split into samples containing charged leptons or not, to further increase the search sensitivity. No excess above the predicted SM background is found, hence upper limits (at 95% confidence level) have been placed on the models under investigation. For $\tilde{\chi}_1^0$ masses below 300 GeV, gluino masses up to 1.97 (1.92) TeV have been excluded in models involving decays via top (bottom) squarks. An interpretation of the limits as function of the branching ratio of the gluinos into the various third generation squark configurations is provided as well.

A search for the pair production of bottom squarks (sbottoms) is also presented. This work use the full LHC Run 2 dataset that amounts to a total of 139 fb^{-1} . Specifically, the sbottoms are searched for in scenarios in which they decay to the second-lightest neutralino ($\tilde{\chi}_2^0$) and a b-quark. Subsequently, each $\tilde{\chi}_2^0$ is considered to decay to a Higgs boson and the $\tilde{\chi}_1^0$. Two mass configurations are targeted: either the $\tilde{\chi}_1^0$ has a constant mass at 60 GeV or the mass difference between the two neutralino states is constant at 130 GeV. The final state explored consist of zero leptons, at least three b-jets and large missing energy. No significant excess above the predicted SM background is observed in data thus sbottom masses up to 1.5 TeV have been excluded.

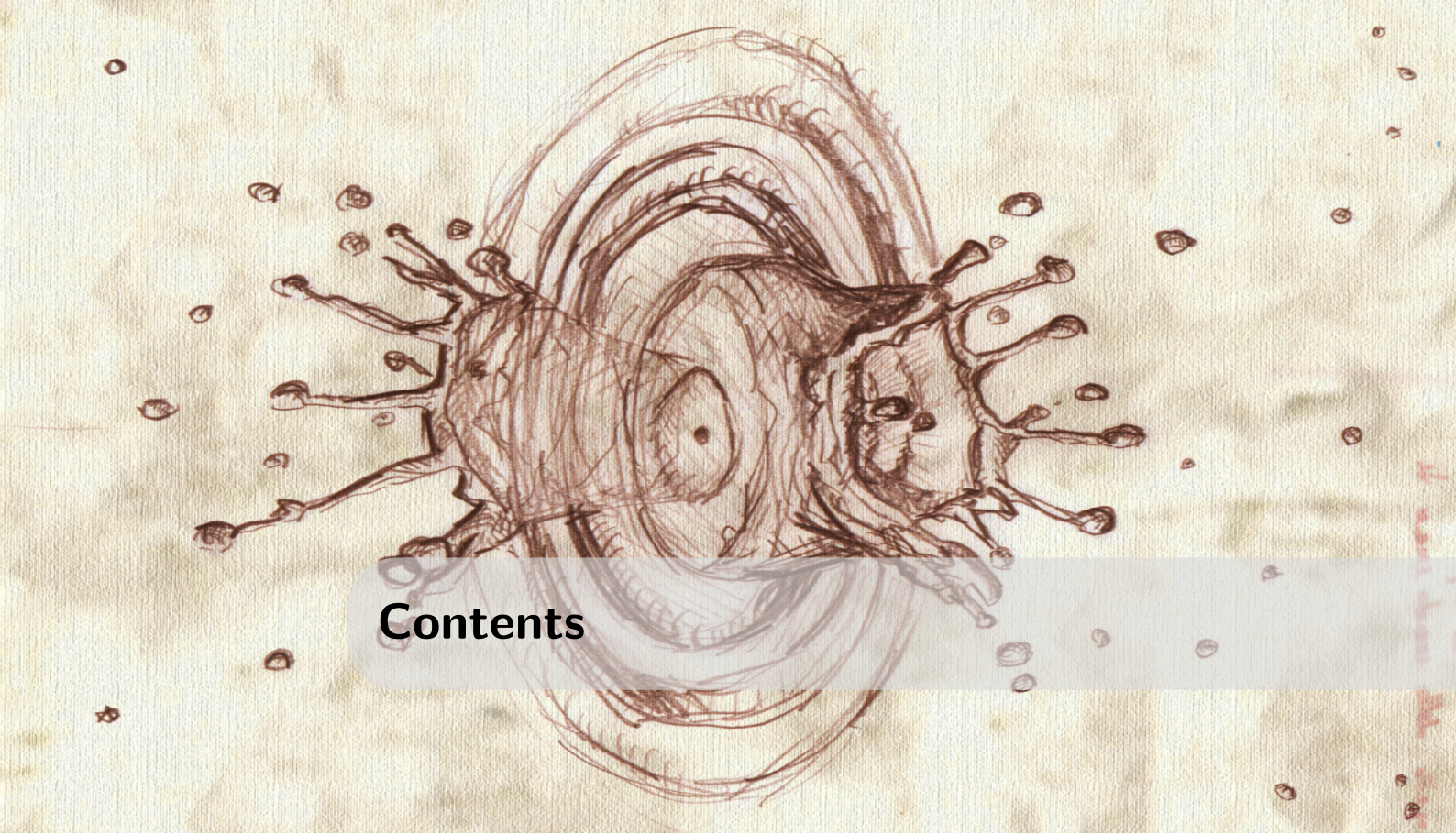
Finally, few concluding remarks and future prospects are discussed.

Acknowledgments

This work would have never been achieved without the priceless support of colleagues, friends, and my family. Foremost, I deeply thank Prof. Davide Costanzo who four years ago trusted a PhD studentship on me and from that time continuously provided me with precious career advices. To compensate for these, I was always trying to surpass his expectations. I am also grateful to the ATLAS group leader in Sheffield, Prof. Dan Tovey, who supported and advised me in various aspects the past years. Regarding the technical part of my work, Dr. Richard French always kindly provided me with the required networking and financial aid. In a more friendly manner, Dr. Kristin Lohwasser and Dr. Christos Anastopoulos were always keen to discuss and advice on professional and career subjects. Significant inspiration to my studies was my friend and fellow PhD student Guillermo Hamity, one of the few people always willing to discuss long and deep scientific thoughts. I also want to thank Prof. Monica D'Onofrio and Dr. Zach Marshall who helped me to make the next step on my career. Last but certainly not least, I genuinely thank my friend and colleague Dr. Calum Macdonald, my personal development and achievements would have never been the same without him. I will always have his scientific insight and skills as a target.

I would have also never arrived Sheffield, or in any other institution abroad, without the support of my teachers and colleagues in my hometown, Thessaloniki. Prof. Chara Petridou and her staff at the Aristotle University of Thessaloniki, Dr. Dinos Bachas and Dr. Giannis Nomidis, were next to me on my first steps to teach me all the basic yet crucial aspects of particle physics and data analysis.

The professional achievements, though, are never realised without the family and friends encouragement. First, I acknowledge my parents who are always aid, both practically and mentally, my life choices. The same applies to my sister Angela, who with her noteworthy maturity is always next to me to discuss and enjoy life. Moving into a new country is rarely easy but I was too lucky to meet my friend and flatmate Dr. Manu Bernhard, the greatest mental support on my PhD studies. I should also thank Alex Bee and Christine Gilliver who introduced me to the English culture the first years of my studies. Finally but just as importantly, I want to thank each member of my extended family for all the unforgettable moments that make my life brighter: Batis, Kostas, Liakos, Fotis, Plekas, Natasa, Mary, Antonis, George and Tasos.



Contents

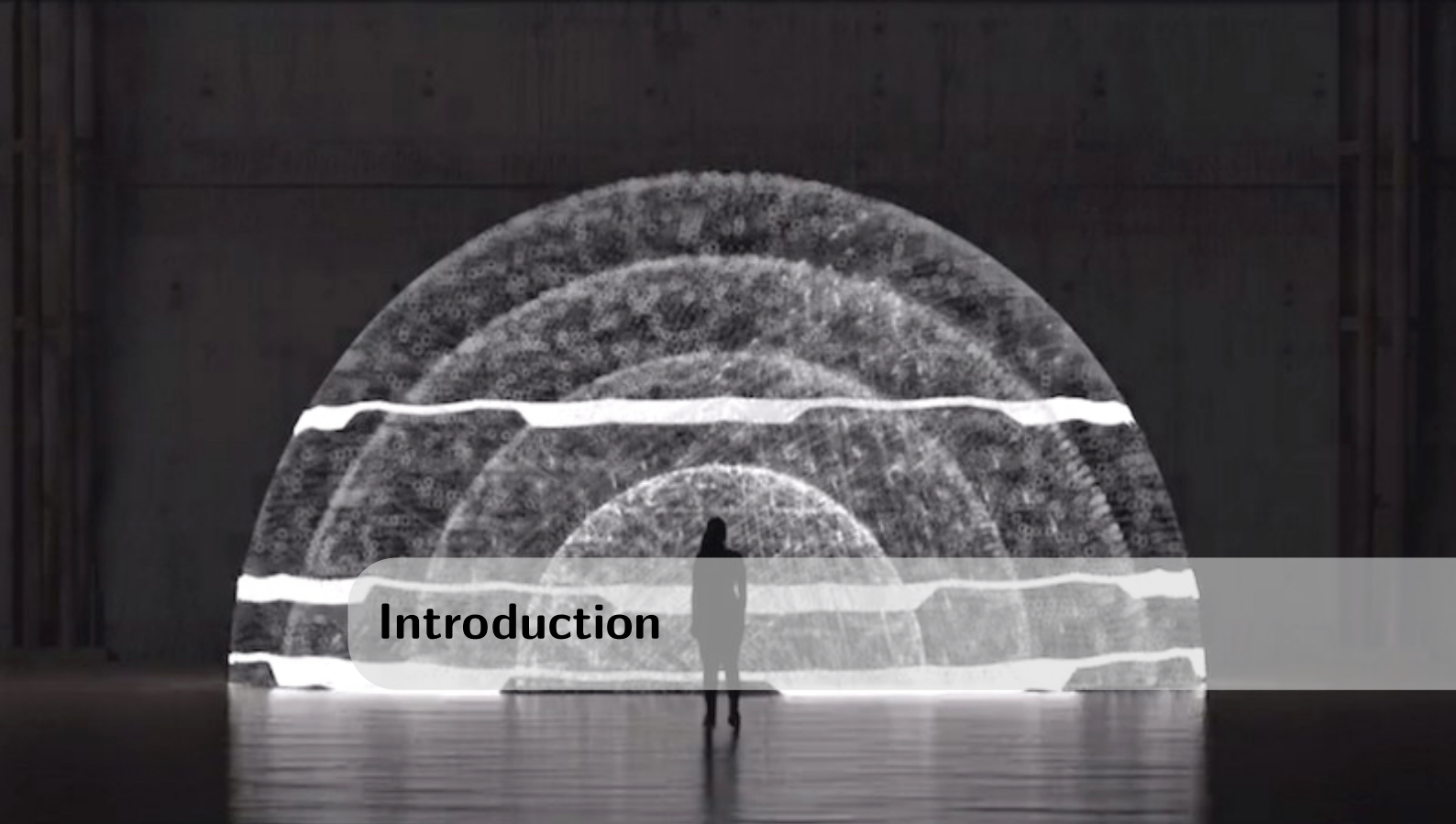
Introduction	17
I Theoretical Background	21
1 The Standard Model	23
1.1 Overview	23
1.2 Fermion Fields	25
1.2.1 Lagrangian and Chirality	25
1.2.2 Fermion States	26
1.3 Boson Fields	30
1.3.1 Lagrangian and Local Gauge Invariance	30
1.3.2 Electroweak Sector	31
1.3.2.1 Bosons and Interactions	31
1.3.2.2 The Brout-Englert-Higgs mechanism	32
1.3.2.3 Boson Decay Properties	35
1.3.3 Strong Sector	35
1.3.3.1 Bosons and Interactions	35
1.3.3.2 Confinement and Asymptotic Freedom	36
1.4 Physics Events Simulation	38
1.4.1 Matrix Elements and Parton Showering	40
1.4.2 Hadronisation and Underlying Event	41

1.5	Status and Deficiencies	42
1.5.1	Precise Predictions	42
1.5.2	Dark Matter	43
1.5.3	Hierarchy Problem	44
2	Supersymmetric Extension	47
2.1	(Super)Symmetries	47
2.2	The Minimal Supersymmetric Standard Model	48
2.2.1	Particle Mass Eigenstates	51
2.2.2	R-Parity	53
2.3	SM Problems Revised	53
2.3.1	Dark Matter	53
2.3.2	Hierarchy Problem	54
2.4	Restricting the MSSM	56
2.4.1	pMSSM	56
2.4.2	Simplified Models	56
II	Experimental Facility	61
3	The LHC & ATLAS Detector	63
3.1	The Large Hadron Collider	63
3.1.1	Accelerator Complex	64
3.1.2	Luminosity & Pile-Up	65
3.2	The ATLAS Detector	67
3.2.1	Coordinate System	67
3.2.2	Inner Detector	69
3.2.2.1	Pixel Detector	70
3.2.2.2	SemiConductor Tracker	70
3.2.2.3	Transition Radiation Tracker	71
3.2.3	Calorimeters	71
3.2.3.1	Electromagnetic Calorimeter	72
3.2.3.2	Hadronic Calorimeter	72
3.2.4	Muon Spectrometer	72
3.2.5	Trigger System	73
3.2.6	Detector Simulation	74

4	Phase II Upgrade	75
4.1	Phase-II LHC and ATLAS Upgrades	75
4.2	Inner Tracker	76
4.2.1	Strip Detector	77
4.2.2	Radiation Effects	78
4.3	Sheffield Characterisation Facility	81
4.3.1	ALiBaVa Read-out System	82
4.3.2	Commissioning Measurements	84
4.3.2.1	Method	85
4.3.2.2	Results	86
4.3.3	Conclusion	88
5	Physics Object Reconstruction	91
5.1	Tracks & Vertices	91
5.2	Electrons & Photons	93
5.3	Muons	95
5.4	Jets	96
5.5	b-Jets	99
5.6	Taus	101
5.7	Overlap Removal	102
5.8	Missing Energy	102
III	Physics Analyses	105
6	Analysis Methodology	107
6.1	Search Strategy	107
6.2	Statistical Treatment	109
6.2.1	Background-only Fit	109
6.2.2	Estimating Deviations	110
6.2.3	Exclusion Fit	111
6.2.4	Discovery Fit	113
7	Glino Search	115
7.1	Introduction	115

7.2	SUSY Model	116
7.2.1	Description	116
7.2.2	Signal Grids	118
7.3	Data, Triggers and Simulations	118
7.4	Event Selection	120
7.4.1	Discriminating Variables	121
7.4.2	Data Modeling	123
7.5	Signal Regions	127
7.5.1	Cut-and-count Regions	129
7.5.2	Multi-bin Regions	140
7.6	Background Estimation	143
7.6.1	Processes and Strategy	143
7.6.2	Cut-and-count Regions	144
7.6.3	Multi-bin Regions	147
7.6.4	Background-only Fit Results	147
7.7	Systematic Uncertainties	150
7.7.1	Experimental Uncertainties	152
7.7.2	Theoretical Uncertainties	154
7.8	Results	156
7.9	Interpretation	159
7.9.1	Model-dependent Limits	161
7.9.2	Model-independent Limits	164
7.10	Conclusion	166
8	Sbottom Search	169
8.1	Introduction	169
8.2	SUSY Model	170
8.2.1	Description	170
8.2.2	Signal Grids	171
8.3	Data, Triggers and Simulations	172
8.4	Signal Event Selection	175
8.4.1	Discriminating Variables	175
8.4.2	Signal Region A	179
8.4.2.1	Max-Min Algorithm	179
8.4.2.2	Definition & Yields	183

8.4.3	Signal Region B	187
8.4.3.1	Alternative <i>Max-Min</i> Algorithm	187
8.4.3.2	Definition & Yields	187
8.4.4	Signal Region C	188
8.5	Background Estimation	192
8.5.1	Processes and Strategy	192
8.5.2	Regions A & B	194
8.5.3	Region C	197
8.5.4	Background-only Fit Results	201
8.6	Systematic Uncertainties	203
8.6.1	Experimental Uncertainties	204
8.6.2	Theoretical Uncertainties	205
8.7	Results	206
8.8	Interpretation	210
8.8.1	Model-dependent Limits	210
8.8.2	Model-independent Limits	213
8.9	Conclusion	214
9	Conclusions and Outlook	217
A	Notation	219
B	Simulated Event Samples Details	223
C	Data-driven Multi-jet Estimation	227
	References	233



Introduction

The concept that the Universe is made of fundamental pieces originates back to the 5th century BC, developed as a natural philosophy by the pre-Socratic Greek philosophers Leucippus and Democritus. Today, this concept is not only well described theoretically but experimentally verified as well; the fundamental pieces are called *elementary particles* and interact with just four *forces*. It is a remarkable achievement that theoretical predictions in an energy scale spanning over 12 orders of magnitude have been confirmed by numerous experiments in the last few decades.

In spite of the apparent success of the *Standard Model* (SM) of particle physics, that is introduced in Chapter 1, there are indisputable observations that cannot be explained thus far, such as the abundance of the *Dark Matter* filling the space among stars and galaxies. This dissertation seeks for experimental evidence of new physics phenomena, in elementary particle level, able to provide insights to the outstanding questions concerning the way the Universe works.

Supersymmetry is a hypothesised feature of nature providing solutions to multiple physics problems and is described in Chapter 2. In extensions of the SM incorporating supersymmetry, an additional symmetry is introduced, effectively doubling the SM particle content by the introduction of supersymmetric partner particles. The only way to observe and systematically study these particles in a laboratory is to produce them at a collider experiment. In the context of this dissertation, this is attempted by the *Large Hadron Collider* (LHC) [1], at CERN in Geneva, that brings into collision quadrillion of high-energy protons per second. The result of these high-energy collisions is the production of (new) particles according to the energy-mass equality, $E = mc^2$. In order to study the collision products, particle detectors are placed around the proton interac-

tion point monitoring the outcoming debris and collecting data. The data used in this dissertation have been collected by the general-purpose ATLAS detector [2], described in Chapter 3.

The LHC is fully operational since 2011 with the Run 1 period that lasted until 2012 and the Run 2 from 2015 to 2018. Between each period, maintenance and upgrade work take place. During the current shutdown (December 2018 - June 2021), minor upgrades are underway and are going to be followed by the Run 3 period until 2024. Eventually, a longer, three-year shutdown will occur when a major upgrade is going to deliver the *High-Luminosity LHC* with a tenfold increase in performance and the corresponding *Phase-II Upgrade* of the ATLAS detector. The whole timeline is illustrated in Figure 1. The author of this dissertation spent about 10% of his time developing a facility at the University of Sheffield in order to study the radiation tolerance of silicon microstrip sensors that are going to provide the tracking capabilities of the upgraded detector. This part of the work is presented in Chapter 4 and published in [3].

Two searches for the production of supersymmetric particles at the LHC, that the author significantly contributed to, are presented in this dissertation. They both use data collected during the Run 2 that are reconstructed as described in Chapter 5, and analysed and statistically interpreted as described in Chapter 6. First, a search for the partner particle of the gluon, the *gluino*, was conducted from June 2016 to August 2018 using a partial Run 2 dataset. The author designed and optimised all the kinematic regions that target the so-called *Gbb* model where the gluino decays into a final state with up to four jets originating from the hadronisation of bottom quarks (b-jets) and missing energy from the lightest supersymmetric particle that escapes undetected. A detailed description of this work is presented in Chapter 7 and published in [4].

Second, a search for the partner particle of the bottom quark, the *bottom squark*¹, was carried out from July 2017 to August 2019 and comprises the main subject of the work of author towards the PhD degree. This search is exploring the final states containing Higgs bosons, b-jets and missing energy of the full Run 2 dataset. In particular, the author developed the analysis strategy, designed most of the kinematic regions and statistically interpret the results. A detailed description of this work is presented in Chapter 8 and published in [5].

Finally, after assessing all the data collected by the ATLAS experiment during the Run 2 in the final states of interest, concluding remarks and future prospects are discussed in Chapter 9.

¹Terms as *bottom squark* and *sbottom* are used interchangeably in literature and this document.

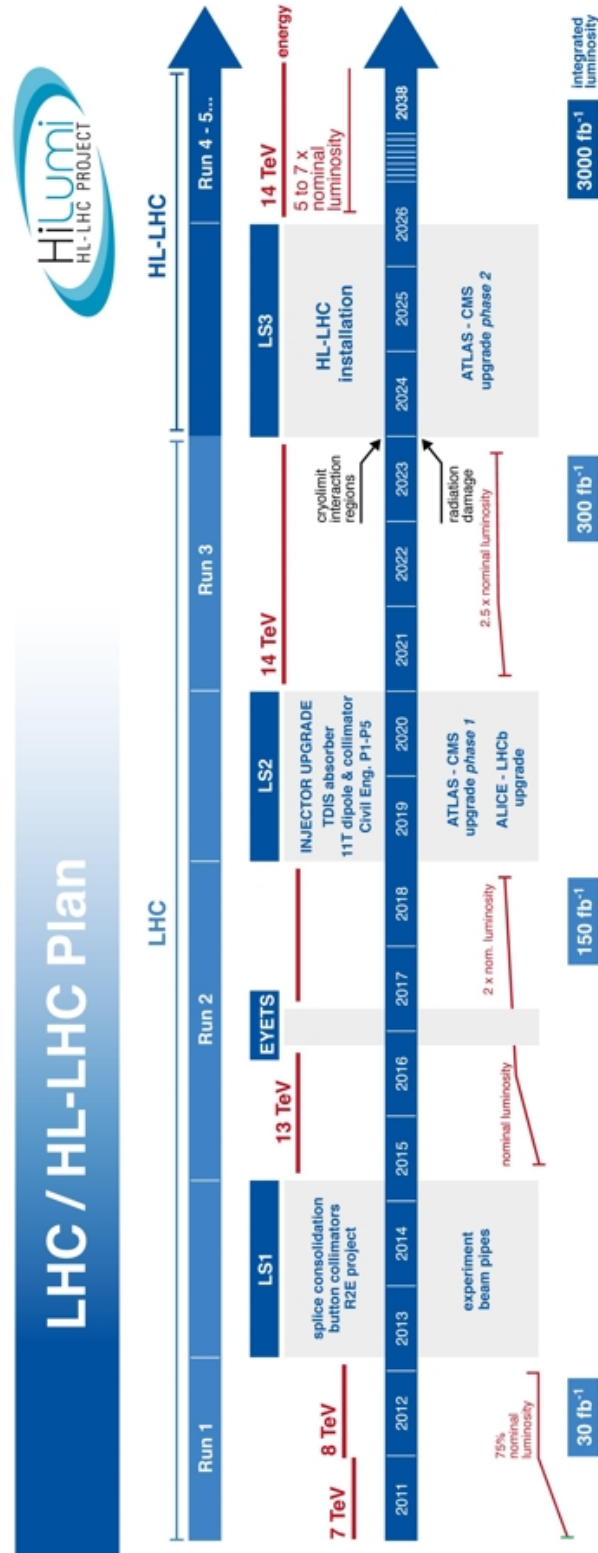
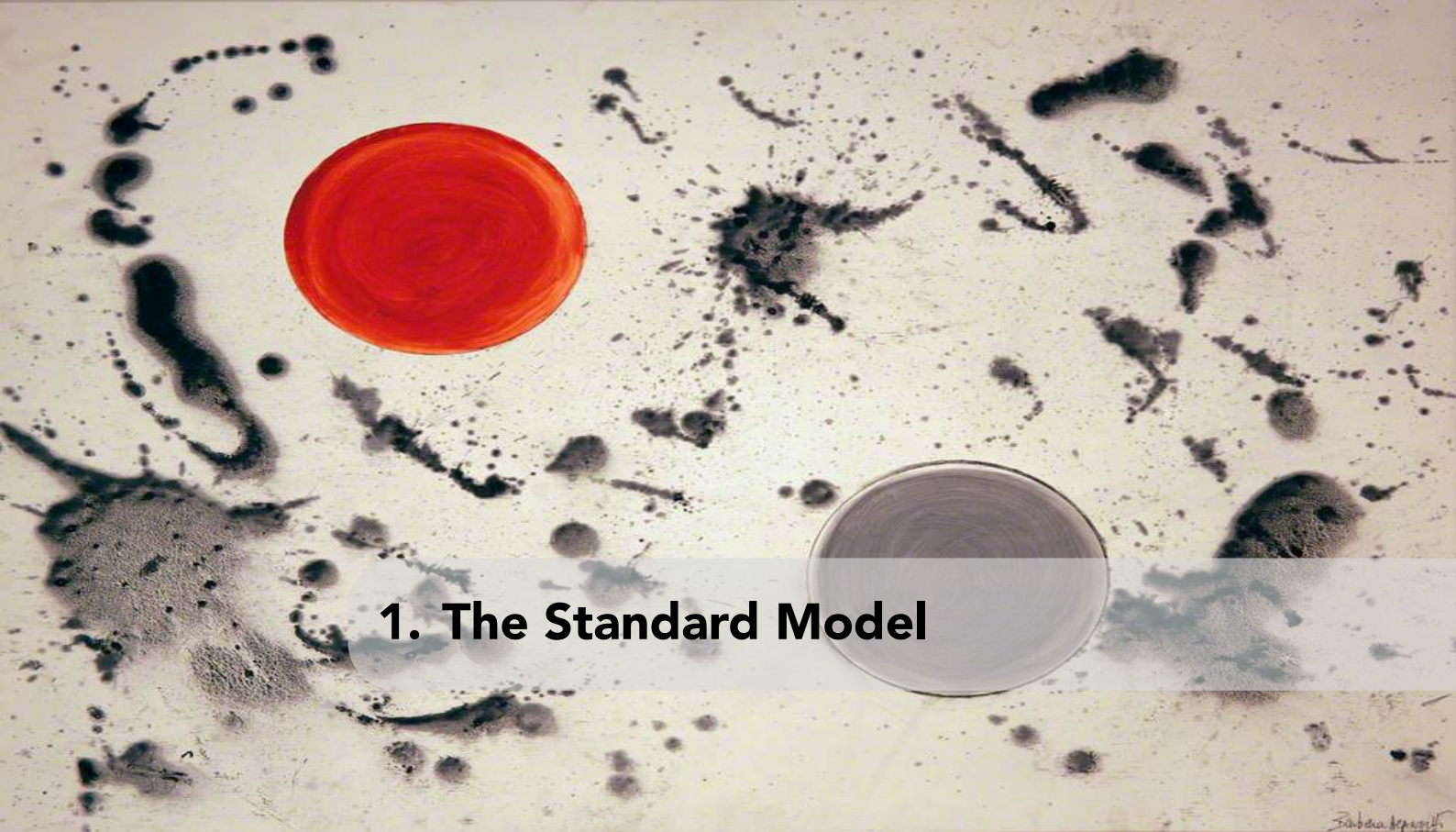


Figure 1: The (High-Luminosity) LHC timeline. [6]

Part I

Theoretical Background



1. The Standard Model

The Standard Model of particle physics is one of the most successful collaborative intellectual achievements, although there is scientific consensus that it is far from complete

1.1 Overview

The Standard Model (SM)¹ of particle physics is the model that describes the behavior of nature at the, so far known, elementary level ($\ll \mathcal{O}(10^{-15})$ m). Mathematically, it is formulated as a relativistic Quantum Field Theory (QFT) with the field excitations (*quanta*) interpreted as elementary particles. The dynamics of a QFT are described by the Lagrangian density (\mathcal{L}), which henceforth will be referred to just as *Lagrangian*.

The particle content of the SM can be classified into two general categories: 1) particles that can comprise matter, or *fermions*, and 2) particles that mediate forces, or

¹A complete list of all the abbreviations used in the text is given in Table [A.2](#)

boson – described in Sections 1.2 and 1.3, respectively. Remarkably, most of the physics phenomena emerge directly from symmetry considerations of the Lagrangian. As an example, the interactions, or *forces*, among the fields are generated by its invariance under local transformations defined by the gauge group of the SM, the $SU(3) \times SU(2)_L \times U(1)$ (Section 1.3).

S *Symmetry* is the property of a physical system to remain unchanged after a transformation. For instance, a spherical object is symmetric under rotations. The symmetries the SM respects are categorised either into:

1. space-time symmetries, related to translations and Lorentz-transformations in the Minkowski spacetime (collectively called *Poincaré* symmetry), or
2. internal symmetries that leave the Minkowski coordinates untouched and transform the fields via abstract phases (gauge symmetries).

The SM unifies under a single model the description of all the so far known elementary particles (henceforth referred to just as particles) and the forces between them. It should be noted, however, that the latter does not include gravity¹. Milestone on this unification was S. Weinberg’s 1967 seminal work, *A Model of Leptons* [8], that actually provided the conceptual basis of the SM. In that manuscript he proposed the unification of the electromagnetic and weak forces into what it is called today *electroweak interaction* (Section 1.3.2). Based on the earlier work of J. Goldstone, A. Salam, R. Brout, F. Englert, P. Higgs, G. Guralnik, C. Hagen and T. Kibble on the phenomenon of spontaneous symmetry breaking [9–13], Weinberg synthesised a model that describes these interactions and the particles mediating it, based on the breaking of $SU(2)_L \times U(1)$ gauge symmetry. A crucial aspect of the model is that it uses the so-called *Brout-Englert-Higgs (BEH) mechanism* in order to explain the origin of mass of the particles. The model was widely ignored until 1971, when G. ‘t Hooft and his doctoral advisor M. Veltman demonstrated its renormalisability [14] (1999 Nobel Prize in Physics). Since then, it became so important that researchers have cited it a dozen times a month throughout half a century!

Weinberg’s ideas stemmed from the 1950-60s classification efforts of the plethora of *hadrons* – composite particles that interact via the strong force (Section 1.3.3) – discovered at accelerator experiments. It was counter-intuitive for all these particles to be elementary thus in 1963 M. Gell-Mann and G. Zweig proposed that hadrons are made by *quarks* [15, 16]. These and the particles that mediate their interaction (*gluons*) carry a charge described by the non-abelian $SU(3)$ gauge symmetry group, the *colour* (O. W. Greenberg, M.-Y. Han and Y. Nambu, 1964–65 [17, 18]). The QFT developed by H. Fritzsch, Gell-Mann and H. Leutwyler and in 1973 to describe the above is called Quantum Chromodynamics (QCD) [19]. Last but not least, the 1973 discovery of the asymptotic

¹Gravitational effects on particles can be neglected as their relative strength compared to the strong force is $\mathcal{O}(10^{-37})$ times weaker [7].

freedom property of the QCD [20, 21] completed the description of the strong interaction at high energies and awarded D. Gross, F. Wilczek and D. Politzer the 2004 Nobel Prize in Physics.

During the past half a century the SM – used as the underlying model to simulate the physics processes produced in the experimental facilities as described in Section 1.4 – has provided numerous results of unprecedented accuracy in quantities spanning many orders of magnitude. Figure 1.1 shows the probability (*cross-section*) of two interacting protons to produce different SM particles as calculated by the SM equations and measured by the ATLAS collaboration. It is impressive that a single model can predict this probability that spans over 12 orders of magnitude and with an accuracy better than what current state-of-the-art experimental facilities can measure.

Nevertheless, multiple observations made during the twentieth century, such as the presence of Dark Matter or the matter-antimatter asymmetry, cannot be explained within the SM (Section 1.5). Motivated by these, the scientific community argues that the SM is incomplete. Many theories Beyond the SM (BSM) have been developed to address these limitations. The current dissertation presents original research from the experimental searches for particles predicted by *Supersymmetry* [22–27], one of the most compelling and extensively studied BSM frameworks. A brief theoretical introduction to Supersymmetry is given in Chapter 2.

1.2 Fermion Fields

1.2.1 Lagrangian and Chirality

One of the two general categories of the SM fields are the fermions. These fields, and the particles that emerge from them, have spin $1/2$ thus obey to the Pauli exclusion principle [29] and the Fermi-Dirac statistics [30, 31]. The former is the reason the fermions are able to build up structures, or matter. In a QFT formalism, the behavior of a free fermion field is derived from the Dirac Lagrangian [7]:

$$\mathcal{L}_D = i\bar{\Psi}\gamma^\mu\partial_\mu\Psi - m\bar{\Psi}\Psi, \quad (1.1)$$

where Ψ is a four-component wavefunction called *Dirac spinor* and describes the fermion field, $\bar{\Psi} = \Psi^\dagger\gamma^0$, ∂_μ is the covariant four-gradient, m is the mass of the field¹. The terms in a Lagrangian as the first one of Eq. 1.1 are called *kinetic terms*, as they give rise to differential operators that describe how a field changes in spacetime, while terms as the second one are called *mass terms* for apparent reasons. As discussed later in Section 1.3.2, explicit mass terms are prohibited in the initial SM Lagrangian for gauge symmetry considerations.

The four degrees of freedom of the Dirac spinor are interpreted as two orthogonal

¹Common symbol definitions, as γ^μ , are given in Appendix A

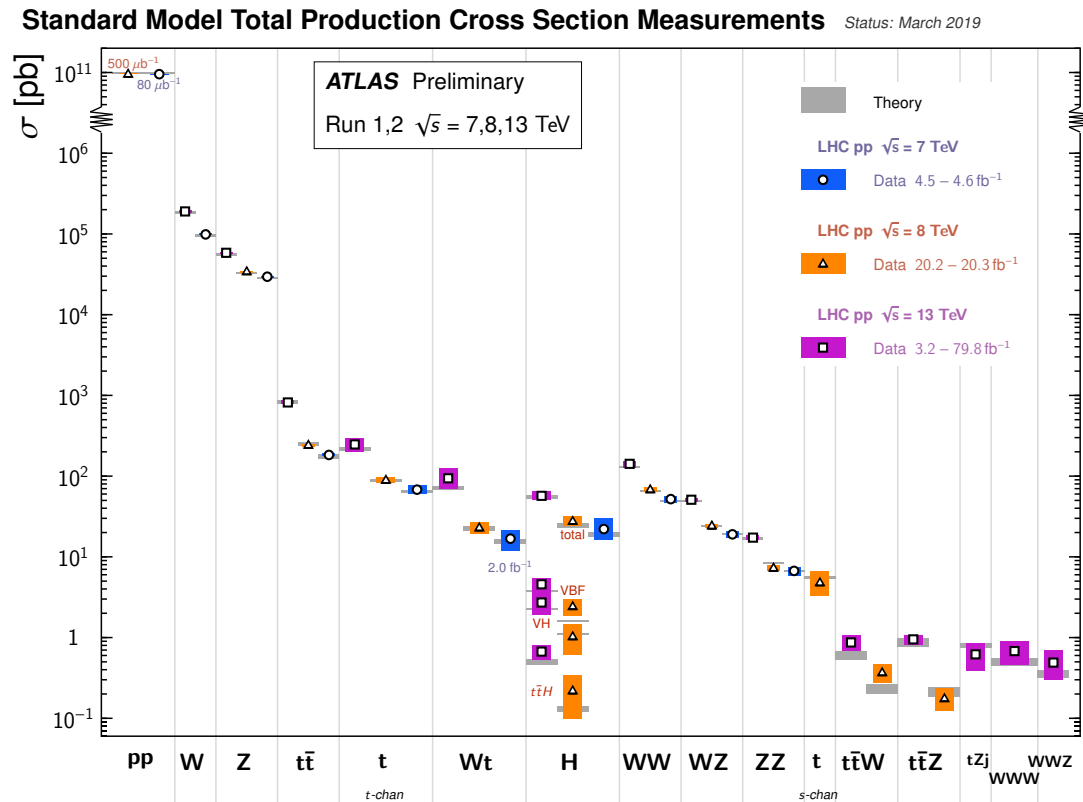


Figure 1.1: Summary of several SM particle production cross-section measurements, compared to their corresponding theoretical expectations, conducted by the ATLAS experiment. The different colours indicate the different experimental setup each measurement is taken. [28]

polarisation states for the particle and two for the anti-particle solutions. The usual choice of the polarisation states basis are the “*spin-up*” and “*spin-down*” configurations. A more convenient choice though, as it will become apparent in Section 1.3.2, for studying the SM are the *Left-* and *Right-handed* (L and R) *chiral* configurations. These are eigenstates of the γ^5 -matrix and any Dirac spinor can be decomposed into L and R components. In the ultra-relativistic limit ($E \gg m$), and only then, the chiral basis can be interpreted as the configurations with anti-parallel (L) and parallel (R) projections of the fermion spin along its direction of motion (Figure 1.2).

1.2.2 Fermion States

The fermions of the SM are categorised into two groups: the leptons and the quarks. The main difference between them is that leptons interact only with the electromagnetic and weak forces, in contrast to the quarks that interact with the strong force as well. Both quarks and leptons are further split into three *generations* of increasing mass. Each generation of quarks or leptons contains two fermions. It is worth noting that all the observable structures of the Universe are made only by fermions of the first generation

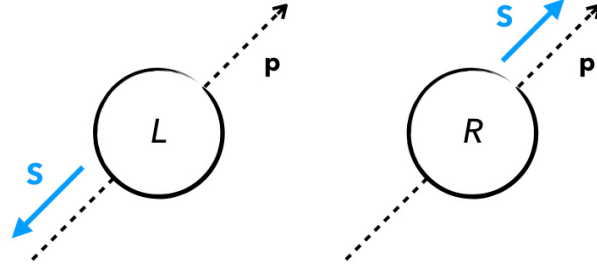


Figure 1.2: The physical interpretation of the L and R chiral states in the ultra-relativistic limit ($E \gg m$). The figure comprises an original work of the author.

as the heavier copies have tiny lifetimes compared to astrophysical scales. For every SM fermion particle, an anti-particle also exists. Overall, the fermion types, or *flavours*, of the SM amount to 12 (6+6) and the picture is summarised in Figure 1.3.

The leptons are either electrically charged (*electron, muon, tau*), with a unit of elementary charge, or neutral (*neutrinos, ν* , one per charged lepton). The first charged lepton discovered was the electron by J. J. Thomson and his colleagues in 1897 in cathode rays [32] and in the twentieth century the discovery of the muon in cosmic radiation [33] and the tau in accelerator experiments [34] followed. As mentioned already, the charged leptons of the second and third generation are unstable and decay via the weak interaction. The tau is the only one that can decay to hadrons, for kinematic considerations as it is the only lepton heavier than the lightest hadron, the *pion*. Their lifetimes along with the decay products are presented in Table 1.1.

Table 1.1: The SM charged leptons mean lifetime and their possible decay products along with the corresponding Branching Ratio (BR). For the tau, only the dominant decay modes are listed. The charge conjugate decays are implied too. [35]

Charged Lepton	Mean Lifetime [s]	Decay Products (BR [%])
electron	stable	-
muon	2.2×10^{-6}	$\nu_\mu + e + \nu_e$ (100)
tau	2.9×10^{-13}	$\nu_\tau + \mu + \nu_\mu$ (17.4)
		$\nu_\tau + e + \nu_e$ (17.8)
		$\nu_\tau + \pi^\pm (+\pi^0)$ (46.6)
		$\nu_\tau + \pi^\pm + \pi^+ + \pi^- (+\pi^0)$ (11.7)

The existence of a neutral lepton was proposed by W. Pauli in 1930 to explain energy conservation in β -decays [36]. Eventually the electron-(anti)neutrino was the first one of

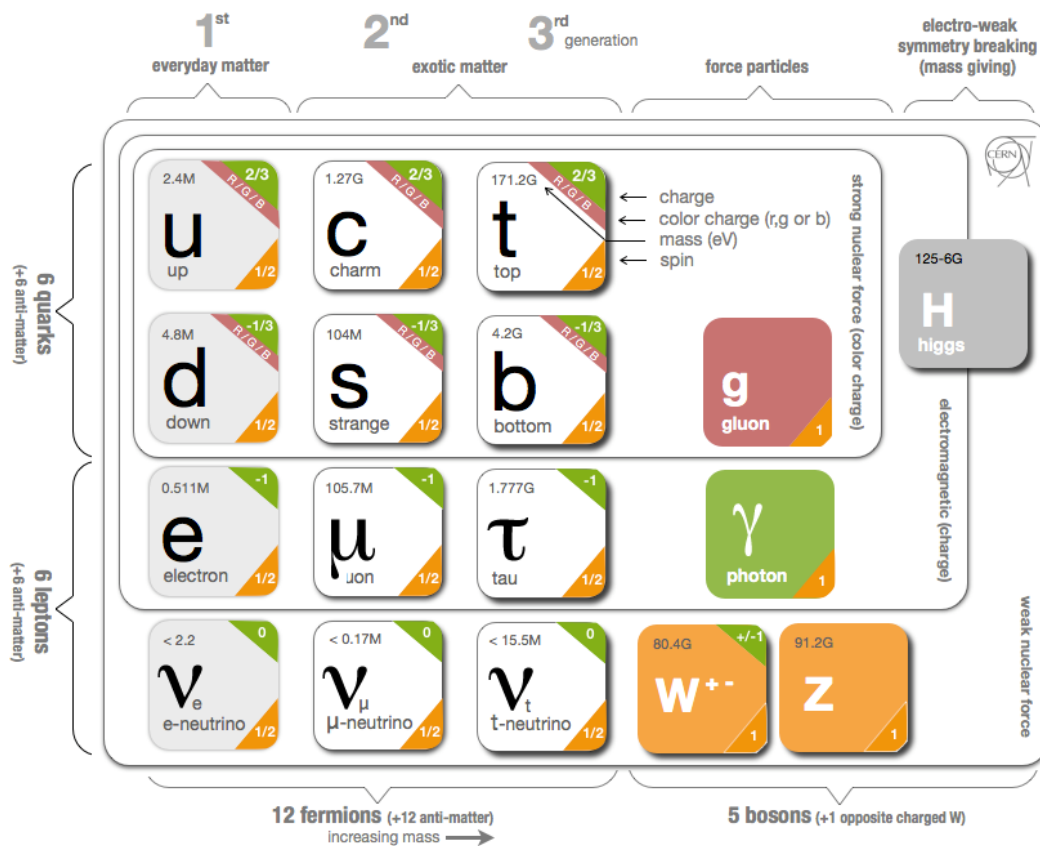


Figure 1.3: The Standard Model particle content. [41]

its kind to be discovered in 1956 by L. Cowan Jr., F. Reines, F. B. Harrison, H. W. Kruse, A. D. McGuire [37] (1995 Nobel Prize in Physics). While it was feasible to measure the masses of the charged leptons, neither the exact value of the mass of the neutrinos nor the mass generation mechanism is clear within the current status of the SM. The discovery of the *neutrino oscillation* phenomenon – when a specific neutrino flavour is created but after sufficient propagation in spacetime another flavour is detected – by the Super-Kamiokande Observatory and the Sudbury Neutrino Observatory in 1998 and 2002 respectively [38, 39] (2015 Nobel Prize in Physics) implied that the neutrinos have non-zero mass. Direct measurements of the electron-neutrino mass, by studying the energy spectrum on the tritium β -decay, recently placed the tightest upper limit at ~ 1 eV [40].

The quarks, as already mentioned, were proposed in an attempt to categorise the plethora of hadrons emerging at accelerator based experiments (e.g. Bevatron at Lawrence Berkeley National Laboratory) over the decades of 1950s-60s [42]. The idea proven correct by deep inelastic scattering experiments at the Stanford Linear Accelerator Center, where high energy electrons (5-20 GeV) fired into a fixed target of hydrogen atoms [43].

The measurements revealed that the electrons were scattering by point-like particles within the proton. The quarks would be the particles that build up the protons, and generally all the hadrons, and carry $+2/3$ or $-1/3$ of elementary charge. The discovery of hadrons with three same-flavour quarks (Δ^{++} and Ω^- with three up and strange quarks respectively [44, 45]) made the introduction of another quantum number inevitable, as otherwise Pauli's exclusion principle would be violated. This quantum number describes the ternary colour charge (r, g or b) that makes the quark interact with the strong force.

Particularly important to this dissertation are the quarks of the third generation or *heavy flavour quarks* - opposed to the *light flavour quarks* of the first two generations - the *top* and the *bottom*. These were predicted by M. Kobayashi and T. Maskawa to explain the difference on the decay rates of particles and anti-particles under spatial coordinate inversion [46] (*CP-symmetry violation*). Both of them were discovered at the Fermilab; the bottom, henceforth referred to as *b-quark*, in 1977 by the E288 experiment [47] while the top in 1995 by the CDF and DØ collaborations [48, 49]. The *mesons* - hadrons composed by two quarks - formed by the bottom quark in combination with another quark flavour (*B-mesons*), have uniquely long lifetimes ($\mathcal{O}(10^{-12})$ s). This is a result of their decay via the weak interaction which changes the flavour of a quark in a rate proportional to the elements of the so-called *Cabibbo-Kobayashi-Maskawa (CKM) matrix* [46, 50]. As qualitatively shown in Figure 1.4, the transition favoured is the $b \rightarrow t$ which is however kinematically forbidden as the top quark is heavier than the bottom, so the dominant transition is $b \rightarrow c$ but with small CKM matrix element, thus small rate. Another distinct characteristic of their decay is the potential presence of leptons, produced by the weak decay (virtual W boson) that mediates the flavour change.

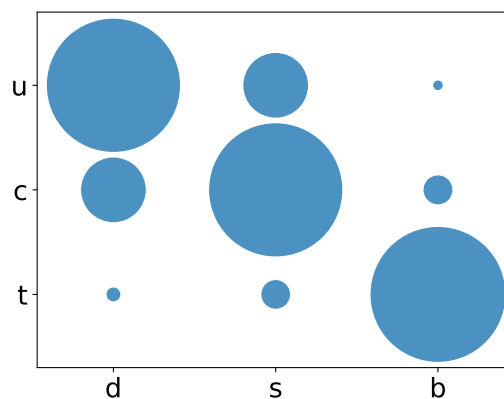


Figure 1.4: CKM matrix elements in qualitative presentation. The area of each circle is proportional to the size of each element. The absolute values of each element are given in Table A.3. Figure is made using data from [51].

On the other hand, the top quark has a very short lifetime ($\mathcal{O}(10^{-25})$ s). Because of its mass being above the W boson mass, it is actually the only quark that decays *on-shell*.

Its decay is not kinematically suppressed and occurs before it can form hadrons – via the hadronisation process described further in Section 1.3.3 – as the strong interaction timescale is at $\mathcal{O}(10^{-24})$ s. Following the size of the CKM matrix elements, its decay predominantly produce a b-quark and a W boson.

1.3 Boson Fields

1.3.1 Lagrangian and Local Gauge Invariance

The second general category of SM fields are the bosons. These fields, and the particles that emerge from them, have integer spin – either 0 and called *scalars* or 1 and called *vectors* – thus obey the Bose-Einstein statistics. In contrast to the fermions, they cannot build up matter but they rather form condensates. The physical interpretation of the vector fields is to mediate the forces acting between the fermions while the only scalar field known, the *Higgs* field, is associated with the mass generating mechanism of the SM (BEH mechanism). In a QFT formalism, the behavior of a free scalar field is derived from the Lagrangian [7]:

$$\mathcal{L}_S = \frac{1}{2}(\partial_\mu\phi)(\partial^\mu\phi) - \frac{1}{2}m^2\phi^2, \quad (1.2)$$

where ϕ denotes the field and m its mass. On the other hand, the behavior of a free vector field is derived from the so-called Proca Lagrangian [7]:

$$\mathcal{L}_{Proca} = -\frac{1}{4}F^{\mu\nu}F_{\mu\nu} + \frac{1}{2}m^2A^\mu A_\mu, \quad (1.3)$$

where A denotes the field, m its mass and F its field-strength tensor.

The SM is a gauge theory, i.e. there are multiple mathematical configurations that describe the same physical system. The transformation rules between these configurations are called *gauge transformations* and form groups called *gauge groups*. In accordance with the terms of relativity, the gauge transformations are spacetime dependent or *local* and affect a field as:

$$\Psi \rightarrow \Psi' = e^{ig\chi(x)\cdot\mathbf{T}}\Psi, \quad (1.4)$$

where x is the position 4-vector, \mathbf{T} are the $n^2 - 1$ (n^2) generators of an $SU(n)$ ($U(n)$) gauge group, g is a constant and $\chi(x)$ a phase in an abstract space. For the physical system described is the same, the Lagrangian should be symmetric, or invariant, under these transformations. The requirement of invariance of the Lagrangian under a local gauge transformation is naturally giving rise to interaction terms between fermions and the vector bosons associated with this particular group via Noether's 2nd theorem [52]. The vector fields are introduced via the replacement of the covariant four-gradients with the *covariant derivatives* in the Lagrangian:

$$\partial_\mu \rightarrow D_\mu = \partial_\mu + ig\mathbf{T}\cdot\mathbf{X}_\mu, \quad (1.5)$$

where \mathbf{X}_μ are the $n^2 - 1$ (n^2) vector fields (gauge bosons) with transformation properties defined by the $SU(n)$ ($U(n)$) gauge group.

The three SM forces are separated into two sectors, the *electroweak* and the *strong*. This separation is motivated by the nature of the BEH mechanism which gives rise to the mixing of the neutral-currents of the electromagnetic and weak forces as described below.

1.3.2 Electroweak Sector

1.3.2.1 Bosons and Interactions

The electroweak sector of the SM describes the unified weak and electromagnetic force under a common concept and by requiring the invariance of the Lagrangian under the $SU(2)_L$ and the $U(1)$ local gauge symmetry groups ($SU(2)_L \times U(1)$). According to Eq. 1.5, three gauge boson fields – $W_\mu^{k=1-3}$ – are introduced by the $SU(2)_L$ gauge group and one – B_μ – by the $U(1)$.

The weak interaction may change the charge of a fermion, in which case it is mediated by charged gauge bosons. However, it acts differently on L and R fermion states; in particular, only L particles and R anti-particles are participating in charged-current interactions and vice versa¹. The fermions can be then categorised into groups of *weak isospin* (I_W) doublets that the weak charged-current allows transitions within or singlets that remain unaffected, for example for the first generation fermions:

$$\begin{pmatrix} u \\ d \end{pmatrix}_L, u_R, d_R \quad \text{and} \quad \begin{pmatrix} \nu_e \\ e^- \end{pmatrix}_L, e_R^- \quad (1.6)$$

It is worth mentioning here that the weak eigenstates of Eq. 1.6 are not identical to the mass eigenstates². The states of Eq. 1.6 are linear combinations of the mass eigenstates and the mixing is given by the CKM matrix (Figure 1.4) for the quarks and the PMNS matrix [35] for the leptons.

The corresponding interaction term in the SM Lagrangian is:

$$g_W \bar{\Psi}_{ij} L T^k \gamma^\mu W_\mu^k \Psi_{ij}, \quad (1.7)$$

with Ψ_{ij} representing members of the weak isospin doublet, g_W the coupling strength of the interaction and $T^k = \frac{\sigma^k}{2}$ the generators of the group, where σ^k the Pauli matrices. It should be highlighted that the non-commutative nature of T^k gives rise to extra self-interaction terms between the gauge bosons of the $SU(2)_L$ group, W_μ^k , so the group is called *non-abelian*. The physical charged fields that mediate these transitions are

¹Thus the subscript L in the symmetry group.

²The mass eigenstates are solutions of the free Hamiltonian opposed to the weak eigenstates that are solutions of the weakly interacting Hamiltonian.

identified as linear combinations of two of the W_μ^k :

$$W_\mu^\pm = \frac{1}{\sqrt{2}} \left(W_\mu^1 \mp W_\mu^2 \right) \quad (1.8)$$

and listed in Figure 1.3.

The third gauge boson field of the group implies the existence of a neutral-current as well, which however do not cause transitions within an isospin doublet, or more technically doesn't change the *third weak isospin component* (I_W^3) of a fermion. It is not straightforward to correspond the W_μ^3 to the physical neutral gauge boson of the weak interaction, the *Z boson*, as experimentally it has been found that couples to both *L* and *R* particles [53]. This can be explained by the mixing of the W_μ^3 with the B_μ boson, whose interaction term:

$$g' \bar{\Psi} \frac{Y}{2} \gamma^\mu B_\mu \Psi \quad (1.9)$$

does not differentiate between chiral states. The g' factor is the coupling strength of the interaction and $\frac{Y}{2}$ the generator of the group. The latter is called *weak hypercharge* and is related to the electric charge (Q) as $Y = 2(Q - I_W^3)$. Then the physical gauge bosons are identified as:

$$\begin{aligned} A_\mu &= +B_\mu \cos \theta_W + W_\mu^3 \sin \theta_W \\ Z_\mu &= -B_\mu \sin \theta_W + W_\mu^3 \cos \theta_W \end{aligned} \quad (1.10)$$

and correspond to the physical states of *photon* and *Z boson* respectively (Figure 1.3). The parameter θ_W is called *Weinberg angle* ($\sin^2 \theta_W \simeq 0.22$ [35]) and dictates the amount of mixing between the two original gauge boson fields. This field mixing is not contrived but arise from the BEH mechanism described below.

1.3.2.2 The Brout-Englert-Higgs mechanism

The local gauge invariance principle provides an elegant and experimentally verified way to generate interactions among fields. However, the explicit mass terms of the fermions (Eq. 1.1) and vector bosons (Eq. 1.3) into the SM Lagrangian violate this invariance. For example, when the fermion mass term is decomposed into the chiral basis:

$$m \bar{\Psi} \Psi = m (\bar{\Psi}_R \Psi_L + \bar{\Psi}_L \Psi_R) \quad (1.11)$$

it is immediately apparent that Eq. 1.1 is not invariant under the $SU(2)_L$ transformation as, according to Eq. 1.6, *L* particles transform as doublets while *R* as singlets. On the other hand, it is experimentally observed that the SM fermions are not massless.

The problem is alleviated by introducing an extra two-component (complex) scalar field with potential:

$$V(\phi) = \frac{\mu^2}{2} (\phi^* \phi) + \frac{\lambda}{4} (\phi^* \phi)^2, \quad (1.12)$$

where $\mu^2 < 0$ ¹ and $\lambda > 0$ parameters that define its shape (Figure 1.5). Its lowest energy, or *vacuum*, state corresponds to $\phi \neq 0$, so the field has a non-zero and degenerate *Vacuum Expectation Value* (VEV), denoted by v . As seen in Figure 1.5, the particular choice of the vacuum state breaks the symmetry of the potential in a phenomenon called *Spontaneous Symmetry Breaking* (SSB). This non-zero VEV is naturally giving rise to mass terms in the Lagrangian of the scalar field; $\mu^2 = -2\lambda v^2$ and $m = \sqrt{2\lambda}v$.

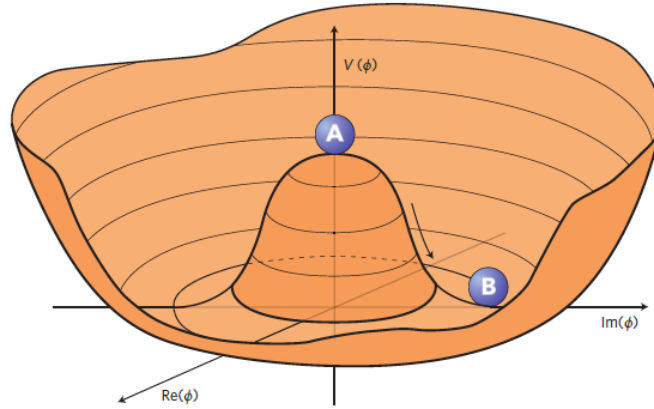


Figure 1.5: Illustration of the potential described by Eq. 1.12. A symmetric, but not the vacuum, state corresponds to $\phi = 0$ (A) while the particular choice of the vacuum (B) breaks this symmetry and gives rise to $v \neq 0$ GeV. [54]

Within the SM the particles acquire mass terms by SSB of the local electroweak gauge symmetry ($SU(2)_L \times U(1)$) and the scalar field introduced is called *Higgs* field. The Higgs field requires at least four degrees of freedom to give rise to the masses of the three physical weak bosons (W^+ , W^- , Z) and the Higgs boson(s) itself, so the minimal model consist of a complex scalar weak isospin doublet of a charged and a neutral component:

$$\phi = \begin{pmatrix} \phi^+ \\ \phi^0 \end{pmatrix} \quad (1.13)$$

and vacuum state:

$$\phi_0 = \frac{1}{\sqrt{2}} \begin{pmatrix} 0 \\ v \end{pmatrix}, \quad (1.14)$$

where $v \approx 246$ GeV is experimentally determined [35]. The choice of the field and its vacuum state has been made by S.Weinberg in 1967 [8] in order to break the $SU(2)_L \times U(1)$ symmetry but leave the subgroup $U(1)_{em}$ with generator $Q = I_W^3 + \frac{Y}{2}$ unbroken, so that the photon remains massless. From this subgroup the electromagnetic interaction between a fermion (matter) and a massless boson (light) can be derived within the QFT

¹As $\mu^2 < 0$, the associated term in the initial Lagrangian cannot be interpreted as the mass term of the field.

called *Quantum Electrodynamics* (QED) with Lagrangian:

$$\mathcal{L}_{\text{QED}} = i\bar{\Psi}\gamma^\mu\partial_\mu\Psi - m\bar{\Psi}\Psi - e\bar{\Psi}\gamma^\mu Q A_\mu\Psi - \frac{1}{4}F_{\mu\nu}F^{\mu\nu}, \quad (1.15)$$

where e is the elementary charge that acts as a coupling constant. The first two terms and the last one originate from the Dirac (Eq. 1.1) and Proca (Eq. 1.3) Lagrangian respectively. The third term is the interaction term of Eq. 1.9.

Summarising, the Lagrangian of the Higgs field is initially invariant under $SU(2)_L \times U(1)$, thus according to Eq. 1.5:

$$\partial_\mu \rightarrow D_\mu = \partial_\mu + ig_W \mathbf{T} \cdot \mathbf{W}_\mu + ig' \frac{Y}{2} B_\mu \quad (1.16)$$

but after the SSB the action of the covariant derivative to the vacuum state of the Higgs field $((D_\mu\phi_0)^\dagger(D^\mu\phi_0))$ according to the first term of Eq. 1.2) generates mass terms for the W_μ^k and mixing between the W_μ^3 and B_μ fields.

It is remarkable that the Higgs doublet of Eq. 1.13 can be used to give mass to the fermions of the SM too. By replacing the mass term of Eq. 1.11 with:

$$g_f(\bar{\Psi}_R\phi^\dagger\Psi_L + \bar{\Psi}_L\phi\Psi_R) \quad (1.17)$$

it becomes $SU(2)_L$ invariant and after the SSB fermion masses are generated:

$$\frac{g_f}{\sqrt{2}}u(\bar{\Psi}_R\Psi_L + \bar{\Psi}_L\Psi_R) = \frac{g_f}{\sqrt{2}}u\bar{\Psi}\Psi = m_f\bar{\Psi}\Psi. \quad (1.18)$$

The constant g_f that couples each fermion to the Higgs field is called *Yukawa coupling* and is a free parameter of the model. The above formulation applies to the down-type fermions while for the up-type the conjugate Higgs doublet is needed, $\phi^c = -i\sigma^2\phi^*$.

The neutrino masses could be introduced on the same way. However, there is no evidence that the R state exists as it doesn't participate in any interaction of the SM. Moreover, their masses have been experimentally limited to the $\mathcal{O}(\text{eV})$ – orders of magnitude smaller than the rest of the SM particles – a fact that makes an alternative mass generation mechanism plausible. Neutrinos being electrically neutral could be their own anti-particles (Ψ^c), this would allow a mass term of the form of:

$$M(\bar{\Psi}_R\Psi_L^c + \bar{\Psi}_L^c\Psi_R) \quad (1.19)$$

to be introduced into the Lagrangian without violating the SM symmetry group thus without the need of SSM of the Higgs field. In that case neutrinos would be *Majorana* particles and experiments are currently looking to determine this [55].

The Higgs boson was the last piece of the SM to be discovered in 2012 by the ATLAS and CMS collaborations at CERN [56, 57]. Its mass is a free parameter of the SM so it

had to be measured experimentally. The most precise estimate currently available is $m_h = 125.26 \pm 0.21$ GeV [58].

1.3.2.3 Boson Decay Properties

Vital for this dissertation are the decay properties of the electroweak gauge and Higgs bosons. The W^\pm bosons can decay to a pair of charged-neutral leptons or an up-down type quarks per generation. The BR to leptons is $\sim 33\%$ and to quarks $\sim 67\%$, while the rate to particular quark flavours is proportional to the square of the corresponding CKM matrix element (Figure 1.4). The Z boson decays to a fermion and its anti-particle pair. In particular, it decays to neutral leptons with BR $\sim 21\%$, to charged leptons with 10% and to quarks with 69%, while down-type quarks are slightly favoured because of the non-zero Weinberg angle. A correction to the BRs is also applied due to increasing masses of the fermions per generation.

The Higgs boson decays, on the other hand, are not limited to fermions, as for the electroweak gauge boson cases. In general, its decay BR is proportional to the (squared-)mass of the (boson) fermion it couples with. Its dominant decay modes are presented in Table 1.2.

Table 1.2: The dominant branching ratios for the SM Higgs boson with mass 125 GeV. [59]

Decay Mode	Branching Ratio [%]
$h \rightarrow b\bar{b}$	58.2
$h \rightarrow W^+W^-$	21.4
$h \rightarrow gg$	8.2
$h \rightarrow \tau^+\tau^-$	6.3
$h \rightarrow c\bar{c}$	2.9
$h \rightarrow ZZ$	2.6
$h \rightarrow \gamma\gamma$	2.3

1.3.3 Strong Sector

1.3.3.1 Bosons and Interactions

The strong sector of the SM describes the strong force acting between the quarks to bound them into hadrons. The underlying gauge symmetry group that generates it is $SU(3)$. Following the local gauge invariance principle and the Eq. 1.5, eight gauge boson fields – $G_\mu^{\alpha=1-8}$ – are introduced. These correspond to the physical massless *gluons* shown in Figure 1.3. The QFT that describes the strong force between quarks and gluons is called *Quantum Chromodynamics* (QCD) and the interaction term induced is:

$$g_s \bar{\psi}_c T^\alpha \gamma^\mu G_\mu^\alpha \Psi_{ij} \quad (1.20)$$

where g_s the coupling strength of the interaction and $T^\alpha = \frac{\lambda^\alpha}{2}$ the generators of the group. Similarly to the $SU(2)_L$ symmetry, the $SU(3)$ group has a non-abelian nature as well that gives rise to extra self-interaction terms between the G_μ^α gauge fields. In this case, though, the Ψ_{ij} represents members of the field triplet:

$$\begin{pmatrix} r \\ g \\ \bar{b} \end{pmatrix}, \quad (1.21)$$

the so-called *colour* triplet. The strong interaction is then allowing transitions between this ternary colour charge.

The QCD is analogous to the QED with the difference of the size of the coupling constant and the fact that gluons are eight and carry colour charge in contrast to the photon that is one and neutral. This characteristic of gluons, give rise to two distinct properties of QCD described below.

1.3.3.2 Confinement and Asymptotic Freedom

There is wide experimental indication that quarks and gluons cannot be isolated and are always found confined into hadrons. Although it is yet to be understood from first principles, starting from the Lagrangian, it is believed that *colour confinement*, which postulates that only colourless states can propagate freely, is a fundamental property of the strong interaction. The phenomenon can qualitatively be explained by the fact that the gluons, the force mediators, carry colour charge themselves. Considering two quarks that interact by exchanging gluons, the strong force among them remains constant with distance. This is an effect after colour charge is filling the space between them by the exchange of gluons. As a consequence, the work needed to separate them is infinite.

The colour confinement property is particularly relevant to this dissertation as it affects the manifestation of quarks and gluons at macroscopic distances. Because the *partons*, as collectively called, cannot propagate freely, they appear as collections (*jets*) of colourless particles (hadrons). These are formed in the process called *hadronisation* that is qualitatively illustrated in Figure 1.6. Two quarks that are produced with high and opposite velocities (i) are interacting with the strong force by exchanging gluons (ii). As the energy stored in the colour field is growing with distance, because of the constant force, at some point is enough to form a new $q\bar{q}$ pair from the vacuum in a more energetically favoured configuration (iii). This process continues and more $q\bar{q}$ are formed (iv) until the velocity of the quarks is small enough to keep them confined into the hadrons (v). Thus in an experimental facility the partons always appear as hadronic jets.

The second distinct property of QCD is related to the behavior of the theory at the

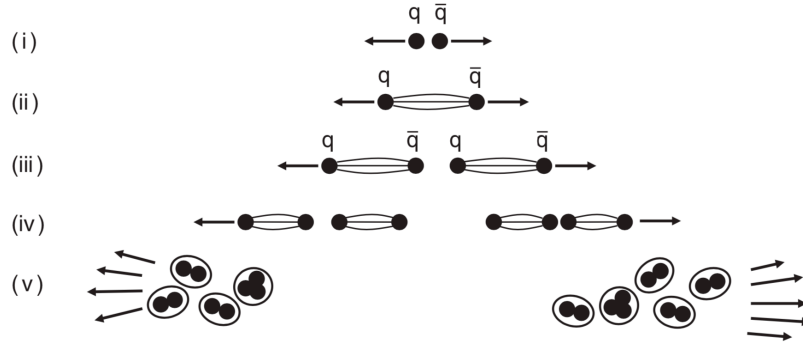


Figure 1.6: Qualitative illustration of the hadronisation process. [7]

high energy regime ($\gg \mathcal{O}(100)$ MeV). In order for this to become apparent, an aspect of the particles behavior should be first discussed – for simplicity in the context of QED. Based on the very basic uncertainty principle ($\Delta E \Delta t \geq 1/2$) the production of particles with arbitrary energy is allowed as long as their lifetimes are short enough; this is illustrated in the Feynman diagram of Figure 1.7a for the case of a fermion pair initiated from a photon. A particle interaction can be then decomposed into a sum of infinite number of diagrams with different number of loops. The example of two electron scattering by exchanging a photon is shown in Figure 1.7c. During a measurement, these diagrams all contribute to an observable. Following the Feynman calculus rules, each interaction vertex contributes a factor of the coupling constant to the matrix element. The QED process of Figure 1.7c then corresponds to the sum of the *Leading Order* (LO) matrix element without any loop, the *Next-to-Leading Order* (NLO) matrix element with one loop, etc.:

$$\mathcal{M} = M_{LO} + M_{NLO} + M_{NNLO} + \dots = \alpha_{em} M_1 + \alpha_{em}^2 M_2 + \alpha_{em}^3 M_3 + \dots \quad (1.22)$$

where $\alpha_{em} = \frac{e^2}{4\pi}$. However, the integration over all the possible momenta of the loops leads to unphysical infinities. In a procedure called *renormalisation*, these infinities can be absorbed in the redefinition of the coupling constant as function of the energy scale of the process: $g = g(Q^2)$. In an experimental measurement, this $g(Q^2)$ is always measured – the *effective coupling*.

The evolution (*running*) of $g(Q^2)$ with the energy scale depends on the type of diagrams involved in an infinite sum as the one in Figure 1.7c. In the case of QED, fermion loops are only allowed and this makes the $\alpha_{em}(Q^2)$ to increase with energy and a divergent behavior eventually appears. On the other hand in the QCD case, loops of gluons as of Figure 1.7b are also allowed. This leads the $g_s(Q^2)$ to decrease with energy leading to an *asymptotic free* theory. It is worth pointing, though, that the effect is much stronger on QCD than on QED. In particular, on energy scales relevant to this work (i.e. $\mathcal{O}(1-100)$ GeV) the g_s changes by $\sim 75\%$ but the α_{em} only by $\sim 5\%$.

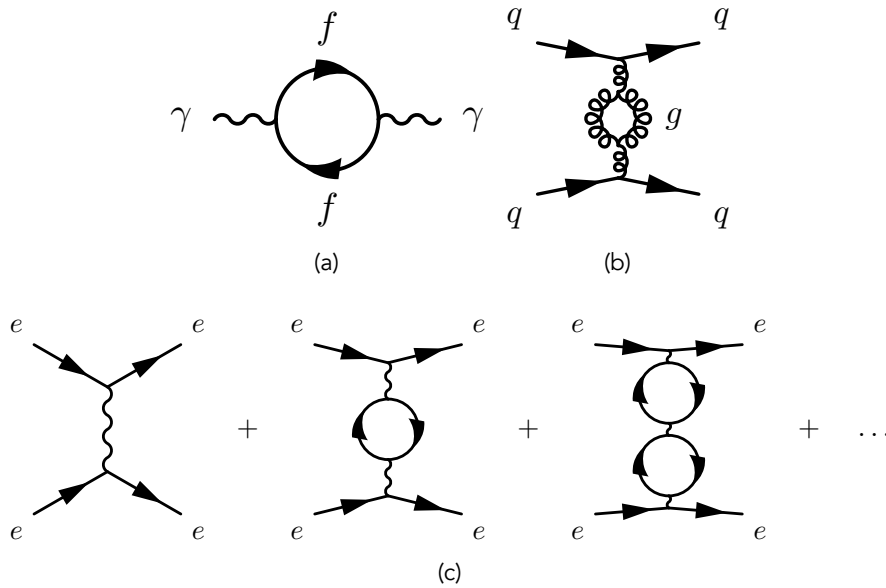


Figure 1.7: (a) The production and annihilation of a fermion pair initiated from a photon (*loop diagram*). (b) The production and annihilation of a gluon pair initiated from gluons mediating a quark scattering. (c) Decomposition of an electron scattering process to the contributing loop diagrams. All the diagrams comprise an original work of the author.

On the other side, at low energy scales ($\lesssim \mathcal{O}(100)$ MeV), the coupling strength of QCD becomes so large ($\mathcal{O}(1)$) that the perturbation theory used to calculate matrix elements, as the one of Eq. 1.22, is no longer valid. This is the reason that hadronic-scale phenomena, such as the hadronisation, are not well understood and calculated¹.

1.4 Physics Events Simulation

The predictions of a model (e.g. SM or BSM) are essential for its reliability as they can be compared with experimental results. Furthermore, they are useful from an experimental point of view to predict the outcome of a measurement and optimise it accordingly. In the context of high energy physics these predictions span over 20 orders of magnitude, from the microscopic scale of partons to the macroscopic scale of a particle detector. Fortunately, the different behavior of physics laws in this vast range can be separated or *factorised* as the energy scales involved are different. The predictions at an energy scale E can be derived from results at a higher energy scale E^n . This approach breaks-down the problem into different components. Another challenge is induced by the indeterministic nature of quantum mechanics that causes fluctuations to the observables. To incorporate this behavior into the predictions, *Monte Carlo* (MC) methods are used to generate them, where numerical results are obtained by randomly

¹Calculations have been only performed in an approach called *lattice QCD* where the spacetime is discretised introducing a momentum cut-off inversely proportional to the lattice spacing.

sampling distributions. The purpose of *events simulation*, in the context of this work, is to create a sample of events, – the “set of outgoing particles produced in the interaction between two incoming particles” [60] – based on a theoretical model, that will accurately resemble the data produced by the LHC. It is worth noting that for reliable predictions to be made, the amount of simulations should exceed the data¹. Because of the law of large numbers the average value of an observable measured in repeated MC experiments corresponds to the expected one – the probability-weighted average – thus it’s only useful if it has small statistical uncertainty.

The event simulation pipeline of this work proceeds on the following consecutive steps and is illustrated in Figure 1.8:

1. Hard-scatter matrix element calculation and parton showering.
2. Hadronisation and underlying event inclusion.
3. Detector simulation.

A brief overview of each one is following.

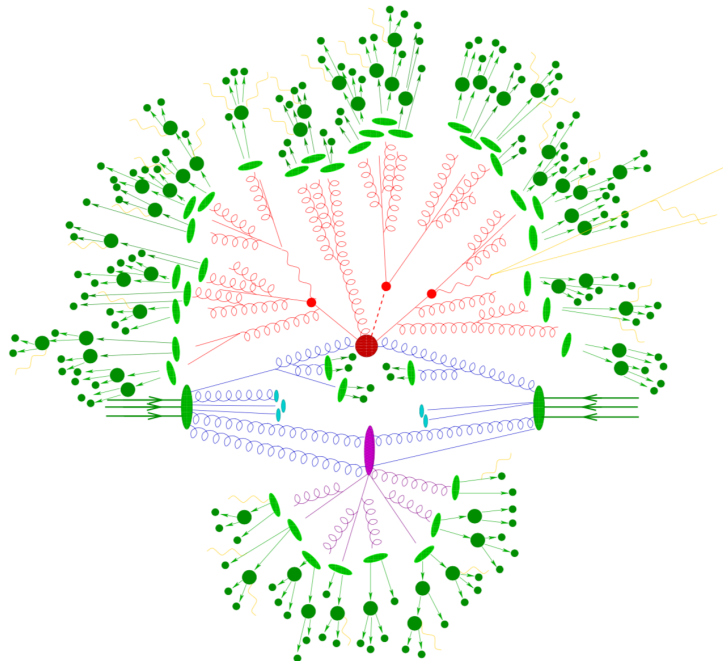


Figure 1.8: A pictorial representation of a simulated event. The big red blob represents the hard-scatter interaction initiated from proton partons (blue spiral lines) and resulting new particles that consecutively decay (red lines and small red blobs). All the partons can shower to produce gluons (spiral lines) or photons (yellow lines). Secondary interactions (underlying event) are taking place (purple blob) producing additional partons. The partons finally hadronise creating colorless hadrons (light green ellipses) that decay to stable hadrons (dark green blobs). [61]

¹Typically three to five times larger for this work.

1.4.1 Matrix Elements and Parton Showering

The generation of physics process events starts with the interaction matrix element calculation of a $2 \rightarrow N$ *hard-scatter* interaction (big red blob in Figure 1.8) where two partons (blue lines in Figure 1.8) collide to produce outgoing particles (SM or Supersymmetry). The inclusive cross-section is given by the convolution of the incoming partons information with the differential cross-section. For an example $pp \rightarrow \chi\bar{\chi}$ process this is:

$$\sigma_{pp \rightarrow \chi\bar{\chi}} = \prod_{i=1,2} \int f^{p_i}(x_i, Q^2) dx_i \times \int \frac{d\sigma_{pp \rightarrow \chi\bar{\chi}}(|\mathcal{M}|^2)}{d\Omega} d\Omega. \quad (1.23)$$

The $f^p(x, Q^2)$ is called *Parton Distribution Function* (PDF) and gives the probability to find a parton p , with proton momentum fraction x , inside the proton at an interaction energy scale or momentum transfer Q^2 . The PDFs are derived from data and as an example, Figure 1.9 shows one of the PDFs used in this work. The differential cross-section $d\sigma/d\Omega$ form is given mainly by the matrix element \mathcal{M} that describes the process $pp \rightarrow \chi\bar{\chi}$. This is computed in a fixed-order in the coupling constant(s) (e.g. \mathcal{M}_{LO} , \mathcal{M}_{NLO} , etc.) and is integrated over the final-state phase space Ω via MC methods.

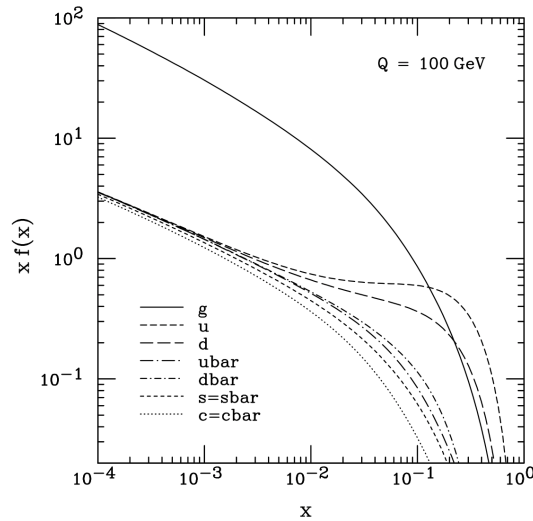


Figure 1.9: The CTEQ6M PDF for momentum transfer $Q^2 = (100 \text{ GeV})^2$. [62] The Q is referred as *factorisation scale*.

The two resulting particles from the collision are usually unstable but as their, typically electroweak, decay does not affect the production cross-section of Eq. 1.23 it is treated in a consecutive step. In particular, particle BR values are read by the *showering* program that takes care of these, and potentially consecutive, decays (small red blobs in Figure 1.8).

For the process at hand to be physically realistic, the showering step is also responsible for generating the QCD, and the minor QED, radiation emitted by both the initial-

and final-state partons (blue and red spiral lines respectively in Figure 1.8), the so-called *Parton Showering* (PS). In a first approximation this is achieved with parametrised branching functions describing higher-order real-emissions, for instance, $q \rightarrow gq$ splittings with particular probability and energy sharing between the daughter partons.

The showering step is extremely important to describe the LHC collision events as most of the large hadronic activity observed is created by QCD radiation. Therefore, to improve the accuracy of the simulation, it is common for explicit matrix element calculations to be performed (e.g. $pp \rightarrow W + 1\text{jet}$). To avoid double counting, these calculations are *merged* with the PS by vetoing particular parton branchings [63].

As mentioned already, the matrix element involved in Eq. 1.23 is calculated at fixed-order. Higher-order matrix elements (NLO, NNLO, etc.) provide loop corrections to a process but also induce overlaps with the real-emissions of the PS. These are *matched* together by either subtracting the overlaps from the matrix element (MC@NLO method [64]) or from the PS (Powheg method [65]).

1.4.2 Hadronisation and Underlying Event

The showering evolution reduce the partons energy scale at $\mathcal{O}(1)$ GeV where the hadronisation, described in Section 1.3.3, takes over to form colorless hadrons (light green ellipses in Figure 1.8). As the process is not calculable from the Lagrangian (non-perturbative regime), phenomenological models are used to describe it. In general, these models have iterative nature and in each parton branching a probability defines a particular flavour and energy sharing occurrence. These hadronisation models are tuned by parameters fit to data, and for this work, LHC Run 1 $\sqrt{s} = 7$ TeV data have been used to do so [66].

Many of the hadrons produced are unstable (e.g. B-mesons). Their decays are treated as a final step of the hadronisation and are dictated by explicit rules regarding the allowed modes and BRs. In general, all the particles with lifetime up to 30 ps^1 are decayed in this step (taus as well). The resulting particles considered stable are then: protons, neutrons, pions, heavier mesons and baryons (e.g. Kaons, Lambdas), electrons, muons, neutrinos (dark green blobs in Figure 1.8) and photons.

Finally, there is an additional hadronic activity in an event that does not directly originate from the hard-scatter interaction. This can be QCD radiation from the proton remnants – the remaining partonic content of the proton is not a colour-singlet anymore – or even products of interactions among them (secondary interactions, purple blob in Figure 1.8). This activity is collectively called *underlying event* and it's important to be modeled as it contributes non-negligibly to a hadronic collision event. As the energy scale of the underlying event is generally low, tunable phenomenological models are used in this case too [66].

¹A relativistic particle with proper lifetime more than 30 ps would decay at the scale of the detector medium (beam pipe), $c\tau \simeq \mathcal{O}(10 \text{ mm})$.

1.5 Status and Deficiencies

1.5.1 Precise Predictions

The elegant mathematical description of the SM is followed by a tremendous experimental verification. For instance, one of the tests of QED is the comparison of the *fine-structure constant* ($\alpha = \alpha_{em}(m_e)$) measurements by independent methods. Experimental inputs are combined with extremely precise SM calculations (α^5 , >10,000 Feynman diagrams) and the current agreement between the two most precise measurements is of the order of one trillionth [67]. This level of precision is equivalent of a model that would be able to calculate the number of galaxies in the observable universe with an uncertainty of ± 1 [68].

Likewise QED, predictions of QCD and the unified electroweak theory have been also verified by numerous high energy experiments. The two examples following are demonstrating this. First, the running of the strong coupling constant, as a result of the perturbative QCD calculations, is in agreement with the experimental data over four orders of magnitude, as it can be seen in Figure 1.10a. Second, after the determination of the Higgs boson mass, the SM is able to predict its couplings to fermions and gauge bosons. These can be parametrised as function of cross-section times branching ratio to measure any deviation from the SM prediction via multiple production and decay channels. In such a combined measurements the coupling modifiers, $\kappa_{F,V} = \frac{\sigma^{\text{measured}} \times BR^{\text{measured}}}{\sigma^{\text{SM}} \times BR^{\text{SM}}}$, are compatible with unity that is expected from SM, as it can be seen in Figure 1.10b.

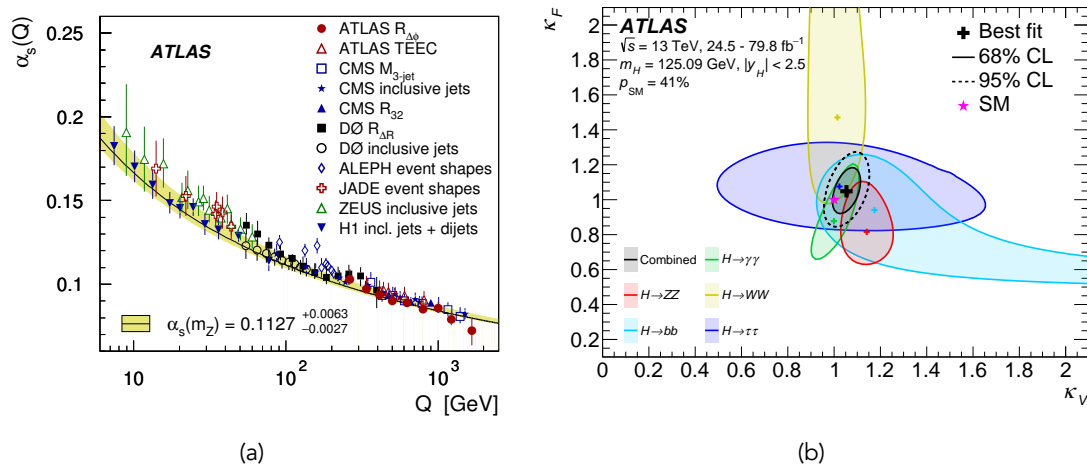


Figure 1.10: (a) Measurement of the QCD coupling constant α_s over a large energy range by several experiments. The result is in agreement with its running behavior predicted by QCD. [69] (b) Combined fit of multiple measurements in the plane of Higgs coupling modifiers indicates the compatibility of the data with the SM prediction. [70]

Finally, the model provides a consistent description in a extensive energy scale as

well. This can be seen in Figure 1.1, where elementary particle production cross-section measurements are able to verify predictions spanning over 12 orders of magnitude.

Despite the apparent success, there is scientific consensus that the model is far from complete. Foremost, there are prominent observations that are not explained by the SM. These include the gravitational force, the presence of Dark Matter and the matter-antimatter asymmetry in the Universe. There are also theoretical puzzles in some aspects of the model, examples are the Hierarchy problem and the Strong CP problem. A review of the different SM problems can be found in the Introduction chapter of [71]. It is important, though, to highlight the two issues that motivate the particle searches of this dissertation.

1.5.2 Dark Matter

Since 1930s there is strong evidence in observational data that the baryonic matter – i.e. matter consisting of atoms in astronomical terms – of galaxies is not enough to justify their motion. The most accepted hypothesis to explain these observations is an extra non-baryonic form of matter called *Dark Matter* (DM)¹. DM seems to span from the core to the outskirts of the galaxies and to actually dominate in abundance the baryonic matter. This has been estimated by measuring the rotation velocity of the stars and the gas of the galaxy as function of the distance from the centre. In Figure 1.11a it can be seen that the data deviate from Kepler’s law considering no DM but only the visible baryonic matter. Recently, observations were able to map the DM distribution (Figure 1.11b) by measuring the distortion of light rays emitted from galaxy clusters, caused by a phenomenon called *gravitational lensing* where the spacetime is curved by the invisible DM mass [73]. The above measurements allows a fermionic nature for DM.

It is clear that DM interacts gravitationally, additionally, evolutionary models of the Universe indicate that DM particles are non-relativistic [72]. Considering also the apparent fact that it does not interact with the electromagnetic nor the strong force, the only possibility is weak interactions with the SM. Thus we refer to a Weakly Interacting Massive Particle (WIMP) type. The DM particle should be also stable enough in order to be abundant from its creation at the Big Bang until today. Concluding, none of the SM particles fulfills all these requirements.

By qualitative arguments the order of strength of a potential DM interaction with the SM particles can be found. In the early Universe, when the energy was high, the DM particles were in thermal equilibrium via same rate of annihilation to and production from lighter SM particles, so the DM density ($\Omega_{\text{DM}}h^2$, where h the normalised Hubble constant) was constant (A in Figure 1.12). As the Universe evolved and the energy dropped the production wasn’t kinematically allowed anymore so the DM abundance started to decrease (B in Figure 1.12). However, because of the continuous expansion of

¹The modification of the Newtonian gravity is also an alternative explanation but faces problems in explaining variety of galaxy cluster data. [72]

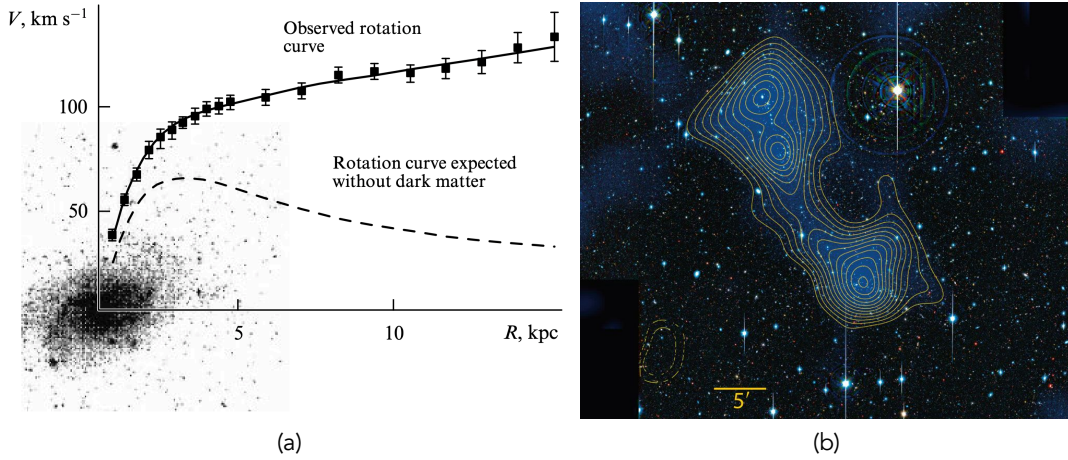


Figure 1.11: (a) Rotation curve of the nearby M33 galaxy. [72] (b) A DM filament connecting the Abell 222 and Abell 233 galaxy clusters separated about 60 million light-years. The image is a superposition of the galaxy clusters in the visible spectrum taken with the Subaru telescope on Mauna Kea, Hawaii and the reconstruction of DM mass density in blue/contours. [73]

the Universe the DM density dropped so much that the annihilation effectively stopped and the DM *froze-out*, up to a dilution by the further expansion of the Universe (C in Figure 1.12). This is the DM density measured today, the *relic density*, and it can be related to the annihilation cross-section (in SI units) by [74]:

$$\Omega_{\text{DM},0} h^2 \simeq \frac{3 \times 10^{-27} \text{ cm}^3 \text{ s}^{-1}}{\langle \sigma v \rangle} \quad (1.24)$$

where $\langle \sigma v \rangle$ the average annihilation cross-section (v is the particle velocity in this context). Since $\Omega_{\text{DM},0} h^2$ has been measured to be ~ 0.1 [35], $\langle \sigma v \rangle \sim 3 \times 10^{-26} \text{ cm}^3 \text{ s}^{-1}$. In natural units, this value corresponds to a cross-section at the order of picobarn¹ and as it can be seen in Figure 1.1, this is a typical cross-section of the electroweak processes. This rough calculation supports a WIMP with mass $\mathcal{O}(100 \text{ GeV})$.

1.5.3 Hierarchy Problem

The Higgs mechanism provides a simple way to generate mass terms into the SM Lagrangian but with the price of introducing an elementary scalar field. Elementary scalars suffer from corrections induced by loop diagrams. For example, the second term of the Higgs potential (Eq. 1.12) describes the self-interaction diagram of Figure 1.13a. As previously discussed, integration over the momenta of the loop leads to infinities. At this time it is rational to perceive the SM as an *effective field theory* of a more fundamental theory² thus valid up to a specific energy scale, the *cut-off scale* (Λ). Then the loop integral should be calculated until Λ . The diagram of Figure 1.13a contributes to

¹ 1 barn = 10^{-24} cm^2 and $v \sim c/3$

² The divergent behavior of QED with energy increase is another hint toward this hypothesis.

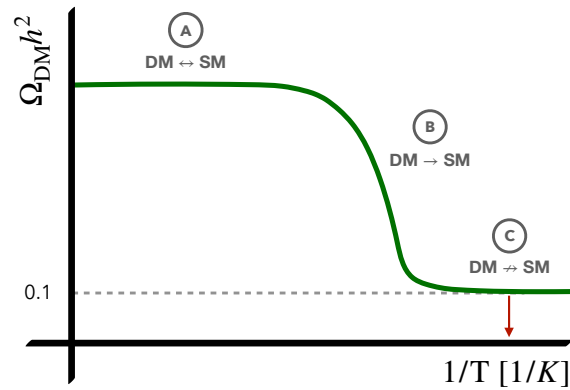


Figure 1.12: Qualitative DM density evolution curve over the temperature of the Universe. The red arrow indicates the present moment. The figure comprises an original work of the author.

the $\phi^\dagger\phi$ term, thus inducing a correction to the mass of the Higgs boson:

$$\delta m_h \sim \lambda \Lambda^2, \tag{1.25}$$

where λ is at the order of 0.1. The choice of Λ should be made at the energy scale where the SM breaks down. Certainly, there should be new phenomena emerging at the Planck scale ($\sim 10^{19}\text{GeV}$) where the effects of quantum gravity become important. Putting the pieces together, an enormous cancellation or *fine-tuning* to the 34th decimal digit is required between the μ^2 parameter of the Higgs potential (see Eq. 1.12) and Λ^2 to arrive to the observed value of $m_h^2 \sim (100 \text{ GeV})^2$. The hierarchy problem is this large discrepancy between the electroweak and the Planck scale.¹

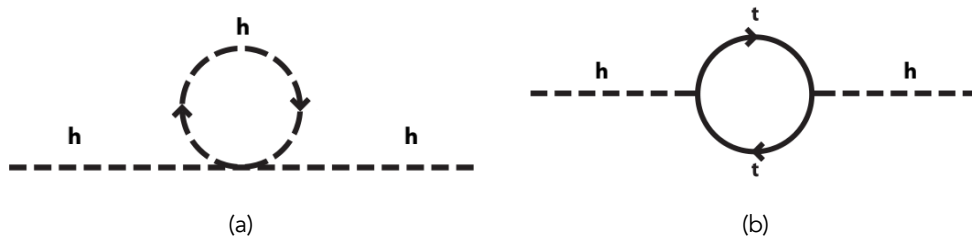


Figure 1.13: Higgs (a) ϕ^4 and (b) fermion loop diagrams. The diagrams comprise an original work of the author.

Furthermore, the problem is not only limited to self-interaction diagrams. All the particles that couple to the Higgs boson (even the ones not discovered yet!) will actually induce corrections to its mass proportional to their coupling. The strongest Higgs coupling known is the top quark Yukawa coupling, g_t . The correction then to the Higgs

¹Although this might not be a problem for an Anthropic Principle believer.

mass coming from the loop diagram of Figure 1.13b is:

$$\delta m_h \sim -g_t \Lambda^2. \quad (1.26)$$

As this is a fermion loop, the correction is negative and its sign becomes important in alleviating this puzzle.

The theoretical framework introduced in the following chapter provides elegant solutions to both the hierarchy and the DM problem of the SM.



2. Supersymmetric Extension

Supersymmetry is one of the most developed theoretical frameworks beyond the Standard Model that provides elegant solutions to various physics problems

2.1 (Super)Symmetries

The notion of symmetries has paramount importance to the SM as all the interactions that induce physical phenomena can be derived by symmetry considerations of the Lagrangian. Owing to Noether's theorems, the invariance of \mathcal{L} under *global* continuous transformations is related to conserved quantities – conservation laws – or under *local* gauge transformations to additional constrain relations giving rise to interaction terms (see Section 1.3).

It is instinctive to investigate whether there are additional symmetries nature might respect beyond the known ones. The discussion focuses on extending the space-time symmetries in a way of achieving algebraic relations where the symmetry generators mix with each other – i.e. do not commute, $[\mathbf{T}^\alpha, \mathbf{T}^\beta] \neq 0$. This has been proven impossible

using the internal symmetry group generators (Coleman-Mandula theorem [75]), yet if new generators that transform the spin of the state they act on are introduced (anti-)commutative relations are allowed (Haag–Lopuszanski–Sohnius theorem [76]). These are called *fermionic* generators and the operators they form (Q) change a fermionic state into a bosonic one and vice versa:

$$Q|\text{Fermion}\rangle = |\text{Boson}\rangle, \quad Q|\text{Boson}\rangle = |\text{Fermion}\rangle. \quad (2.1)$$

The discrete symmetry that leaves the Lagrangian invariant under the above changes is called *Supersymmetry* (SUSY) and the extended space-time, where additional fermionic coordinates exist, *superspace*. Fermionic and bosonic states are then grouped together into *supermultiplets*, called *superpartners* to each other and described by *superfields* that are function of both the Minkowski and the new fermionic coordinates, $\Omega(\chi^\mu, \theta)$.

It is crucial to emphasise that SUSY transformations of Eq. 2.1 change only the spin of a state, leaving the rest of the quantum numbers and properties intact. If SUSY was an exact symmetry of nature the superpartners would all have the same mass. This is not feasible, however, as there is no experimental evidence, for instance, of a charged scalar particle with mass 0.5 MeV. As S.P. Martin emphasise, “these particles would have been extraordinarily easy to detect long ago” [77]. Therefore, SUSY has to be a broken symmetry and this can be realised by either explicit SUSY-violating terms or SSB, such as the electroweak $SU(2)_L \times U(1)$ of the SM, presented in Section 1.3.2. The latter is theoretically favoured but in the context of this dissertation we will refrain ourselves from specifying a particular SUSY-breaking mechanism. Nevertheless, phenomenological predictions can be made in an effective theory approach where the unknown breaking mechanism effects are parametrised in a “low” energy regime ($\mathcal{O}(\text{TeV})$) by explicit SUSY-violating terms. This is referred to as *soft* SUSY-breaking, while the form and size of the SUSY-violating terms is constrained by both theoretical and phenomenological arguments as presented below. The SUSY-breaking mechanism that is realised in nature could be determined by the experimental constrain of the soft SUSY-breaking parameters.

2.2 The Minimal Supersymmetric Standard Model

Having the SM, as presented in Chapter 1, as a basis, this section introduces its minimal SUSY extension, called *Minimal Supersymmetric Standard Model* (MSSM). The driving property for its construction is that supermultiplets should have the same number of fermionic and bosonic degrees of freedom. Thus a (massless) vector boson would group

with a two-component spinor describing a spin-1/2 fermion¹. It can be argued that the SM particle content is not enough to account for the fermions needed to group with the SM gauge bosons. For example, there is no fermion which is an $SU(3)$ octet as the gluon, while similar arguments hold for the electroweak bosons too. Therefore, new fermion fields are introduced to form the so-called *vector supermultiplets* (VSMs). The names of the states emerging from these new fields is derived from the associated gauge boson by appending the word "ino", e.g. gluino (\tilde{g}).

A VSM, however, do not allow its component fields to transform differently based on their chirality. As this is the case for all the SM fermions under the $SU(2)_L$ transformation, these are grouped into so-called *chiral supermultiplets* (χ SM) with complex scalar fields. Quantum number arguments indicate that the scalar field content of the SM should also be extended to include the superpartners of the fermions. The name of the latter derives from the SM associated states by prepending an "s", for instance the first generation leptons are grouped with selectrons and sneutrinos:

$$\begin{aligned} \begin{pmatrix} \nu_e \\ e \end{pmatrix}_L & \text{ grouped with } \begin{pmatrix} \tilde{\nu}_e \\ \tilde{e} \end{pmatrix}_L, \\ e_R & \text{ grouped with } \tilde{e}_R. \end{aligned} \quad (2.2)$$

Similar supermultiplets are formed for the rest of the generations and the quarks as well. It is subtle, yet important, to mention that the \tilde{e}_L and \tilde{e}_R states have both spin zero, thus the L/R notation indicates the associated SM field only.

Regarding the Higgs sector, spin-1/2 fermionic superpartners, called *higgsinos*, are introduced to group with the SM Higgs boson into χ SM. An important consequence of SUSY is that the Higgs sector should be extended in order to generate mass for the up-type fermions. In the SM this is happening via the conjugate Higgs doublet (ϕ^c) but a term of the form of $g_f \bar{L} \phi^c R + \text{h.c.}$ (Eq. 1.17) explicitly violates SUSY [78]. The solution comes by the addition of an extra doublet so that the Higgs sector is composed by four complex scalar fields:

$$H_u = \begin{pmatrix} H_u^+ \\ H_u^0 \end{pmatrix}, \quad H_d = \begin{pmatrix} H_d^0 \\ H_d^- \end{pmatrix} \quad (2.3)$$

and the corresponding higgsino fields.

The aforementioned field content is summarised in Table 2.1 and completes the MSSM. No new force carriers are introduced and the local gauge invariance principle is still used to generate interactions mediated by the spin-1 components of the VSM (gauge bosons), as described in Section 1.3. Invariance under the $SU(3) \times SU(2)_L \times U(1)$ symmetry would give rise to interaction terms between gauge bosons and both components of the χ SMs. Especially for the non-abelian gauge groups, interactions among

¹The two-component spinors used for the MSSM formulation are called Weyl spinors and are related to the Dirac spinors as: $\Psi = \begin{pmatrix} \psi \\ \chi \end{pmatrix}$.

Table 2.1: The field content of MSSM. For simplicity only one generation of chiral supermultiplets is listed.

Supermultiplets		Bosonic Fields		Fermionic Fields
		<i>Spin-0</i>	<i>Spin-1</i>	
VSM	gluons & gluinos		g	\tilde{g}
	W & winos	-	W^\pm, W^0	$\tilde{W}^\pm, \tilde{W}^0$
	B & binos		B	\tilde{B}
χ SM	squarks & quarks ($\times 3$ generations)	$(\tilde{u}_L, \tilde{d}_L)$		(u_L, d_L)
		\tilde{u}_R		u_R
		\tilde{d}_R		d_R
	sleptons & leptons ($\times 3$ generations)	$(\tilde{\nu}_L, \tilde{e}_L)$	-	(ν_L, e_L)
		\tilde{e}_R		e_R
	Higgs & higgsinos	(H_u^+, H_u^0)		$(\tilde{H}_u^+, \tilde{H}_u^0)$
(H_d^0, H_d^-)			$(\tilde{H}_d^0, \tilde{H}_d^-)$	

the gauge bosons and their fermionic components (gauginos) would be generated besides the self-interactions present in the SM. Furthermore, the additional interactions allowed are: 1) gaugino - χ SM with strength proportional to the corresponding gauge coupling (e.g. Figure 2.1a) and the non-gauge 2) Yukawa-type interactions between the Higgs/higgsinos and χ SM (e.g. Figure 2.1b), 3) scalar ϕ^3 and 4) ϕ^4 (similar to the one appearing in Eq. 1.12) interactions with strengths proportional to either Yukawa or gauge couplings (e.g. Figures 2.1c and 2.1d respectively). To summarise, the MSSM does not contain new forces and due to the fact that supermultiplet component fields have the same quantum numbers. Feynman diagrams can be easily drawn from the SM ones by replacing (two) particles with their superpartners in an interaction vertex as long as the spin is conserved.

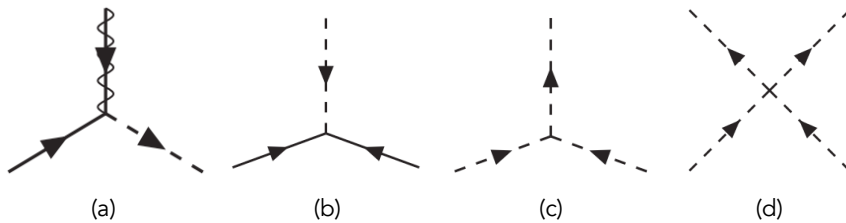


Figure 2.1: Examples of interaction vertices: (a) gaugino-fermion-scalar, (b) scalar-fermion-fermion (Yukawa-type), (c) cubic scalar and (d) quadratic scalar. Diagrams are taken from [77].

Similarly to the SM, the gauge bosons and the (χ SM) fermions of the MSSM cannot have mass terms into the Lagrangian for symmetry considerations¹. Once again, the

¹It is noteworthy though that mass terms can be written for all the unobserved particles so far.

Higgs mechanism is used to spontaneously break the $SU(2)_L \times U(1)$ gauge symmetry by the non-zero VEVs of the neutral components of the Higgs fields (v_u and v_d with $\sqrt{v_u + v_d} \approx 246$ GeV and the parameter $\tan \beta = v_u/v_d$). At this time, after three of the degrees of freedom are allocated to give mass to the gauge bosons, five physical Higgs bosons are residual: a charged pair H^\pm , two neutral CP-even h and H^0 and a neutral CP-odd A^0 . As $m_h < m_{H^0}$ in this framework, it is assumed that the h is the Higgs boson discovered in 2012 by the ATLAS and CMS collaborations. As in the SM, fermionic masses rise via Yukawa couplings which would be the same as their corresponding sfermions if SUSY was unbroken. Interestingly, this seem tightly related to the $SU(2)_L \times U(1)$, SSB as the SUSY-preserving Higgs potential in the MSSM [79]:

$$V(H)_{\text{MSSM}} = |\mu|^2 (|H_u^+|^2 + |H_d^-|^2 + |H_u^0|^2 + |H_d^0|^2), \quad (2.4)$$

where μ is the coupling of the two Higgs doublets, do not include any negative sign term, essential for the SSB as in Eq. 1.12. Consequently, some SUSY-breaking terms are necessary to accommodate the electroweak symmetry breaking.

The SUSY-breaking in the MSSM is accomplished via the soft parametrisation approach mentioned above. This induce the following SUSY-violating parameters: 1) three gaugino masses, 2) five sfermion squared-masses and 3) three trilinear couplings¹ for the Higgs-sfermion interactions (per generation) and 4) three Higgs square-mass parameters that can be negative.

2.2.1 Particle Mass Eigenstates

The sfermion fields with the same quantum numbers can in principle all mix together because of their common gauge interactions. In this case, there is no reason for the gauge eigenstates to be identical with the mass eigenstates. The latter, are obtained by diagonalising a mass-mixing matrix of the chiral eigenstates \tilde{f}_L and \tilde{f}_R – a picture similar to the one presented in Eq. 1.6. The sfermion mass eigenstates are then denoted as \tilde{f}_1 and \tilde{f}_2 , ordered by increasing mass. Because of flavour- and CP-violation measurement constrains [80] and the negligible Yukawa couplings of the first two generations χ^{SM} , the mixing of the last can be neglected [77]. The squared-mass-mixing matrix regarding the third generation squarks – the particles this work is focused on – is then [77]:

$$M^2 = \begin{pmatrix} m_{\tilde{Q}_3}^2 + m_q^2 + L_q & m_q X_q \\ m_q X_q & m_{\tilde{q}_3}^2 + m_q^2 + R_q \end{pmatrix}, \quad (2.5)$$

¹These are acting as Yukawa coupling modifiers to generate different mass to a sfermion with respect to the corresponding fermion.

with:

$$\begin{aligned} X_q &\equiv A_q - \mu(\cot \beta)^{2I_W^3}, \\ L_q &\equiv (I_W^3 - Q_q \sin^2 \theta_W) m_Z^2 \cos 2\beta, \\ R_q &\equiv -Q_q \sin^2 \theta_W m_Z^2 \cos 2\beta, \end{aligned}$$

where $q = t$ (b) and the soft SUSY-breaking parameters: $m_{\tilde{Q}_3}^2$ the common L -handed squark squared-mass, $m_{\tilde{q}_3}^2$ the stop (sbottom) R -handed squared-mass, and A_q the corresponding trilinear coupling. Then the \tilde{q}_1 and \tilde{q}_2 masses are determined by diagonalising the matrix of Eq. 2.5.

In the MSSM the SSB of the electroweak symmetry will not only mix the W^0 and B fields, to form the physical Z boson and photon (and their corresponding superpartners to form the zino and photino), but also the neutral higgsino fields ($\tilde{H}_u^0, \tilde{H}_d^0$) with the neutral and colorless gauginos (\tilde{W}^0, \tilde{B}). As a result, four neutral mass eigenstates are formed and called *neutralinos* ($\tilde{\chi}_i^0$ with $i \in [1, 4]$, ordered by increasing mass) with their masses to be given by diagonalisation of the matrix [77]:

$$N = \begin{pmatrix} M_1 & 0 & -\cos \beta \sin \theta_W m_Z & \sin \beta \sin \theta_W m_Z \\ 0 & M_2 & \cos \beta \cos \theta_W m_Z & -\sin \beta \cos \theta_W m_Z \\ -\cos \beta \sin \theta_W m_Z & \cos \beta \cos \theta_W m_Z & 0 & -\mu \\ \sin \beta \sin \theta_W m_Z & -\sin \beta \cos \theta_W m_Z & -\mu & 0 \end{pmatrix}, \quad (2.6)$$

where $M_{1(2)}$ is the soft SUSY-breaking bino (wino) mass parameter. A similar statement holds for the charged colorless gaugino fields ($\tilde{W}^\pm, \tilde{H}_u^\pm, \tilde{H}_d^\pm$) that mix to form the charged mass eigenstates called *charginos* ($\tilde{\chi}_i^\pm$ with $i \in [1, 2]$, ordered by increasing mass).

Depending on the MSSM parameters values, the neutralinos and charginos can approximate a particular gaugino state or being a homogeneous (or not) mixture of them. In the former case, they take the name of the state they approximate, e.g. bino-like. The rough categories of the lightest neutralino ($\tilde{\chi}_1^0$) are presented in Table 2.2. Each $\tilde{\chi}_1^0$ -type is leading to striking different phenomenology and cases relevant to this work are discussed in Sections 7.2 and 8.2.

Table 2.2: Categorisation of the $\tilde{\chi}_1^0$ -type base on the MSSM parameter hierarchy.

Parameter Configuration	$\tilde{\chi}_1^0$ -type
$ M_1 < M_2 , \mu $	bino-like
$ M_2 < M_1 , \mu $	wino-like
$ \mu < M_1 , M_2 $	higgsino-like

2.2.2 R-Parity

Following the discussion on the allowed interaction terms of the MSSM, more of them can be added. In particular, arbitrary large baryon and lepton number violating couplings between the different χ SMs are allowed in the MSSM Lagrangian. Yet if these were present, the proton would be allowed to decay to $\pi^0 + e^+$ via interaction vertices as in Figure 2.1b. However, its lifetime has been experimentally constrained to more than 10^{34} years [81]. To restrict this possibility, an extra multiplicative symmetry is imposed called *R-parity* and is defined as [77]:

$$R = (-1)^{3B+L+2s}, \quad (2.7)$$

where B the baryon number, L the lepton number, and s the spin of a particle. It follows that all the SM particles have even *R-parity* (+1) while their superpartners – referred to as *sparticles* henceforth – odd one (-1).

The conservation of *R-parity* has two important, for this work, phenomenological implications:

1. The Lightest Supersymmetric Particle (LSP) is stable.
2. Sparticles can only be produced in pairs at the LHC.

The *R-parity* can of course be violated – leading to different phenomenology where the LSP decays to SM particles – but in the context of this work, all the SUSY models discussed and studied assume the absolute conservation of the *R-parity*.

2.3 SM Problems Revised

The MSSM has been developed as the minimal model, based on the SM, with the Poincaré symmetry extended with SUSY. Besides the natural inclination towards models with extended symmetry groups, the MSSM also addresses important deficiencies of the SM. Two of these, that motivate the particle searches in this dissertation, have been highlighted in Section 1.5 and are revised again in the following in light of SUSY introduction.

2.3.1 Dark Matter

The conservation of the *R-parity* within the MSSM has the consequence of rendering the LSP stable. In order to construct a phenomenologically viable model, the LSP should also be colorless and neutral, otherwise relics from the Big Bang would have formed exotic nuclei that are not observed experimentally. Based on these arguments the LSP is a WIMP and widely considered a DM candidate. In the context of this dissertation the LSP is assumed to be the lightest neutralino ($\tilde{\chi}_1^0$) – thus these two terms are used interchangeably henceforth.

It is interesting to assess the viability of this scenario in light of recent experimental

results. A likelihood fit has been performed in a reduced version of the MSSM (pMSSM11, Section 2.4.1) including constrains from DM production searches during the LHC Run 1 and Run 2 periods, DM scattering searches, electroweak, flavour and cosmological measurements and the muon anomalous magnetic dipole moment measurement [82]. In Figure 2.2 the favoured parameter space in a two-dimensional projection of the $\tilde{\chi}_1^0$ mass value versus its spin-independent proton scattering cross-section is presented. It is intriguing that the allowed region (95% CL) favours a $\tilde{\chi}_1^0$ with mass $\mathcal{O}(100 \text{ GeV})$, the same scale that the qualitative arguments of Section 1.5 led.

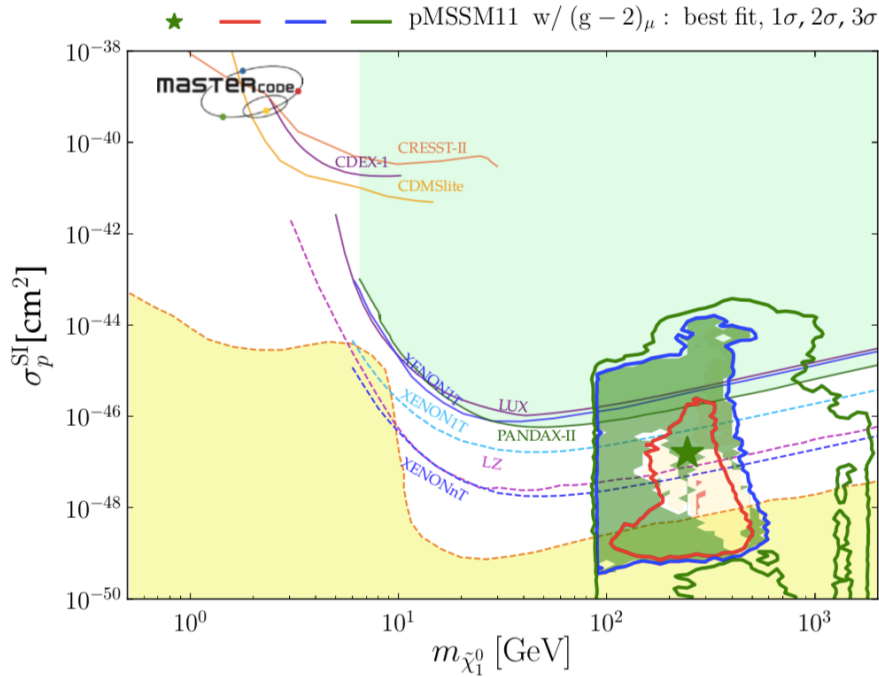


Figure 2.2: $m(\tilde{\chi}_1^0) - \sigma_p^{\text{SI}}$ projection of the likelihood function for the pMSSM11. On the best fitted point the LSP is bino-like and mainly annihilates with $\tilde{\chi}_1^\pm$ in the early Universe to produce the observed relic density. [82]

2.3.2 Hierarchy Problem

SUSY groups scalars with fermions in χ SMs with related interaction couplings, as described in Section 2.2. In particular, the assignment of fermionic Higgsino states to Higgs bosons has the consequence of canceling the Λ dependent term in its mass correction (see Eq. 1.25) via a loop diagram similar to Figure 1.13b that yields to a correction:

$$\delta m_h \sim -\lambda \Lambda^2. \quad (2.8)$$

Equivalent relationships hold between the corrections induced by all the SM fermions and their scalar superpartners. For instance, a stop quark loop will cancel the Λ -dependent term of the top quark loop (Eq. 1.26). It should be noted that the presence

of additional Λ -dependent terms is prohibited in the soft SUSY breaking parametrisation.

The following most divergent Higgs mass correction term is logarithmic in Λ and proportional to the particle mass that induces it. For the case of top and stop quark loops this is:

$$\delta m_h \sim (-\alpha g_t m_t + \beta A_t m_{\tilde{t}}) \log \Lambda, \quad (2.9)$$

where α and β are numerical factors. This is the exact relationship that motivates the mass of the stop quark to be at similar order of magnitude as the top quark, so the Λ dependence vanishes. Furthermore, the common soft SUSY breaking third generation mass parameter ($m_{Q_3}^2$) drives the sbottom quark mass to the same scale as well. The above arguments are considered indications towards the existence of light third generation squark states and make their experimental search at the LHC an appealing endeavor.

One can further constrain the mass scale of the sparticles (M_S) by trying to calculate the mass of the observed Higgs boson at the MSSM. At the tree level this is bounded by the Z mass. However, radiative corrections, that are mainly regulated by the top and stop quarks, can raise the Higgs mass value to the observed one. Recent precise estimates [83] place the M_S at the $\mathcal{O}(\text{TeV})$ with the exact value to depend on the stop mixing (X_t parameter in Eq. 2.5) as shown in Figure 2.3a.

In the case that M_S is at the $\mathcal{O}(\text{TeV})$ the fine-tuning of the model is only at $\mathcal{O}(1\%)$ thus called *natural* – although it would be premature to emphasise to this number too much. Most importantly, this energy scale is accessible by the LHC, fact that utterly motivates the current experimental searches of SUSY particles. For instance, the number of stop and gluino pairs predicted to be produced so far is shown in Figure 2.3b.

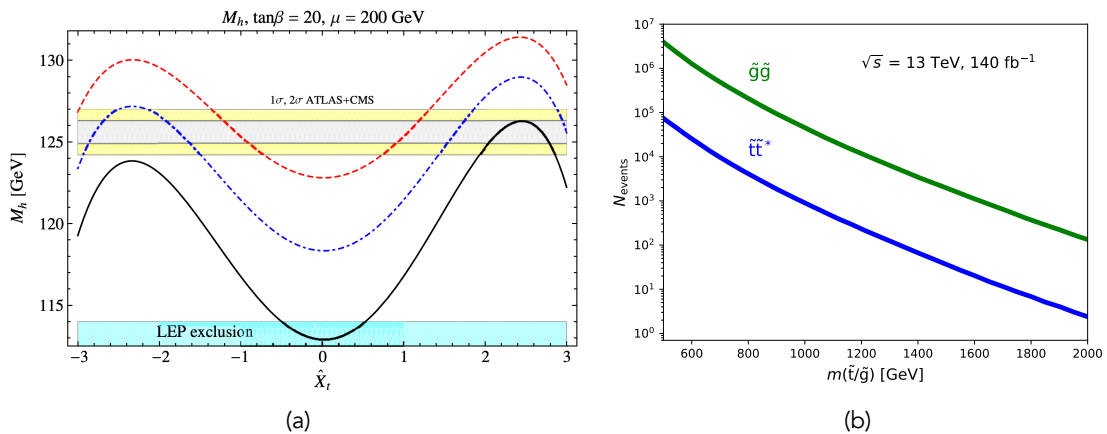


Figure 2.3: (a) The mass of the lightest Higgs boson calculated at the MSSM as function of the stop mixing parameter normalised to the M_S , $\hat{X}_t = X_t/M_S$. The (black, blue, red) curves correspond to $M_S = (1, 2, 4)$ TeV. [83] (b) The number of stop and gluino pairs predicted to be produced by the end of the Run 2 period of the LHC as function of the sparticle mass. Figure made with data from [84].

2.4 Restricting the MSSM

The MSSM formulation includes a large number of free parameters. In particular, more than 100 physical parameters can be identified [77]. It is worth mentioning, however, that most of these parametrise the SUSY breaking (soft SUSY breaking). In order to make systematic studies feasible, reduced models have been developed based on different physical or arbitrary assumptions. Two of these models used at the LHC experiments are described below.

2.4.1 pMSSM

In an approach that refrains from making particular assumptions on the nature of SUSY breaking, one can impose low-energy constraints to the MSSM. Motivated by measurements, these are:

1. no new CP-violating phases,
2. absence of flavour-changing neutral currents and
3. negligible size of the first two generation Yukawa couplings compared to the third one.

The resulting model is then described by 19 parameters and is referred as *phenomenological MSSM* (pMSSM) [85].

Its parameters describe the gauginos (three mass parameters), the Higgs sector ($\tan\beta$ and two mass parameters), the degenerate first two generation sfermions (five mass parameters) and the third generation sfermions (five mass parameters and three trilinear couplings). All the pMSSM parameters are listed in Table 2.3.

A comprehensive study of the pMSSM was performed by the ATLAS collaboration after the Run 1 period of the LHC, by combining results from 22 collider sparticle searches [86]. The parameter space is first constrained by recent precision electroweak, Higgs and flavour physics measurements along with the cosmological DM relic density. In Figure 2.4 the results regarding the lightest third generation squarks are shown, indicating that almost no pMSSM models survive the direct searches with squark masses lower than ~ 500 GeV (for light $\tilde{\chi}_1^0$).

2.4.2 Simplified Models

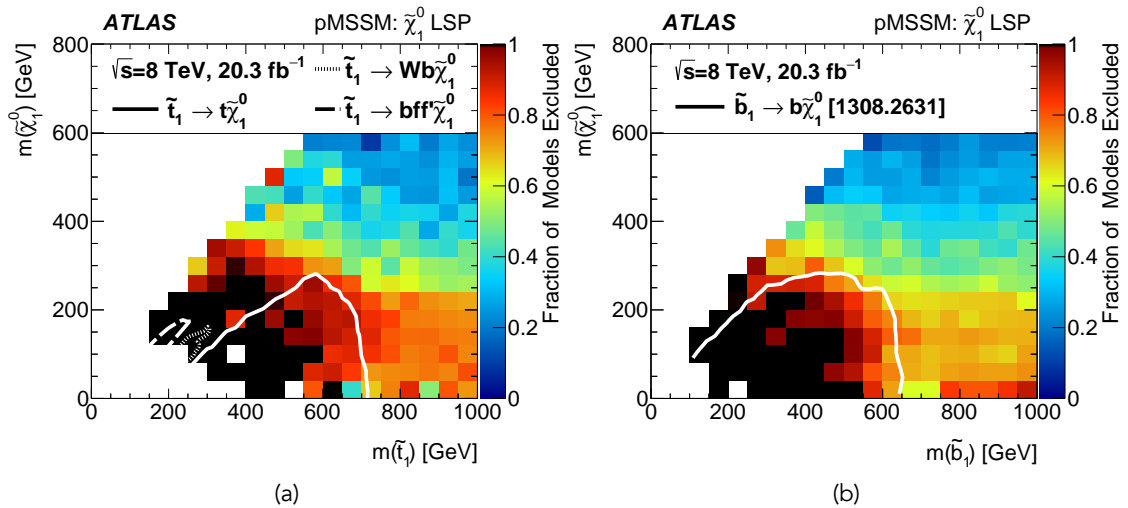
Although the pMSSM provides a much lower dimensional model-space than the full MSSM, is still impractically large for individual sparticle searches result interpretation. Therefore, in a bottom-up approach, the so-called *simplified models* [87] with only two free parameters have been proposed and used for this purpose. These are build on the following assumptions:

1. only few sparticles are accessible by the LHC and
2. these decay (usually) with 100% BR via a particular decay chain.

The simplified models are feasible phenomenological models to be studied experiment-

Table 2.3: Summary of the 19 parameters describing the pMSSM model. Table adapted from [86].

Parameter	Note
$m_{\tilde{L}_1} (= m_{\tilde{L}_2})$	Left-handed slepton (first two gens.) mass
$m_{\tilde{e}_1} (= m_{\tilde{e}_2})$	Right-handed slepton (first two gens.) mass
$m_{\tilde{L}_3}$	Left-handed stau doublet mass
$m_{\tilde{e}_3}$	Right-handed stau mass
$m_{\tilde{Q}_1} (= m_{\tilde{Q}_2})$	Left-handed squark (first two gens.) mass
$m_{\tilde{u}_1} (= m_{\tilde{u}_2})$	Right-handed up-type squark (first two gens.) mass
$m_{\tilde{d}_1} (= m_{\tilde{d}_2})$	Right-handed down-type squark (first two gens.) mass
$m_{\tilde{Q}_3}$	Left-handed squark (third gen.) mass
$m_{\tilde{u}_3}$	Right-handed top squark mass
$m_{\tilde{d}_3}$	Right-handed bottom squark mass
$ M_1 $	Bino mass parameter
$ M_2 $	Wino mass parameter
$ \mu $	Bilinear Higgs mass parameter
M_3	Gluino mass parameter
$ A_t $	Trilinear top coupling
$ A_b $	Trilinear bottom coupling
$ A_\tau $	Trilinear τ lepton coupling
M_A	Pseudoscalar Higgs boson mass
$\tan\beta$	Ratio of the Higgs vacuum expectation values

Figure 2.4: The fraction of surviving pMSSM models (95% CL) after the ATLAS Run 1 direct search results in the two-dimensional planes (a) $m(\tilde{\tau}_1) - m(\tilde{\chi}_1^0)$ and (b) $m(\tilde{b}_1) - m(\tilde{\chi}_1^0)$. The white contours indicate the simplified model (Section 2.4.2) exclusion limit. The white cells are regions of the parameter space with no models surviving the initial constrains mentioned in the main text. [86]

ally and in a sparticle search are used to both optimise the analysis and interpret the results.

As an example, the main simplified model used by the LHC searches looking for the production of sbottom quarks assumes that its lightest mass eigenstates (\tilde{b}_1) are the only sparticles able to be produced by the LHC proton-proton (pp) collisions and that a sbottom quark decays solely to a b-quark and an LSP (Figure 2.5). It is quite interesting to compare the coverage of the simplified model to the exclusion of the more realistic pMSSM. In Figure 2.4b the white contour indicates the exclusion limit obtained by the usage of the simplified model of Figure 2.5 – and in Figure 2.4a from the corresponding one with (s)top quarks instead of (s)bottom. It is apparent that the limit is overestimated when compared to the full pMSSM as there are regions of the contour where only $\sim 70\%$ of the models have been actually excluded.

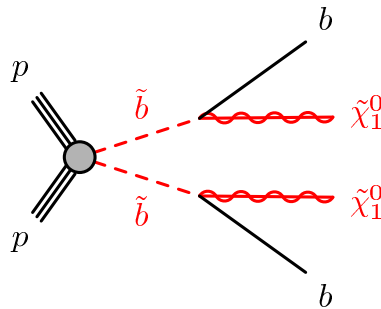


Figure 2.5: Simplified model of sbottom production. Each sbottom quark decays with 100% BR to a b-quark and the LSP. [88]

It is worth highlighting a couple of the main production channels of simplified models at the LHC pp collisions which will be used in the following. In particular, the production of two types of sparticles is relevant in the context of this dissertation: 1) gluinos and 2) sbottom quarks. As mentioned already, SUSY Feynman diagrams can be derived by the SM ones by replacing two¹ particles with sparticles in an interaction vertex. For instance, the diagram of Figure 2.6a (Figure 2.6c) shows the production of gluinos (sbottoms) via gluon-gluon fusion (quark-quark annihilation), while the diagram of Figure 2.6b (Figure 2.6d) via quark-quark (gluon-gluon) scattering.

In conclusion, the simplified models are useful to estimate the mass scale reach of the experimental searches. By studying the limits achieved by a few representative searches targeting generic final states with different kind of particles one can have a global view of the experimental sensitivity to M_S . At the present time, for instance, the sensitivity to third generation squark mass scale can be placed just below 1 TeV, as it can be seen in Figure 2.7. It should be noted that at the start of this work, right after the Run 1, this sensitivity was placed at about 0.5 TeV.

¹As a consequence of R -parity conservation.

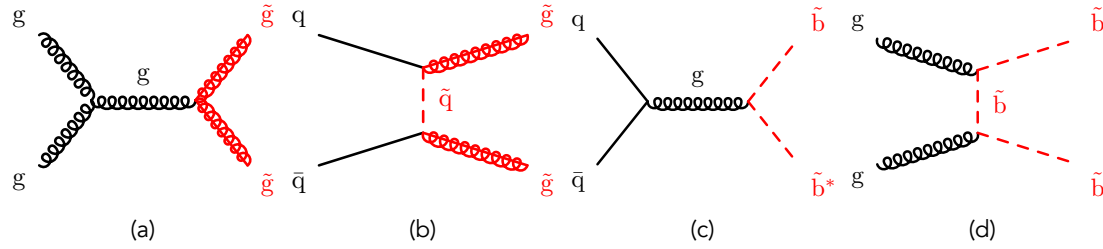


Figure 2.6: Feynman diagrams for (a and b) gluino and (c and d) sbottom quark production. The diagrams comprise an original work of the author.

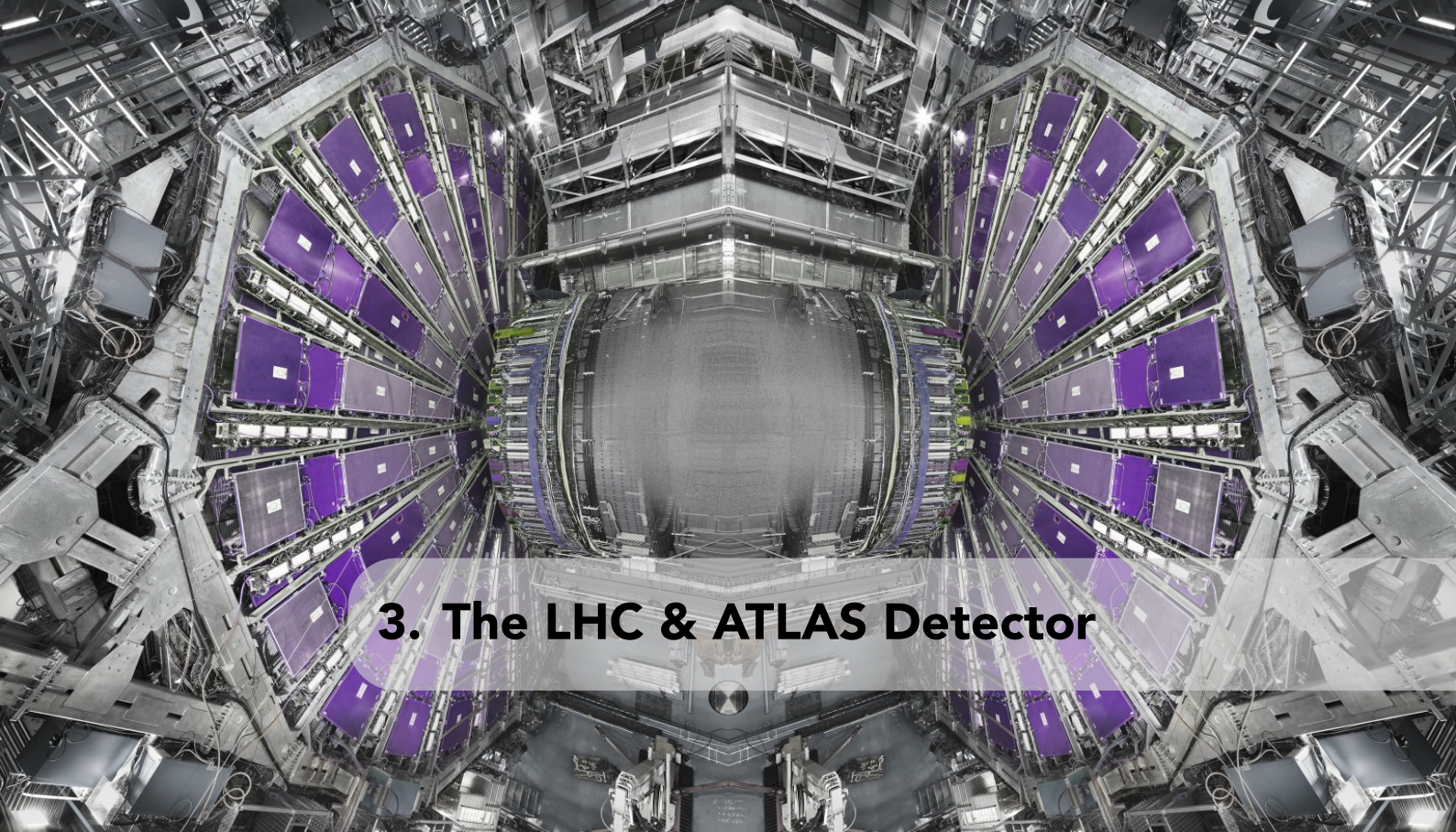
ATLAS SUSY Searches* - 95% CL Lower Limits		ATLAS Preliminary	
July 2019		$\sqrt{s} = 13 \text{ TeV}$	
Model	Signature	$\mathcal{J} \cdot \text{Br} [\text{fb}^{-1}]$	Reference
Inclusive Searches	$0 \text{ } e, \mu$	$E_{\text{T}}^{\text{miss}}$	$m(\tilde{g}) < 100 \text{ GeV}$
	mono-jet	$E_{\text{T}}^{\text{miss}}$	$m(\tilde{g}) - m(\tilde{t}^0) = 5 \text{ GeV}$
	$0 \text{ } e, \mu$	$E_{\text{T}}^{\text{miss}}$	$m(\tilde{g}) = 200 \text{ GeV}$
	2 jets	$E_{\text{T}}^{\text{miss}}$	$m(\tilde{g}) = 300 \text{ GeV}$
	2 jets	$E_{\text{T}}^{\text{miss}}$	$m(\tilde{g}) = 300 \text{ GeV}$
Inclusive Searches	$0 \text{ } e, \mu$	$E_{\text{T}}^{\text{miss}}$	$m(\tilde{g}) = 300 \text{ GeV}$
	2 jets	$E_{\text{T}}^{\text{miss}}$	$m(\tilde{g}) = 300 \text{ GeV}$
	4 jets	$E_{\text{T}}^{\text{miss}}$	$m(\tilde{g}) = 300 \text{ GeV}$
	$7-11 \text{ jets}$	$E_{\text{T}}^{\text{miss}}$	$m(\tilde{g}) = 300 \text{ GeV}$
	6 jets	$E_{\text{T}}^{\text{miss}}$	$m(\tilde{g}) = 300 \text{ GeV}$
Inclusive Searches	$0-1 \text{ } e, \mu$	0 jets	$m(\tilde{g}) = 200 \text{ GeV}$
	3 jets	0 jets	$m(\tilde{g}) = 200 \text{ GeV}$
	6 jets	0 jets	$m(\tilde{g}) = 200 \text{ GeV}$
	6 jets	0 jets	$m(\tilde{g}) = 200 \text{ GeV}$
	6 jets	0 jets	$m(\tilde{g}) = 200 \text{ GeV}$
3rd gen. squarks	$b_1 \tilde{b}_1, \tilde{b}_1 \rightarrow b \tilde{t}^0, \tilde{t}^0$	Multiple	$m(\tilde{b}_1) = 300 \text{ GeV}, \text{BR}(\tilde{b}_1^0) = 1$
	$b_1 \tilde{b}_1, \tilde{b}_1 \rightarrow b \tilde{t}^0, \tilde{t}^0$	Multiple	$m(\tilde{b}_1) = 300 \text{ GeV}, \text{BR}(\tilde{b}_1^0) = 0.5$
	$b_1 \tilde{b}_1, \tilde{b}_1 \rightarrow b \tilde{t}^0, \tilde{t}^0$	Multiple	$m(\tilde{b}_1) = 300 \text{ GeV}, \text{BR}(\tilde{b}_1^0) = 1$
	$b_1 \tilde{b}_1, \tilde{b}_1 \rightarrow b \tilde{t}^0, \tilde{t}^0$	Multiple	$m(\tilde{b}_1) = 300 \text{ GeV}, \text{BR}(\tilde{b}_1^0) = 1$
	$b_1 \tilde{b}_1, \tilde{b}_1 \rightarrow b \tilde{t}^0, \tilde{t}^0$	Multiple	$m(\tilde{b}_1) = 300 \text{ GeV}, \text{BR}(\tilde{b}_1^0) = 1$
EW	$\tilde{\chi}_1^0 \tilde{\chi}_1^0 \rightarrow \text{WW}$	≥ 1	$m(\tilde{\chi}_1^0) = 100 \text{ GeV}$
	$\tilde{\chi}_1^0 \tilde{\chi}_1^0 \rightarrow \text{WW}$	≥ 1	$m(\tilde{\chi}_1^0) = 100 \text{ GeV}$
	$\tilde{\chi}_1^0 \tilde{\chi}_1^0 \rightarrow \text{WW}$	≥ 1	$m(\tilde{\chi}_1^0) = 100 \text{ GeV}$
	$\tilde{\chi}_1^0 \tilde{\chi}_1^0 \rightarrow \text{WW}$	≥ 1	$m(\tilde{\chi}_1^0) = 100 \text{ GeV}$
	$\tilde{\chi}_1^0 \tilde{\chi}_1^0 \rightarrow \text{WW}$	≥ 1	$m(\tilde{\chi}_1^0) = 100 \text{ GeV}$
Long-lived particles	Stable \tilde{g} R-hadron	Multiple	$m(\tilde{g}) = 100 \text{ GeV}$
	Metastable \tilde{g} R-hadron, $\tilde{g} \rightarrow \text{qq} \tilde{t}^0$	Multiple	$m(\tilde{g}) = 100 \text{ GeV}$
	$\tilde{g} \rightarrow \text{qq} \tilde{t}^0$	Multiple	$m(\tilde{g}) = 100 \text{ GeV}$
	$\tilde{g} \rightarrow \text{qq} \tilde{t}^0$	Multiple	$m(\tilde{g}) = 100 \text{ GeV}$
	$\tilde{g} \rightarrow \text{qq} \tilde{t}^0$	Multiple	$m(\tilde{g}) = 100 \text{ GeV}$
RPV	$\tilde{\chi}_1^0 \tilde{\chi}_1^0 \rightarrow \text{WW}$	≥ 1	$m(\tilde{\chi}_1^0) = 100 \text{ GeV}$
	$\tilde{\chi}_1^0 \tilde{\chi}_1^0 \rightarrow \text{WW}$	≥ 1	$m(\tilde{\chi}_1^0) = 100 \text{ GeV}$
	$\tilde{\chi}_1^0 \tilde{\chi}_1^0 \rightarrow \text{WW}$	≥ 1	$m(\tilde{\chi}_1^0) = 100 \text{ GeV}$
	$\tilde{\chi}_1^0 \tilde{\chi}_1^0 \rightarrow \text{WW}$	≥ 1	$m(\tilde{\chi}_1^0) = 100 \text{ GeV}$
	$\tilde{\chi}_1^0 \tilde{\chi}_1^0 \rightarrow \text{WW}$	≥ 1	$m(\tilde{\chi}_1^0) = 100 \text{ GeV}$

*Only a selection of the available mass limits on new states or parameters for the different simplified models. For the highlighted rows indicate inputs for the two searches presented in this work. [89]

Figure 2.7: The mass scale reach of a selection of ATLAS searches for SUSY in simplified models. The highlighted rows indicate inputs from the two searches presented in this work. [89]

Part II

Experimental Facility



3. The LHC & ATLAS Detector

The facilities at CERN are designed to address Universe most fundamental questions

This chapter briefly describes the experimental apparatus used to conduct the accelerator particle physics experiments that provided the data for this work. First, the Large Hadron Collider is introduced, and then the ATLAS detector and its main sub-components are described.

3.1 The Large Hadron Collider

A typical method to study the microscopic properties of matter is to shot a probe projectile to an object. The projectile wavelength should be no larger than the object dimensions in order to resolve it. The same principle applies to a wide range of experimental facilities, from optical microscopes to particle accelerators. In a quantum mechanical approach, the projectile wavelength is inversely proportional to its momentum, $\lambda \propto \frac{1}{p}$ [90]. Using the most powerful particle accelerator ever made, the *Large Hadron Collider* (LHC) – hosted at CERN in Geneva, Switzerland – scales as small as 10^{-20} m can be resolved by the centre-of-mass energy (\sqrt{s}) 13 TeV particle collisions it provides.

3.1.1 Accelerator Complex

The LHC is a circular synchrotron of 27 km circumference which accelerates two opposite direction proton¹ beams which are eventually brought into collision at *Interaction Points* (IPs). The protons used in the LHC originate from hydrogen gas that is broken down and electrically stripped of electrons. Initially, their energy is increased to 50 MeV by a linear accelerator (*Linac 2* [91]). Afterwards, the protons are fed into a series of circular accelerators before reaching the LHC. First, the *Proton Synchrotron Booster* (Booster) [92] increase their energy to 1.4 GeV, the *Proton Synchrotron* (PS) [93] to 25 GeV and the *Super Proton Synchrotron* (SPS) to 450 GeV. In a final step, the beams are fed to the LHC to increase their energy up to currently maximum value of 6.5 TeV. The whole accelerator complex at CERN is shown in Figure 3.1.

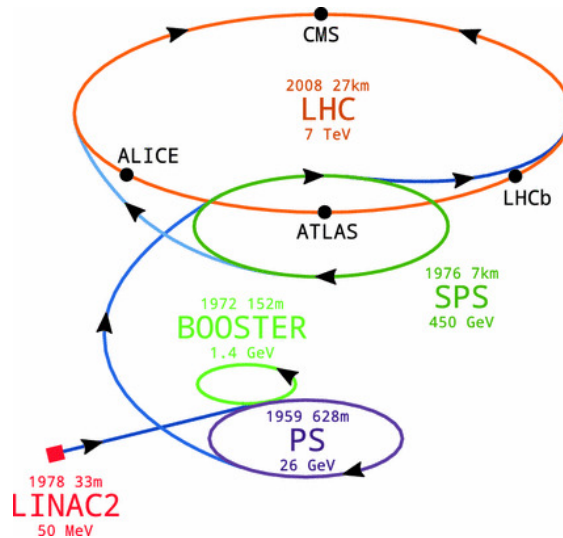


Figure 3.1: The relevant to this work elements of the accelerator complex at CERN. For each accelerator, its length, commissioning year and maximum beam energies are given. The tunnel of the LHC is up to 175 metres underground and used to host the *Large Electron-Positron* collider decommissioned in 2000. The experiments located in the LHC IPs also shown. [94]

The acceleration at the LHC is performed by superconducting radiofrequency cavities, powered by klystrons, where oscillating electric fields impulsing the protons. Eight cavities per beam provide an energy increase of 16 MeV per revolution, thus the beams are reaching the collision energy in about 20 min. The wave nature of the acceleration method inevitably implies that the beam is not continuous but rather segmented into *bunches*. For the LHC the number of possible bunches is about 36000². During the Run 2 period of the LHC, only about 2000 to 2500 bunches were filled with $\mathcal{O}(10^{11})$ protons and on an IP collision occurred every 25 ns.

¹The LHC is also accelerate and collide heavy ions (Pb) mainly for quark-gluon plasma studies but this topic falls beyond the scope of this dissertation.

² $N_{\text{bunches}} = \frac{f_{\text{RF}}}{f_{\text{revolution}}} = \frac{400 \text{ MHz}}{c/27 \text{ km}}$, where c the speed of light in metre per second.

The two beams are kept on track using magnetic fields generated by superconducting electromagnets. The steering into the circular path is achieved by 1232 dipole magnets providing a field up to about 8 T while the focusing by numerous multipole (mainly quadrupole) magnets.

In four, of the overall eight, IPs of the LHC particle detectors are located (Figure 3.1). By measuring the proton collision debris the underlying physics laws can be inferred. Particularly, there are two general purpose detectors, the ATLAS and CMS [95] that are both used to conduct precision particle physics measurements or search for new physics phenomena (such as Supersymmetry). The LHCb [96] detector is dedicated to conduct B-hadron related measurements in order to study the matter-antimatter asymmetry of the Universe. The ALICE [97] detector is the main experiment used to conduct heavy-ion collision measurements to study the quark-gluon plasma. Furthermore, there are three detectors located in off-IPs; these are the TOTEM [98] and LHCf [99] that focus on performing “forward physics”¹ measurements and the MoEDAL [100] detector searching for the production of magnetic monopoles. The work of this dissertation is solely using data collected with the ATLAS detector that is briefly described in section Section 3.2.

3.1.2 Luminosity & Pile-Up

The figure of merit for a collider is the so-called (instantaneous) *luminosity*, calculated as:

$$L = \frac{N_b N_p^2 f_{rev}}{4\pi\sigma_T^2}, \quad (3.1)$$

where N_b is the number of bunches, N_p is the number of protons per bunch, f_{rev} is the bunch revolution frequency and σ_T^2 is the transverse area of the beam. It should be noted that, for a realistic experimental facility correction factors should be applied to the above equation to account for imperfections (e.g. collision angle, transverse offset, non-Gaussian beam profiles). The product of L with a physics process cross-section gives the expected number of events produced per second:

$$\frac{N_{events}}{\Delta t} = L \cdot \sigma, \quad (3.2)$$

while the total number of events can be calculated by integrating the luminosity over the experiment running time, leading to the quantity called *integrated luminosity*:

$$L = \int L dt. \quad (3.3)$$

The daily integrated cumulative luminosity of the Run 2 period per year of operation delivered to the ATLAS experiment is shown in Figure 3.2a.

From the ATLAS point of view, the LHC delivered luminosity is measured using the

¹Particles that emerge from collisions at small angles with respect to the beam.

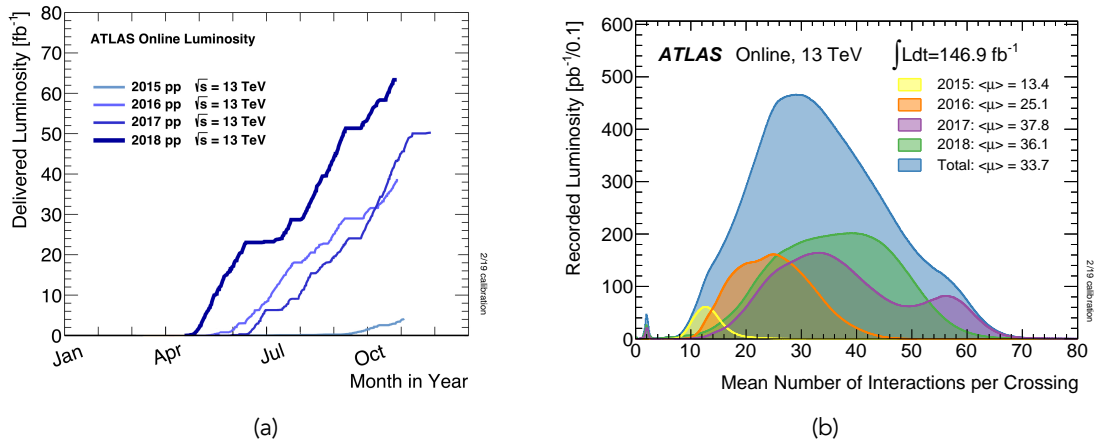


Figure 3.2: (a) Cumulative daily integrated luminosity delivered the ATLAS experiment per year of the Run 2 period of the LHC. Figure courtesy of the ATLAS Collaboration. (b) The luminosity-weighted distributions of the mean number of interactions per bunch crossing for the Run 2 period of the LHC, per year. [101]

dedicated LUCID2 Cherenkov detector [102] that is composed of photomultipliers surrounding the beam pipe on both sides of ATLAS. By measuring the Cherenkov radiation produced in each bunch crossing, an interaction rate can be determined. The latter is proportional to the luminosity. The proportionality constant is determined via a dedicated LHC calibration run taking place once per year. During the scan the beams are separated vertically and horizontally and by measuring the interaction rate in each position the transverse area of the beam, σ_{\perp}^2 , can be determined. The σ_{\perp}^2 along with the beam current – the number of protons per bunch – enable to calculate the calibration constant. Finally, the calibration constant is extrapolated to the nominal LHC running conditions. During this procedure the calibration uncertainties are calculated and propagated to the final luminosity estimation. More details on the Run 2 luminosity determination are given in [103].

The required increase in luminosity is achieved by “squeezing” the beams, increasing the current or the number of bunches (or a combination of them) and offers higher number of collisions thus a higher chance of rare phenomena to occur. This comes at the price of higher number of simultaneous (inelastic) interactions per bunch crossing, apart from the main hard-scatter, referred to as *Pile-Up* (PU). Particles from the PU interactions are recorded by the detectors and overshadow the result of the hard-scatter interaction. This overpopulated environment deteriorates the detector triggering, tracking and calorimetry capabilities and can be a significant bottleneck on its performance. Apart from the *in-time* PU, where the particles originate from the same bunch crossing, there might be particles from neighbouring bunch crossings, referred as *out-of-time* PU. The mean number of PU, $\langle \mu \rangle$, follows a Poisson distribution and the one recorded by the ATLAS detector during the Run 2 period of the LHC is shown in Figure 3.2b.

3.2 The ATLAS Detector

The ATLAS (A *Toroidal LHC ApparatuS*) detector is a 7000 tonnes general purpose particle detector located at the IP no. 1 of the LHC. It has a cylindrical shape of 44 m length and 25 m diameter (with the cylinder axis along the beam pipe and backward-forward symmetry with respect to its centre) with almost 4π solid angle coverage while the proton collisions occur at its centre. In order to shield the detector from cosmic radiation it is located about 100 m underground.

The ATLAS detector is composed by multiple sub-detectors, with a total read-out of about 10 M channels, in an onion-layered arrangement as shown in Figure 3.3. In the innermost part, a tracker called *Inner Detector* (ID) is found with a set of calorimeters surrounding it, while in the outermost layer, furthest from the IP, a muon spectrometer is installed. As the detected particle density decrease with increasing angle with respect to the beam, all the sub-detectors are segmented in a *barrel* and two *end-cap* sections to maintain high reconstruction efficiency. The aforementioned sub-detectors are further detailed in the following sections, after the description of the ATLAS coordinate system.

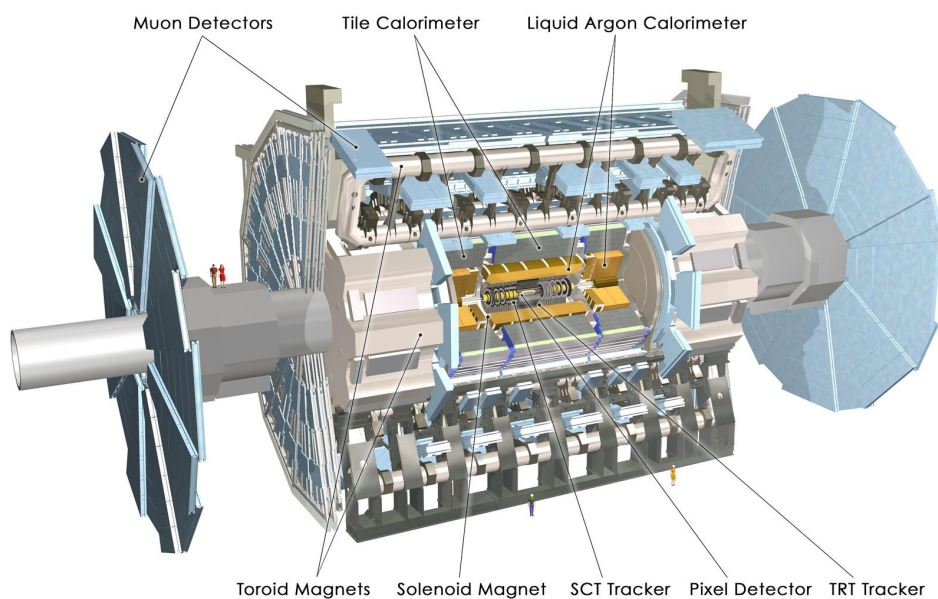


Figure 3.3: Illustration of the ATLAS detector and its component sub-detectors. The Pixel, SCT and TRT trackers consist the ID. Human figures have been superimposed to give a sense of the apparatus scale. [104]

3.2.1 Coordinate System

ATLAS uses a right-handed coordinate system with origin the IP. The positive direction of the x -axis points towards the centre of the LHC ring and the y -axis upwards, towards the Earth's surface. The z -axis runs along the beam direction. It is more common, however,

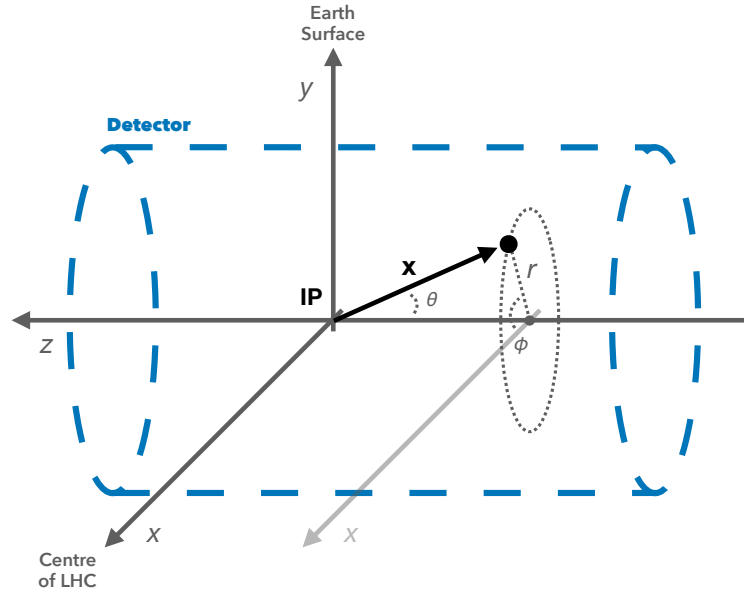


Figure 3.4: Illustration of the coordinate system used at the ATLAS detector. The figure comprises an original work of the author.

to use cylindrical coordinates with r the radius and ϕ the azimuthal angle around the z -axis, measured with respect to the positive of the x -axis ($\phi \in [-\pi, \pi]$). Additionally, the polar angle θ – the angle of the particle position vector (\mathbf{x}) with respect to the z -axis ($\theta \in [-\pi/2, \pi/2]$) – is also used. An illustration of the coordinate system is presented in Figure 3.4.

As the two colliding partons usually carry different momentum, the collision centre-of-mass is shifted (Lorentz boosted) from the IP along the z -axis. Thus a Lorentz-invariant quantity, under boosts along the z -axis, is useful to measure the polar angle. For this reason, the so-called *rapidity* is defined:

$$y = \frac{1}{2} \ln \frac{E + p_z}{E - p_z}, \quad (3.4)$$

with rapidity differences (Δy) to be Lorentz-invariant. As it is experimentally difficult to measure the z -component of the momentum, the *pseudorapidity* is commonly used instead, defined as:

$$\eta = \ln \tan \frac{\theta}{2}. \quad (3.5)$$

For ultra-relativistic particles ($E \gg m$) $y \approx \eta$ ($\eta \in (-\infty, +\infty)$).

Using the above coordinate system, two *impact parameter* distances are defined and are used further in this work. First, the *transverse impact parameter* (d_0) is defined as the minimum distance of an object (track) from the IP in the transverse plane $x - y$. Second, the *longitudinal impact parameter* is defined as the distance, along the z -axis, of the point the d_0 is calculated at, and multiplied by the sine of the polar angle, $z_0 \sin(\theta)$.

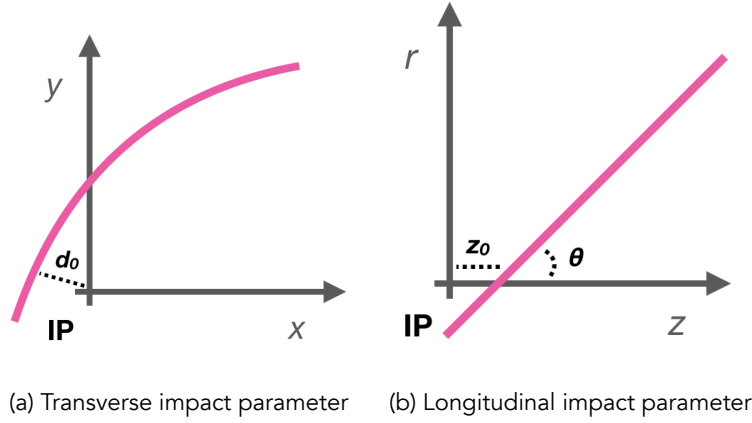


Figure 3.5: Schematic representation of the two impact parameter quantities used further in this work. The figures comprise an original work of the author.

Both the impact and longitudinal parameter distances are illustrated in Figure 3.5.

3.2.2 Inner Detector

The ID is located in the innermost part of the ATLAS detector, just 33 mm away from the beam pipe. The ID is a tracker, meaning that it can measure charged particles trajectories and momenta with minimal interference on their energy. In particular, the ID is surrounded by a superconducting solenoid coil producing a 2 T uniform magnetic field parallel to the beam. As the charged particle flight paths are bent by the magnetic field, multiple measurements at different r are used to reconstruct their trajectory and consequently measure their momenta. By equating the magnetic force (F_B) to the centripetal force (F_c):

$$\underbrace{qvB}_{F_B} = \underbrace{\frac{mu^2}{r}}_{F_c}, \quad (3.6)$$

where q , m and v the charge, mass and velocity of the particle respectively and B the strength of the magnetic field, using the small-angle approximation of the sagitta ($s \approx l^2/4r$, where l the measurements distance over the particle trajectory) and finally propagating the errors, it is shown that the relative transverse momentum resolution ($\frac{\sigma_{p_T}}{p_T}$) worsens with p_T but can be improved with higher magnetic field and more measurements (N) along a longer distance [105]:

$$\frac{\sigma_{p_T}}{p_T} \propto \frac{p_T}{\sqrt{N}l^2B}. \quad (3.7)$$

The ID has 6.2 m length and 2.1 m diameter and coverage up to $|\eta| < 2.5$. It is composed of three sub-detectors: the *Pixel Detector*, the *SemiConductor Tracker* (SCT)

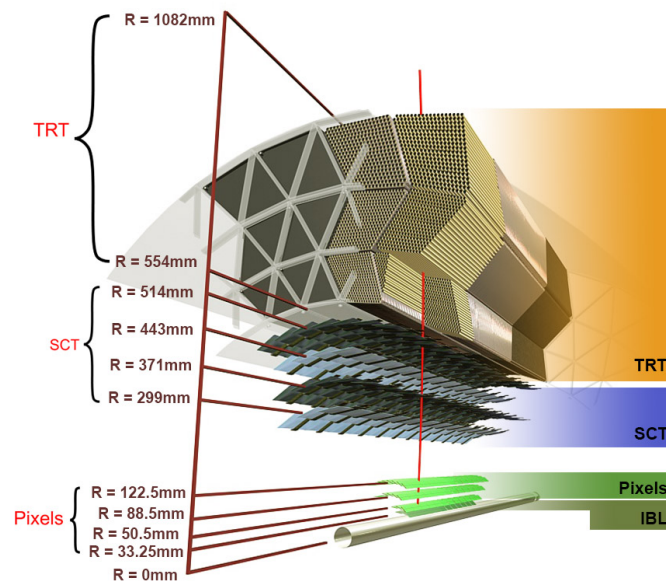


Figure 3.6: Transverse view of the ID with the different layers of the Pixel, SCT and TRT sub-detectors along with the radius each one covers. The innermost and newest layer of the Pixel detector is called IBL. [106]

and the *Transition Radiation Tracker* (TRT) as shown in Figure 3.6.

3.2.2.1 Pixel Detector

The Pixel detector is the innermost part of the ID, spanning in a radius from 33.25 mm to 242 mm and it consist of more than 80 M pixels grouped in 1,744 modules containing power supply and read-out electronics. The modules are placed in four layers in the barrel section (67 M pixels) (Figure 3.6) and three discs in each end-cap section (6.6 M pixels). A typical pixel consist of a n^+ -in- n Si sensor of $50 \times 400 \mu\text{m}^2$ area and 250 μm thickness that is read-out individually. Overall, a resolution of $14 \times 115 \mu\text{m}^2$ in $\phi \times z$ is achieved.

The Pixel detector is used for track and vertex reconstruction and its performance has been significantly improved by the installation of an additional layer after the Run 1 period of the LHC. This is called *Insertable B-Layer* (IBL) and hosts the closest to the beam pipe sensors. The upgrade had a direct consequence to the b-tagging performance, which is particularly relevant to this work, as the light-jet (c-jet¹) rejection has been improved by a factor of 4-5 (1.1) for a 70% b-jet identification efficiency compared to Run 1 [107].

3.2.2.2 SemiConductor Tracker

Around the Pixed detector, another silicon-based tracker, the SCT, is located at radius spanning from 255 mm to 610 mm. The SCT consist of 4,088 modules, each one with two sides of silicon microstrip (henceforth referred to as just strip) sensors. These mod-

¹Jets originating from the hadronisation of charm quarks, akin to b-jet definition.

ules, as the Pixels, are placed in four barrel layers (Figure 3.6) and nine end-cap discs on each side of the detector. Each side of a barrel module hosts two rectangular strip sensors of area $63.96 \times 63.56 \text{ mm}^2$ (the end-cap sensors have trapezoidal geometry) and thickness $285 \text{ }\mu\text{m}$. Each sensor consist of 768 p strips, of $16 \text{ }\mu\text{m}$ width, in n-type bulk (p-in-n). The two sensors are chained making the active length of a strip 12.8 cm . As the strips are places along the z -axis the two sides of a modules are tilted in an angle of 20 mrad in order to provide a z -direction measurement of $580 \text{ }\mu\text{m}$ resolution while the azimuthal resolution achieved is $17 \text{ }\mu\text{m}$.

The p-in-n strip sensors of the SCT have been designed to withstand radiation fluences corresponding to an integrated luminosity up to 750 fb^{-1} [108]. As the integrated luminosity of the High-Luminosity LHC is expected to surpass these levels, novel silicon strip sensor technology is been developed and planned to replace the SCT. To study the radiation tolerance of the upgraded sensors, a characterisation facility has been developed and commissioned at the University of Sheffield. This is the subject of Chapter 4.

3.2.2.3 Transition Radiation Tracker

The outermost part of the ID is the TRT and spans from 554 mm to 1106 mm in radius. In contrast to the Pixel and SCT, the TRT sensitive elements are drift tubes. The tubes are made of kapton in straw geometry with diameter of 4 mm and a gold-plated tungsten wire in the middle acting as the anode. They are filled with a gas mixture of Xe, CO_2 and O_2 and there are 370,000 of them in the barrel (144 cm length, Figure 3.6) and end-cap (37 cm length arranged radially) sections. The TRT provide tracking capabilities in large radius with $\sim 130 \text{ }\mu\text{m}$ resolution. Besides that, the TRT has particle identification capabilities. The inter-tube space is filled with radiator material (polypropylene) that enhance the emission of γ -dependent transition radiation that causes increased ionisation in the tubes. This radiation is a feature to distinguish electrons from pions.

3.2.3 Calorimeters

Contrary to the trackers, the calorimeters are measuring the energy of an incoming particle by completely stopping it and recording the deposited energy. They are composed of two parts, a high-density material called *absorber* that cause the particle to shower while passing through it, and an *active* material where the secondary particles of the shower deposit their energy. The three-dimensional shower shape and direction provide information regarding the inducing particle kind and momentum direction. As the energy deposited is related to the number of secondary particles produced, it follows a Poisson distribution thus the energy resolution improves with energy:

$$\frac{\sigma_E}{E} \propto \frac{1}{\sqrt{E}}. \quad (3.8)$$

The calorimeters of the ATLAS detector are segmented in sampling layers of varying granularity and placed right after the ID solenoid magnet. First is an electromagnetic (EMCal) and then a hadronic calorimeter (HCal), as described below.

3.2.3.1 Electromagnetic Calorimeter

The EMCal measures the energy of electrons and photons offering a coverage up to $|\eta| < 3.2$. It consists of alternating layers of lead (absorber) and liquid argon (active material) in an accordion geometry – transverse to the direction of the incident particles – in both the barrel and end-cap sections (Figure 3.3). The lead induces an electromagnetic shower mainly via Bremsstrahlung radiation and electron pair-production and the secondary particles ionise the argon. The total thickness of the EMCal is about 22 radiation lengths¹ in the barrel and 24 in the end-cap sections. The typical relative energy resolution achieved in units of GeV is $\frac{\sigma_E}{E} = \frac{10}{\sqrt{E}} \oplus 0.7\%^2$.

3.2.3.2 Hadronic Calorimeter

Right after the EMCal, the HCal is placed to measure the energy of hadrons. In the barrel section ($|\eta| < 1.7$) the HCal is composed of the so-called *Tile Calorimeter* (Figure 3.3) made of layers – along the direction of the incident particles – of steel (absorber), that induce a hadronic shower by both electromagnetic and nuclear interactions, and scintillating tiles (active material). The end-cap sections ($1.5 < |\eta| < 3.2$) are made of wheels with alternating layers – again along the direction of the incident particles – of copper (absorber) and liquid argon (active material). The total HCal thickness is about 10 nuclear interaction lengths³ at $|\eta| \sim 0$. The typical relative energy resolution achieved in units of GeV is $\frac{\sigma_E}{E} = \frac{50}{\sqrt{E}} \oplus 3\%$.

Finally, there is a *Forward Calorimeter* (FCal) in the end-cap sections, offering coverage up to $|\eta| < 4.7$, using copper and tungsten as absorbers, to induce the electromagnetic and the hadronic part of the shower respectively, and liquid argon as active material. The FCal is made of a metal matrix and absorber tubes, parallel to the beam, that enclose the active material. The typical relative energy resolution achieved in units of GeV is $\frac{\sigma_E}{E} = \frac{100}{\sqrt{E}} \oplus 10\%$.

3.2.4 Muon Spectrometer

The muons are not stopped by the calorimeters as the amount of Bremsstrahlung radiation emitted is inversely proportional to powers (square or cubic) of the incident particle mass. Therefore, a dedicated *Muon Spectrometer* (MS) (Figure 3.3) is placed in the outermost layers of the ATLAS detector ($5 < r < 11$ m) to track the deflection of their trajectory from a magnetic field and thus measure their momentum. The mag-

¹One radiation length is the distance that a high-energy electron loses all but $\frac{1}{e}$ of its energy by Bremsstrahlung radiation and $\frac{7}{9}$ of the free path of a photon undergoing pair-production [109].

²The \oplus symbol denotes addition in quadrature.

³The mean distance a hadron travels before undergoing an inelastic nuclear interaction.

netic field is provided by superconducting air core toroid magnets, separated in barrel and end-cap sections, placed radially and symmetrically around the beam pipe. Each section is composed by eight coils providing a maximum 4 T magnetic field, transverse to the direction of the incident muons.

In most of the polar range ($|\eta| < 2.7$) the tracking is provided by *Monitored Drift Tubes* (MDTs) filled with Ar/CO₂ gas mixture. There are 354,240 MDTs placed in 1,171 chambers in three layers (before, into and after the magnetic field) and offers about 50 μm spacial resolution along the z -axis. At large polar angles ($2 < |\eta| < 2.7$) the tracking is assisted by *Cathode Strip Chambers* – which are proportional multi-wire chambers with segmented cathode and Ar/CO₂ gas as an active material – in trapezoidal shape placed in wheels around the beam pipe and offer a spacial resolution of up to 60 μm in the azimuthal direction and 5 mm in the radial. For triggering purposes, the long drift time is an impediment, thus fast *Resistive Plate Chambers* and *Thin Gap Chambers* are used in the barrel and end-cap sections respectively covering a range up to $|\eta| < 2.4$.

3.2.5 Trigger System

The size of an event as registered by the ATLAS detector is $\mathcal{O}(1 \text{ MB})$ and the LHC collision rate is 40 MHz. If the ATLAS detector was recording all the produced events, a storage rate of $\mathcal{O}(100 \text{ TB s}^{-1})$ would be required. Additionally, a typical SUSY production cross-section at the $\sqrt{s} = 13 \text{ TeV}$ pp collisions of the LHC is at $\mathcal{O}(10 \text{ fb})$ [84] while, as seen in Figure 1.1, the total inelastic pp cross-section is $\mathcal{O}(10^{11} \text{ pb})$ – a 13 orders of magnitude difference. There is no capability or need to record all but the most “interesting” events regarding each physics analysis. This is achieved by a sophisticated triggering system that consist of both hardware- and software-based parts.

The first part of the trigger (L1) is hardware-based and designed to reduce the event rate from 40 MHz to 100 kHz. It is composed by custom-made electronics that receive reduced granularity information from the calorimeters and the MS. By using approximations of the object reconstruction, event features are calculated. These are individual ($p_{\text{T}}^{\text{jet}}$) and/or associated object quantities, such as topological relations among the calorimeter and MS signals (e.g. $\Delta\phi(e, \mu)$). The regions of the detector transversed by a high-energy particle, as identified by the L1 trigger, are referred to as *Regions of Interest*. These are propagated to the the next, software-based trigger, the *High Level Trigger* (HLT) for more accurate object reconstruction. The HLT is seeded by the L1 trigger and use offline-like reconstruction algorithms and information from all the sub-detectors (ID, calorimeters and MS) to refine the L1 decision and conclude on recording the event or not. Eventually after the HLT, the recording event rate of the ATLAS detector is 1 kHz.

In order to use the triggering system efficiently, multiple *trigger chains*, composed of combinations of L1 and HLT objects, have been defined and an event is recorded

if at least one of them returns a positive decision.¹ The nomenclature of the trigger chains used further in this work first describes the HLT trigger threshold and the PU suppression algorithm used and then the L1 seed threshold. For instance, the `HLT_xe100_mht_L1XE50` describes a missing energy trigger with L1 seed threshold of 50 GeV and HLT of 50 GeV calculated after applying the `mht` PU suppression algorithm. More details regarding the triggers and the HLT algorithms used are given in [110]. The exact trigger chains used to collect data events for the two analysis of this work are listed in Tables 7.1 and 8.1.

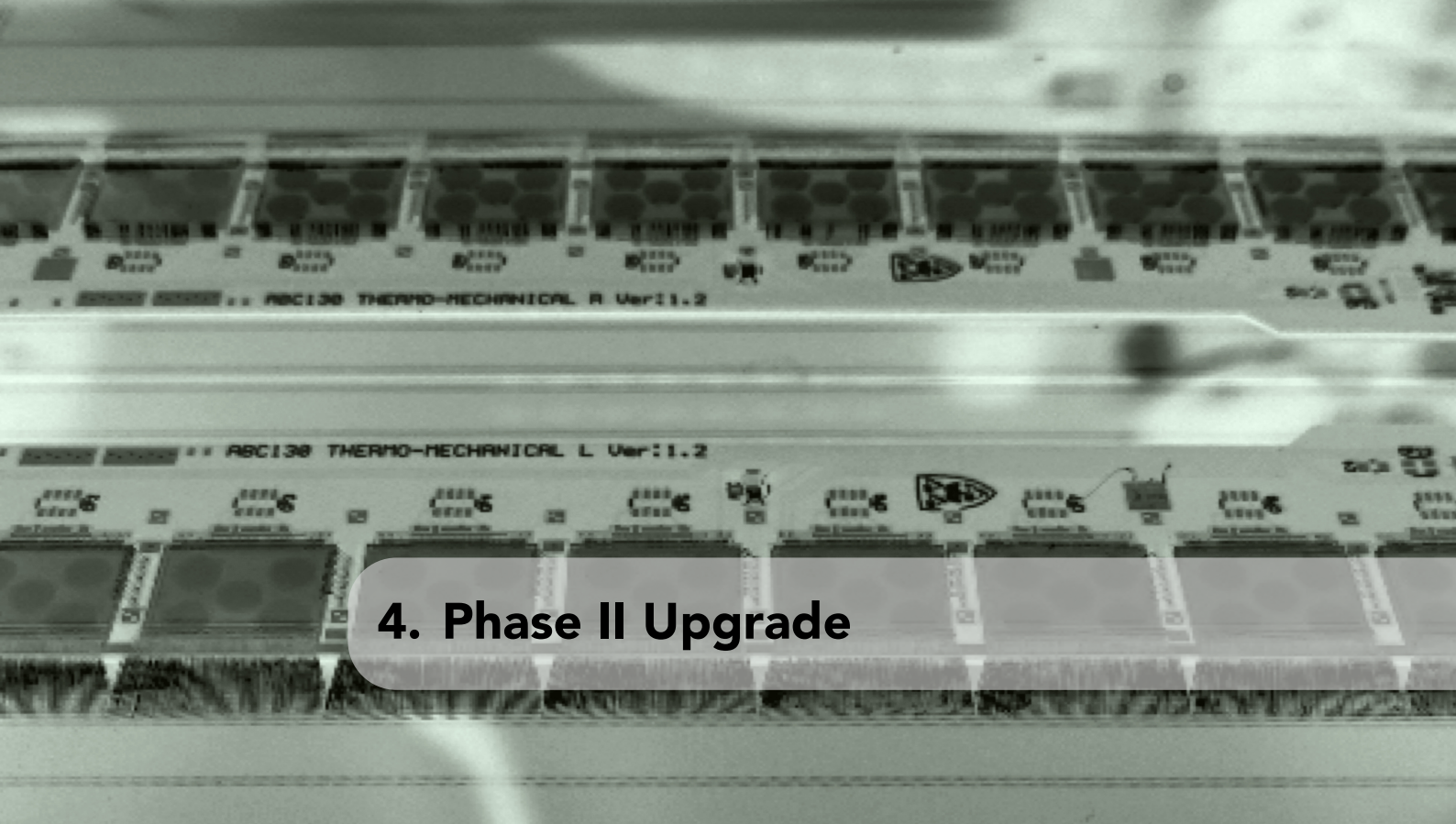
3.2.6 Detector Simulation

The physics event view derived by the event simulation process, described in Section 1.4, is complete but far from representative to what a particle physics detector, as the ATLAS, is recording. To produce a realistic view, the interactions of the stable particles with the detector material, the signal induced and its readout should be simulated in a step called *detector simulation* [111]. It should be noted, that prior to the detector simulation step the so-called *truth* physics objects are defined and represent directly the particles of an event without any assumptions of the experimental facility.

The detector simulation is achieved by propagating the generated stable particles of an event through the ATLAS detector geometry using the GEANT4 toolkit [112]. The software simulates the particle - material interactions and the corresponding energy deposits to the sensitive detector elements in spatiotemporal *hits*. These hits are used in a consecutive step called *digitisation* to emulate the detector signal and its readout after introducing noise effects. The output has the same format as the data coming from the detector itself, thus the same reconstruction algorithms, described in Section 5, can be applied in both simulated and real data. During the digitisation, the events are overlaid with minimum-bias hadronic activity² to emulate the PU effects and the L1 trigger decision. As the simulations are produced during the data-taking, a further re-weighting is applied at the analysis level to correct the predicted PU distribution to the actual one measured. Last but not least, as the detector simulation is a computationally expensive process, so cases where accuracy can be compromised – as the signal processes for this work – fast-simulations of the calorimeter response using a parametrisation are used [113].

¹All the triggers used in this work are *unprescaled*, meaning that all the events that return a positive decision are recorded.

²Inelastic hadronic activity in a loose definition including diffractive and non-diffractive collisions.



4. Phase II Upgrade

Sensor radiation tolerance is crucial in harsh environments such as the HL-LHC, thus only extensively tested technology can be used

The main subject of this chapter is the description of the Sheffield microstrip sensor characterisation facility developed to test the radiation tolerance of the sensor technology to be installed in the Inner Tracker of the upgraded ATLAS detector in 2024. Commissioning measurements supporting the successful operation of the facility are also presented.

4.1 Phase-II LHC and ATLAS Upgrades

During the Run 2 period, the LHC has surpassed its design luminosity by a factor of ~ 2 with the peak luminosity achieved to be $2.1 \times 10^{34} \text{ cm}^{-2} \text{ s}^{-1}$. In order to fully exploit the machine potential, a major upgrade (Phase-II Upgrade) is planned for 2024 to 2026 that will lead to the *High-Luminosity LHC* (HL-LHC) [114] (Figure 1). The HL-LHC is designed to increase the luminosity, compared to the current LHC, by a factor of 5 to 7 and after more than a decade of operation to collect 3000 fb^{-1} of data. This increase would be achieved by directly improving the parameters of Eq. 3.1. In particular, the number of

protons per bunch N_p is expected to be doubled, the transverse area of the beam σ_T^2 to be decreased and the beams overlap at the collision points to be maximised.

To cope with this increase in luminosity, the ATLAS detector is going to be upgraded as well [115]. The increased luminosity comes at the price of increased PU and radiation damage, thus parts of the detector should be replaced to maintain its performance. The main operation regards the complete replacement of the ID by the *Inner Tracker* (ITk). The ID is designed to withstand *fluences* – i.e. number of radiated particles – corresponding to an integrated luminosity of 400 fb^{-1} (Pixid detector bottleneck), while higher values would increase the leakage current more than the available powering and cooling can compensate for. Another limitation comes from the currently available bandwidth between its front-end electronics and the read-out drivers that is saturated at luminosities of $3 \times 10^{34} \text{ cm}^{-2} \text{ s}^{-1}$. Finally, the increased PU leads to increased track density and unaffordable occupancy at the current sensors size (TRT bottleneck) [116]. The above deficits are going to be addressed by the ITk that is briefly described below.

4.2 Inner Tracker

The ITk will be an all-silicon detector replacing all the ID sub-detectors (Pixels, SCT and TRT). It is designed to operate at luminosities up to $7.5 \times 10^{34} \text{ cm}^{-2} \text{ s}^{-1}$ for up to about a decade and able to provide superior tracking performance up to $\langle \mu \rangle = 200$. It is composed of two sensor technologies, pixel sensors near the beam pipe and strip sensors in the outer layer. Both of them are arranged in barrel layers and end-cap sections that provide rapidity coverage up to $|\eta| < 4$. The proposed layout is shown in Figure 4.1. The research conducted in the context of this dissertation is focused on the strip sensors thus only this part of the ITk is detailed below.

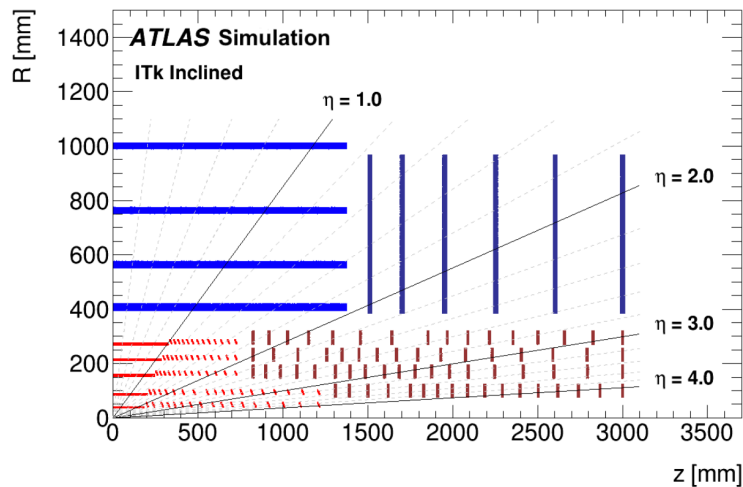


Figure 4.1: Layout of the future ITk detector. Only one quadrant is shown with the axis origin being the IP, the horizontal axis the z -axis of the ATLAS coordinate system and the vertical the y -axis ($|\eta| = 0$). The red (blue) marks represent pixel (strip) sensors. [116]

4.2.1 Strip Detector

The strip detector part of the ITk [116] consist of about 18,000 modules arranged in support structures in four barrel layers and six end-cap discs per side (called *staves* and *petals* respectively). These structures provide the required mechanical stability and cooling of the detector modules. A detector module consist of a single silicon strip sensor, one or two hybrids with up to twelve read-out chips (ABCStar) glued directly onto the silicon, one or two hybrid control chips (HCCStar) and a power board (Figure 4.2). The ABCStar are wire-bonded onto each individual strip to read-it-out.

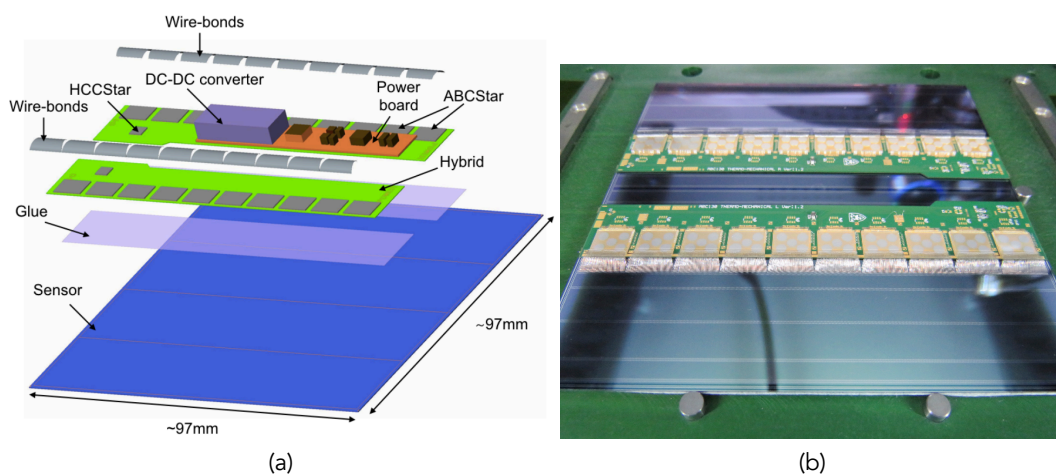


Figure 4.2: (a) Layout of a typical barrel ITk strip module. [116] (b) Picture of a similar dummy module taken into the Sheffield clean-room, only the silicon sensor is operational and the power board is missing. Picture courtesy of Dr. Guillermo Nicolas Hamity.

A typical barrel detector module consist of a $97 \times 97 \text{ mm}^2$ area and $320 \pm 15 \text{ }\mu\text{m}$ thick sensor (sensors vary in shape and dimensions depending on their location, for details refer to Table 6.2 of [116]). Its strip implants are made from n-type silicon in a p-type bulk (n^+ -in-p)¹ while the inter-strip isolation is provided by p-stop implants (p-type silicon lines places between adjacent strips). The active area of the sensor is enclosed by a bias ring that provides High-Voltage (HV) to the strips and separates them (along with other rings) from the in-active area. The strips are read-out by wire-bonds on AC-pads, which are openings of the top insulation layer of the sensor bringing contact to the aluminum strips placed on top (capacity coupled) of the n-type silicon strips. The above main elements of the sensor are illustrated in Figure 4.3. The prototype sensors used for the studies of this work are called ATLAS12 [117] and they have the same architecture with the final design to be used in the ITk, the ATLAS17. In particular, only *miniature* ATLAS12 sensors are used for practical purposes. These have dimensions $1 \times 1 \text{ cm}^2$ and 128 strips/read-out channels.

¹The choice of n^+ -in-p technology, against the p-in-n of the SCT, has been made as in high radiation environments it provides a factor of two more charge. [116]

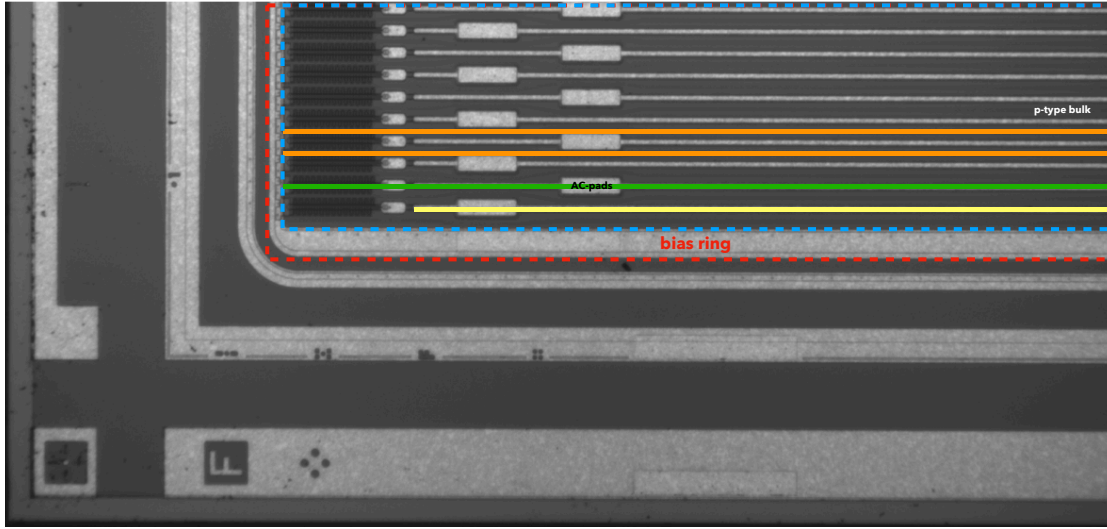


Figure 4.3: Picture of an ATLAS12 strip sensor. An n-type strip is shown in green, two p-stops in orange and an aluminum (visible) strip in yellow. The active area of the sensor is enclosed with the blue dashed line and the bias ring with the red. Edited picture from [118].

4.2.2 Radiation Effects

As mentioned already, the higher luminosity of the HL-LHC translates into higher PU and radiation doses to the detector. Simulation studies have shown that the ITk strip sensors should be able to withstand fluences up to $10^{15} \text{ 1 MeV n}_{\text{eq}}\text{cm}^{-2}$ (definition follows from Eq. 4.2) at the outer end-cap discs (including a safety factor of 1.5) after about a decade of operation, as shown in Figure 4.4a. The sensors should also withstand a total ionisation dose up to 0.5 MGy but the work presented here is focused on the bulk material radiation damage caused by nuclear recoils, thus the radiation effects are studied mainly as function of the fluence.

Hadrons and high-energy leptons transversing a silicon sensor are causing damage on its bulk material by displacing the lattice atoms. These atom displacements create individual vacancies and interstitials as well as more complex structures that lead to permanent defects (reactions of the vacancies and interstitials with themselves and impurity atoms) that alter the electrical properties of the silicon [119]. As the displacement damage to the material depends on the type of interaction occurs, the *Non Ionizing Energy Loss* (NIEL) hypothesis is used to quantify these phenomena as function of the incident particle energy. In particular, the amount of energy deposited is given by [120]:

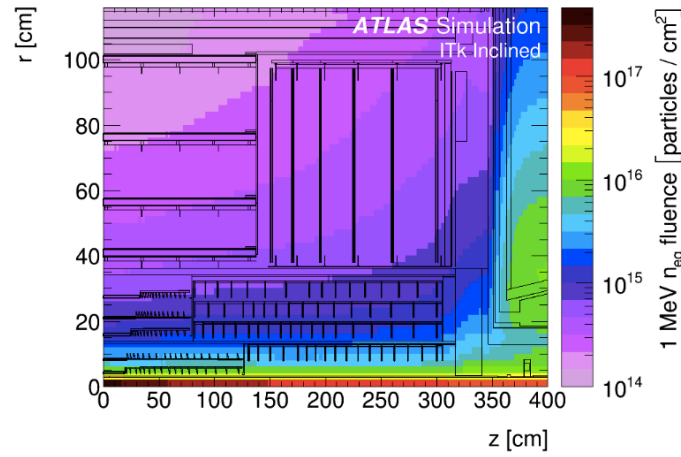
$$D(E) = \sum_i \sigma_i(E) \int_0^{E_{R,\text{max}}} f_i(E, E_R) P(E_R) dE_R, \quad (4.1)$$

where $P(E_R)$ describes the portion of the incident particle energy ending at displacing silicon atoms (*Lindhard partition function*) [121], $f_i(E, E_R)$ the probability of an incident particle with energy E to knock an atom with recoil energy E_R (integrated over all

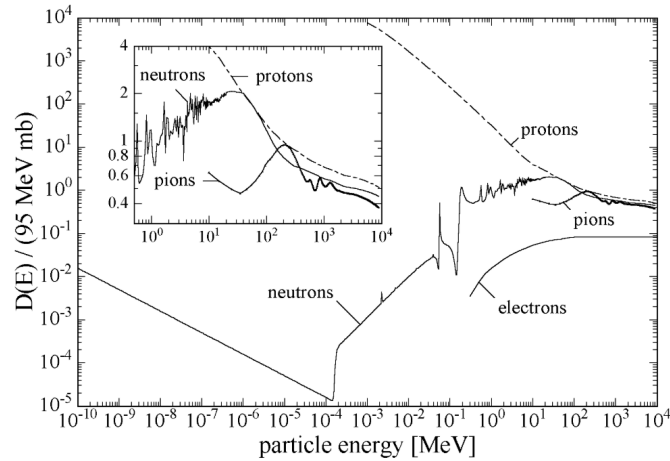
possible recoil energies) and $\sigma_i(E)$ the cross-section of a particular interactions with the silicon lattice. The whole Eq. 4.1 is summed over all possible interactions i . The $D(E)$ for different particles is shown in Figure 4.4b, where as standard the 1 MeV *neutron equivalent fluence* ($n_{\text{eq}}\text{cm}^{-2}$) is used. The standardisation across the different radiation sources is achieved by the so-called *hardness factor* [120]:

$$k = \frac{\int D(E)\Phi(E)dE}{D(E_{\text{neq}})\int \Phi(E)dE}, \quad (4.2)$$

where $\Phi(E)$ is the particle energy spectrum and $\int \Phi(E)dE$ is the irradiation fluence.



(a)



(b)

Figure 4.4: (a) The expected fluence at the ITk after about a decade of operation and integrated luminosity of 3000 fb^{-1} . [116] (b) The NIEL displacement damage for different particles normalised to $1 \text{ MeV } n_{\text{eq}}\text{cm}^{-2} = 95 \text{ MeV mb cm}^{-2}$, where b is the cross-section unit barn. [119]

The radiation damage to the bulk material of the sensor induce macroscopic effects. These are evaluated in *characterisation facilities* by measuring sensor properties

to gauge the degradation of its performance. The main defining characteristics studied at the facility developed for this work – and in general in literature [108, 116, 118] – are:

1. **Depletion Voltage:** In the n-p junction there is an area “free” of charge carriers (due to the different Fermi energy between the n-doped and p-doped silicon) that is used as the active material of the sensor; an incident charged particle interacts with the silicon atoms and produces electron-hole pairs that drift towards the anode (n-type strips) and cathode (p-type bulk) respectively. This *depleted area* is increased by applying (reverse) bias voltage, reducing the charge carriers density and allowing the junction to be used as a particle detector. Particular defects add energy levels to the material that lead to an increased charge carrier density thus higher bias voltage needs to be applied to fully deplete the sensor. Increased depletion voltage translates into higher power demands during the operation of the sensor.
2. **Leakage Current:** The current caused by electron-hole pairs while the sensor is fully depleted is called *leakage current* and acts as a noise against the signal of incident particles. In an unirradiated sensor the leakage current increase with the bias voltage ($I \propto \sqrt{V}$) until the sensor is fully depleted while afterwards show only a small increase [108]. As the defects act as electron-hole generators, the leakage current of an irradiated sensor is higher than an unirradiated one and lower temperatures are needed during its operation to maintain the same Signal-to-Noise ratio (S/N), as the leakage current strongly depends on temperature as well ($I \propto e^{-1/T}$) [122].
3. **Charge Collection Efficiency:** As mentioned already, when charged particles transverse the depleted area, they deposit energy by creating electron-hole pairs. The ability of a sensor to collect this charge is of particular importance regarding the amount of generated signal. Certain defects act as charge traps, preventing the full amount of charge induced to be collected and resulting in lower generated signal. In particular, the trapping rate is proportional to the number of defects thus the irradiation fluence received, and at high values ($> 10^{15} \text{ 1 MeV n}_{\text{eq}}\text{cm}^{-2}$) this becomes the main limiting factor on the silicon sensor usage [120].

The average energy deposited per unit length while a relativistic charged particle transversing a material is given by the *Bethe-Bloch* formula [35]:

$$\left\langle -\frac{dE}{dx} \right\rangle = Kz^2 \frac{Z\rho}{A} \frac{1}{\beta^2} \left[\frac{1}{2} \ln \frac{2m_e c^2 \beta^2 \gamma^2 W_{\text{max}}}{I^2} - \beta^2 - \frac{\delta(\beta\gamma)}{2} \right], \quad (4.3)$$

where $K = 0.307 \text{ MeV mol}^{-1} \text{ cm}^2$, z the incident particle charge, the Z (A) and ρ the material atomic number (mass) and density respectively, m_e the electron mass, W_{max} the maximum energy transfered in a collision, I the average excitation energy of the material and $\delta(\beta\gamma)$ correction term to the ionisation energy losses.

The distribution of Eq. 4.3 exhibits a minimum and the estimates of the deposited energy use this minimum as a worst case scenario (*Minimum-Ionizing Particle* (MIP)). For the silicon, the average energy deposited by a MIP is $390 \text{ eV}\mu\text{m}^{-1}$. However, due to large energy transfers from central collisions with silicon electrons (δ -electrons) the dE/dx distribution has a long high-tail and is described by a Landau *Probability Density Function* (pdf). The most probable value then is about 30% less than the average, so $275 \text{ eV}\mu\text{m}^{-1}$ [108]. For a fully depleted ATLAS12 sensors this corresponds to $88 \pm 4 \text{ keV}$ and the creation of $24,000 \pm 1,000$ electron-hole pairs. The ratio of the latter, theoretically calculated value and the measured one defines the *Charge Collection Efficiency* (CCE) of a sensor and is an important gauge for its performance.

4. **Hit Cluster Size:** The cluster size is defined as the number of strips, with S/N above a threshold¹, considered to collect the induced charged on the sensor (typically one to two). A large cluster size (few strips) impacts negatively the spacial resolution of the reconstructed track. Ionising radiation permanently damages the insulating material at the surface of the sensor (SiO_2) and increase the inter-strip capacitance, effectively leading to broader clusters and degrading the sensor performance [120].

4.3 Sheffield Characterisation Facility

To evaluate the performance of irradiated prototype strip sensors for the ITk, a characterisation facility has been developed in the clean-room of the Hicks Building at the University of Sheffield [3]. In order to deliver trustful estimations of the detector performance, key elements of the measurements, such as the signal generation, the detector read-out and the data-taking environmental conditions, resemble the operational conditions of the ITk as closely as possible.

To begin with, the high-energy particles (β -radiation) needed to induce signal to the sensor are emitted from a ^{90}Sr radioactive source, offering electrons with energies up to $\sim 2.3 \text{ MeV}$ [123]. The source is sealed in a metallic (stainless-steel or lead) container and collimated by an acrylic (polymethylmethacrylate) glass collimator. The experimental setup is composed by three layers. The source is placed on the upper layer and right underneath, on the middle layer, the sensor is mounted. The electrons emitted from above transverse the sensor inducing charge in its depleted area which is collected by the strips. As the electrons continue after crossing the sensor, they reach the lower layer where a triggering system has been placed to trigger the data acquisition. The distance among the layers has been minimised as much as possible so the electron beam remains as collimated as possible. The triggering system consist of two duplicate modules working in coincidence to further reduce the environmental radiation back-

¹In general, a detector element with S/N above a threshold registers what is referred to as a *hit*.

ground. Each module consist of a plastic scintillator (polyvinyltoluene) [124] glued to a light-guide, both cut in cuboid shapes. The light-guide is mounted on a Hamamatsu H10721-01 photosensor module [125] (photomultiplier and power-supply module, referred as PMT henceforth) that is powered by a 5 V DC supply and generates a signal pulse each time a particle crosses the scintillator. The triggering module along with a schematic view of the whole experimental setup is shown in Picture 4.5 and Figure 4.6a respectively.

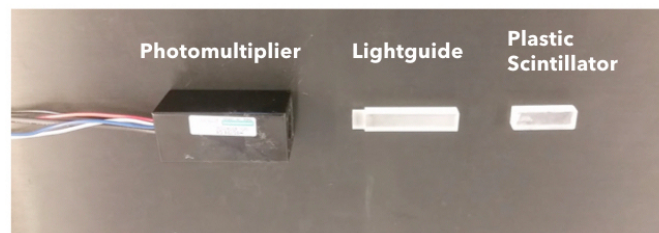


Figure 4.5: The triggering system before gluing and mounting its parts. The picture comprises an original work of the author.

The whole experimental setup described above, and shown in Figure 4.6a, is placed inside an insulated controlled environment (fridge) that provides certain temperature and humidity levels resembling the operational conditions of the ITk. As explained above, the irradiated sensors exhibit increased leakage current. This is seen as excessive heat that needs to be dissipated in order to maintain a reasonable S/N. Therefore, all the measurements are conducted in a temperature of ~ -30 °C. It should be noted that this is the case for the unirradiated sensors as well, as the measurements are heavily temperature-dependended and the purpose of the characterisation is to compare the features of irradiated to unirradiated sensors. Nitrogen is also purged into the fridge to reduce the humidity levels to about 20% RH thus preventing condensations to form. The whole experimental setup inside the fridge is shown in Picture 4.6b.

4.3.1 ALiBaVa Read-out System

The sensor read-out and data analysis is performed by using the ALiBaVa system [126]. The system is composed by two hardware components and a software to analyse the acquired data. The two hardware components are:

1. **Daughter-board:** The purpose of the daughter-board is to read-out the sensor signal in each strip. This is achieved by an analogue Beetle chip [127] with 128 channels, originally developed for the silicon sensors of the LHCb experiment. Each channel is wire-bonded to the AC pad of each strip of the sensor. The analogue signal is sampled by the chip with 40 MHz frequency, resembling the data-taking conditions of the (HL-)LHC while the full Landau pulse is reconstructed by acquiring multiple events (usually 200,000). Each daughter-board consist of two Beetle chips (thus two sensors can be tested simultaneously), sensor mountings

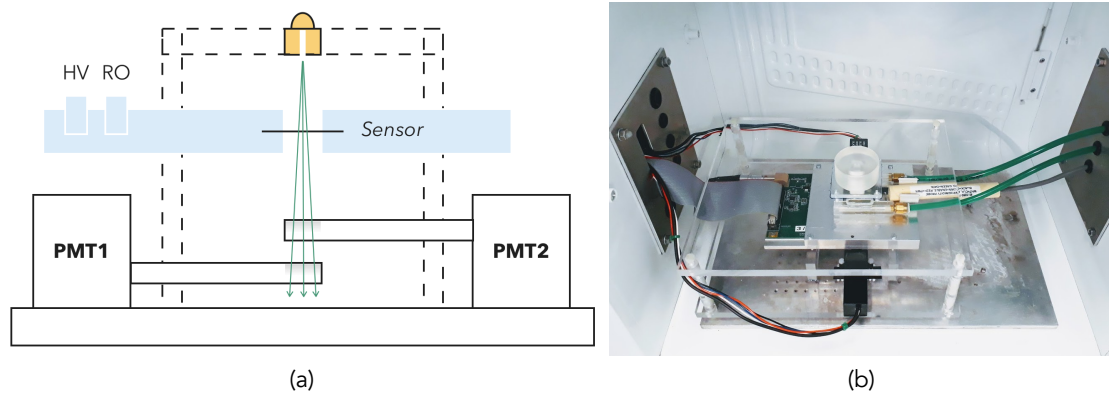


Figure 4.6: (a) Schematic view of the experimental setup. The yellow artifact on the upper layer is the radioactive source that emits β -radiation through the sensor on the middle layer and the triggering system on the bottom layer. Figure published in [3]. (b) The whole experimental setup inside the fridge at the Sheffield clean-room. The green tubes are pumping nitrogen gas near the sensor to prevent condensations to form while the beige tube encloses sensors for real-time temperature and humidity measurements. The picture comprises an original work of the author.

and power supplies – low-voltage for the board and bias HV for the sensor (the power supply units are shown in Figure 4.8b). The daughter-board is placed in the middle layer of the experimental setup (ciel colour in Figure 4.6a) and shown in Picture 4.7.

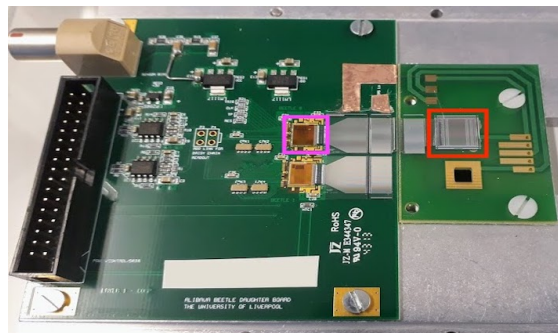
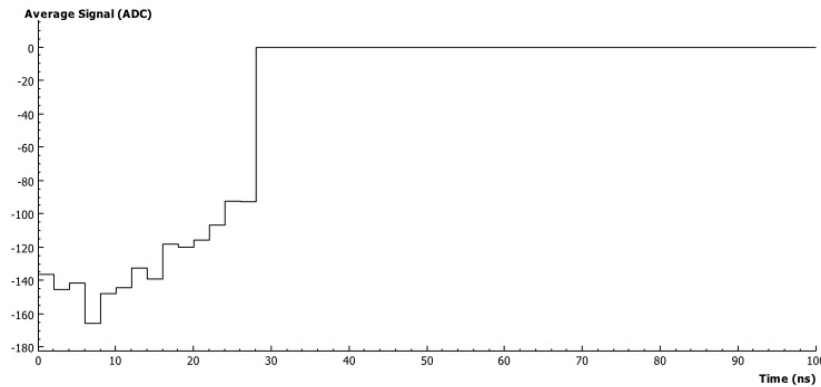
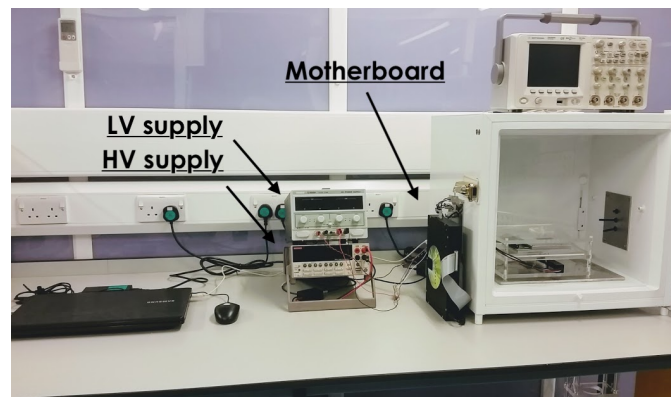


Figure 4.7: The ALiBaVa daughter-board with a mounted sensor on (red box) and the corresponding read-out Beetle chip (pink box). Picture published in [3].

2. **Mother-board:** The mother-board main purpose is to acquire the analogue signal from the daughter-board and digitise it, converting it to *Analogue to Digital Converted* (ADC) counts. It also handles the triggering signal and synchronise it with a particular position in the pipe-line the Beetle chip outputs. As the sampling window is shorter than the signal pulse, the peak of the pulse should be inside it. This has been achieved by tuning the *latency* between the triggering and the sensor signal resulting in the example reconstructed pulse shown in Figure 4.8a. Exploring the separability of the system, the mother-board is placed outside of the fridge and is connected by a USB connection to a computer in order the data



(a)



(b)

Figure 4.8: (a) An example of a reconstructed pulse after tuning the latency between the triggering and the sensor signal. The peak (minimum) of the pulse is clearly inside the sampling window. The particular pulse has been reconstructed by 40,000 events while its shape would be smoother with a higher statistics sample. The figure comprises an original work of the author. (b) The view of the experimental modules outside of the fridge at the Sheffield clean-room. Picture published in [3].

to be stored and analysed by the software, as shown in Figure 4.8b.

4.3.2 Commissioning Measurements

The commissioning of the Sheffield characterisation facility is completed by indicative measurements of unirradiated and irradiated miniature ATLAS12 strip sensors. These measurements serve the purpose to verify the operational readiness of the facility. In particular, the sensor features studied are the ones listed and explained above: the depletion voltage, the leakage current, the CCE and the hit cluster size. The whole development of the facility was assisted by collaborators from the University of Birmingham and the University of Liverpool, where similar facilities are located to test sensors. Therefore, the commissioning measurements are evaluated in comparison to similar ones taken at the aforementioned facilities in the UK.

4.3.2.1 Method

To conduct the measurements a particular procedure is followed and is described in the following steps:

1. **Sensor mounting:** The sensor is wire-bonded on the mounting board (right, small board in Figure 4.7) that also provides it with HV. The mounting board is consecutively wire-bonded to the Beetle chip.
2. **Setup preparation:** The daughter-board is placed in the middle layer of the experimental setup and the radioactive source, right above, on the upper layer. The HV and data-transfer cables are plugged into the daughter-board as well.
3. **Environment preparation:** The whole experimental setup is placed inside the fridge and is sealed. The fridge is purged with nitrogen and when the humidity reach the desired level, the fridge is cooled-down to ~ -30 °C. This step takes up to an hour to complete.
4. **Powering-up:** The PMT are powered on their operational voltage. The HV supply is turned on and a leakage current limit is applied to safely test the sensor. This is $0.5 \mu\text{A}$ ($15 \mu\text{A}$) for unirradiated (irradiated) sensors. Afterwards, the required bias voltage is applied in small incremental steps (0.1, 1, 10 V).
5. **Data-taking:** The data-taking procedure consist of recording multiple events in order to reconstruct the Landau pulse in a later time during the data analysis. A typical sample of 200,000 events is acquired in a period of about 20 min. The data-taking step is usually repeated for different values of bias voltage to measure the CCE and determine the sensor full depletion regime.
6. **Powering-down & Cooling-up:** After all the datasets have been taken the sensor and PMTs are powered-down and the fridge is slowly warmed-up.

An important measurement should also be taken before each sensor data analysis. The ALiBaVa system is designed to read-out both n-type and p-type strip sensors thus it can register both negative and positive signals. Therefore, the middle of ADC range (0 - 1023) at 512 corresponds to zero charge collected by a strip. A so-called *pedestal run* is conducted before each set of measurements, by random triggering the system, to record the exact value of this baseline and its fluctuation (noise) by fitting a Gaussian per channel. Any deviation (up or down) during the actual data-taking would mean the recording of a signal. Tests have shown no strong dependence of this baseline on the presence of the radioactive source or the value of the bias voltage applied to the sensor thus the pedestal measurement is taken once per sensor tested with the radioactive source and the sensor fully depleted. An example of a pedestal measurement is shown in Figure 4.9.

The commissioning measurements conducted regard an unirradiated and two irradiated sensors. The sensor irradiation was performed in 2014 at the Birmingham MC40 irradiation facility [128] with the purpose to define few benchmark samples to compare

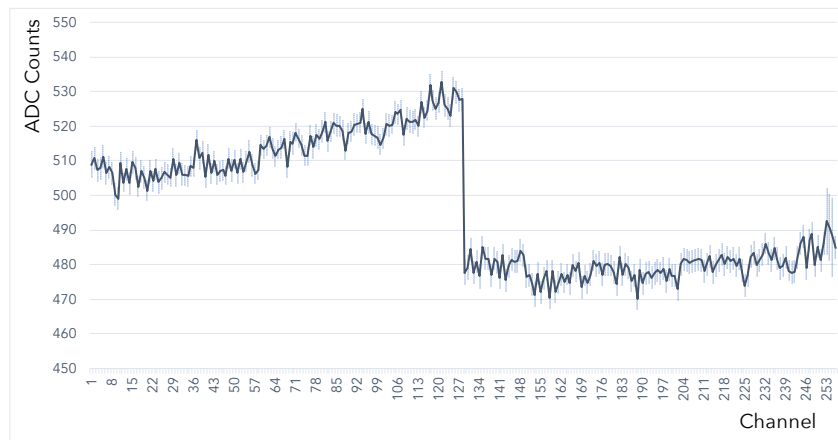


Figure 4.9: Example of the pedestal measurement of an unirradiated ATLAS12 sensor. The solid line shows the baseline (mean of the Gaussian) and the dotted the noise (width of the Gaussian) per channel. The sensor is mounted on the first Beetle chip thus the first 128 channels show higher baseline. The figure comprises an original work of the author.

the characterisation studies among different facilities in the UK. The two sensors were irradiated to fluence of 10^{15} $1 \text{ MeV n}_{\text{eq}}\text{cm}^{-2}$ by a 24 MeV proton beam of $1 \mu\text{A}$ current ($k = 1.76$). The irradiation methodology followed is referred to as *scanning* irradiation as the samples are placed in front of the incident beam and are scanned horizontally using an XY-axis robotic system. This irradiation methodology allows for beam intensity non-uniformities to be eliminated by multiple passes of the beam over the sample. The two samples are scanned in different speeds (8 and 1 mm s^{-1}) in order for potential thermal effects during the irradiation to be apparent on the performance measurements results. The sensors have been subsequently stored and transferred in sub-zero temperatures to reduce any post-irradiation annealing effects¹ to negligible levels.

4.3.2.2 Results

The first measurement taken concerns the leakage current of the sensors, which is measured by the HV power unit over different bias voltages applied. The result is presented in Figure 4.10 for the two irradiated sensors. While the unirradiated sensor current has been measured to be few nA at maximum [3], the irradiated ones show a clear increase with values up to few μA .

The following measurements are conducted using the data acquired by the ALiBaVa system. After the data-taking procedure described above, the off-line analysis occurs in the following steps:

1. The pedestal values are subtracted from the signal acquired from each channel of the sensor based on a measurement similar to the one presented in Figure 4.9. A correction of the common noise, induced to all the channels simultaneously due

¹The term *annealing* refers to the diffusion process of the defects that leads to their (re)combination, with both positive and negative effects to the performance of the sensor. For a detailed description, refer to Section 2.1.2 of [120].

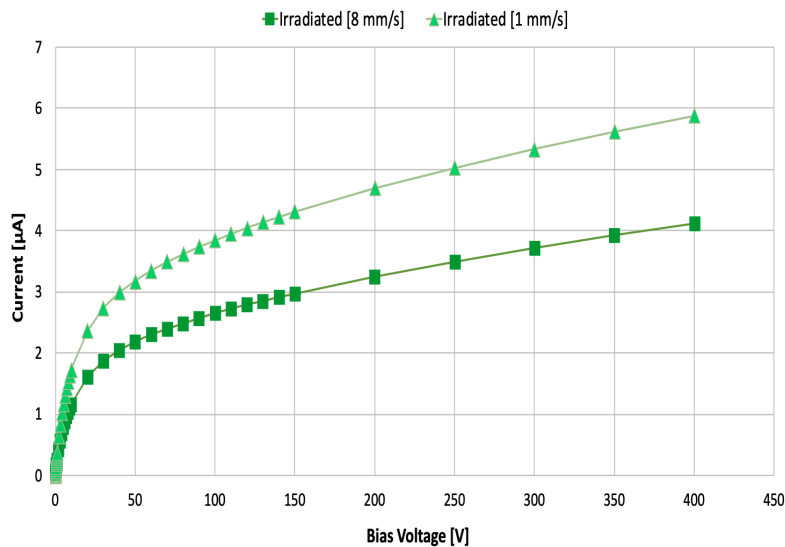


Figure 4.10: The leakage current measurement for different bias voltages applied and for the two irradiated sensors studied. Figure published in [3].

to random fluctuations in HV, is also applied per event in this step.

2. In each event, the signal is registered for a given channel if its $S/N > 5$ (*primary channel*). Only one primary channel is registered per event, the channel with the highest S/N . Afterwards, a clustering procedure takes place, where the signal of neighbouring channels is added to the primary channel if their $S/N > 3$. The ADC value of the cluster signal is added to a histogram and the procedure is repeated for all the events of the dataset. An example ADC histogram for a fully biased unirradiated sensor is shown in Figure 4.11a.
3. The constructed histogram is fitted by a Landau curve to estimate its peak that corresponds to the measurement of the most probable value of the collected charge, thus the deposited energy. An example Landau fit for a fully biased unirradiated sensor is shown in Figure 4.11a.
4. Using as a reference the unirradiated sensor, its ADC peak value, when fully depleted, is corresponded to the theoretically calculated $24,000 \pm 1,000$ electron-hole pairs. Using this calibration, the response of the irradiated sensors is measured and their CCE is calculated.

The above procedure is repeated for all the three sensors tested and for measurements taken under different bias voltages. The measured collected charge for each sensor and each bias voltage is presented in Figure 4.11b. From the unirradiated sensor measurements, it can be seen that the sensor is fully biased already at 300 V, as it doesn't collect more charge even in higher bias voltage values. The same applies to the irradiated sensors as well, thus no apparent increase of the depletion voltage is seen. This might be an artifact, although, of the coarse granularity of the measurements. Regard-

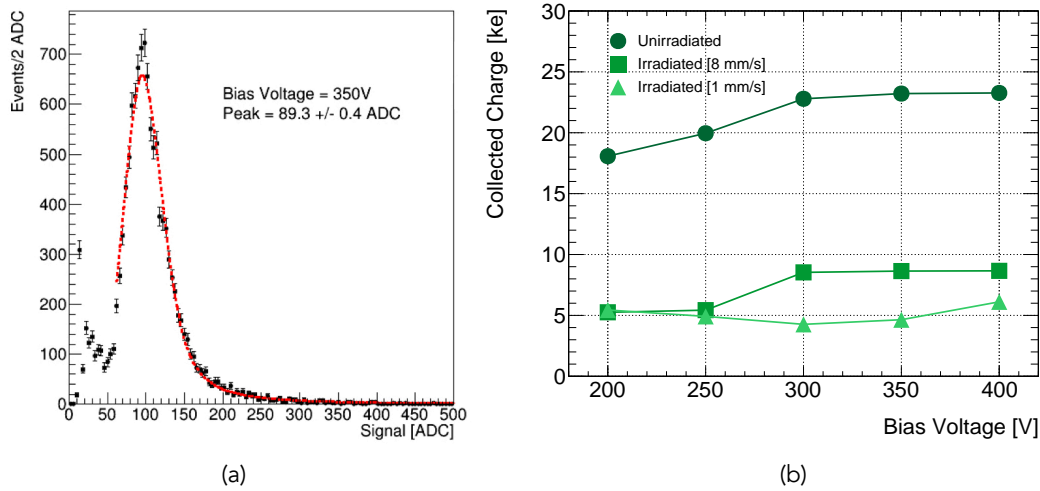


Figure 4.11: (a) The distribution of the cluster ADC signal of a 200,000 event dataset taken on an unirradiated sensor biased at 350 V and fitted by a Landau curve. The estimated peak value is also noted. The figure comprises an original work of the author. (b) Measurements of the most probable value of the collected charge for different value of bias voltage and all the sensors tested. Figure published in [3].

ing the irradiated sensor CCE, this is reduced by 65% (80%) to the sensor irradiated at scanning speed of 8(1) mm s^{-1} , clearly indicating degraded performance after the irradiation. The higher leakage current and lower CCE of the sensor irradiated at lower scanning speed indicates that the increased heat induced during the irradiation, as the sensor stayed for longer period in front of the incident beam, further degrade its performance.

Finally, a hit cluster size comparison between the unirradiated and the irradiated sensor (8 mm s^{-1}) is made. This is presented in Figure 4.12 and shows a distribution with a higher tail (four- and five-strip clusters) for the irradiated sensor. One would expect a higher number of two-strip clusters as well thus this measurement is not considered conclusive. This particular measurement, however, is heavily dependent of the collimation of the β -radiation beam; a wider beam would naturally produce wider clusters in both unirradiated and irradiated sensors. The beam collimation (and the distance of the source to the sensor) has been varied during the measurements due to the facility development thus this is a possible explanation of the different shape observed between the two distributions of Figure 4.12.

4.3.3 Conclusion

A silicon strip sensors characterisation facility was designed, developed and commissioned in order to test irradiated sensors for the ITk upgrade of the ATLAS detector. The sensors arrive already irradiated at the University of Sheffield and are stored and tested in a insulated controlled environment resembling the ITk operational conditions.

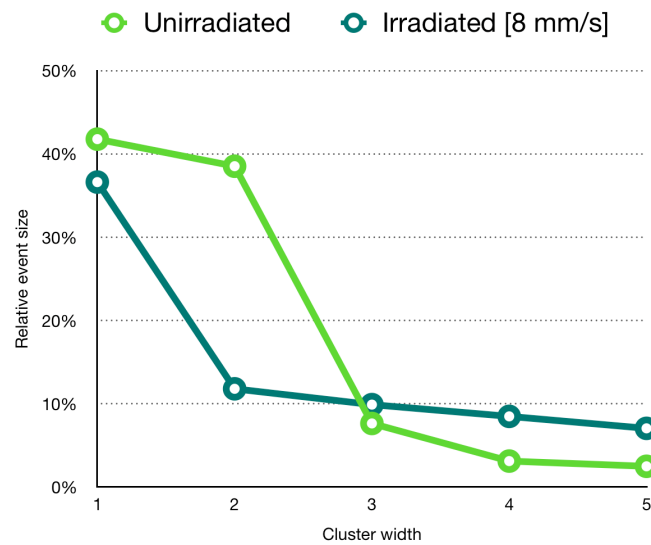


Figure 4.12: Hit cluster size distributions for the unirradiated and the irradiated (8 mm s^{-1}) sensor. Figure published in [3].

The signal is induced by β -radiation and is read-out and analysed by the ALiBaVa system.

Commissioning measurements are conducted to verify the facility operational readiness. The sensor properties studied are the leakage current, the depletion voltage, the CCEs and the hit cluster sizes. In all cases the results of irradiated sensors are compared to unirradiated ones. The results have been discussed with collaborators from the University of Birmingham and the University of Liverpool and have been found compatible with similar ones performed and published by the characterisation facility of the University of Birmingham [128]. Therefore, the commissioning of the Sheffield silicon strip sensor characterisation facility is considered successful.



5. Physics Object Reconstruction

Physics objects are particle representations reconstructed from the electronic signal of the detector

The purpose of this chapter is to introduce the procedures used to translate the signals acquired from the ATLAS detector (real or simulated) to representations of the particles that induced them. These representations are called *physics objects* and the relevant ones for the physics analyses of this work are: (1) electrons, (2) muons, (3) jets and (4) missing energy.

5.1 Tracks & Vertices

One of the first steps towards an event characterisation is the reconstruction of the trajectories of charged particles (*tracks*) that cross the ID of the ATLAS experiment [129, 130]. Charged particles deposit energy on the silicon sensors, as described in Section 4.2.1. Usually this energy is spread over adjacent active elements (pixels or strips) thus firstly, a clustering procedure that groups (up to three) hits into a single cluster is performed. Clusters form space-points, representing the points the particle transversed the ID. Track seeds are formed from three space-points and quality criteria (momentum, impact parameter, proximity to other space-points, etc.) are applied to increase their

purity¹. A Kalman filter [131] then constructs (silicon) track candidates by extending the track seed hits to the outer layers of the ID. Track candidates with shared clusters, either because two particles crossed the same active element or because they were incorrectly assigned, are removed by an ambiguity solver algorithm. The algorithm first ranks the candidates with a score based on their quality and then removes clusters or whole tracks that fail specific criteria. The foremost are:

1. $p_T > 400$ GeV,
2. $|\eta| < 2.5$,
3. distance from measured beam-spot ($|d_0| < 2$ mm and $|z_0 \sin \theta| < 3$ mm),
4. at least 7 clusters,
5. maximum of one or two shared clusters,
6. less than three holes.²

The remaining tracks are used to find compatible TRT hits in a procedure called *TRT extension*. Generally, an algorithm assigns TRT hits to a silicon track and a consequent high resolution fit forms extended track candidates that pass through the ambiguity resolving stages as previously. The remaining tracks are the final ones of the track collection. After the end of the so-called *inside-out* track reconstruction described above, another *outside-in* pass (starting from TRT hits) occurs to recover missing tracks, for instance, from secondary decays of unstable hadrons (B mesons) that decay within the volume of ID.

The final tracks are used to define *vertices*, the signatures of particle interactions. Initially, a vertex seed is defined by the beam-spot position. The seed and all the tracks of the event are fitted together to estimate the best vertex position. The tracks are then weighted to reflect their compatibility with the estimated vertex. The fit runs iteratively until it converges and then the incompatible tracks are removed from the vertex. Consecutively, the procedure continues defining another vertex until all the tracks are used or a vertex cannot be found. Vertices are kept only if at least two tracks are associated with them. The algorithm is described in detail in [132] while Figure 5.1 shows the decrease in efficiency of vertex reconstruction as the average interactions per bunch crossing (PU) increase.

It is important to assess from which interaction a particle originates from (e.g. hard-scatter or PU) so the vertices of an event are ranked in descending order based on the sum of squares of the associated tracks p_T . The vertex that corresponds to the hard-scatter interaction is called *Primary Vertex* (PV) and is the one highest ordered while the rest are considered PU vertices.

¹The fraction of the seeds that result in good-quality tracks.

²An active element where a hit is expected but not found.

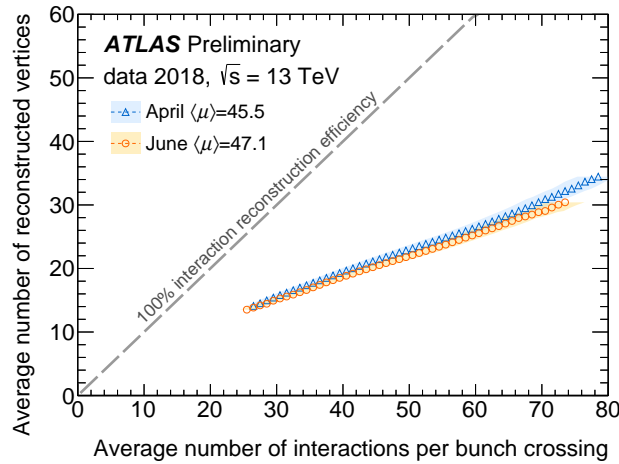


Figure 5.1: The number of reconstructed vertices as a function of the average number of interactions per bunch crossing, in two fills with different average number of interactions per bunch crossing (μ) taken at different points in 2018. [133]

5.2 Electrons & Photons

The electrons, as charged particles, are expected to leave both a track and an energy deposit signature in the detector. Their reconstruction is starting by forming energy clusters at the electromagnetic calorimeter by grouping and summing energy deposits in many calorimeter cells. The clustering algorithm used to achieve this is based on a fixed-sized rectangular sliding window that is looking for localised energy deposits (> 2.5 GeV). The tracks are formed in the ID by a similar approach as described in Section 5.1. The difference is that the track extension and fitting are adjusted to account for the electron energy losses via Bremsstrahlung radiation while transversing the detector material. Eventually, tracks are matched to clusters by $\eta \times \phi$ proximity requirements and the cluster is expanded to form the final candidate. The candidates energy is calibrated to the absolute energy scale correcting for detector effects using using multivariate techniques based on data and simulation that are detailed in [134].

Electrons are identified as prompt (signal) against non-prompt (background) – jets that fake electrons, electrons from photon conversions or electrons from heavy flavour hadron decay – based on a likelihood ratio discriminant. For different track and calorimeter quantities, *pdfs* are extracted from simulations and their product defines the signal and background likelihoods used to define the final discriminant. The latter is calculated for the reconstructed candidates and different values define overlapping identification classes that are summarised, along with their corresponding efficiencies, in Table 5.1. Correction factors are finally applied to the simulation to match the efficiency measured in data, henceforth referred to as *Scale Factors* (SF), and are 10% at maximum. The analysis-specific choices of electron identification classes used in this work are detailed in Tables 7.3 and 8.3. Electrons are always required to be within $|\eta| < 2.47$ and

are matched to the primary vertex by requiring $|d_0|/\sigma_{d_0} < 5$ and $|z_0 \sin(\theta)| < 0.5$ mm.

Table 5.1: The electron identification classes and their corresponding designed efficiency based on simulations as measured in [135].

Identification Class (Id)	Prompt e efficiency
Loose	93%
Medium	88%
Tight	80%

In order to further increase the prompt electron purity, isolated electrons from surrounding detector activity are required. Isolation variables are constructed using either track or calorimeter measurements. In both cases a cone is drawn around the reconstructed electron and the track p_T or the clusters energy of the objects inside the cone are compared to the electron. The cone radius can be momentum-dependent to account for the collimation of particles with increased energy as schematically shown in Figure 5.2. Isolation *operating points* are defined to either maintain a constant efficiency for prompt electron selection over the p_T and η spectrum (*Loose*) or to impose a fixed requirement on the isolation variable (*Fixed*). The latter operating point is in general tighter than the former, i.e. provides lower prompt selection efficiency but higher non-prompt rejection. The two isolation operating points used for this work are detailed in Table 5.2 while SF are also applied to simulation to match the efficiencies measured in data.

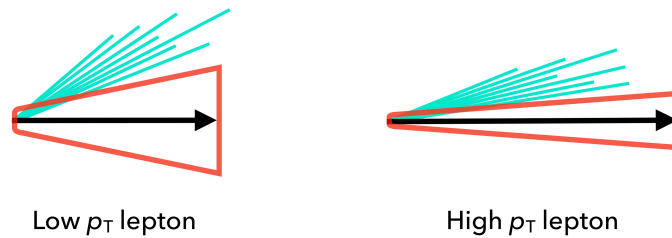


Figure 5.2: The different cone radii used for the calculation of the isolation variables as function of the lepton p_T . Smaller radius is used for leptons with high p_T to account for the higher particle collimation. The figure comprises an original work of the author.

Photons are reconstructed at the ATLAS experiment in a very similar way as electrons. The main difference is that tracks are not associated to clusters and different identification classes are defined. Photons are used in this work only for the calculation of the missing energy, as described in Section 5.8. In particular, these photons are required to have energy of at least 25 GeV and to belong to a *Tight* identification class that has been measured to efficiently identify prompt photons at a rate above 85% ($> 92\%$ for

¹For the gluino search presented in Chapter 7 the maximum radius of the cone used is 0.2.

Table 5.2: Definition of the electron and muon isolation operating points used for this work. E_{\top}^{cone} and p_{\top}^{cone} are the sum of the clusters energy and track p_{\top} of the objects inside the cone respectively. $p_{\top}^{e,\mu}$ is the transverse momentum of the lepton.

Operating point	Calorimeter Isolation		Track Isolation	
	Variable	Selection	Variable	Selection
e	Loose	-	$p_{\top}^{\text{cone}, R_{\text{max}}=0.2}/p_{\top}^e$	$\epsilon = 99\%$
	Fixed	$E_{\top}^{\text{cone}, R=0.2}/p_{\top}^e$	< 0.06	< 0.06
μ	Loose	-	$p_{\top}^{\text{cone}, R_{\text{max}}=0.3^1}/p_{\top}^{\mu}$	$\epsilon = 99\%$
	Fixed	$E_{\top}^{\text{cone}, R=0.2}/p_{\top}^{\mu}$	< 0.15	< 0.04

$E > 100$ GeV).

Details on the electron reconstruction, identification and isolation can be found in [135] and for the photons in [136].

5.3 Muons

Although muons are charged particles, due to their large mass they don't stop at the calorimeter but penetrate it and thus expected to leave signatures only in the ID and MS subdetectors. The track reconstruction in the ID follows the description of Section 5.1. In the MS chambers, hits are used to form segments (i.e. small tracks from single layer hits). Track candidates are then formed from segments taking into account potential overlaps and the final tracks are selected after imposing requirements on the quality of a χ^2 fit on the associated hits.

As the ID and MS reconstruction steps proceed mainly independently the information is combined at the end. The combination schemes relevant to this work are referred as *Combined Muons* and *Extrapolated Muons*. For the first, a global fit, proceeding from outside-in, define a combined track and quality criteria veto events with problematic tracks. As the ID is used, the combined muons cover an $|\eta|$ region up to 2.5. Beyond that, extrapolated muons are formed by the MS information while only a loose requirement with compatibility with the interaction point is applied. Thus the muons used further cover an $|\eta|$ range up to 2.7. However, the gluino search presented in Chapter 7, uses combined muons only thus are limited to $|\eta| < 2.5$. Finally, the muon momentum scale is calibrated to the absolute scale using $J/\psi \rightarrow \mu\mu$ and $Z \rightarrow \mu\mu$ data.

As for the case of electrons, identification classes are defined to separate prompt from non-prompt muons – non-prompt muons originate from in-flight decays of charged hadrons. For this work, the `Medium` identification class used has been measured to provide an efficiency higher than 98% in data. SF are also applied to simulations to match the identification efficiency measured in data and are about 1%.

In order to further increase the prompt muon purity, isolation from surrounding de-

tor activity is required. This methodology follows closely the one of electrons and the operating points used are summarised in Table 5.2.

Finally, muons originating from cosmic radiation are removed by requiring them to have $|d_0| < 0.2$ mm and $|z_0 \sin(\theta)| < 1$ mm with respect to the PV¹. The remaining candidates are matched to the PV by requiring $|d_0|/\sigma_{d_0} < 3$ and $|z_0 \sin(\theta)| < 0.5$ mm.

Details on the muon reconstruction, identification, isolation and calibration can be found in [137].

5.4 Jets

Basic elements of the jet reconstruction are topologically connected calorimeter cell signals that are grouped together to form three-dimensional *topo-clusters* [138]. Topo-clusters are calibrated² energy deposits that represent the calorimeter response to particle showering. The grouping is based on the signal significance of the cells:

$$\zeta_{cell} = \frac{E_{cell}}{\sigma_{E_{cell}}} \quad (5.1)$$

where E_{cell} is the cell signal and $\sigma_{E_{cell}}$ is its noise. An iterative growing-volume algorithm starts from cells with high ζ and groups them with their neighbours with lower ζ . The signals from cells grouped together are summed to reconstruct the energy and direction of the showering particle. An implicit noise suppression is also applied by removing cells with insignificant signal located far from cells with significant signal. Finally, the topo-clusters are split, to correct for multiple particles depositing energy in close proximity (e.g. $\pi^0 \rightarrow \gamma\gamma$). Jets are finally formed by clustering the positive-energy calorimeter topo-clusters.

Jets provide the link between the observed colourless stable hadrons and the underlying QCD physics. Thus their definition should be robust in collinear and infrared aspects, i.e. the jet structure shouldn't be affected by the collinear or soft QCD radiation of the hadronisation. The sequential clustering algorithm used, the so-called anti- k_t [139], respects the above requirements and is based on two distances. First, the momentum and space distance of two topo-clusters i, j (d_{ij}) and second, the equivalent distance of a topo-cluster i and the beam (d_{iB}). The distances are defined as:

$$d_{ij} = \min\left(\frac{1}{p_{T_i}^2}, \frac{1}{p_{T_j}^2}\right) \times \frac{\Delta R_{ij}^2}{R^2}, \quad (5.2)$$

$$d_{iB} = \frac{1}{p_{T_i}^2}, \quad (5.3)$$

¹For the gluino search presented in Chapter 7 any event containing cosmic muons is completely disregarded.

²Calibrated to the an energy scale correct for electrons and photons (EM scale).

where $\Delta R_{ij}^2 = \Delta y_{ij}^2 + \Delta \phi_{ij}^2$ (rapidity - azimuthal angle) and R is the radius parameter that regulates the maximum size of the jet. The R chosen in the jet reconstruction for this work is 0.4. The algorithm first lists all the possible d_{ij} , d_{iB} of an event and identifies the smallest. If it is a d_{ij} , the entities i and j are grouped together (by summing their four-vectors) and the distances are updated. Otherwise, if it is a d_{iB} the entity i is defined as a jet, removed from the list and the distances are updated. The algorithm runs iteratively until there are no entities left.

Effectively, the anti- k_t algorithm clusters energy deposits starting from high p_T ones while lower energy ones added further. This provides stability against softer deposits from PU or underlying events and produce cone-shaped jets in case of absence of nearby high p_T energy deposit, as it can be seen in Figure 5.3a.

A crucial step for the jet definition is the calibration [140]. The Jet Energy Scale (JES) calibration corrects the reconstructed jet energy to the *particle-level* one, calculated by clustering the stable particles of a jet before reaching the detector. The calibration also accounts for detector, PU and modeling effects. This is achieved in several steps based on simulations:

1. *Origin correction* to correct for the reconstructed jet direction and improve angular resolution.
2. PU contribution removal by subtracting the average PU energy density. This correction is proportional to the reconstructed jet area, the LHC operating conditions (e.g. average μ) and the number of reconstructed vertices by the ATLAS detector.
3. Absolute energy scale and $|\eta|$ correction based on simulated particle-level jets.
4. *Global sequential calibration* to reduce residual biases introduced by the jet flavour and any energy leakage beyond the calorimeter layers.

Finally, corrections derived with *in situ* techniques account for differences between data and simulation, these are less than 5% and shown in Figure 5.3b.

Unfortunately, not all the PU contribution to the hard-scatter jets is removed by the calibration. Hard jets originating from PU vertices or localised PU fluctuations can give rise to PU jets. By using tracking information and associating tracks (and consequently vertices) to jets, PU jets can be identified and suppressed. Tracks are associated to jets using a technique known as ghost association [143] where tracks of infinitesimally small p_T are added to the jet clustering process. The amount of tracks momentum associated to the PV can be then estimated and information is combined in a likelihood discriminant called *Jet Vertex Tagger* (JVT) that essentially estimates the probability of a jet to originate from the PV [144]. For the work of this dissertation, jets up to 60 GeV are required to pass the JVT selections detailed in Table 5.3. This threshold is increased to 120 GeV for the jets used for the sbottom search described in Chapter 8 as the amount of PU was increased for the last years of the LHC Run 2 (see Figure 3.2b). The specific selection used was measured to provide 92% efficiency in data to correctly associate

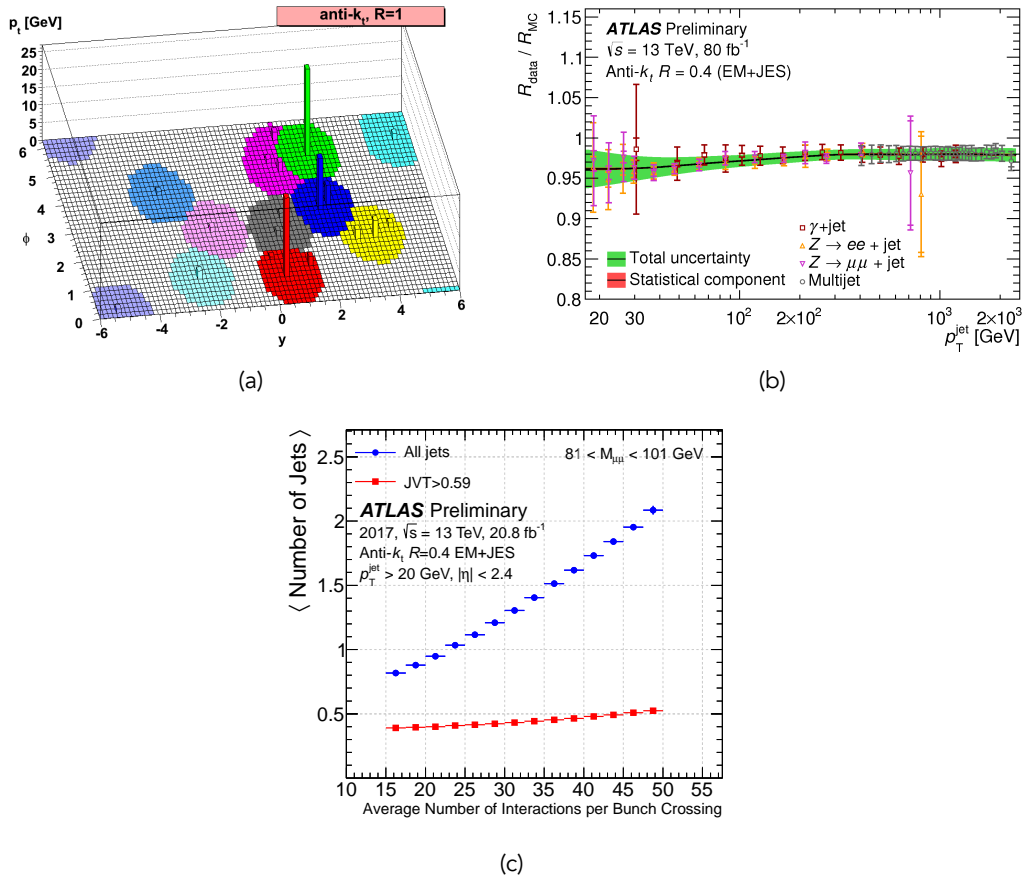


Figure 5.3: (a) Clustering effect of the anti- k_t algorithm with $R = 1$ on partons before hadronisation (hard-scatter plus soft particles), different colours represent different jets. [139] (b) EM+JES correction between data and simulation derived using 2015-17 data as function of jet p_T . [141] (c) The average number of reconstructed jets as function of the amount of PU, expressed as the average number of pp interactions per LHC bunch crossing, before and after the JVT selection. The data were collected during 2017 and the selection requires the presence of two muons reconstructed as originating from a Z resonance. The additional jets are required to be spatially separated from the muons. [142]

jets to the PV and its stabilising effect in the average number of jets as function of the amount of PU is shown in Figure 5.3c. Finally, SF are applied to the simulation to match the efficiency measured in data.

Jet quality criteria are also applied to reject *fake jets*. These can arise from non-collision background (proton losses away of the IP), catastrophic energy deposit of cosmic-ray muons or calorimeter cell noise. The Loose selection applied is designed to preserve above 99.5% of the jets originating from proton-proton collisions and is described in [145]. The quality criteria are applied after the Overlap Removal procedure described in Section 5.7. Finally, the jets considered for this work should have $p_T > 20$ GeV and $|\eta| < 2.8$.

For the gluino search, presented in Chapter 7, an extra re-clustering step of the jets

Table 5.3: The selection on the JVT discriminant (ranging from 0 to 1) based on the jet $|\eta|$.

$ \eta $ range	JVT selection
< 2.4	> 0.59
$\in [2.4, 2.5]$	> 0.11

defined above takes place [146]. This technique is used to fully contain the collimated decay products of boosted top quarks, originating mainly from the \tilde{g} decay, within a single jet. After the overlap removal procedure, described in Section 5.7, the anti- k_t algorithm with $R = 0.8$ is operating on the initial $R = 0.4$ jets to define larger radius jets. To reduce the PU jet contamination, the re-clustered jets are “trimmed” by removing constituents with p_T less than 10% of the original re-clustered jet p_T . The virtue of the re-clustered jets is that no further calibration is needed as it is propagated via the $R = 0.4$ jet constituents. The same applies for the experimental uncertainties.

5.5 b-Jets

The identification or *tagging* of jets originating from the hadronisation of b-quark (*b-jets*) is of particular importance for this dissertation. The flavour-tagging algorithms used exploit distinct characteristics of B mesons (described in Section 1.2) such as the long lifetime that gives rise to high impact parameter tracks and secondary vertices inside the jet and the presence of B- and C-hadrons (Figure 5.4). After jets are associated to nearby in ΔR tracks, three basic algorithms are used [147, 148]:

1. **IP2/3D** The tracks from the decay products of B-hadrons tend to have larger separation from the IP in both the transverse plane and the longitudinal direction. The IP2D algorithm exploits the former while the IP3D both and their correlation to discriminate b-jets against c- and light-jets. A log-likelihood ratio discriminant is built by track d_0 and $z_0 \sin(\theta)$ *pdfs* obtained from simulations. It worths mentioning that the simulation is a mixture (50/50) of SM $t\bar{t}$ and BSM $Z' \rightarrow b\bar{b}$ processes¹, where the latter is used to enhance the statistics of high p_T tracks that usually start beyond the IBL.
2. **SV** The SV algorithm is designed to reconstruct secondary vertices inside a jet. All the two-track combinations are tested for their compatibility with a displaced vertex and then a fitting, similar to the one described in Section 5.1, is performed. Track and vertex quality criteria are applied to reject vertices from other long-lived hadrons (K_S^0 or Λ), photon conversions or hadronic interactions with detector material.
3. **JetFitter** The decay chain reconstruction algorithm JetFitter tries to reconstruct the full $PV \rightarrow B- \rightarrow C$ -hadron decay chain. It exploits the topological features of

¹Hypothetical heavy neutral gauge boson.

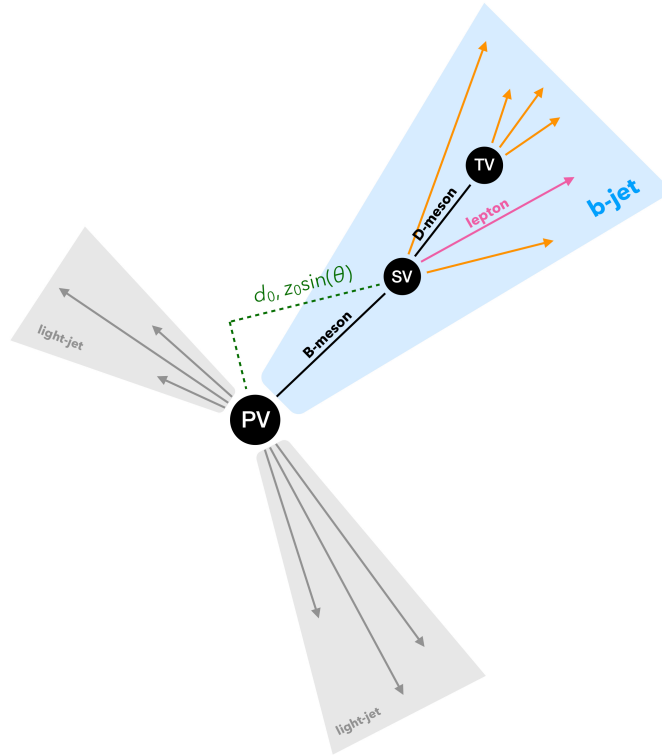


Figure 5.4: Schematic display of an event containing a b-jet. Apart from the PV, a secondary (SV) and a tertiary (TV) vertex can be found inside a b-jet from the decay of the B- and D- hadrons respectively. The tracks originate from the SV have usually large separation from the PV while potentially a lepton is present as well. The black lines and blobs indicate the flight path the JetFitter algorithm tries to reconstruct. The figure comprises an original work of the author.

the hadron decays and by using a Kalman filter finds the common line the PV, the B-hadron and C-hadron decay vertices are lying and reconstructs them.

As the b-tagging is based on ID tracks, the pseudorapidity of the b-jets considered on this work should be less than 2.5. In order to further increase the tagging performance, the outputs of the three algorithms listed above are combined, along with jet kinematic properties, using a Boosted Decision Tree (BDT) algorithm to a single classifier, called *MV2* [107]. The BDT is trained on simulated $t\bar{t}$ events to discriminate b-jets (signal) against c- and light-jets (background) – with c-jets to light-jets ratio 1/9 defining the *MV2c10* variant. For the work of this dissertation, a specific selection on the *MV2c10* output was chosen in order to provide 77% b-jet identification efficiency. For this selection, different misidentification efficiencies are calculated for the two datasets used in this work (Chapters 7 and 8) and are summarised in Table 5.4 while the p_T dependence of all the aforementioned efficiencies is shown in Figure 5.5. The same efficiencies are also measured in data and SF are applied to simulations to correct them according to these measurements. The SFs are always less than 6% for b-jets and 25% for the rest of the jet flavours. [148–151].

Table 5.4: The misidentification efficiencies for the 77% b-jet identification efficiency selection on the MV2c10 discriminant over the data-taking years calculated in simulated $t\bar{t}$ events. [148, 152] The reconstruction of τ_{had} -jets is following in Section 5.6.

Data-taking Years (Analysis)	c-jet [%]	τ_{had} -jet [%]	light-jet [%]
2015-2016 (Chapter 7)	17	4.5	0.75
2015-2018 (Chapter 8)	20	6.7	0.90

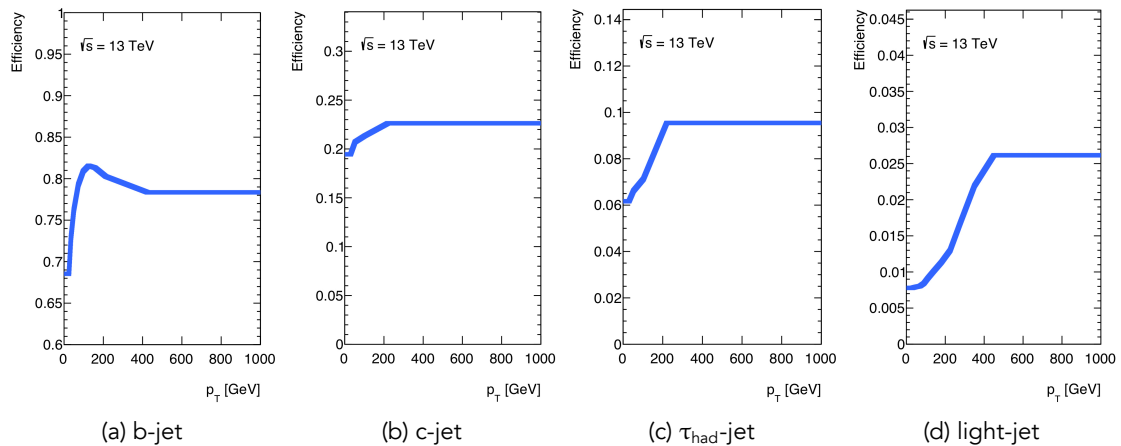


Figure 5.5: (a) Identification and (b-d) misidentification probabilities (smoothed and extrapolated up to 1 TeV) for the 77% b-jet identification efficiency selection on the MV2c10 discriminant as function of the jet p_T calculated in simulated $t\bar{t}$ events. The performance degradation in the high- p_T regime is due to both the collimation of the B-hadron decay products resulting in denser silicon hits and the intenser hadronisation that generates more tracks increasing the fake rate. Figure data courtesy of the ATLAS Collaboration.

5.6 Taus

Leptonically decaying taus are considered via their subsequent decay products, electrons and muons, and are reconstructed as described above. Hadronically decaying taus are not fully reconstructed for this work but a simple tau definition has been developed for background suppression purposes only. In particular, tau candidates are identified within the reconstructed jet collection (Section 5.4) when a non-b-jet has one to four associated tracks ($p_T^{\text{track}} > 500$ MeV) with it – potentially originating from the daughter pions. An event is then considered to contain a tau if the azimuthal distance $|\Delta\phi|$ between the jet and the E_T^{miss} (Section 5.8) is smaller than $\pi/5$. This definition has been found about 60% efficient in identifying hadronically decaying taus in a relevant for this work phase space (0 leptons, ≥ 4 jets, ≥ 2 b-jets and $E_T^{\text{miss}} > 250$ GeV).

The ATLAS detector can fully reconstruct and identify hadronically decaying taus in order to study their properties and their implication to BSM physics. Details of this procedure can be found in [153].

In the context of this dissertation the term *leptons* will henceforth refer to the first and

second generation leptons only (e, μ) while the term *taus* will explicitly mean *hadronically decaying taus*, unless is is clearly stated otherwise.

5.7 Overlap Removal

The physics objects reconstruction algorithms described above operate independently to each other. In order to ensure that a particle is not reconstructed as two objects and double-counted, an overlap removal procedure is essential. This is applied in sequential steps and decisions to keep or reject an object are based on tracks quantities and the $\Delta R = \sqrt{(\Delta y)^2 + (\Delta \phi)^2}$ proximity to another kind of object. First, overlaps between leptons are resolved, then between electrons and jets and finally between muons and jets. All the overlap removal steps used in this work, sorted in priority, are summarised in Table 5.5.

Table 5.5: The steps of the overlap removal procedure, applied to the physics object reconstructed as explained above, sorted in order of priority. If an object falls into the criterion, is rejected it does not participate in the next step.

	Reject	Against	Criterion
1	electron	electron	shared track, $p_{\text{T}}^1 < p_{\text{T}}^2$
2	electron	muon	shared track or $\Delta R < 0.01$
3	non-b-jet	electron	$\Delta R < 0.2$
4	electron	jet	$\Delta R < 0.4$
5	non-b-jet	muon	< 3 tracks, $\Delta R < 0.2$
6	muon	jet	$\Delta R < 0.4$

The jets participating into the overlap removal are actually the candidates before the JVT discriminant selection of Table 5.3. However in the steps 4 and 6, the JVT decision is applied so PU jets are not rejecting leptons. The b-jet specific option at the steps 3 and 5 has been developed because nearby leptons are expected by the B-hadron decay, thus the jet should be retained and the lepton is removed on the next step. An analysis-specific option has made for the gluino search of Chapter 7, as boosted top quarks are expected thus boosted B-hadrons, from the daughter b-quark, as well. In those cases, the ΔR requirement rejecting the leptons of the B-hadron decay is adjusted as function of the lepton p_{T} , with a relationship defined by an optimisation procedure: $\Delta R = \min(0.4, 0.04 + 10 \text{ GeV}/p_{\text{T}}^{\ell})$.

5.8 Missing Energy

A basic principle of physics, the momentum conservation, helps on the definition of a signature for the particles escaping detection (e.g. ν , $\tilde{\chi}_1^0$). As all the momentum before the collision is in the direction of the beam (z -axis), the transverse plane ($x - y$)

momentum should be zero both before and after the collision. This means that any post-collision transverse momentum imbalance indicates the production of particles escaped detection. The amount of this imbalance is called missing energy (E_T^{miss}) [154].

The E_T^{miss} is reconstructed by considering the transverse momentum contributions of all the reconstructed, identified and calibrated physics objects described above. Additionally, an extra term, called *soft*, is accounting for the ambient energy of the detector not associated to any physics object (hard-scatter remnants, PU contributions, etc.) and is calculated using unassociated ID tracks (Section 5.1). In particular, the missing transverse momentum vector is defined as:

$$\mathbf{p}_T^{\text{miss}} = \mathbf{p}_T^{\text{miss,jet}} + \mathbf{p}_T^{\text{miss,e}} + \mathbf{p}_T^{\text{miss,\mu}} + \mathbf{p}_T^{\text{miss,\gamma}} + \mathbf{p}_T^{\text{miss,soft}}, \quad (5.4)$$

where $\mathbf{p}_T^{\text{miss},i} = -\sum \mathbf{p}_T^i$, i.e the negative vectorial sum of the transverse component of the momentum of the corresponding object. To reduce the PU dependency, the low energy jets (< 60 GeV) entering into the calculation of Eq. 5.4 should pass the a JVT > 0.59 selection if they are located within $|\eta| < 2.4$, or otherwise have $p_T > 30$ GeV.

The E_T^{miss} is then defined as the magnitude of $\mathbf{p}_T^{\text{miss}}$:

$$E_T^{\text{miss}} \equiv |\mathbf{p}_T^{\text{miss}}| \quad (5.5)$$

and ϕ^{miss} is its azimuthal direction of $\mathbf{p}_T^{\text{miss}}$ on the transverse plane.

An overlap removal procedure, similar to the one described in Section 5.7 is also taking place to avoid double counting of momentum contributions [154]. In this case careful treatment of the energy signals associated to each term is needed as they are subject to different calibrations. Particularly for the muon contribution in Eq. 5.5, further considerations are necessary. Muons can overlap with jets that are created via three processes; 1) from energy losses of a muon that crosses the calorimeter, 2) from PU interactions – these jets are not rejected by JVT as their tracks are overlapping with the muon one that genuinely originates from the PV – and 3) from final state radiation photons emitted by the muon. In the first two cases the jets should be rejected to avoid energy over counting, while in the last one, the jets should be retained to correctly account for the initial energy of the muon. For these reasons, special selection criteria are applied to the jet and muon related quantities.

Finally, it's worth mentioning that the stochastic nature of calorimetry along with detector and algorithmic imperfections and inefficiencies give rise to *fake* E_T^{miss} by inducing imbalances between the components of Eq. 5.4. As the relevant phase space studied in this work is comprised of multiple high energy jets and no leptons, the main source of fake E_T^{miss} is the non-zero Jet Energy Resolution (JER) – the error on the estimated jet energy – shown in Figure 5.6a. This effectively generates abnormally high E_T^{miss} in processes that is not physically expected. For instance, in Figure 5.6b, the amount of

E_T^{miss} for simulated multi-jet events, where E_T^{miss} is expected to be zero, is shown. It can be seen that the more energetic an event is – larger scalar sum of the p_T of all the reconstructed objects and soft-term signals that contribute to the E_T^{miss} calculation (Eq. 5.4), $\sum E_T$ – the longer the distribution tail appears. Consequently, fake E_T^{miss} gives rise to backgrounds against the searches of this work that look for events with genuine E_T^{miss} .

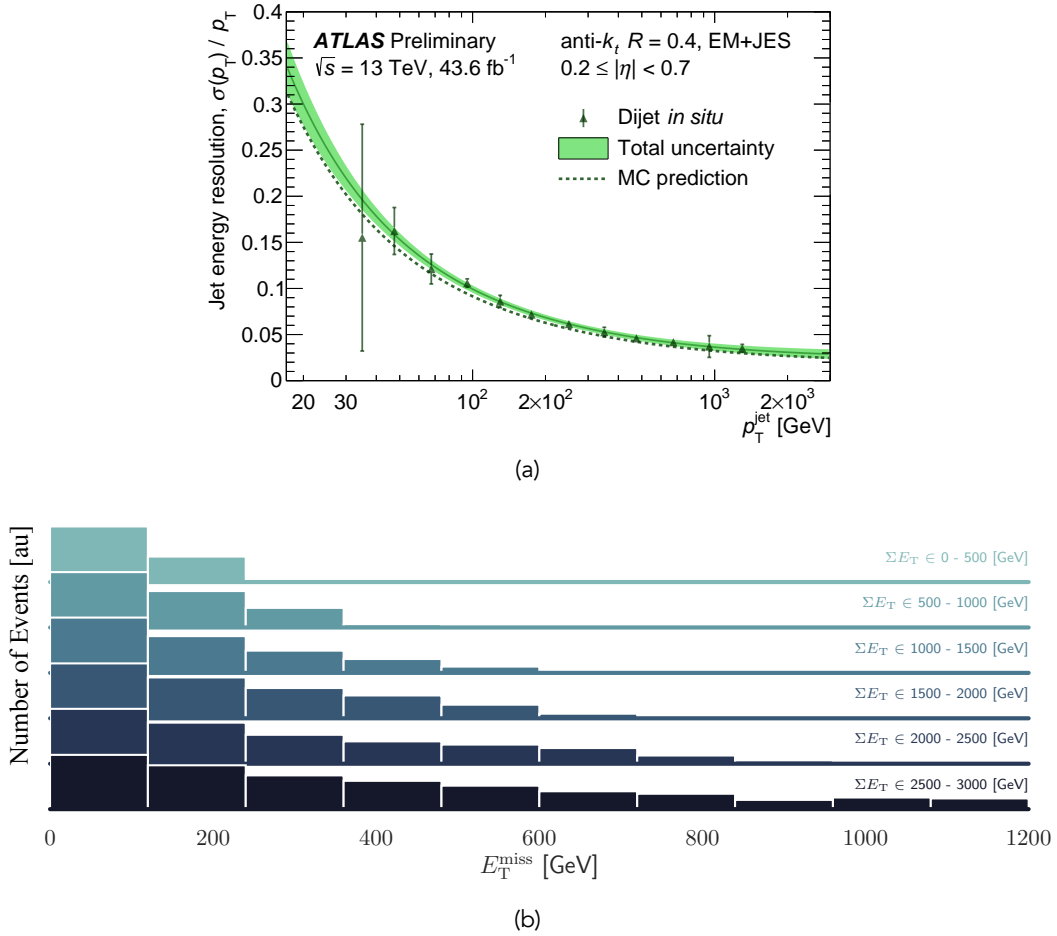


Figure 5.6: (a) The relative jet energy resolution as function of p_T as measured in 2017 dataset overlaid with the expectation from simulation. [155] The simulations are eventually smeared based on a Gaussian to match the JER measured in data. (b) The E_T^{miss} distribution in simulated multi-jet events at $\sqrt{s} = 13$ TeV pp collisions. The figure comprises an original work of the author.

Part III

Physics Analyses



6. Analysis Methodology

The degree of belief in an experimental result is heavily based on the robustness of the scientific methodology used

This chapter introduces the scientific methods used to conduct the analyses of this dissertation. The strategy of the event counting experiments is first introduced in Section 6.1. The statistical methods to estimate the SM processes, quantify any potential deviation of data from them and finally interpret the results in terms of claiming a discovery or an exclusion of potential SUSY scenarios are then discussed in Section 6.2.

6.1 Search Strategy

The subject of research of this dissertation is to search for the production of sparticles in the dataset recorded during the Run 2 period of the LHC and collected with the ATLAS detector. In a typical scenario, a sparticle pair is expected to be produced in a pp collision and subsequently decay to a final state reconstructed by the detector. For instance, within the simplified model of Figure 2.5, the lightest sbottom quark (\tilde{b}_1) pair would decay to two b-quarks and two $\tilde{\chi}_1^0$. The b-quarks would be reconstructed as b-jets and the $\tilde{\chi}_1^0$ causes E_T^{miss} . The $\tilde{\chi}_1^0$ information (four-vector) is incomplete, since the

z -component of the missing momentum is unknown, thus the intermediate \tilde{b}_1 resonances cannot be fully reconstructed. This limitation led the searches of this work to be performed in *event-counting* fashion, i.e. the number of observed events in a kinematic region is counted and compared to the expected number of events from the SM processes simulation (background). The production of sparticles would then manifest itself as an excess of events above the expected SM background.

In order to effectively identify any SUSY signal contribution on the collected dataset – $\mathcal{O}(20)$ billion events during Run 2 – a subset of it should be isolated from the vast majority. This is accomplished by imposing kinematic selections on the events based on the expected signal characteristics, for instance the number of b-jets and the amount of E_T^{miss} for the sbottom case mentioned above. The resulting regions of the phase space where the signal is expected to be prevalent, compared to the SM background, are called *Signal Regions* (SRs, Figure 6.1). It should be highlighted that in order to eliminate any bias, the data events that fall into (or even near) the SRs phase space are kept out of the study (*blinded*) until the very final moment when the SM background has been robustly estimated and validated as described below.

The majority of the SM background contaminating the SRs is estimated in a semi-data-driven way. In particular, the shape of each kinematic observables (e.g. E_T^{miss}) is taken from MC simulations, while the normalisation is extracted from data. For the latter, background enriched regions, called *Control Regions* (CRs, Figure 6.1), are used to scale the initial MC predictions to the observed event levels. Statistically this is performed by the background-only fit, described in Section 6.2.1, that computes a normalisation factor (μ -factor) per SM process normalised. After the μ -factors computation in the CRs, they are extrapolated to the regions of interest (e.g. SR $_i$) to scale the corresponding background and provide the final SM estimate. Driving principles on the CRs design are the high background purity and the absence of expected signal contamination, that would otherwise bias the extracted μ -factor value. On the other hand, in order to minimise the extrapolation uncertainties the CRs should be placed near the SRs.

Last but not least, the derived background model is always validated before the data are revealed in the SRs (*unblinding*). For this, a third set of phase space regions called *Validation Regions* (VRs, Figure 6.1) is utilised. These are defined in a kinematic regime between the CRs and SRs and their background composition resembles as close as possible the corresponding SR but keeping the signal contamination minimal. Again, there is a trade-off between minimising the validation sample signal contamination or its statistical uncertainty as it approaches the extreme phase space of the SRs. The μ -factors are first extrapolated to the VRs and if the agreement between the observed data and the scaled background estimate is adequate the background model is considered robust and can be used for the estimation of the SM event yield in the SRs.

The three aforementioned kinematic regions (signal, control, validation) can have

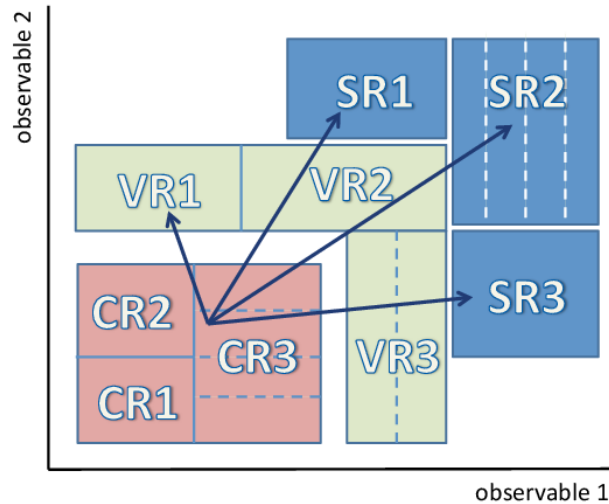


Figure 6.1: A schematic overview of an analysis using multiple signal, control and validation regions, with potential sub-divisions denoted by dashed lines. The extrapolation from the control to either the validation or signal regions is denoted by the arrows. [156]

multiple sub-divisions (*multi-bin* approach) but are always designed to be mutually exclusive (orthogonal) to each other. The analysis setup described above is schematically presented in Figure 6.1.

6.2 Statistical Treatment

In the following section a brief overview of the statistical methods used to compute the background normalisation factors (Section 6.2.1), quantify any deviation between the observed data and the fitted background prediction (Section 6.2.2), and finally to interpret the results, in case of no significant event excess (Sections 6.2.3 and 6.2.4) is observed. The statistical model building along with all the different fits described below is performed using the HistFitter software [156].

To begin with, in order to truthfully describe and fit the event yields in the various kinematic regions, parametrised *pdfs* are constructed and used. As the different set of regions used are orthogonal to each other, separate *pdfs* but with common parameters across all the regions (CRs, VRs, and SRs) are used. In this way the constrains of a CR can be extrapolated to an SR while correlations among the different regions are preserved.

6.2.1 Background-only Fit

One of the most crucial parts of an event-counting experiment is the robust extraction of the background model. For this to happen in an unbiased and signal-independent

way, only the CRs events are used without any signal information, i.e. assuming the CRs are completely signal-free. The purpose of the so-called *background-only* fit is then to compute the normalisation factors of each SM process of interest by maximising a likelihood built by products of CR-only dependent *pdfs*:

$$L(\mathbf{n}, \boldsymbol{\theta}^0 | \boldsymbol{\mu}, \boldsymbol{\theta}) = \prod_{i \in \text{CR}} \mathcal{P}(n_i | \lambda_i(\boldsymbol{\mu}, \boldsymbol{\theta})) \times C(\boldsymbol{\theta}^0, \boldsymbol{\theta}). \quad (6.1)$$

The first term of the likelihood is the Poisson *pdf* that describes the event yield of a CR:

$$\mathcal{P}(n | \lambda(\boldsymbol{\mu}, \boldsymbol{\theta})) = e^{-\lambda} \frac{\lambda^n}{n!}, \quad (6.2)$$

where n is the number of observed events and λ the number of expected events as a function of the normalisation factors of the relevant SM processes ($\boldsymbol{\mu}$) and the nuisance parameters of the fit that parametrise the analysis systematic uncertainties ($\boldsymbol{\theta}$). In particular:

$$\lambda(\boldsymbol{\mu}, \boldsymbol{\theta}) = \sum_{p \in \text{SM}} \mu_p N_p(\boldsymbol{\theta}) + N_{\text{other}}(\boldsymbol{\theta}), \quad (6.3)$$

where N is the predicted from MC simulations number of events for a SM process that is either normalised (p) or not (other). The second factor of Eq. 6.1 represents the *pdfs* of the nuisance parameters that are allowed to vary around the central values of auxiliary measurements ($\boldsymbol{\theta}^0$). In the context of this work, various systematic uncertainties of an analysis (j) are treated as independent¹, thus C can be expressed as a product of Gaussian *pdfs* that constrain each nuisance parameter:

$$C(\boldsymbol{\theta}^0, \boldsymbol{\theta}) = \prod_{j \in \text{Syst.}} \mathcal{G}(\theta | \theta_j^0, w_j). \quad (6.4)$$

By convention the mean value is fixed to zero ($\theta_j^0 = 0$) and the width to one ($w_j = 1$). Then the values of $\theta = \pm 1$ corresponds to the $\pm 1\sigma$ relative variation of the systematic uncertainty defined by the auxiliary measurement. The dependence of the expectation λ to a nuisance parameters is completely fixed by the $N(\theta) = N_0(1 + \theta\sigma)^2$ of Eq. 6.3, where N_0 the nominal event yield.

6.2.2 Estimating Deviations

After the μ -factors extraction by the background-only fit described above, these are extrapolated to the VRs and SRs to scale the SM processes of interest so the final (*post-fit*) background estimate can be computed.

Next step would be to quantify any deviation of the observed event yield from the

¹Although correlations can be induced by the data after the fit.

²Assuming symmetric uncertainties ($\sigma = \sigma^+ = \sigma^-$) but minimal adjustment can incorporate asymmetric as well.

predicted in a bin of an SR (or VR). This is achieved by testing the so-called “background-only hypothesis”, i.e. the hypothesis that the SM describes correctly the LHC experimental results. The probability then to find a deviation at least as extreme as the one observed in data is called *p-value* (p). Frequently the p -value is presented in terms of standard deviations σ of a unit Gaussian, the so-called *Z-value* (or *significance*):

$$Z = \Phi^{-1}(1 - p), \quad (6.5)$$

where Φ^{-1} is the inverse of the cumulative Gaussian distribution. In general, two *significance levels* are important for this work; 3σ when the observation is considered an “evidence” against a hypothesis and 5σ when the observation is considered an “observation” against a hypothesis. It should be noted that only upward deviations of the data are considered to oppose the background-only hypothesis.

A key element to assess the agreement of an observation with the hypothesis is the *test statistic*, a variable constructed by the measurements alone but distributed differently in different hypotheses. In a counting experiment one can use the number of events as a test statistic thus it follows a Poisson distribution. In cases when the number of expected events is large, the average of the Poisson distribution is approximated by a Gaussian (Central Limit Theorem) and the significance is calculated as:

$$Z = \frac{n_{\text{obs}} - n_{\text{pred}}}{\sigma_{\text{tot}}}, \quad (6.6)$$

where the numerator is the difference between observed and predicted number of events and in the denominator the total background uncertainty. This is the figure of merit used for comparisons made in the gluino search of Chapter 7. For a more accurate treatment though, one has to compute the Poisson p -value incorporating the uncertainty of the background too:

$$p = \begin{cases} 1 - \sum_{n=0}^{n_{\text{obs}}-1} \mathcal{P}(n|n_{\text{pred}}) \times \mathcal{GA}(n_{\text{pred}}) & \text{if } n_{\text{obs}} > n_{\text{pred}} \\ \sum_{n=0}^{n_{\text{obs}}} \mathcal{P}(n|n_{\text{pred}}) \times \mathcal{GA}(n_{\text{pred}}) & \text{if } n_{\text{obs}} \leq n_{\text{pred}} \end{cases}, \quad (6.7)$$

where $\mathcal{GA}(n_{\text{pred}})$ is a Gamma *pdf* describing the uncertainty of the background prediction [157]. The Z -value can be then calculated using Eq. 6.5. This is the figure of merit used for comparisons made in the sbottom search of Chapter 8.

6.2.3 Exclusion Fit

In the case of no significant deviation of data above the expected background is observed (*null-results*), exclusion limits can be placed for particular signal scenarios. First,

a likelihood fit, called *exclusion fit*, is repeated with the addition of a signal normalisation parameter (*signal strength*, μ_{sig}) and the yield information of the SRs:

$$\begin{aligned} L(\mu_{\text{sig}}, \boldsymbol{\mu}') &= L(\mathbf{n}, \boldsymbol{\theta}^0 | \mu_{\text{sig}}, \boldsymbol{\mu}, \boldsymbol{\theta}) \\ &= \prod_{i \in \text{SR}} \mathcal{P}(n_i | \lambda_i(\mu_{\text{sig}}, \boldsymbol{\mu}, \boldsymbol{\theta})) \times \prod_{i \in \text{CR}} \mathcal{P}(n_i | \lambda_i(\mu_{\text{sig}}, \boldsymbol{\mu}, \boldsymbol{\theta})) \times C(\boldsymbol{\theta}^0, \boldsymbol{\theta}). \end{aligned} \quad (6.8)$$

In this case all the μ -parameters are constrained in all the analysis regions thus the signal contamination of the CRs is also taken into account.

Second, a hypothesis test is taking place to reject (or not) the signal-plus-background hypothesis ($H1$) in favour of the background-only hypothesis ($H0$). Based on the Neyman–Pearson lemma, a test statistic is formed as a likelihood ratio:

$$\tilde{q}_1 = \begin{cases} -2 \ln \frac{L(1, \hat{\boldsymbol{\mu}}')}{L(0, \hat{\boldsymbol{\mu}}')} & \text{if } \hat{\mu}_{\text{sig}} < 0 \\ -2 \ln \frac{L(1, \hat{\boldsymbol{\mu}}')}{L(\hat{\mu}_{\text{sig}}, \hat{\boldsymbol{\mu}}')} & \text{if } 0 \leq \hat{\mu}_{\text{sig}} \leq 1 \\ 0 & \text{if } \hat{\mu}_{\text{sig}} > 1 \end{cases}, \quad (6.9)$$

where $\hat{\mu}_{\text{sig}}$ and $\hat{\boldsymbol{\mu}}'$ globally maximise the likelihood while $\hat{\boldsymbol{\mu}}'$ maximise it for a specific value of μ_{sig} (*profiling*) [158]. Exclusion of a particular signal scenario at 95% Confidence Level (CL) is then claimed if the *normalised p-value*, defined using the *ad hoc* CL_s technique [159]:

$$p = CL_s = \frac{\int_{\tilde{q}_{\text{obs}}}^{\infty} f(\tilde{q}_1 | H1) d\tilde{q}_1}{\int_{\tilde{q}_{\text{obs}}}^{\infty} f(\tilde{q}_1 | H0) d\tilde{q}_1} \quad (6.10)$$

is less than 0.05. The above conservative definition protects the exclusion of a signal scenario from statistical under-fluctuations of the data or lack of experimental sensitivity. The distributions $f(\tilde{q}_1 | Hi)$ are taken from analytic asymptotic approximations [158] and an example is shown in Figure 6.2a. These approximations have been verified in low event number cases by MC pseudo-experiments [4].

The above procedure is repeated for multiple potential signal scenarios thus an exclusion contour can be drawn. In the simplified model (Section 2.4.2) cases, this contour is expressed in a two-dimensional plane as function of the model parameters (e.g. $m(\tilde{g}) - m(\tilde{\chi}_1^0)$).

It should be stressed that in the multi-bin approach, where multiple orthogonal SRs or bins of a discriminating variable are simultaneously used and statistically combined in the exclusion fit, the significance obtained is in general better than the one obtained by a single inclusive selection. This is a virtue of the additional shape information implied, as a signal model can have different observables shape across multiple bins compared to the background. In the likelihood ratios of Eq. 6.9 then, the bins with higher signal to background ratio would contribute more while in an inclusive selection this power is diluted. This behavior has been demonstrated in the context of the sbottom analysis

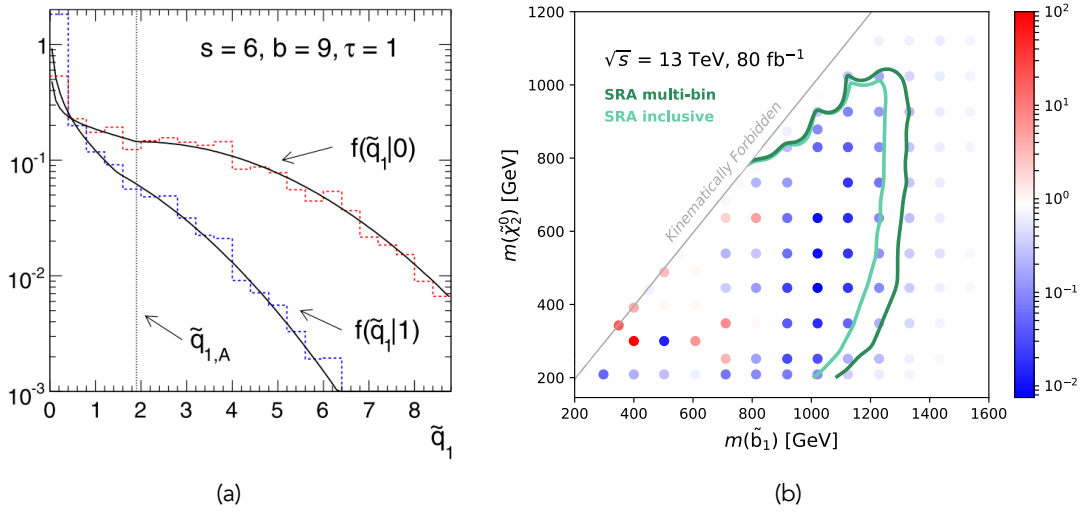


Figure 6.2: (a) The distribution of \tilde{q}_1 for an example experiment (6 signal, 9 background events with μ -factor 1) for the background-only (H_0) and signal-plus-background (H_1) hypotheses. The vertical axis shows the number of events in an arbitrary unit. The solid lines are drawn by the asymptotic approximation formulas and the dotted by MC pseudo-experiments. The $\tilde{q}_{1,A}$ indicates the value obtained from the Asimov dataset with $\mu_{\text{sig}} = 0$. [158] (b) Comparison of the 95% CL expected exclusion limits derived by the SRA of [160], fit either inclusively or in three orthogonal m_{eff} bins (SRA-L, SRA-M, SRA-H). The color map indicates the ratio $CL_s^{\text{multi-bin}} / CL_s^{\text{inclusive}}$ per model-point. The figure comprises an original work of the author.

of Chapter 8 where a SR is fit both inclusively and in three orthogonal bins and the derived expected exclusion limits – limits derived by the exclusion fit using the result of the background-only hypothesis as observations – are compared Figure 6.2b.

6.2.4 Discovery Fit

Beyond the *model-dependent* exclusion limits, derived as described above, a BSM physics search is useful to place *model-independent* limits as well. In essence, an upper limit (at 95% CL) on the number of signal events on top of the predicted background yield, given the observation in a SR. This is achieved by the *discovery fit* and the CL_s technique.

Akin to to the model-dependent limit setting, a likelihood fit is first performed. In this case though the μ_{sig} parameter represents a “dummy” signal scenario where $\mu_{\text{sig}} = 1$ corresponds to 1.0 signal events in the SR. The only differences with the likelihood of Eq. 6.8 are that the CRs signal contamination is not considered and that only one single-bin (inclusive) SR is used per fit. To account for these it would require the knowledge of the signal distribution over the observables, opposite to the notion of “dummy” signal.

Second, a test statistic is formed based on Eq. 6.9 but with parameter μ instead of 1 (\tilde{q}_μ). After multiple hypothesis tests, the value of the parameter μ for which the CL_s falls below 0.05 is estimated. This corresponds to the upper limit on the BSM signal

events.

Finally, by setting the $\mu_{\text{sig}} = 0$ in the likelihood of Eq. 6.8, the discovery fit is used to derive the so-called *discovery* p-value (p_0); the probability that a background fluctuation would induce an event excess at least as extreme as the one observed. The difference with p-value calculated by the background-only fit (e.g. Eq. 6.7) is that the SRs are also incorporated in the likelihood. The same discovery p-value concept (and its corresponding significance) is used for the optimisation studies of the two analyses of this work, where the sensitivity to a signal scenario in an SR is evaluated by calculating the *discovery significance* of the signal-plus-background yield.



7. Gluino Search

Searching for Supersymmetry in final states with missing transverse momentum and multiple b-jets using early LHC Run 2 data

7.1 Introduction

Naturalness argues that third-generation squarks should have TeV-scale masses to ease the fine-tuned radiative corrections to the Higgs mass, as explained in Section 2.3. Indirectly, the same applies to gluinos so their radiative corrections to $m(\tilde{t})$ are reduced as well [161]. The above two arguments, along with the large production cross-section expected for the gluinos (see Figure 2.3b), highly motivates the search for their pair production and subsequent decay via third-generation squarks. The search presented in this chapter is performed on the dataset collected during the first two years of the Run 2 period of the LHC (2015-16), on events with large missing energy, multiple b-jets and potentially a lepton.

In this chapter, the SUSY models under investigation are introduced in Section 7.2. The datasets – comprised both of real and simulated events – used along with the event selection applied to them are detailed in Sections 7.3 and 7.4 respectively. The

strategies employed for the SRs selections and the SM backgrounds estimation are presented in Sections 7.5 and 7.6 respectively, while the systematic uncertainties are considered in Section 7.7. Finally, the results of the search are given in Section 7.8 and their interpretation in Section 7.9. Concluding remarks can be found in Section 7.10.

7.2 SUSY Model

7.2.1 Description

The scenario investigated by this analysis has a general motivation and can be realised in many natural SUSY models. To accommodate the wide model spectrum, optimise the search and interpret the results, simplified models of \tilde{g} production and decay are considered. In these models the \tilde{g} is the only SUSY particle that can be pair produced by the LHC and is assumed to decay with a 100% BR to third-generation squarks either as $\tilde{g} \rightarrow \tilde{t}_1 \bar{t}$ or $\tilde{g} \rightarrow \tilde{b}_1 \bar{b}$ (the charge conjugate processes are implied here and henceforth). Each \tilde{t}_1 (\tilde{b}_1) decays to a top (bottom) quark and the LSP as $\tilde{t}_1 \rightarrow t \tilde{\chi}_1^0$ ($\tilde{b}_1 \rightarrow b \tilde{\chi}_1^0$). These models are named Gtt (Gbb) models. To reduce the dimensionality of the models from three (e.g. $m(\tilde{g}), m(\tilde{t}_1), m(\tilde{\chi}_1^0)$) to two ($m(\tilde{g}), m(\tilde{\chi}_1^0)$) free parameters the third-generation squark production is considered off-shell (e.g. $m(\tilde{t}_1) \gg m(\tilde{g})$). In any case, previous work using the LHC Run 1 data [162] has found limited sensitivity to the $m(\tilde{t}_1)$ or $m(\tilde{b}_1)$ values¹. After this assumption the \tilde{g} effectively undergoes the three-body decays shown in the diagrams of Figures 7.1a and 7.1b.

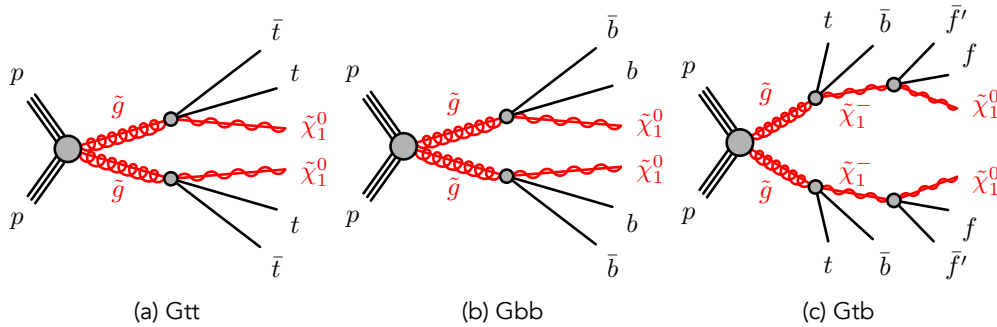


Figure 7.1: The simplified model topologies of pair produced gluinos considered in this analysis. The gluinos decay in a three-body configuration to (a) top quarks or (b) bottom quarks and a neutralino. The three-body decay into both top and bottom quarks and a chargino is also considered (c). Figures published in [4].

The final state generated by the Gtt and Gbb models consist of large missing energy, originating from the $\tilde{\chi}_1^0$ that evades detection, and multiple b-jets. The b-jets in the Gbb model originate directly from the \tilde{b}_1 decay while in the Gtt model from the top quark decay $t \rightarrow Wb$. The W bosons are targeted either in their hadronic or leptonic decays,

¹If \tilde{t}_1 or \tilde{b}_1 are very light, however, the sensitivity is reduced as in these cases the final state E_T^{miss} is lower.

thus a final state with higher jet multiplicity and potential leptons is generated by the Gtt model.

The missing energy of an event is generated because the $\tilde{\chi}_1^0$ escapes detection and it is proportional to its momentum boost (Lorentz factor). Thus it is proportional to the mass splitting of the two involved states \tilde{g} and $\tilde{\chi}_1^0$. This analysis is designed and optimised to select final states with large missing energy and it might not be sensitive to small mass splittings. To tackle this, signal topologies where a significantly energetic Initial-State Radiation (ISR) hadron recoils against the SUSY system are exploited. An example Feynman diagram is shown in Figure 7.2. In these cases, the momentum conservation of the recoil provides additional momentum boost to the $\tilde{\chi}_1^0$ so large missing energy is generated.

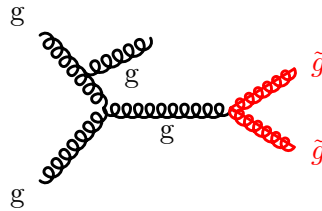


Figure 7.2: Feynman diagram of an \tilde{g} pair production with emission of an ISR gluon. The figure comprises an original work of the author.

An additional \tilde{g} decay mode is considered for result interpretation purposes only. This is the three-body $\tilde{g} \rightarrow \bar{t}b\tilde{\chi}_1^+$ (Gtb model), comprising of gluino decays via stop quarks ($\tilde{g} \rightarrow \tilde{t}_1\bar{t}$) decay and the consecutive off-shell $\tilde{t}_1 \rightarrow b\tilde{\chi}_1^+$. The $\tilde{\chi}_1^+$ is unstable and decays to a W boson and the LSP ($\tilde{\chi}_1^+ \rightarrow W^+\tilde{\chi}_1^0$). The mass splitting between $\tilde{\chi}_1^+$ and $\tilde{\chi}_1^0$ is chosen to be 2 GeV, thus the W boson is produced off-shell and its decay products are typically too soft to be detected. Such small mass splittings between the gauginos are motivated by natural higgsino-like LSP scenarios (Table 2.2) [163]. The same final state can be generated by gluino decays via sbottom quarks ($\tilde{g} \rightarrow \tilde{b}_1\bar{b}$) and the consecutive off-shell $\tilde{b}_1 \rightarrow t\tilde{\chi}_1^+$, thus the Gtb model probes both cases. The topology of the model is shown in Figure 7.1c. The final state is comprised of large missing energy (from the $\tilde{\chi}_1^0$ escape) while the jet and lepton multiplicities are higher than the Gbb models but lower than the Gtt.

By combining the Gtt, Gtb, and Gbb models an interpretation of the result as function of the gluino BR is derived in Section 7.9.1. In the combined model the gluino can decay to $\tilde{g} \rightarrow \tilde{t}_1\bar{t}$, $\tilde{g} \rightarrow \bar{t}b\tilde{\chi}_1^+$ or $\tilde{g} \rightarrow \tilde{b}_1\bar{b}$ with the sum of their BRs to add up to 100%. Such models probe more realistic SUSY scenarios where more than one decay modes exist for the \tilde{g} .

The analysis presented in this chapter supersedes and improves the previous one of the ATLAS collaboration using the same strategy with the 2015 only dataset (3.2 fb^{-1}) [164]. The Gtt model can be also targeted in final states with higher lepton multiplicities, due

to the presence of W bosons from the top quark decays. In particular, and as of 2017 when the work described here was published, the ATLAS collaboration had searched for the Gtt model in the 2015-16 LHC dataset (36.1 fb^{-1}) and in final states with two same-sign or three leptons. Due to null-results, exclusion limits have been placed up to about 1750 GeV on \tilde{g} masses, for almost massless¹ LSP [165]. Similar searches have been conducted by the CMS collaboration on the analogous dataset and in all-hadronic, single-lepton or two-lepton final states [166–169]. The sensitivity achieved is weaker or comparable with the one of this analysis while due to null-results \tilde{g} masses up to about 2 TeV have been excluded.

7.2.2 Signal Grids

Multiple potential versions of the Gtt and Gbb models with different values of their free parameters ($m(\tilde{g}), m(\tilde{\chi}_1^0)$) were considered for optimisation and interpretation purposes. The final state kinematics heavily depend on the $\Delta m(\tilde{g}, \tilde{\chi}_1^0)$ while the model cross-section on $m(\tilde{g})$. In particular, the mass of the \tilde{g} , for both models, varies from 900 to 2400 GeV while the $\tilde{\chi}_1^0$ mass from 1 GeV up to 2000 GeV (2200 GeV) for the Gtt (Gbb) model. The different model-points form the *grids* of Figure 7.3. To generate the off-shell decay described above, the squark masses are set to 5 TeV for both models to ensure $m(\tilde{t}_1 \setminus \tilde{b}_1) \gg m(\tilde{g})$.

Regarding the Gtb model, as it is used just for BR interpretations, only few model-points are considered. In particular, for massless $\tilde{\chi}_1^0$, three $m(\tilde{g})$ values are studied: 1.8 TeV, 1.9 TeV and 2 TeV. For the 1.9 TeV point, two extra models with $m(\tilde{\chi}_1^0)$ 600 GeV and 1000 GeV are also studied. In this way the sensitivity of the analysis can be evaluated as function of both the \tilde{g} BR and the mass parameters.

7.3 Data, Triggers and Simulations

The dataset used in this analysis corresponds to the LHC Run 2 pp collision data collected by the ATLAS detector during the years 2015 and 2016. The integrated luminosity corresponds to $36.1 \pm 0.8 \text{ fb}^{-1}$.

The events are collected using E_T^{miss} triggers only (see Section 3.2.5). The trigger thresholds vary as a function of the data-taking period following the increased instantaneous luminosity of the LHC. The exact trigger chains used for this analysis are listed in Table 7.1 with trigger thresholds varying from 70 to 110 GeV.

As the online reconstruction is faster thus poorer in quality than the offline presented in Chapter 5, a higher offline selection on E_T^{miss} is required to ensure that the trigger decision is fully efficient. Events are selected using a reference trigger and the online trigger decision is compared with the offline reconstructed E_T^{miss} value. In particular,

¹A particle with mass at $\mathcal{O}(1 \text{ GeV})$ is considered effectively massless for the LHC processes energy scale.

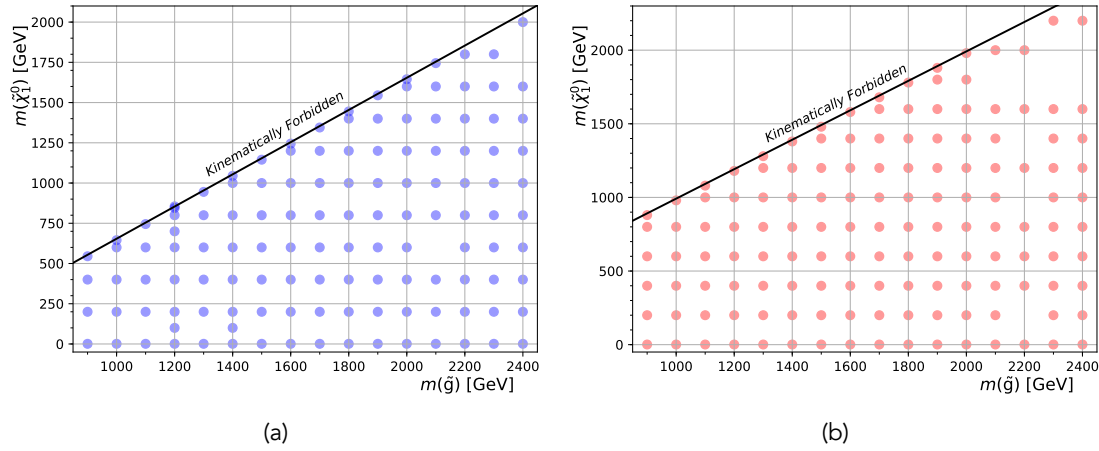


Figure 7.3: The model-points considered for the (a) Gtt and (b) Gbb models. The figure comprises an original work of the author.

Data period	$E_{\text{T}}^{\text{miss}}$ Trigger
2015	HLT_xe70_mht_L1XE50
2016 A-D3	HLT_xe90_mht_L1XE50
2016 D4-F1	HLT_xe100_mht_L1XE50
2016 F2-	HLT_xe110_mht_L1XE50

Table 7.1: The list of $E_{\text{T}}^{\text{miss}}$ triggers per data-taking period used for this analysis.

single-muon triggers have been used as a reference, which are fully efficient after requiring the muon p_{T} to be higher than 27 GeV. The required offline $E_{\text{T}}^{\text{miss}}$ threshold is then determined when the ratio of the events firing the $E_{\text{T}}^{\text{miss}}$ trigger over the events fired the reference trigger is about one. This ratio as function of the offline $E_{\text{T}}^{\text{miss}}$ is shown in the relevant phase space and for a late 2016 data-taking period in Figure 7.4. The offline $E_{\text{T}}^{\text{miss}}$ threshold has been determined at 200 GeV.

MC simulated event samples are used to model both the SUSY signal and all the SM background processes, except for multi-jet the production processes that are modeled using the data-driven technique documented in Appendix C. These are generated and detector-simulated as described in Sections 1.4 and 3.2.6, and afterwards reconstructed as described in Chapter 5. The background processes considered in this analysis are:

1. top quark pair production ($t\bar{t}$),
2. single-top quark production,
3. Z and W bosons production in association with jets (Z/W + jets),
4. top quark pair production in association with vector bosons ($t\bar{t}V$), Higgs bosons ($t\bar{t}H$) or four top quark production ($t\bar{t}t\bar{t}$) – collectively referred as $t\bar{t}X$ and
5. diboson production (ZZ,ZW,WW).

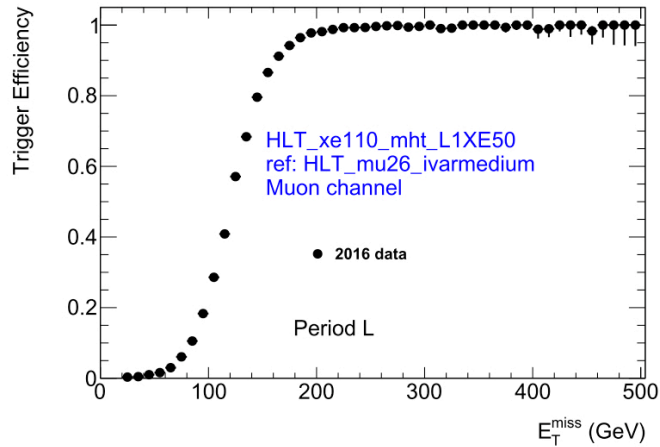


Figure 7.4: The trigger efficiency curve for a period of the 2016 dataset in the relevant phase space (≥ 1 leptons, ≥ 4 jets and ≥ 2 b-jets). The E_T^{miss} shown on the horizontal axis is the offline reconstructed but considering the muons as invisible particles to compensate the bias introduced by the lack of MS information on the online E_T^{miss} calculation. Figure courtesy of the ATLAS Collaboration.

Other background sources, such as the production of three top quarks or three vector bosons, have been found to be negligible and are not considered further. In Table 7.2 the programs used for the hard-scatter generation, parton showering, hadronisation and underlying event simulation are listed for the signal and all the SM backgrounds. All the simulated processes are normalised to the best available theoretically calculated cross-section. Further technical details along with references on the sample production can be found in Appendix B.

Table 7.2: List of the event generation, parton shower, hadronisation and underlying event programs used for the different physics processes. The tunes and the PDF set used are also listed. In the last column, the accuracy of the theoretical cross-section used to normalise each sample is quoted.

Process	Generator	PS + Hadronisation + UE	Tune	PDF Set	cross-section Order
SUSY signal	MadGraph5_aMC@NLO v2.2	Pythia v8.1	A14	NNPDF23LO	NLO+NLL [84, 170–174]
$t\bar{t}$	Powheg-Box v2	Pythia v6.4	PERUGIA2012	CT10	NNLO+NNLL [175, 176]
Single-top					
$t\bar{t}V, t\bar{t}t\bar{t}$	MadGraph5_aMC@NLO v2.2	Pythia v8.1	A14	NNPDF23LO	NLO [59, 177]
$t\bar{t}H$		Herwig++ v2.7	UEEE5	CT10	
Z/W + jets	Sherpa v2.2.0		Default	NNPDF30NNLO	NNLO [178]
Diboson	Sherpa v2.2.1			CT10	NLO [179]

7.4 Event Selection

Generally, physics processes (signal or background) are targeted using kinematic regions. These are defined by selections on the analysis physics objects reconstructed, as described in Chapter 5, from detector signal that is either generated by real data

or simulated by MC samples. The same selection criteria applied to data are applied to simulated samples as well so the expected signal and background yields can be modeled in each of the kinematic regions.

Two levels of the physics objects quality are defined, these are called `baseline` and `signal`. The `signal` criteria are tighter than the `baseline` thus the `signal` objects comprise a subset of the `baseline`. This categorisation stems from the need to first define loose quality objects in order to be used as inputs to the overlap removal procedure described in Section 5.7. The surviving objects are usually required to fulfill tighter quality criteria and are used further into the analyses. The different object selection criteria used for this analysis are listed in Table 7.3.

Table 7.3: The selection criteria of the `baseline` and `signal` physics objects used for this analysis.

Physics Object	Baseline Definition	Signal Definition
Jets	$p_T > 20 \text{ GeV}, \eta < 2.8$	$p_T > 30 \text{ GeV}, \text{JVT selection}$
b-Jets	-	$p_T > 30 \text{ GeV}, \eta < 2.5$
Re-clustered Jets	-	$p_T > 100 \text{ GeV}, \eta < 2$
Electrons	Loose Id, $p_T > 20 \text{ GeV}, \eta < 2.47$	Medium Id, Loose Isolation, $ z_0 \sin(\theta) < 0.5 \text{ mm}, d_0 /\sigma(d_0) < 5$
Muons	Medium Id, $p_T > 20 \text{ GeV}, \eta < 2.5$	Loose Isolation, $ z_0 \sin(\theta) < 0.5 \text{ mm}, d_0 /\sigma(d_0) < 3$

7.4.1 Discriminating Variables

As mentioned already, the relevant final state of this gluino search is characterised by large missing energy, multiple b-jets and potentially the presence of leptons. Especially the latter characteristic is used to split the analysis phase space into regions with or without leptons, denoted as *1-lepton* or *1L*, and *0-lepton* or *0L* respectively. Several discriminating variables have been studied and are exploited to separate the signal events from the SM background processes. The variables used in this analysis are *event-variables*, i.e. based on global event characteristics (e.g. E_T^{miss} or jet multiplicity) and constructed from `signal` objects. A list of the discriminating variables with a short description for each one follows.

- N_{jets} ($N_{\text{b-jets}}$): The number of jets (b-jets) of an event. Large number of jets is expected from the Gtt model, 12 at maximum in cases that all the top quarks decay hadronically. Similarly for the Gbb model, up to 4 b-jets are expected from the \tilde{g} and \tilde{b}_1 decays. As there are only rare SM processes providing such large jet multiplicities this event variable is a powerful discriminant, as it can be seen in Figures 7.5a and 7.8a for events without or with leptons respectively. The same applies to the b-jets multiplicity shown in Figures 7.5b and 7.8b.
- E_T^{miss} : The missing energy of an event, reconstructed as described in Section 5.8.

Signal model events are expected to have larger E_T^{miss} compared to SM processes as the weakly interacting particles escaping detection ($\tilde{\chi}_1^0$) are produced by heavier resonances (\tilde{g}) than the ones found in the SM. This feature is shown in Figures 7.5c and 7.8c.

- m_{eff} : The effective mass of an event is defined as the scalar sum of the p_T of all jets and leptons and the E_T^{miss} of the event:

$$m_{\text{eff}} = \sum p_T^{\text{jet}} + p_T^\ell + E_T^{\text{miss}}. \quad (7.1)$$

This variable essentially measures how energetic an event is. As the SUSY particles are heavier, their decays lead to more energetic products thus the m_{eff} is expected to have large values for the SUSY model compared to the SM background. This is shown in Figures 7.5d and 7.8d.

- m_T : For regions where leptons are present, the transverse mass between the leading¹ in p_T lepton and the E_T^{miss} defined as:

$$m_T = \sqrt{2p_T^\ell E_T^{\text{miss}}(1 - \cos \Delta\phi(\ell, \mathbf{p}_T^{\text{miss}}))}, \quad (7.2)$$

where $\Delta\phi(\ell, \mathbf{p}_T^{\text{miss}})$ is the azimuthal angle between the lepton and the $\mathbf{p}_T^{\text{miss}}$. A selection on this variable is used to suppress $t\bar{t}$ and $W + \text{jets}$ processes as its value is bounded by the W mass for these processes, if one neglects detector resolution and inefficiency effects. The drop on the m_T distribution for $W + \text{jets}$ events can be clearly seen in Figure 7.8f.

- $m_{T,\text{min}}^{\text{b-jets}}$: A second transverse mass variable is used in events with or without leptons and is defined as:

$$m_{T,\text{min}}^{\text{b-jets}} = \min_{i \leq 3} \left(\sqrt{2p_T^{\text{b-jet}_i} E_T^{\text{miss}}(1 - \cos \Delta\phi(\text{b-jet}_i, \mathbf{p}_T^{\text{miss}}))} \right), \quad (7.3)$$

where $\Delta\phi(\text{b-jet}_i, \mathbf{p}_T^{\text{miss}})$ is the azimuthal angle between the b-jet_i and the $\mathbf{p}_T^{\text{miss}}$. The minimum transverse mass between each of the three highest in p_T b-jets and the E_T^{miss} is used to suppress $t\bar{t}$ events. When a top quark decays leptonically the $m_{T,\text{min}}^{\text{b-jets}}$ distribution is expected to have an upper bound corresponding to the top quark mass, again if detector effects are neglected. Its distribution for events without leptons can be seen in Figure 7.5f.

¹The term "leading" in the context of the physics analyses of this work will explicitly refer in p_T ordering henceforth.

- M_J^Σ : The total jet mass is defined as the mass of the four leading re-clustered jets of an event:

$$M_J^\Sigma = \sum_{i \leq 4} m^{j_i}. \quad (7.4)$$

The M_J^Σ is used to reconstruct the decay products of a boosted top quark within a jet of radius $R = 0.8$. It's a powerful discriminant as top quarks from SM $t\bar{t}$ processes enter the regions of interest mainly via their leptonic decays, as the presence of neutrinos is the only way for large E_T^{miss} to be generated. On the other hand, the top quarks from the SUSY decay chain do not have this restriction – as the E_T^{miss} is mainly originating from the $\tilde{\chi}_1^0$ – thus it is more probable to be found via their hadronic decays resulting larger values of M_J^Σ . This difference is shown in Figures 7.5e and 7.8e for events without or with leptons respectively.

- $\Delta\phi^{j_1}$: The azimuthal angle between the leading, non-b-tagged jet and the $\mathbf{p}_T^{\text{miss}}$, $\Delta\phi(j_1, \mathbf{p}_T^{\text{miss}})$. This variable, combined with a high p_T selection on the j_1 , is used to select events where the E_T^{miss} is back-to-back with the leading jet, effectively topologies where very energetic ISR recoils against the SUSY system.
- $\Delta\phi_{\min}^{4j}$: The minimum azimuthal angle between the leading four jets and the $\mathbf{p}_T^{\text{miss}}$:

$$\Delta\phi_{\min}^{4j} = \min[\Delta\phi(\text{jet}_{1-4}, \mathbf{p}_T^{\text{miss}})] \quad (7.5)$$

This variable proves to be a powerful discriminating tool against multi-jet events containing large amount of fake E_T^{miss} . The fake E_T^{miss} originates from jet mismeasurements as described in Section 5.8 thus the $\mathbf{p}_T^{\text{miss}}$ direction is expected to be aligned with the most energetic jets. Studies based on a data-driven technique (Appendix C) indicate that a selection of $\Delta\phi_{\min}^{4j} > 0.4$ rad is reducing this background to almost negligible levels. However, this is not the case for the preselection distributions presented in Figure 7.5 where multi-jet events are still abundant. The 0.4 selection is applied to all the 0L regions described in this chapter. There is no selection in regions with leptons as the multi-jet background is heavily suppressed by the `signal` lepton requirement.

7.4.2 Data Modeling

In order to check the modeling of primary discriminating variables from the above list two phase space regions, referred as *preselection* are defined. These have relevant characteristics as the final state of the Gtt and Gbb models but the selection criteria are relaxed so the signal is effectively depleted. In particular, they are categorised by the potential presence of leptons. The full selections are listed in Table 7.4.

Table 7.4: The criteria defining the preselection regions used to check the variables modeling in this analysis.

Variable	0L Preselection	1L Preselection
N_{leptons}	0	≥ 1
N_{jets}		≥ 4
$N_{\text{b-jets}}$		≥ 2
$E_{\text{T}}^{\text{miss}}$ [GeV]		> 200
$\Delta\phi_{\text{min}}^{4j}$ [rad]	> 0.4	-

Distributions of data in the 0L Preselection region are shown in Figure 7.5 and they are generally well described by the simulation. Contrary, in the 1L Preselection region important variables have been found to be mismodeled by the simulation, as it can be seen in Figures 7.6a–7.6c. The discrepancy can be up to 25% in bins with reasonable statistics. As the biggest difference is observed in the m_{eff} distribution, the p_{T} of the jets, electrons and muons considered in the variable calculation (Eq. 7.1) are studied in detail in Figures 7.6d–7.6f. All the distributions follow the same pattern, with the simulations overestimating the data yield in the high energy regime.

To rectify this behavior, correction factors are applied to the simulation to adjust the m_{eff} shape. These factors are extracted in a region kinematically close and with similar background composition to the preselection regions ($N_{\text{leptons}} \geq 1$, $E_{\text{T}}^{\text{miss}} > 200$ GeV, $N_{\text{b-jets}} = 2$). An inverted $m_{\text{T,min}}^{\text{b-jets}}$ selection¹ ($m_{\text{T,min}}^{\text{b-jets}} < 140$ GeV) ensures that the region is signal free. The factors are defined as the ratio of the number of data events over the total number of predicted background events from simulation in a m_{eff} bin. The binning is chosen at 50 GeV but enlarged in the tails to accommodate the reduced statistics. The m_{eff} distributions of data and the SM simulation are shown in Figure 7.7 while the bottom panel shows the extracted correction factors which range from 0.7 to 1.1. Finally, the total background prediction, for events with at least one lepton, is reweighted by the correction factors. Reweighted distributions of important kinematic observables are presented in Figure 7.8 where it can be seen that the problem has been alleviated.

Although another mismodeling is observed on the $N_{\text{b-jets}}$ distributions even after the reweighting (Figures 7.5b and 7.8b), the analysis is not sensitive to it. This is because of two reasons; 1) the mismodeling is equally observed in both the 0L and 1L Preselection regions and 2) the analysis CRs that extract the background estimation are designed to have the same b-jet multiplicity with the corresponding SRs, eliminating any extrapolation over the mismodeled $N_{\text{b-jets}}$ distribution.

¹The term “inverted selection” in the context this work indicates a selection ranging from zero to an upper bound. As BSM searches are usually conducted in the high-end tails of observables distributions the selections applied range from a lower bound to infinity.

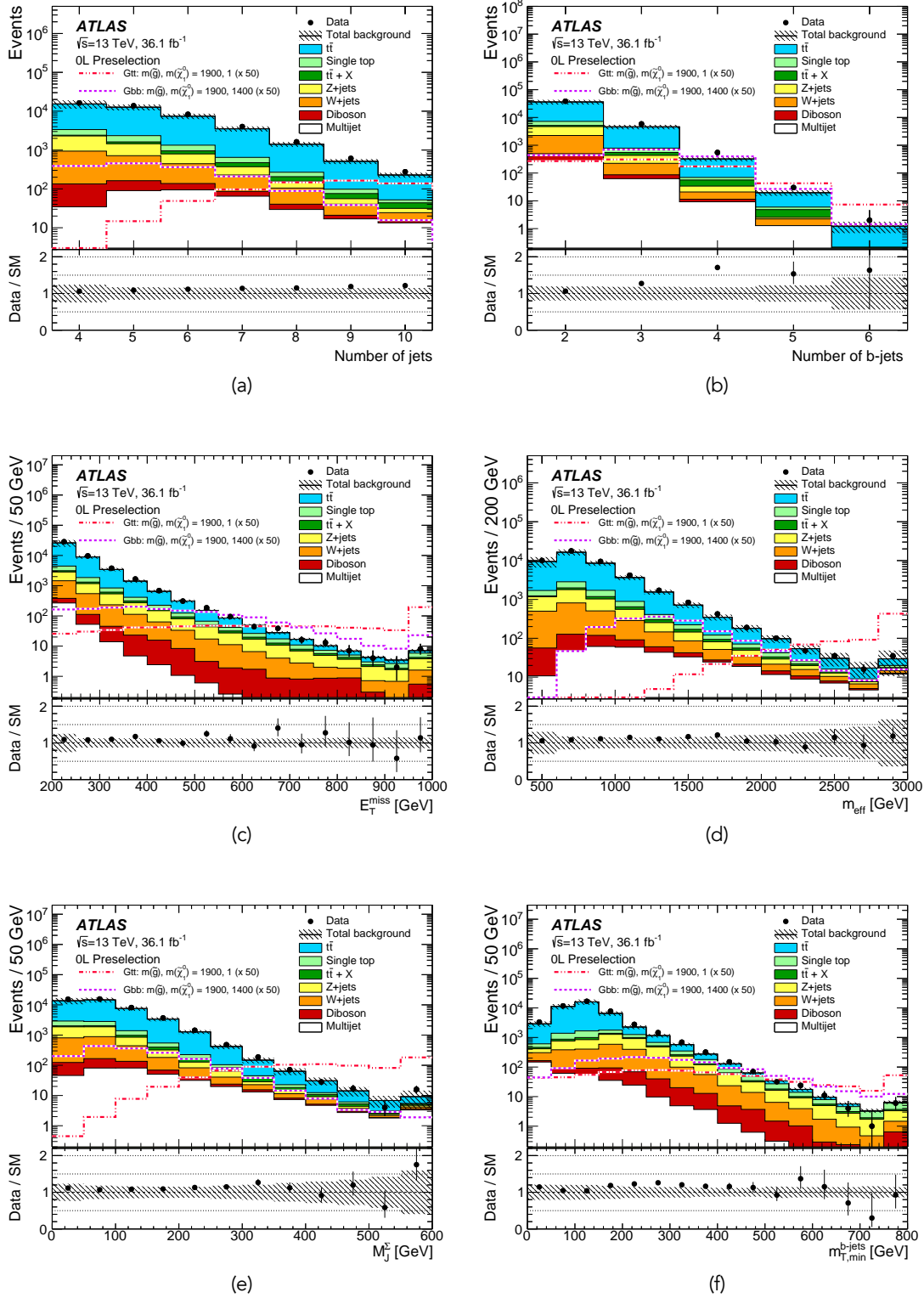


Figure 7.5: Distributions of (a) N_{jets} , (b) $N_{\text{b-jets}}$, (c) E_T^{miss} , (d) m_{eff} , (e) M_j^{Σ} and (f) $m_{T,\text{min}}^{\text{b-jets}}$ in events passing the 0L Preselection criteria (Table 7.4). Two signal models have been overlaid with their cross-section enhanced 50 times for comparison purposes. The bottom panel shows the ratio of data over SM background expectation. Both statistical and the systematic uncertainties listed in Section 7.7 are included. Figures published in [4].

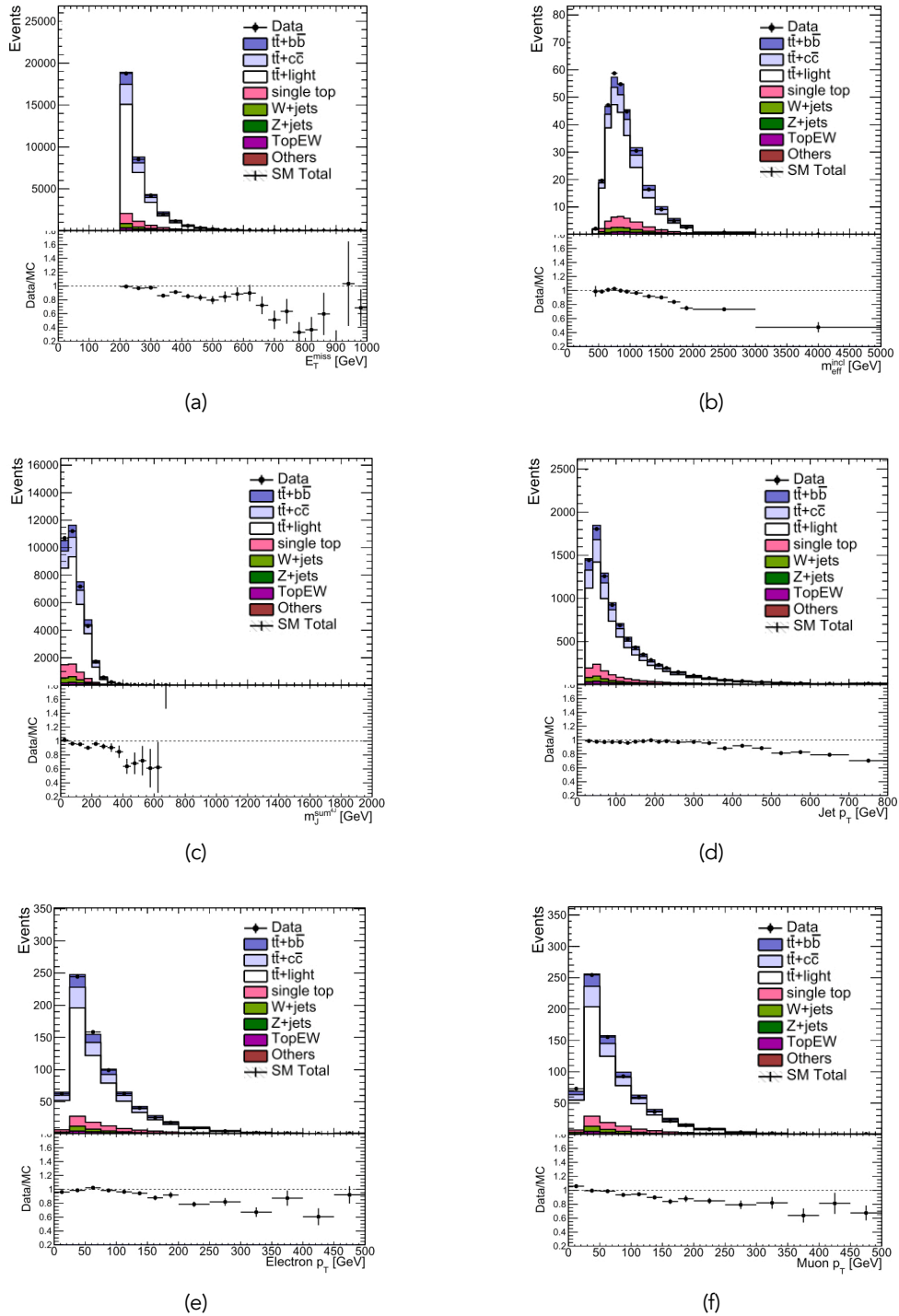


Figure 7.6: Distributions of (a) E_T^{miss} , (b) m_{eff} (c) M_J^{Σ} , (d) p_T^j , (e) p_T^e and (f) p_T^μ in events passing the 1L Preselection criteria. The bottom panel shows the ratio of data over SM background expectation. The $t\bar{t}$ background is split according to the flavour of the additional jets (beyond the two b-jets) present in the event. Figure courtesy of the ATLAS Collaboration.

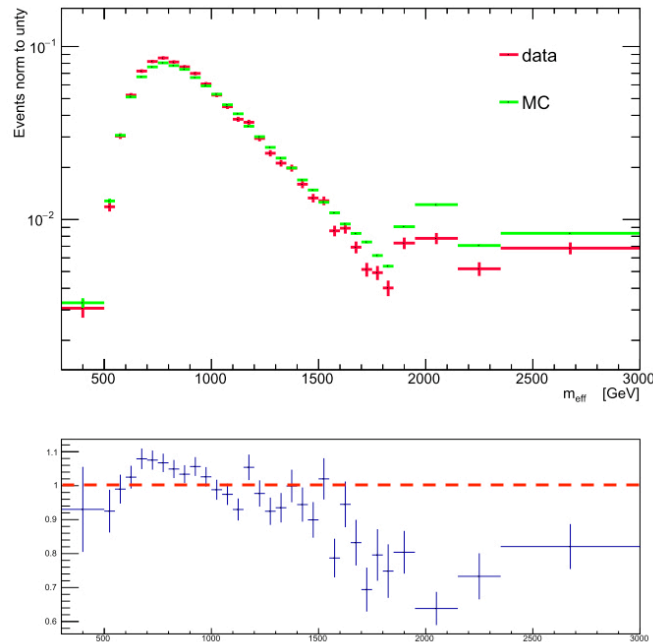


Figure 7.7: The m_{eff} distribution in data and simulation in the signal free, 2-b-jet region described in the text. The bottom panel shows the extracted correction factors with the dotted red line to indicate the unity. Figure courtesy of the ATLAS Collaboration.

7.5 Signal Regions

The main objective of this analysis is to select events that potentially originate from the SUSY signal models described in Section 7.2 in the vast dataset collected with the ATLAS detector. As described in Section 6.1, this is accomplished by the use of SRs. In this particular case, the SRs are tailored to enhance the sensitivity to both the different models (Gtt or Gbb) and the different kinematic configurations of the final state of each model. For this analysis two categories of SRs are used based on two strategies:

1. **Cut-and-count** The cut-and-count SRs are designed with the purpose to assess any deviation of the data from the SM prediction, in the phase space the SUSY models under study are expected to appear. They are, in general, overlapping and single-bin regions optimised to maximise the discovery significance of the relevant signals. In case of null-results the cut-and-count SRs are used to place model-independent limits.
2. **Multi-bin** The multi-bin SRs, on the other hand, are designed to provide maximal model exclusion power, in case of absence of significant deviation of data above the predicted SM background. They are all mutually exclusive in order to be statistically combined, a feature that in general provides better exclusion sensitivity compared to inclusive regions.

On the following sections the kinematic selection and yields of all the SRs are detailed.

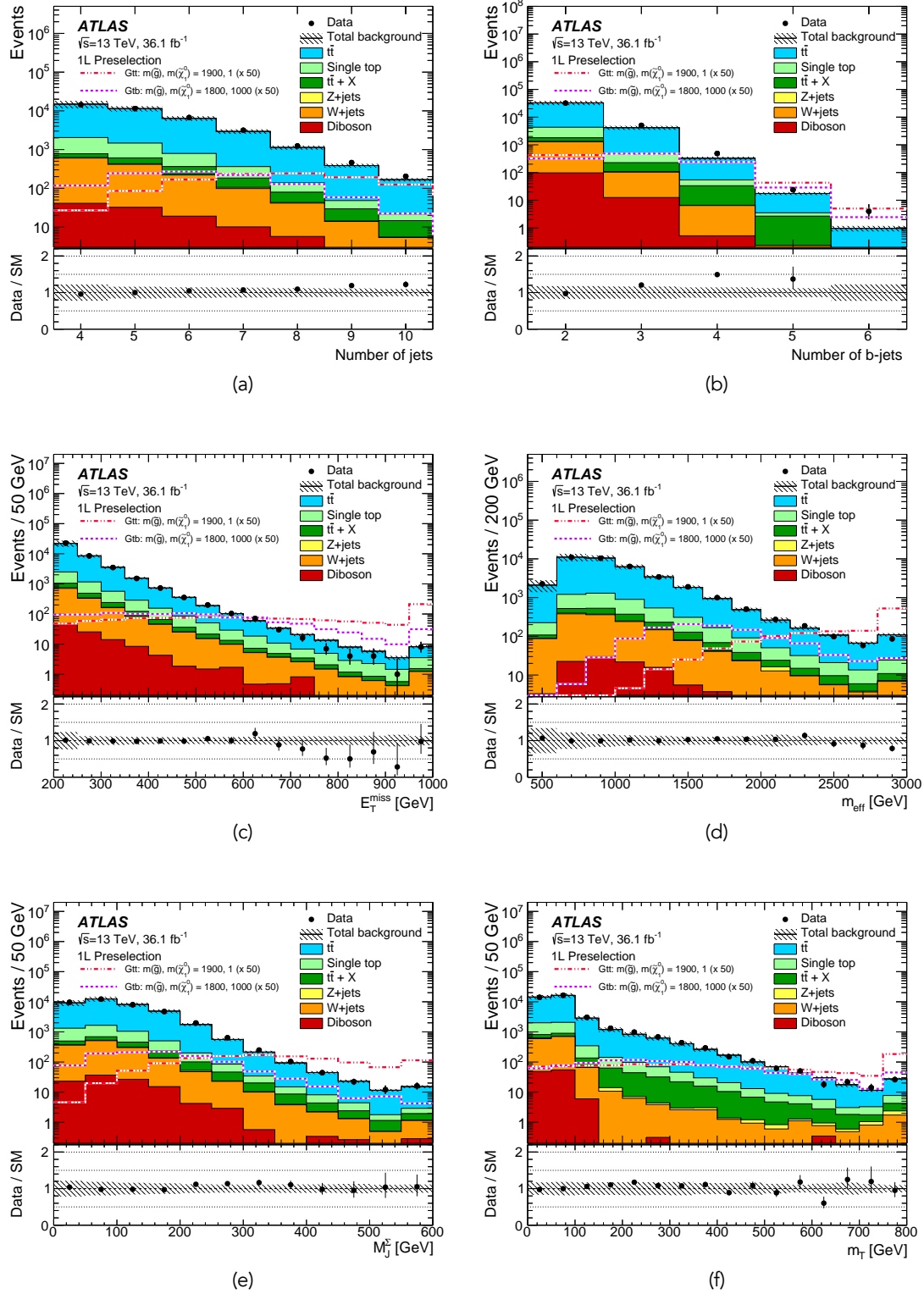


Figure 7.8: Distributions of (a) N_{jets} , (b) $N_{\text{b-jets}}$, (c) E_T^{miss} , (d) m_{eff} , (e) M_J^{sum} and (f) m_T in events passing the 1L Preselection criteria (Table 7.4), after applying the kinematic reweighting described. Two signal models have been overlaid with their cross-section enhanced 50 times for comparison purposes. The bottom panel shows the ratio of data over SM background expectation. Both statistical and the systematic uncertainties listed in Section 7.7 are included. Figures published in [4].

7.5.1 Cut-and-count Regions

Different cut-and-count SRs are used to target the final states arising from the Gbb and Gtt models. For the the Gtt model, two SR types are used; selecting events with zero or at least one lepton. As this is not relevant to the Gbb model – no leptons are expected – only one SR type, without any lepton is used. Furthermore, various regions are used to target the different kinematic configuration of each model that are in general governed by the mass splitting $\Delta m(\tilde{g}, \tilde{\chi}_1^0)$. Regions labeled as B (for “Boosted”) target very large mass splitting scenarios ($\Delta m \gtrsim 1.5$ TeV) that lead to highly boosted, thus collimated, final state objects. Contrary, regions labeled as C (for “Compressed”) target small mass splittings ($\Delta m \lesssim 300$ GeV) with significantly softer objects. Regions labeled as M (for “Moderate”) target the intermediate Δm cases. This architecture leads to gradually decreasing thresholds on the on the discriminating variables selection moving from the B towards the C regions.

Especially for the Gbb model an additional VC (for “Very Compressed”) region is defined to target mass splittings small as such $\Delta m \leq 200$ GeV. In these cases the Δm is too small for large E_T^{miss} to be generated and trigger the event, unless an energetic ISR jet recoils against the SUSY system (e.g. Figure 7.2) to provide further and sufficient momentum boost. The VC region is designed to select this particular topology. Figure 7.9 shows simulations of the $\tilde{g} \rightarrow b\bar{b}\tilde{\chi}_1^0$ three-body decay topology for a 2 TeV \tilde{g} and different $\Delta m(\tilde{g}, \tilde{\chi}_1^0)$ scenarios with different boost of the initial \tilde{g} along the transverse plane. The vertical axis shows how the amount of E_T^{miss} is increased with the boost, especially for small Δm .

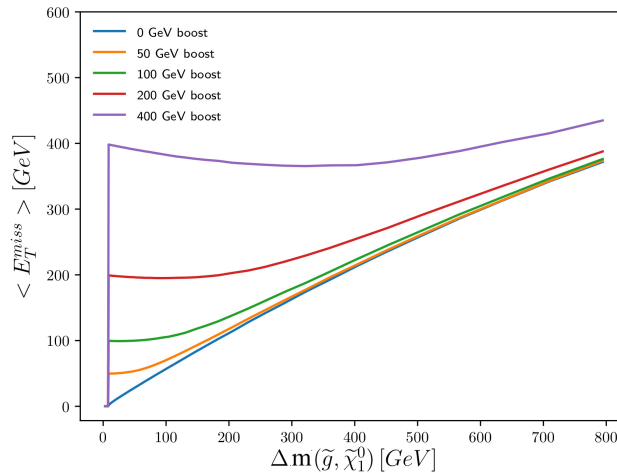


Figure 7.9: Truth-level simulations of the three-body $\tilde{g} \rightarrow b\bar{b}\tilde{\chi}_1^0$ decay for different transverse plane boost of the \tilde{g} . The modal value of E_T^{miss} as function of the $\Delta m(\tilde{g}, \tilde{\chi}_1^0)$ is shown for different boost scenarios. The figure comprises an original work of the author.

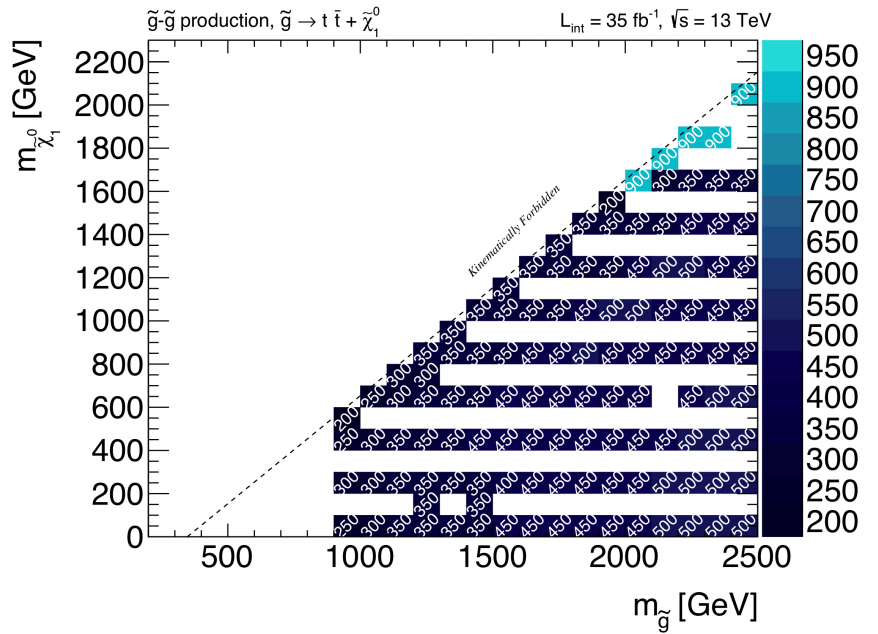
An optimisation procedure defines the selection of each region. As mentioned above, the figure of merit is the expected discovery significance of the signal models, as

explained in Section 6.2.4. Additional constraints on the simulated SM background are also applied; it should be dominated by $t\bar{t}$ production only ($\geq 70\%$) with maximum statistical uncertainty of 30%. The background constraints are added to the optimisation in order to make the analysis simpler and more reliable. At the same time, it is found that do not degrade the sensitivity significantly. In general, all the relevant discriminating variables of the above list are optimised in the two preselection regions for the Gtt model and only in the zero-lepton preselection for the Gbb model.

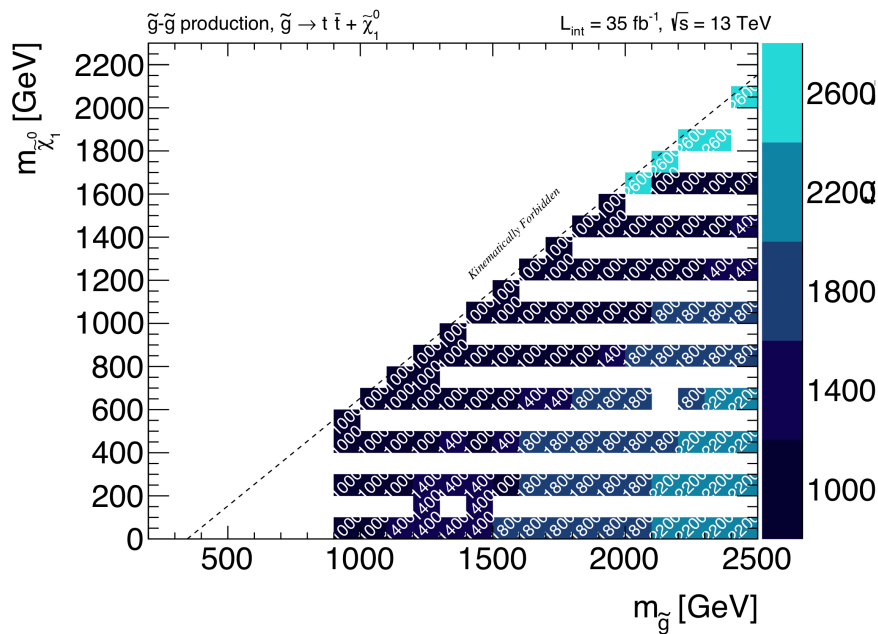
Starting with the lepton regions targeting the Gtt model (Gtt 1-lepton), the optimal selection per model-point, i.e. the selection that provides the maximum significance, of the four discriminating variables E_T^{miss} , m_{eff} , M_J^Σ and N_{jets} can be seen in Figures 7.10 and 7.11. In each plot, selections on the variables not studied is also applied, this is always the optimal one determined at the end of the optimisation procedure. Relaxed requirements are proposed moving towards smaller Δm to increase the acceptance of softer objects. The increased background rate is compensated by higher N_{jets} (and $N_{\text{b-jets}}$) requirement. For instance, as it can be seen in Figure 7.12¹, requiring more than six jets can reduce significantly the signal yield of moderately boosted scenarios ($\Delta m = 1.2$ TeV, pink distribution). This is not the case for compressed scenarios ($\Delta m = 600$ GeV, purple distribution) and the SM background is compensated by a higher requirement. The final three SR (B, M and C) selections are presented in Table 7.5 and the expected SM yields from simulation in Table 7.6.

Similarly, for the regions without leptons targeting the Gtt model (Gtt 0-lepton), optimal selections of the discriminating variables E_T^{miss} , m_{eff} , M_J^Σ and N_{jets} per model-point are shown in Figures 7.13 and 7.14. The final three SR (B, M and C) selections are presented in Table 7.7 and the expected SM yields from simulation in Table 7.6.

¹This is the so-called $N-1$ selection, a phase space before a particular selection.

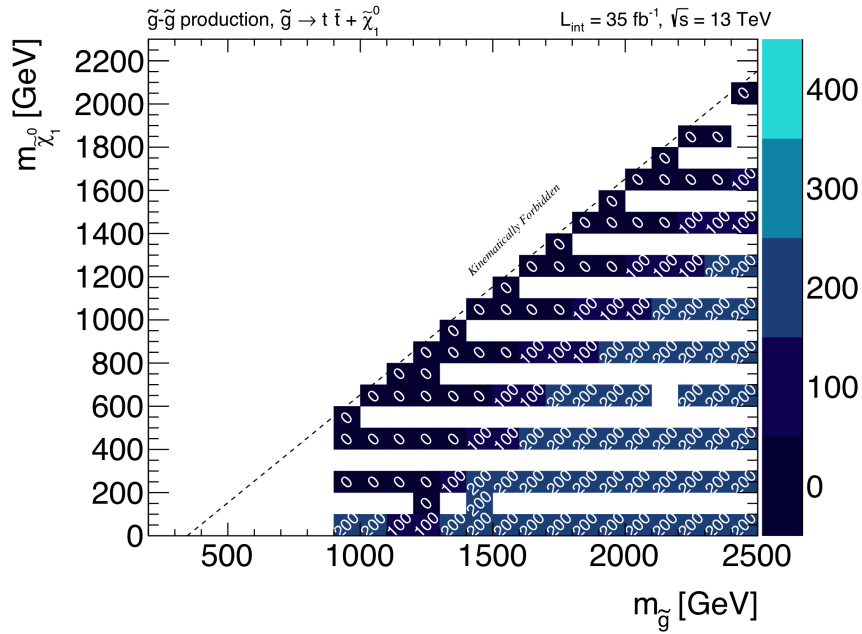


(a) E_T^{miss}

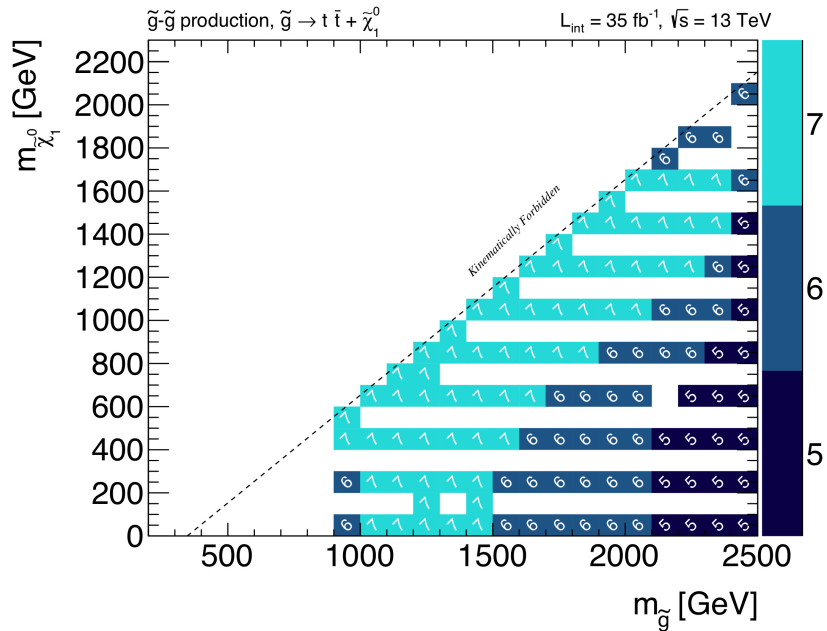


(b) m_{eff}

Figure 7.10: The optimal selection of (a) E_T^{miss} and (b) m_{eff} per Gtt model-point in the 1L channel. Figure courtesy of the ATLAS Collaboration.



(a) M_J^Σ



(b) N_{jets}

Figure 7.11: The optimal selection of (a) M_J^Σ and (b) N_{jets} per Gtt model-point in the 1L channel. Figure courtesy of the ATLAS Collaboration.

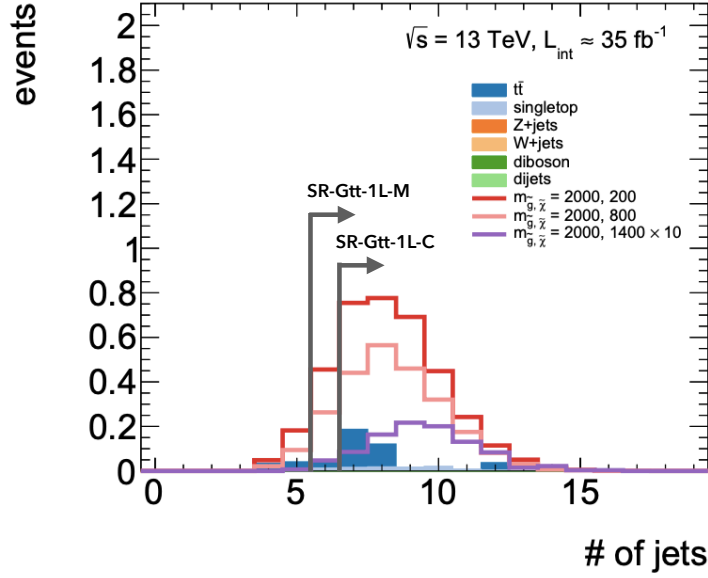


Figure 7.12: The N_{jets} distribution of simulated events in the SR-Gtt-1L-B region before the N_{jets} selection. More compressed signal scenarios show higher jet multiplicity thus the signal region that targets them has a higher optimal selection on N_{jets} . Figure courtesy of the ATLAS Collaboration.

Table 7.5: Selection criteria for the Signal, Control and Validation cut-and-count regions targeting the Gtt model in events with at least one lepton. All kinematic variables are expressed in GeV except $\Delta\phi_{\text{min}}^{4j}$, which is in radians. Table published in [4].

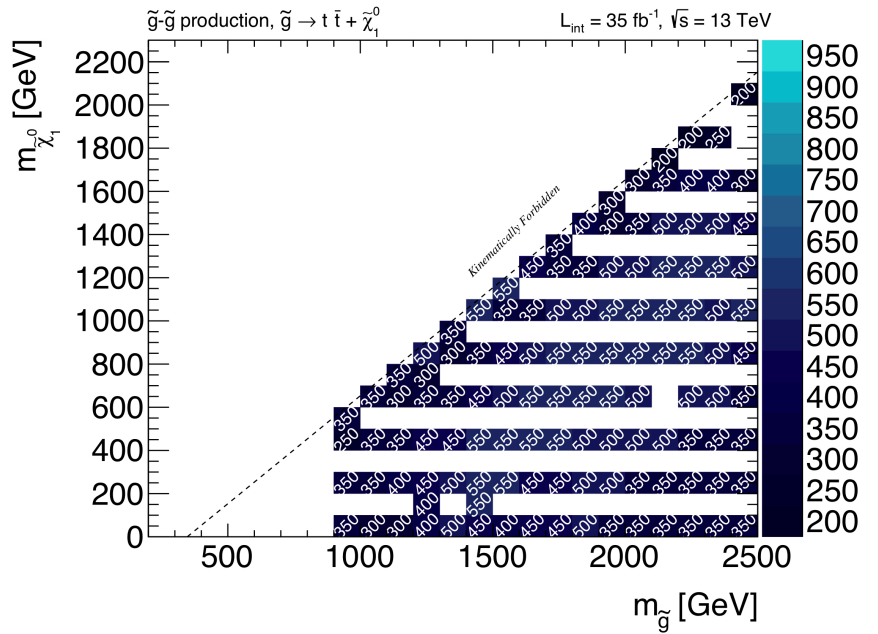
Gtt 1-lepton							
Criteria common to all regions: ≥ 1 signal lepton, $p_{\text{T}}^{\text{jet}} > 30$ GeV, $N_{b\text{-jets}} \geq 3$							
Targeted kinematics	Type	N_{jet}	m_{T}	$m_{\text{T},\text{min}}^{b\text{-jets}}$	$E_{\text{T}}^{\text{miss}}$	$m_{\text{eff}}^{\text{incl}}$	M_{J}^{Σ}
Region B (Boosted, Large Δm)	SR	≥ 5	> 150	> 120	> 500	> 2200	> 200
	CR	$= 5$	< 150	–	> 300	> 1700	> 150
	VR- m_{T}	≥ 5	> 150	–	> 300	> 1600	< 200
	VR- $m_{\text{T},\text{min}}^{b\text{-jets}}$	> 5	< 150	> 120	> 400	> 1400	> 200
Region M (Moderate Δm)	SR	≥ 6	> 150	> 160	> 450	> 1800	> 200
	CR	$= 6$	< 150	–	> 400	> 1500	> 100
	VR- m_{T}	≥ 6	> 200	–	> 250	> 1200	< 100
	VR- $m_{\text{T},\text{min}}^{b\text{-jets}}$	> 6	< 150	> 140	> 350	> 1200	> 150
Region C (Compressed, small Δm)	SR	≥ 7	> 150	> 160	> 350	> 1000	–
	CR	$= 7$	< 150	–	> 350	> 1000	–
	VR- m_{T}	≥ 7	> 150	< 160	> 300	> 1000	–
	VR- $m_{\text{T},\text{min}}^{b\text{-jets}}$	> 7	< 150	> 160	> 300	> 1000	–

Table 7.6: Expected background yields for the Gtt 1-lepton, Gtt 0-lepton and Gbb SRs at 36.1 fb^{-1} . The acceptance of the Gtt 1-lepton regions to the signal models they target is about 50% while for the Gtt 1-lepton regions is about 10% for the B and M and 5% for the C. The acceptance of the Gbb regions vary from 30% to 40% for the B, M and C but it's only $\sim 1\%$ for the VC.

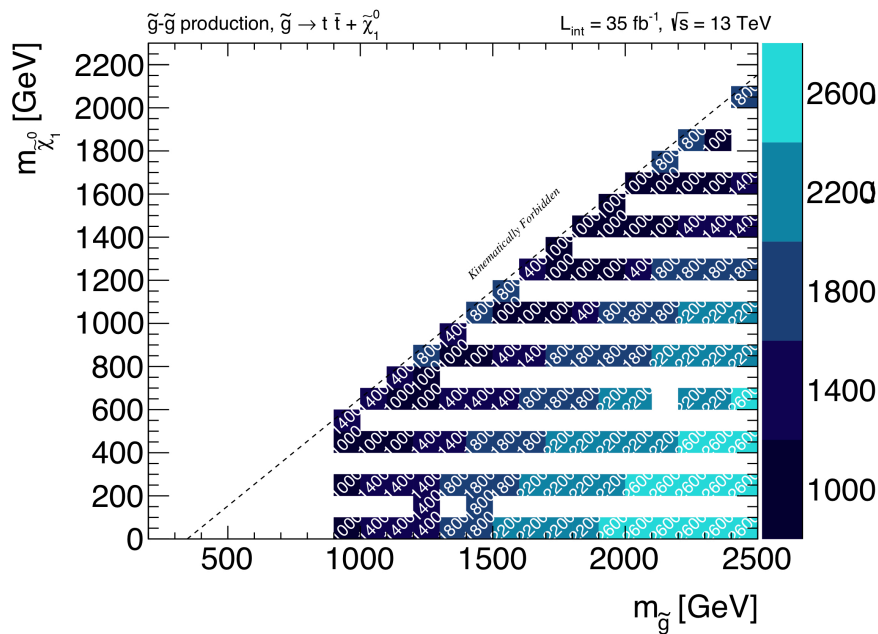
Process	Gtt 1-lepton			Gtt 0-lepton			Gbb			
	B	M	C	B	M	C	B	M	C	VC
$t\bar{t}$	0.42	0.38	1.04	0.37	1.90	15.60	0.73	1.50	2.29	7.07
Single-top	0.03	0.03	0.38	0.19	0.62	1.48	0.28	0.41	0.48	0.87
$t\bar{t}X$	0.09	0.10	0.55	0.09	0.41	3.13	0.11	0.34	0.69	1.50
Z + jets	0.00	0.00	0.00	0.05	0.28	0.38	0.13	0.20	0.51	0.82
W + jets	0.00	0.01	0.02	0.06	0.15	0.83	0.09	0.10	0.24	0.45
Diboson	0.00	0.00	0.00	0.00	0.00	0.00	0.00	0.00	0.00	0.25
SM	0.54	0.52	1.98	0.76	3.35	21.42	1.34	2.55	4.20	10.95

Table 7.7: Selection criteria for the Signal, Control and Validation cut-and-count regions targeting the Gtt model in events without leptons. All kinematic variables are expressed in GeV except $\Delta\phi_{\min}^{4j}$, which is in radians. Table published in [4].

Gtt 0-lepton										
Criteria common to all regions: $p_T^{\text{jet}} > 30 \text{ GeV}$										
Targeted kinematics	Type	N_{lepton}	$N_{b\text{-jets}}$	N_{jet}	$\Delta\phi_{\min}^{4j}$	m_T	$m_{T,\min}^{b\text{-jets}}$	E_T^{miss}	$m_{\text{eff}}^{\text{incl}}$	M_J^Σ
Region B (Boosted, Large Δm)	SR	= 0	≥ 3	≥ 7	> 0.4	–	> 60	> 350	> 2600	> 300
	CR	= 1	≥ 3	≥ 6	–	< 150	–	> 275	> 1800	> 300
	VR	= 0	≥ 3	≥ 6	> 0.4	–	–	> 250	> 2000	< 300
Region M (Moderate Δm)	SR	= 0	≥ 3	≥ 7	> 0.4	–	> 120	> 500	> 1800	> 200
	CR	= 1	≥ 3	≥ 6	–	< 150	–	> 400	> 1700	> 200
	VR	= 0	≥ 3	≥ 6	> 0.4	–	–	> 450	> 1400	< 200
Region C (Compressed, moderate Δm)	SR	= 0	≥ 4	≥ 8	> 0.4	–	> 120	> 250	> 1000	> 100
	CR	= 1	≥ 4	≥ 7	–	< 150	–	> 250	> 1000	> 100
	VR	= 0	≥ 4	≥ 7	> 0.4	–	–	> 250	> 1000	< 100

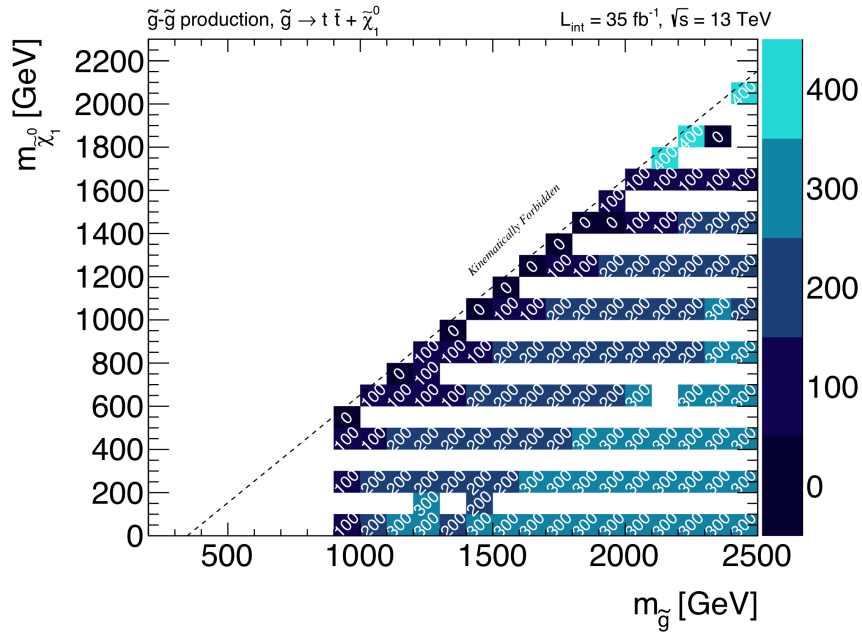


(a) E_T^{miss}

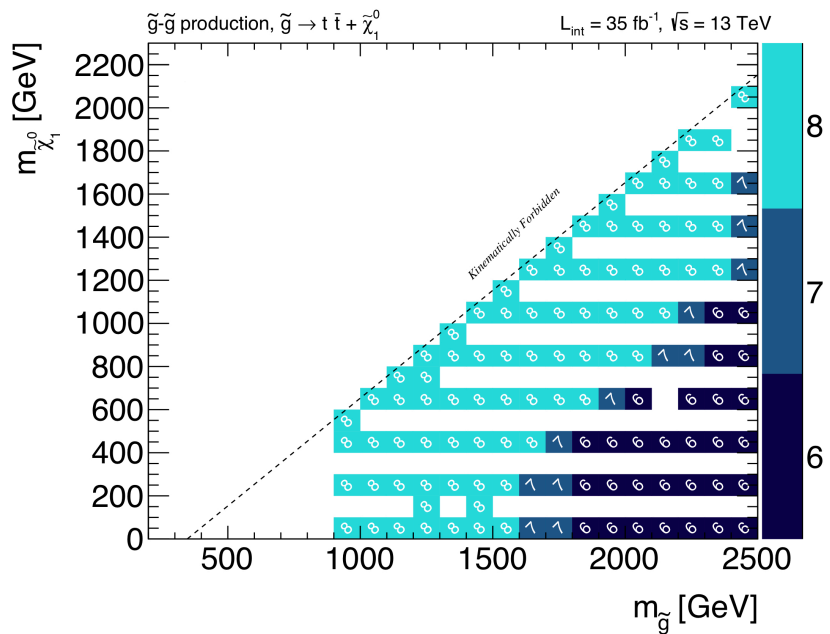


(b) m_{eff}

Figure 7.13: The optimal selection of (a) E_T^{miss} and (b) m_{eff} per Gtt model-points in the 0L channel. Figure courtesy of the ATLAS Collaboration.



(a) M_J^Σ



(b) N_{jets}

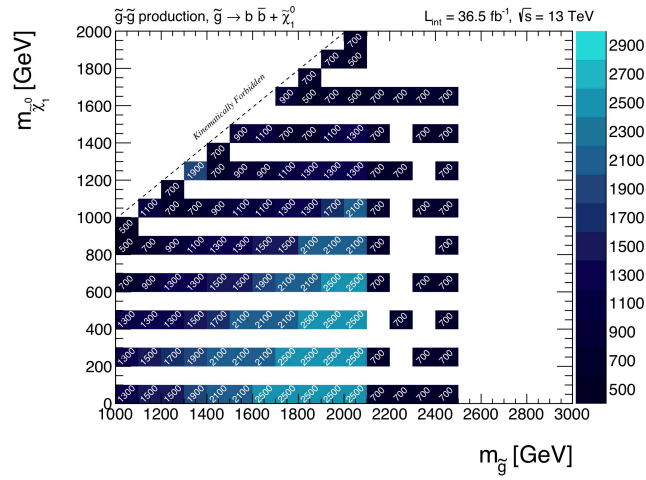
Figure 7.14: The optimal selection of (a) M_J^Σ and (b) N_{jets} per Gtt model-points in the 0L channel. Figure courtesy of the ATLAS Collaboration.

An equivalent optimisation is performed for the final state of the Gbb model. However, only events without leptons are relevant in this case thus the optimisation was performed on top of the 0L Preselection only and without the use of m_T and M_J^Σ variables that are constructed to operate on events with leptons and top quarks respectively. Optimal selections on m_{eff} , E_T^{miss} and $N_{b\text{-jets}}$ per model-point can be seen in Figure 7.15. In this case the m_{eff} requirement decrease moving towards compressed scenarios but the E_T^{miss} and $N_{b\text{-jets}}$ increase in order to promote effectively softer jets and compensate the increased background respectively. For instance, as it can be seen in Figure 7.16, signal scenarios with $\Delta m = 400$ GeV (black distribution) have lower m_{eff} values compared to moderately boosted ones with $\Delta m = 800$ GeV (pink distribution) thus the optimisation propose lower m_{eff} selection to target them.

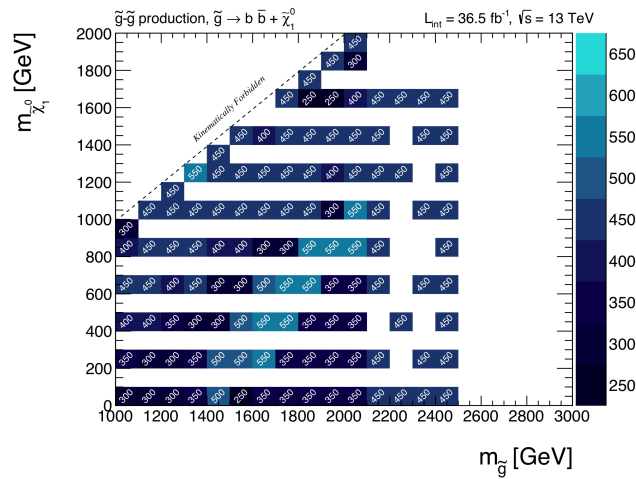
Regarding the VC region, the ISR topology is selected by requiring the leading jet not being b-tagged, have high p_T ($p_T^{j_1} > 400$ GeV) and large separation from the direction of the $\mathbf{p}_T^{\text{miss}}$ ($\Delta\phi^{j_1} > 2.5$). The E_T^{miss} distribution of a compressed signal against the SM background can be then seen in Figure 7.17. The latter motivated a 600 GeV selection while the m_{eff} selection is completely dropped. The final selection criteria of all the regions targeting the Gbb model are presented in Table 7.8 and the expected SM yields from simulation in Table 7.6.

Table 7.8: Selection criteria for the Signal, Control and Validation cut-and-count regions targeting the Gbb model. All kinematic variables are expressed in GeV except $\Delta\phi_{\text{min}}^{4j}$, which is in radians. The $j_1 \neq b$ requirement denotes that the leading jet is not a b-jet. Table published in [4].

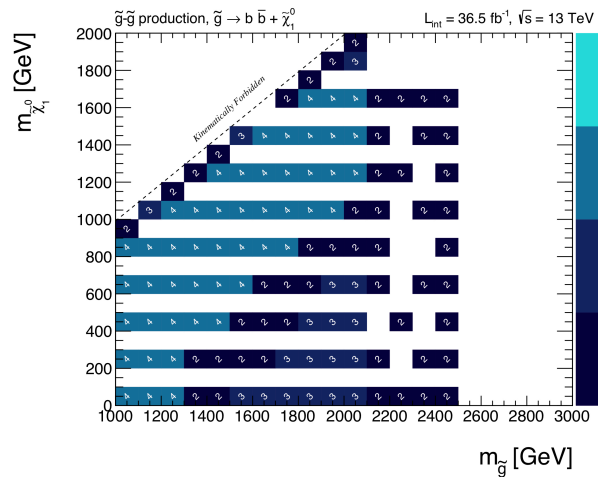
Gbb									
Criteria common to all regions: $N_{\text{jet}} \geq 4$, $p_T^{\text{jet}} > 30$ GeV									
Targeted kinematics	Type	N_{lepton}	$N_{b\text{-jets}}$	$\Delta\phi_{\text{min}}^{4j}$	m_T	$m_{T,\text{min}}^{b\text{-jets}}$	E_T^{miss}	m_{eff}	Others
Region B (Boosted, Large Δm)	SR	= 0	≥ 3	> 0.4	–	–	> 400	> 2800	–
	CR	= 1	≥ 3	–	< 150	–	> 400	> 2500	–
	VR	= 0	≥ 3	> 0.4	–	–	> 350	1900–2800	–
Region M (Moderate Δm)	SR	= 0	≥ 4	> 0.4	–	> 90	> 450	> 1600	–
	CR	= 1	≥ 4	–	< 150	–	> 300	> 1600	–
	VR	= 0	≥ 4	> 0.4	–	> 100	250–450	1600–1900	–
Region C (Compressed, small Δm)	SR	= 0	≥ 4	> 0.4	–	> 155	> 450	–	–
	CR	= 1	≥ 4	–	< 150	–	> 375	–	–
	VR	= 0	≥ 4	> 0.4	–	> 125	350–450	–	–
Region VC (Very Compressed, very small Δm)	SR	= 0	≥ 3	> 0.4	–	> 100	> 600	–	$p_T^{j_1} > 400$, $j_1 \neq b$, $\Delta\phi^{j_1} > 2.5$
	CR	= 1	≥ 3	–	< 150	–	> 600	–	
	VR	= 0	≥ 3	> 0.4	–	> 100	225–600	–	



(a) m_{eff}



(b) E_T^{miss}



(c) $N_{b\text{-jets}}$

Figure 7.15: The optimal selection of (a) m_{eff} , (b) E_T^{miss} and (c) $N_{b\text{-jets}}$ per Gbb model-points in the OL channel. The figures comprise an original work of the author.

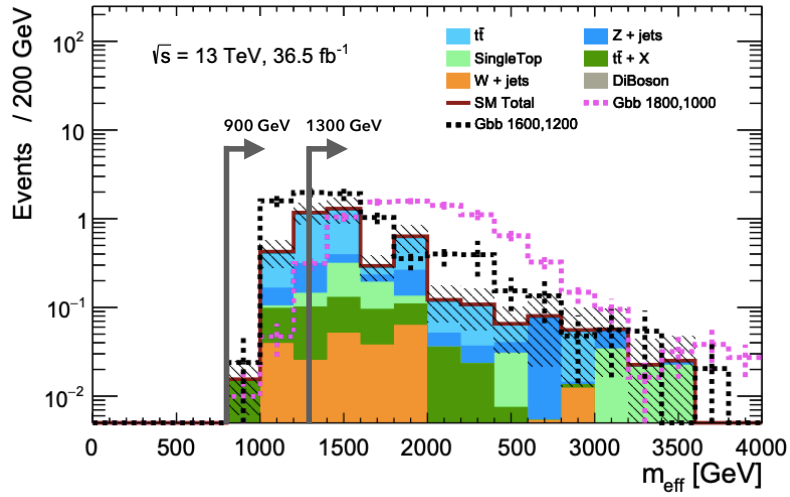


Figure 7.16: The m_{eff} distribution of simulated events in the SR-Gbb-C region before the m_{eff} selection. More compressed signal scenarios show lower m_{eff} values thus the optimisation propose a lower selection to target them. The arrows indicate the optimal selections from Figure 7.15a. The figures comprise an original work of the author.

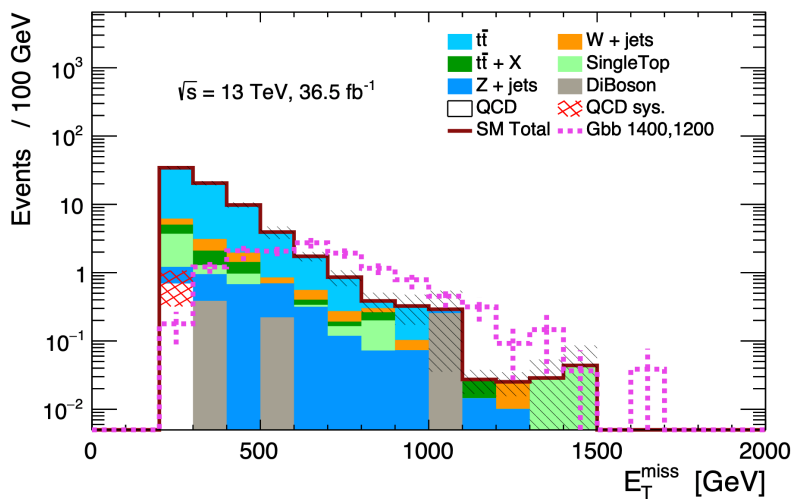


Figure 7.17: The E_T^{miss} distribution in events of the Gbb-VC region before the E_T^{miss} selection. The figure comprises an original work of the author.

7.5.2 Multi-bin Regions

Two inclusive discriminating variables of the above list (N_{jets} and m_{eff}) show wide range of values for the models under investigation. First, the N_{jets} is usually low for the Gbb models and large for the Gtt. Intermediate multiplicities can be generated by additional hadronic radiation during the parton showering of the Gbb events or by jets falling out of acceptance in Gtt events. It's noteworthy that Gtb events are also expected to have intermediate jet multiplicities as two top quarks and two b-jet are produced in the final state. Second, the value of m_{eff} varies in both models as is heavily dependent on the $\tilde{g} - \tilde{\chi}_1^0$ mass splitting. The above observations motivated the slicing of the phase space into mutually exclusive bins based on the jet multiplicity, m_{eff} value and the presence of leptons. This approach provides a natural sensitivity gradient to the emerging signal topology and in case of no BSM signal discovery, the bins are used to achieve stronger model exclusion by statistical combination, as explained in Section 6.2.3.

In particular, two regions are defined by the presence of leptons or not. These regions are sliced into Low, Intermediate and High (L, I and H) jet multiplicities. The low jet multiplicity bin is used only for the 0L regions as it is designed to provide sensitivity to the Gbb model. The intermediate and high jet multiplicity selections differ between the 0L and 1L regions by one. This is because if a W boson decays leptonically the number of expected jets is lower. Each of the five bins is further divided in Low, Intermediate and High m_{eff} regimes. This slicing leads to 15 orthogonal regions. Because of limited statistics the high m_{eff} bins with intermediate and high N_{jets} multiplicities are merged together to sustain the analysis reliability. This reduces the number of bins to 13.

Additionally an ISR selection bin is defined in order to provide sensitivity to very compressed scenarios with soft objects, in accordance to the cut-and-count ISR region defined above. The rest of the bins are kept orthogonal to the ISR by requiring either the leading jet to be a b-jet or the $\Delta\phi^j$ to be small. With this last addition the final number of the orthogonal bins used is 14.

The bins are named based on the pattern SR- X L- Y Z, where X denotes the number of leptons (zero or at least one), Y the N_{jets} multiplicity (L, I, H) and Z the m_{eff} regime (L, I, H). They are all schematically presented in Figure 7.18.

Beyond the number of leptons, jets and m_{eff} that characterise each bin, additional selections are also applied. They are optimised based on few Gbb and Gtt signal benchmarks for very large, intermediate and small $\Delta m(\tilde{g}, \tilde{\chi}_1^0)$ (as in the case of the cut-and-count regions) in order to maximise the model exclusion, using the CL_s prescription described in Section 6.2.3 and considering all the 14 bins simultaneously. The final selections are presented in Tables 7.9–7.12. The expected SM yield from simulations vary from about 0.5 to 40 events for a tight (SR-1L-HH) and a loose (SR-0L-IL) bin respectively.

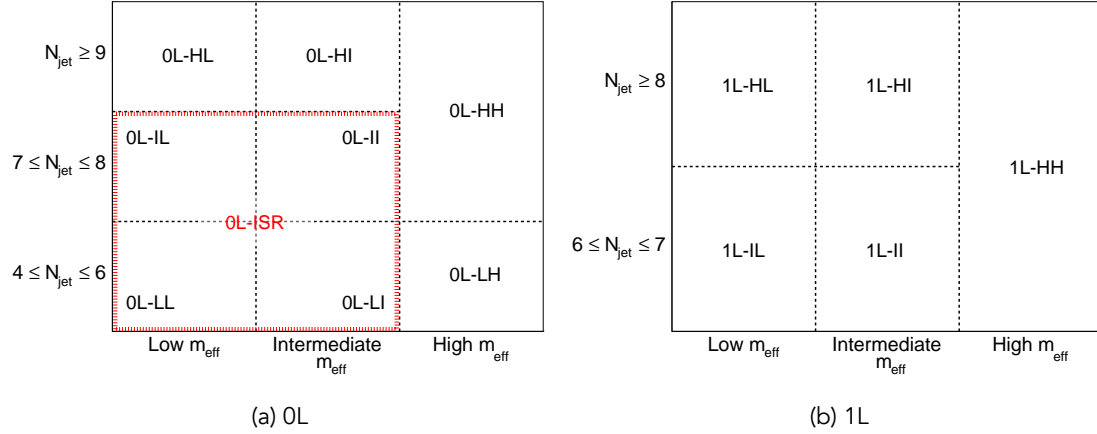


Figure 7.18: Schematic representation of the orthogonal bins used for model exclusion. Figures published in [4].

Table 7.9: Selection criteria for the Signal, Control and Validation multi-bin regions (High N_{jets} multiplicities). All kinematic variables are expressed in GeV except $\Delta\phi_{\text{min}}^{4j}$, which is in radians. The $j_1 = b$ requirement denotes that the leading jet is a b-jet. Tables published in [4].

(a)

High- N_{jet} regions									
Criteria common to all regions: $N_{b\text{-jets}} \geq 3, p_{\text{T}}^{\text{jet}} > 30$ GeV									
Targeted kinematics	Type	N_{lepton}	$\Delta\phi_{\text{min}}^{4j}$	m_{T}	N_{jet}	$m_{\text{T},\text{min}}^{b\text{-jets}}$	M_J^Σ	$E_{\text{T}}^{\text{miss}}$	m_{eff}
High- m_{eff} (HH) (Large Δm)	SR-0L	= 0	> 0.4	—	≥ 7	> 100	> 200	> 400	> 2500
	SR-1L	≥ 1	—	> 150	≥ 6	> 120	> 200	> 500	> 2300
	CR	≥ 1	—	< 150	≥ 6	> 60	> 150	> 300	> 2100
	VR-0L	= 0	> 0.4	—	≥ 7	< 100 if $E_{\text{T}}^{\text{miss}} > 300$	—	< 300 if $m_{\text{T},\text{min}}^{b\text{-jets}} > 100$	> 2100
	VR-1L	≥ 1	—	> 150	≥ 6	< 140 if $m_{\text{eff}} > 2300$	—	< 500	> 2100
Intermediate- m_{eff} (HI) (Intermediate Δm)	SR-0L	= 0	> 0.4	—	≥ 9	> 140	> 150	> 300	[1800, 2500]
	SR-1L	≥ 1	—	> 150	≥ 8	> 140	> 150	> 300	[1800, 2300]
	CR	≥ 1	—	< 150	≥ 8	> 60	> 150	> 200	[1700, 2100]
	VR-0L	= 0	> 0.4	—	≥ 9	< 140 if $E_{\text{T}}^{\text{miss}} > 300$	—	< 300 if $m_{\text{T},\text{min}}^{b\text{-jets}} > 140$	[1650, 2100]
	VR-1L	≥ 1	—	> 150	≥ 8	< 140 if $E_{\text{T}}^{\text{miss}} > 300$	—	< 300 if $m_{\text{T},\text{min}}^{b\text{-jets}} > 140$	[1600, 2100]
Low- m_{eff} (HL) (Small Δm)	SR-0L	= 0	> 0.4	—	≥ 9	> 140	—	> 300	[900, 1800]
	SR-1L	≥ 1	—	> 150	≥ 8	> 140	—	> 300	[900, 1800]
	CR	≥ 1	—	< 150	≥ 8	> 130	—	> 250	[900, 1700]
	VR-0L	= 0	> 0.4	—	≥ 9	< 140	—	> 300	[900, 1650]
	VR-1L	≥ 1	—	> 150	≥ 8	< 140	—	> 225	[900, 1650]

Table 7.10: Selection criteria for the Signal, Control and Validation multi-bin regions (Intermediate N_{jets} multiplicities). All kinematic variables are expressed in GeV except $\Delta\phi_{\text{min}}^{4j}$, which is in radians. The $j_1 = b$ requirement denotes that the leading jet is a b-jet. Tables published in [4].

(a)

Intermediate-N_{jet} regions											
Criteria common to all regions: $N_{b\text{-jets}} \geq 3, p_{\text{T}}^{\text{jet}} > 30$ GeV											
Targeted kinematics	Type	N_{lepton}	$\Delta\phi_{\text{min}}^{4j}$	m_{T}	N_{jet}	$j_1 = b$ or $\Delta\phi^{j_1} \leq 2.9$	$m_{\text{T,min}}^{b\text{-jets}}$	M_{J}^{Σ}	$E_{\text{T}}^{\text{miss}}$	m_{eff}	
Intermediate- m_{eff} (II) (Intermediate Δm)	SR-0L	= 0	> 0.4	–	[7, 8]	✓	> 140	> 150	> 300	[1600, 2500]	
	SR-1L	≥ 1	–	> 150	[6, 7]	–	> 140	> 150	> 300	[1600, 2300]	
	CR	≥ 1	–	< 150	[6, 7]	✓	> 110	> 150	> 200	[1600, 2100]	
	VR-0L	= 0	> 0.4	–	[7, 8]	✓	< 140	–	> 300	[1450, 2000]	
	VR-1L	≥ 1	–	> 150	[6, 7]	–	< 140	–	> 225	[1450, 2000]	
Low- m_{eff} (II) (Low Δm)	SR-0L	= 0	> 0.4	–	[7, 8]	✓	> 140	–	> 300	[800, 1600]	
	SR-1L	≥ 1	–	> 150	[6, 7]	–	> 140	–	> 300	[800, 1600]	
	CR	≥ 1	–	< 150	[6, 7]	✓	> 130	–	> 300	[800, 1600]	
	VR-0L	= 0	> 0.4	–	[7, 8]	✓	< 140	–	> 300	[800, 1450]	
	VR-1L	≥ 1	–	> 150	[6, 7]	–	< 140	–	> 300	[800, 1450]	

Table 7.11: Selection criteria for the Signal, Control and Validation multi-bin regions (Low N_{jets} multiplicities). All kinematic variables are expressed in GeV except $\Delta\phi_{\text{min}}^{4j}$, which is in radians. The $j_1 = b$ requirement denotes that the leading jet is a b-jet. Tables published in [4].

(a)

Low-N_{jet} regions											
Criteria common to all regions: $N_{b\text{-jets}} \geq 3, p_{\text{T}}^{\text{jet}} > 30$ GeV											
Targeted kinematics	Type	N_{lepton}	$\Delta\phi_{\text{min}}^{4j}$	m_{T}	N_{jet}	$j_1 = b$ or $\Delta\phi^{j_1} \leq 2.9$	$p_{\text{T}}^{j_1}$	$m_{\text{T,min}}^{b\text{-jets}}$	$E_{\text{T}}^{\text{miss}}$	m_{eff}	
High- m_{eff} (LH) (Large Δm)	SR	= 0	> 0.4	–	[4, 6]	–	> 90	–	> 300	> 2400	
	CR	≥ 1	–	< 150	[4, 5]	–	–	–	> 200	> 2100	
	VR	= 0	> 0.4	–	[4, 6]	–	> 90 if $E_{\text{T}}^{\text{miss}} < 300$	–	> 200	[2000, 2400]	
Intermediate- m_{eff} (LI) (Intermediate Δm)	SR	= 0	> 0.4	–	[4, 6]	✓	> 90	> 140	> 350	[1400, 2400]	
	CR	≥ 1	–	< 150	[4, 5]	✓	> 70	–	> 300	[1400, 2000]	
	VR	= 0	> 0.4	–	[4, 6]	✓	> 90	< 140	> 300	[1250, 1800]	
Low- m_{eff} (LL) (Low Δm)	SR	= 0	> 0.4	–	[4, 6]	✓	> 90	> 140	> 350	[800, 1400]	
	CR	≥ 1	–	< 150	[4, 5]	✓	> 70	–	> 300	[800, 1400]	
	VR	= 0	> 0.4	–	[4, 6]	✓	> 90	< 140	> 300	[800, 1250]	

Table 7.12: Selection criteria for the Signal, Control and Validation ISR multi-bin regions. All kinematic variables are expressed in GeV except $\Delta\phi_{\min}^{4j}$, which is in radians. The $j_1 \neq b$ requirement denotes that the leading jet is not a b-jet. Tables published in [4].

ISR regions							
Criteria common to all regions: $N_{b\text{-jets}} \geq 3$, $\Delta\phi_{\min}^{4j} > 2.9$, $p_{T1}^j > 400$ GeV, $p_{T}^{\text{jet}} > 30$ GeV, $j_1 \neq b$							
Type	N_{lepton}	$\Delta\phi_{\min}^{4j}$	m_T	N_{jet}	$m_{T,\min}^{b\text{-jets}}$	E_T^{miss}	m_{eff}
SR	= 0	> 0.4	–	[4, 8]	> 100	> 600	< 2200
CR	≥ 1	–	< 150	[4, 7]	–	> 400	< 2000
VR	= 0	> 0.4	–	[4, 8]	> 100	> 250	< 2000

7.6 Background Estimation

7.6.1 Processes and Strategy

In all the analysis regions the main SM background is the $t\bar{t}$ production in association with additional jets – needed in order to fulfill the high $N_{b\text{-jets}}$ and N_{jets} requirements. These are produced via hadronic radiation of the initial or final state partons. Also, at least one of the W bosons of the $t\bar{t}$ decay chain should decay leptonically so large E_T^{miss} is generated by the neutrino that escapes detection. The Feynman diagram of the process is shown in Figure 7.19a.

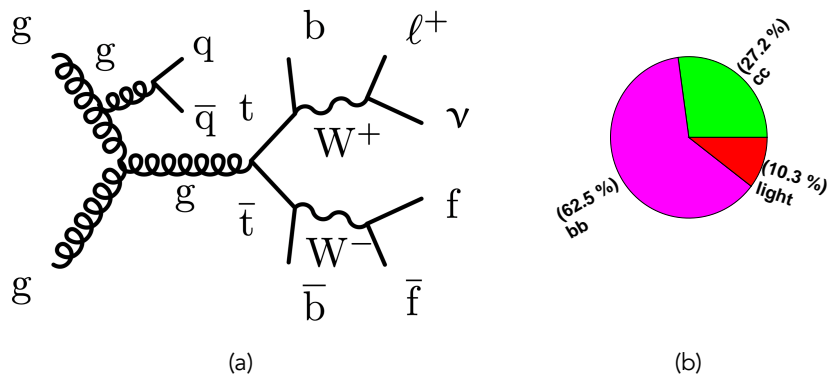


Figure 7.19: (a) Example of Feynman diagram of the production of a $t\bar{t}$ pair in association with additional jets (here from gluon ISR emission and consecutive spitting to b-quarks) decaying semi-leptonically. The charge conjugate diagram is implied. The diagram comprises an original work of the author. (b) The relative contribution of the flavour of the additional jet produced in association with the $t\bar{t}$ pair for the SR-Gtt-1L-C region. Figure courtesy of the ATLAS Collaboration.

The additional jets usually originate from the hadronisation of a b-quark. However,

other jet flavours are also common; jets from the hadronisation of a c-quark or a light-quark/gluon. The latter cases can be misidentified as b-jets with rates given in Table 5.4. The relative contribution of the additional jets flavour has been calculated using truth information and, as an example, the breakdown of SR-Gtt-1L-C is shown in Figure 7.19b. The rest of the regions show similar results except of the ISR topology selections where the b-flavour is reduced (to $\sim 30\%$) from the non-b-tag and large $\Delta\phi^{\text{J1}}$ requirements.

The $t\bar{t}$ events enter the 0L regions mainly via their semi-leptonic decay (e.g. Figure 7.20a). The lepton from the W decay is either falling out of acceptance or misidentified as a jet (relevant for electrons). Hadronically decaying taus can be also misidentified as b-jets in a non-negligible rate given in Table 5.4. Truth-level studies on the lepton flavour composition, presented in Figure 7.20b, show increased τ fraction but this is because both hadronically and leptonically decaying τ -leptons are included into the plot.

On the other hand, $t\bar{t}$ events enter the 1L regions mainly via their di-leptonic decay (e.g. Figure 7.20c). This is result of both the ≥ 1 lepton requirement and the high m_T selection that promotes events with at least one hadronically decaying tau, as shown in Figure 7.20d.

In general, the $t\bar{t}$ background is estimated in the semi-data-driven manner introduced in Section 6.1. In other words, observables shape are taken from MC simulations but the normalisation is extracted from data. For the rest of the backgrounds, both the shape and the normalisation are taken from simulations. As the different SRs vary on event kinematic configuration and $t\bar{t}$ background composition, different normalisations are extracted for each SR from corresponding $t\bar{t}$ enriched CRs that closely resemble each SR selection – SRs and CRs are mutually exclusive to reduce any signal contamination and bias. The background-only fit, described in Section 6.2.1, is performed to each CR independently to determine the μ -factors by maximising the corresponding likelihood (Eq. 6.1). After the background model extraction, its validation follows in VRs defined with similar requirements to the corresponding SRs in order to check the $t\bar{t}$ background prediction in a relevant phase space.

In all cases, the $t\bar{t}$ background is normalised in regions with leptons and validated in regions with or without leptons, according to the corresponding SR selection. All the control and validation regions used are described in the following sections.

7.6.2 Cut-and-count Regions

The control and validation regions defined to extract and validate the three $t\bar{t}$ normalisations correspond to the Gtt 1L SRs of Table 7.5 are based on the same lepton multiplicity with them (≥ 1). The CRs are defined in a low m_T regime (< 150 GeV), in order to be orthogonal to the high- m_T selection of the SRs, and in an exclusive N_{jets} selection, providing orthogonality with the VRs. Additionally, the $m_{T,\text{min}}^{\text{b-jets}}$ requirement is removed

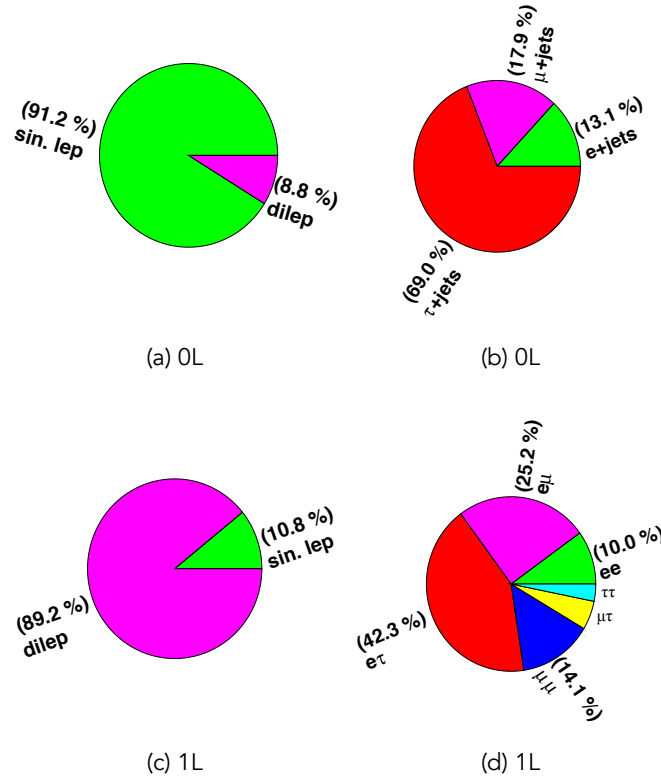


Figure 7.20: The relative fraction of the $t\bar{t}$ decay mode in SR-Gtt-OL-C and its major component lepton flavour composition ((a) and (b)). The same fractions for SR-Gtt-1L-C are shown in (c) and (d). Similar conclusions apply to all the OL and 1L regions respectively. The τ component includes both hadronically and leptonically decaying τ -leptons. Figures courtesy of the ATLAS Collaboration.

and E_T^{miss} , m_{eff} and M_J^Σ selections are relaxed to enhance the sample in events and reduce the statistical uncertainty. All the CR definitions are presented in Table 7.5.

The validation of the predictions is taking place in two regions. First, a high m_T region, called VR- m_T , with similar threshold as the SRs is checking the extrapolation from low to high m_T values. As this region is kept orthogonal to the SR with a low M_J^Σ or $m_{T,\text{min}}^{\text{b-jets}}$ selection a second VR (VR- $m_{T,\text{min}}^{\text{b-jets}}$) is defined to verify the prediction in the high values of these two variables. The VR- $m_{T,\text{min}}^{\text{b-jets}}$ is kept orthogonal to the SR with an inverted $m_{T,\text{min}}^{\text{b-jets}}$ selection and to the CR with a higher jet multiplicity. Again, E_T^{miss} and m_{eff} selections are relaxed (compared to the corresponding SRs) to enhance the sample in statistics. All the VR definitions are presented in Table 7.5.

The above strategy with the two VRs has the additional advantage to check the $t\bar{t}$ background estimation over its different decay modes. As mentioned before, the high m_T selection (SR and VR- m_T) promotes events with di-leptonic decays and increased hadronically decaying tau fraction. On the other hand a low m_T selection (CR and VR- $m_{T,\text{min}}^{\text{b-jets}}$) is dominated by semi-leptonic $t\bar{t}$ decays. The different $t\bar{t}$ fractions for the Gtt-1L-

A regions can be seen in Figure 7.21.

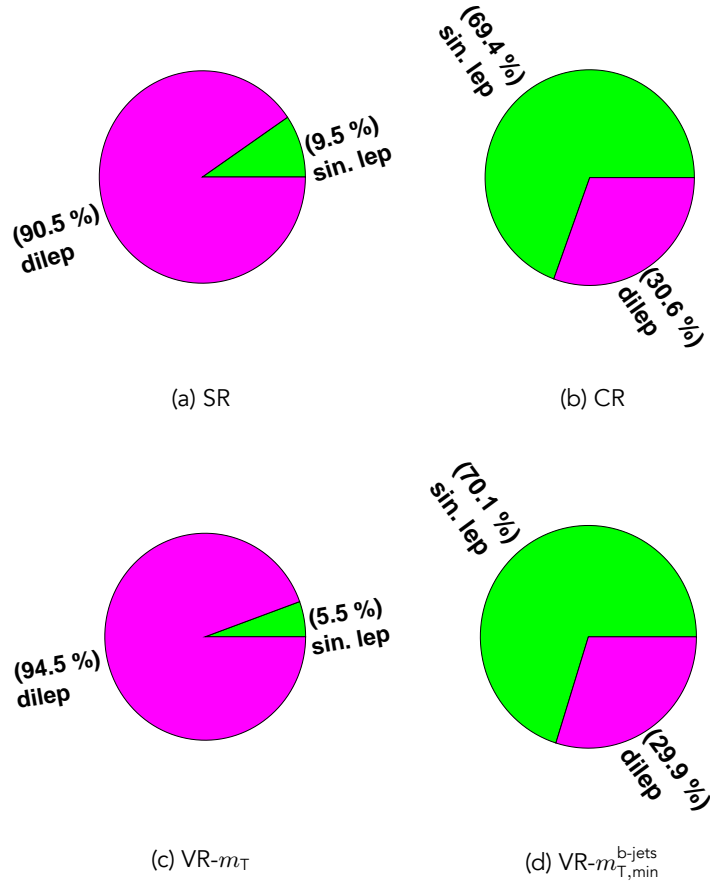


Figure 7.21: The relative fraction of the $t\bar{t}$ decay mode in the Gtt-1L-A regions. Figures courtesy of the ATLAS Collaboration.

For the Gtt 0L SRs of Table 7.7, the corresponding CRs are defined by explicitly selecting one lepton and with an upper bound on m_T in order to be orthogonal to both the 0L and 1L SRs. All the regions are dominated by semi-leptonic $t\bar{t}$ decays. The VRs, on the other hand, are defined in the 0L channel and kept orthogonal to the SRs with an inverted M_{J}^{Σ} selection. As before, CR and VR selections on N_{jets} , $E_{\text{T}}^{\text{miss}}$ and m_{eff} are relaxed to enhance the samples statistics. The definitions of the control and validation regions corresponding to the three Gtt 0L SRs can be found in Table 7.7.

Similarly, the Gbb CRs are using events with a lepton, low m_T values and relaxed $E_{\text{T}}^{\text{miss}}$ or m_{eff} selections. The VRs at this time are kept orthogonal to the SRs by lower m_{eff} or $E_{\text{T}}^{\text{miss}}$ selections. In particular for the Gbb-VC SR that targets an ISR topology, the corresponding CR and VR are also based on the same ISR criteria. All the region definitions relevant to the Gbb model are detailed in Table 7.8.

Finally, signal contamination studies have been performed for all the CRs and VRs defined above. The contamination in the CRs is at the majority negligible, though for

few compressed scenarios can be up to $\sim 5\%$. Relaxed signal contamination requirements are imposed to the VRs. Overall, this is minimal for the bulk of the model-points ($\lesssim 10\%$) but for few compressed scenarios can be up to $\sim 30\%$. All the above numbers refer to surviving model-points from previous iteration of the analysis using LHC Run 2 data [164].

7.6.3 Multi-bin Regions

The normalisation and validation of the $t\bar{t}$ background for the multi-bin regions closely resembles the strategy employed for the cut-and-count regions described above. The main difference is that corresponding 0L and 1L SRs share a single CR (e.g. there is one CR for the SR-0L-1L and SR-1L-1L) thus the same μ -factor normalise the $t\bar{t}$ process in both cases.

All the CR bins require the presence of at least one lepton and have a low m_T requirement in order to be orthogonal to the SRs employing events with leptons. The N_{jets} selection is the same as the 1L SRs (lower than the 0L SRs). Finally, discriminating variable criteria have been relaxed to increase statistics.

In contrast with the CR, a VR corresponds to each SR bin. These follow the corresponding SR lepton (and m_T) requirement while remain orthogonal by inversed $m_{T,\text{min}}^{\text{b-jets}}$ or E_T^{miss} selection.

As previously, the control and validation regions concerning the ISR topology bin follow the same requirement on the anti-b-tagging of the leading jet and the large $\Delta\phi^1$. All the multi-bin control and validation region selection criteria are detailed in Tables 7.9–7.12.

7.6.4 Background-only Fit Results

In a nutshell, the normalisation of the $t\bar{t}$ background is derived from data while its shape from MC simulations. The rest of the SM backgrounds are taken directly from simulations. The CRs use events with leptons while the VRs follow the corresponding SR lepton selection. In a set of signal, control and validation regions, selections to retain them orthogonal have been employed. Additionally, signal contamination has been minimised to all the control and validation regions.

After performing multiple background-only fits (one for each CR) for the cut-and-count regions, the normalisation factors extracted are shown in the bottom panel of Figure 7.22 while the top panel shows the observed and simulated yields before the fit. In general, the μ -factors are greater than one but almost all compatible to unity within their (statistical) uncertainty. To some extent, this is due to the underestimation of the $t\bar{t}$ in association with heavy flavour partons production cross-section in simulations as identified by other studies as well [180, 181]. An important check is also the modeling of the variables over which the extrapolation from the CRs to VRs and eventually to SRs

is happening. Selected representative distributions are shown in Figure 7.23 for the m_T , $m_{T,\min}^{\text{b-jets}}$, N_{jets} , M_J^Σ , m_{eff} and E_T^{miss} where it can be seen that the data are always in agreement with the prediction within the uncertainties. Of course, for the zero-lepton SRs extrapolation over the lepton number is happening from the corresponding CR but the lepton multiplicity is generally considered a well modeled quantity thus is not shown.

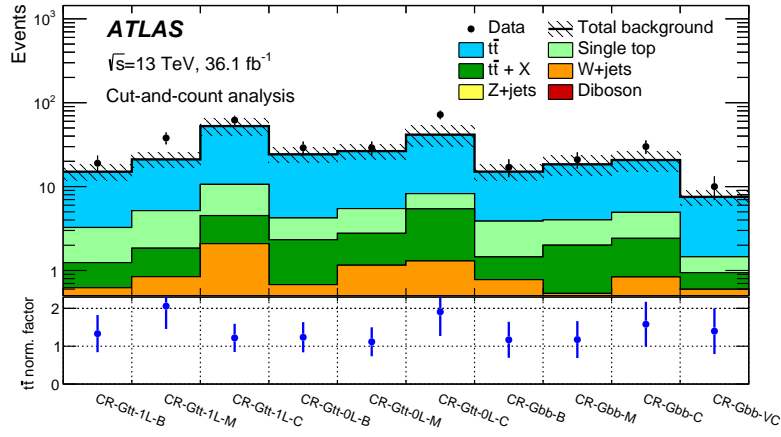


Figure 7.22: Normalisation results for the cut-and-count regions. The top panel shows the observed and simulated yields before the fit, the bottom panel shows the normalisation factors derived from each CR. The uncertainty band on the total SM background includes the statistical and systematic components listed in Section 7.7. Figure published in [4].

The expected background yield in a VR can be then estimated by extrapolating each μ -factor from the corresponding CR and using the formula:

$$N_{\text{bkg}}(\text{VR}) = \mu_{\text{t}\bar{\text{t}}} \times N_{\text{t}\bar{\text{t}}}^{\text{MC}}(\text{VR}) + N_{\text{Other}}^{\text{MC}}(\text{VR}), \quad (7.6)$$

where “Other” the rest of the processes taken directly from simulations. The results are presented in Figure 7.24 where it can be seen that there is a very good agreement between the observed number of events and the fitted background in all regions. As a reminder to the reader, the significance definition used in this analysis is given in Eq. 6.6.

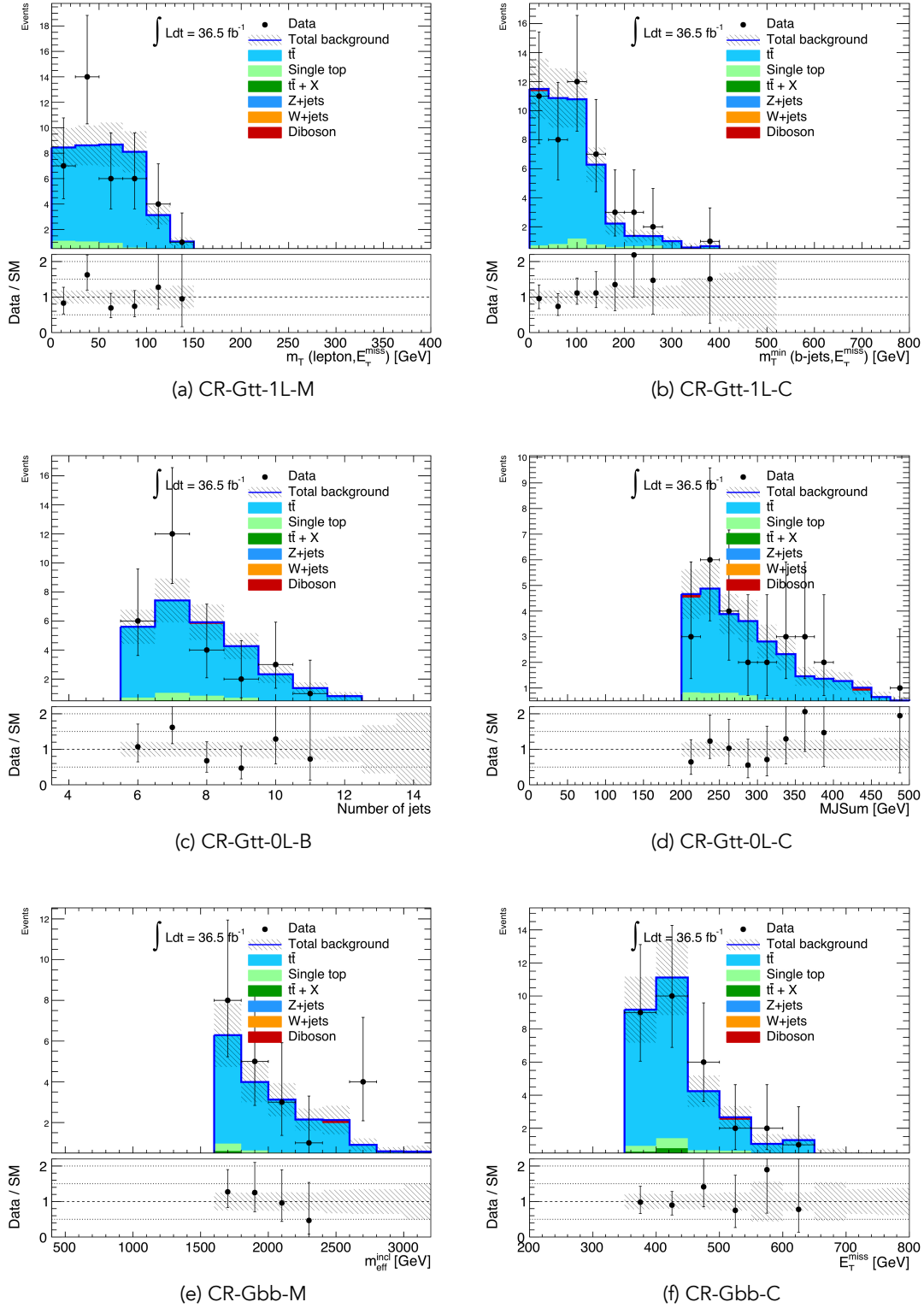


Figure 7.23: Distributions of (a) m_T , (b) $m_T^{\text{b-jets}}$, (c) N_{jets} , (d) M_J^{Σ} , (e) m_{eff} and (f) E_T^{miss} in the corresponding CR after the fit. The bottom panel shows the ratio of data over the fitter SM background. Both statistical and the systematic uncertainties listed in Section 7.7 are included. Figures courtesy of the ATLAS Collaboration.

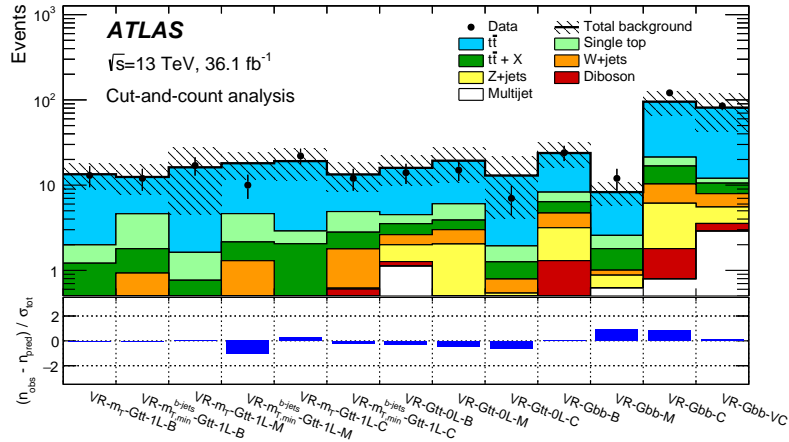


Figure 7.24: Background-only fit results extrapolated to the cut-and-count VRs. The top panel shows the observed number of events and the predicted background, the bottom panel shows the observed significance in each region. The uncertainty band on the total SM background includes the statistical and systematic components listed in Section 7.7. Figure published in [4].

Equivalent background-only fit results for the multi-bin regions are presented in Figures 7.25 and 7.26. The μ -factors show milder deviations from unity while the agreement on the various VRs is overall good. The largest excess of observed events over all the 15 VR bins is found in VR-1L-II and the difference with the prediction is about twice the background uncertainty.

In the background-only fit and all the results of this section the full set of the systematic uncertainties of this analysis is included. A description of each one of them is following in the next section.

7.7 Systematic Uncertainties

The systematic uncertainties considered are categorised into 1) experimental uncertainties, encapsulating the systematically limited knowledge of the detector response and 2) theoretical uncertainties, to counter the biases imposed by specific choices made to model the physics processes, as described in Appendix B. In general, they are estimated by varying various parameters, within their uncertainties (1σ), on the simulated events only, and measuring the effect on the final observables (yields, CL_s value, etc.). This section describes each one of these parameters. Furthermore, a statistical uncertainty is included into the results to account for the finite size of the event samples. This concerns both real and simulated data.

It should be emphasized that the effect of systematic uncertainties on the estimated background (e.g. SR yields) is substantially reduced after the fit. This is a virtue of normalising the simulation in CRs and extrapolating the μ -factors to VRs and SRs. For

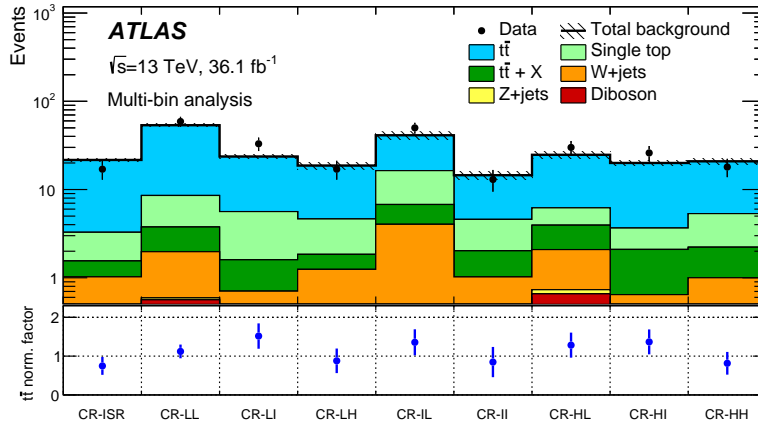


Figure 7.25: The background-only fit results for the multi-bin control regions. The top panel shows the observed and simulated yields before the fit in each CR, the bottom panel shows the normalisation factors derived. The uncertainty band on the total SM background includes the statistical and systematic components listed in Section 7.7. Figure published in [4].

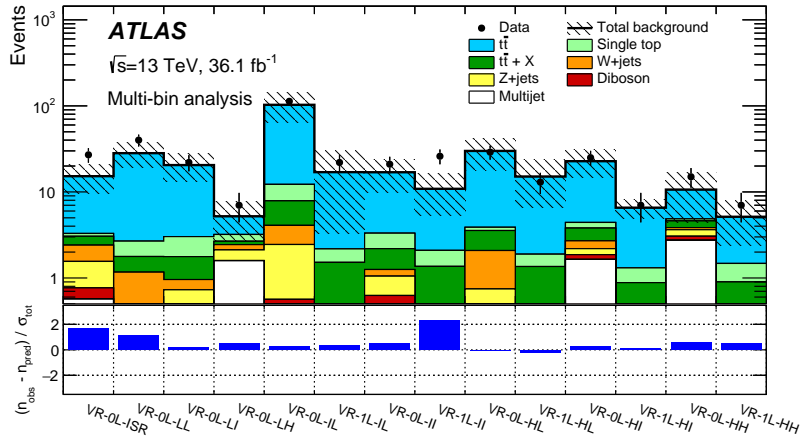


Figure 7.26: The background-only fit results for the multi-bin validation regions. The top panel shows the observed number of events and the predicted background in each VR, the bottom panel shows the observed significance in each region. The uncertainty band on the total SM background includes the statistical and systematic components listed in Section 7.7. Figure published in [4].

instance, the estimated yield of a SM process p in a SR is [156]:

$$\begin{aligned}
 SR_p^{\text{est.}} &= \mu_p \times SR_p^{\text{MC}} \\
 &= \frac{CR_p^{\text{est.}}}{CR_p^{\text{MC}}} \times SR_p^{\text{MC}} \\
 &= CR_p^{\text{est.}} \times \left[\frac{SR_p^{\text{MC}}}{CR_p^{\text{MC}}} \right].
 \end{aligned} \tag{7.7}$$

The ratio in the bracket is causing a (partial) cancellation of the systematic uncertainties between the SR and CR, thus only residual uncertainties on the extrapolation will affect the SR_p^{est} . That is the reason the CRs are designed to closely resemble the SRs so the residual uncertainty is minimal.

The above statement is true only for background processes normalised in CRs. The systematic uncertainties on the signal model, that are included only during the result interpretation via the exclusion fit described in Section 6.2.3, are not canceled at all. The same applies to the experimental uncertainties of the minor SM backgrounds which are included in all the fits but have minimal contribution.

7.7.1 Experimental Uncertainties

The experimental uncertainties are related to the objects reconstruction and the data-taking conditions. They are applied to both all the SM processes and the SUSY signals considered. The different components are described below:

Jets

1. Energy Scale: The calibration procedure of the reconstructed jet energy has been described in Section 5.4. Its uncertainty is mainly originating from the *in situ* techniques used to correct for differences between data and simulation. The final JET uncertainty has roughly 100 components but are combined in a reduced set of three for this analysis. This combination is blind on correlations among the different uncertainty sources but the final observables have been found to be insensitive to it. To estimate its effect to the analysis, each of the three components is varied by $\pm 1\sigma$.
2. Energy Resolution: The important relation of the JER with fake backgrounds has been explained in Section 5.8. Its uncertainty has similarities with the JES; originates from the data measurements used for its derivation and has roughly 100 components that are reduced to one. For this analysis, these uncertainties are extrapolated from $\sqrt{s} = 8$ TeV data measurements using MC simulations and are shown in Figure 7.27 as function of the jet p_T . To account for a possible underestimate of the JER in the MC simulation the reconstructed jet energy is smeared based on Gaussians with mean value one and width the value of the uncertainty.

Flavour-tagging

1. Efficiency: The efficiency to (mis-)identify (c-jets/light-jets) b-jets in data is presented in Table 5.4 and in Figure 5.5 as function of the jet p_T . From these measurements, SFs have been extracted to correct the rates of simulated events. The SFs uncertainties arising mainly from the processes modeling, while the jet energy uncertainties (described above) become dominant only in extreme (low or high) p_T regimes. To assess the impact of these uncertainties the three SFs (b-jet, c-jet,

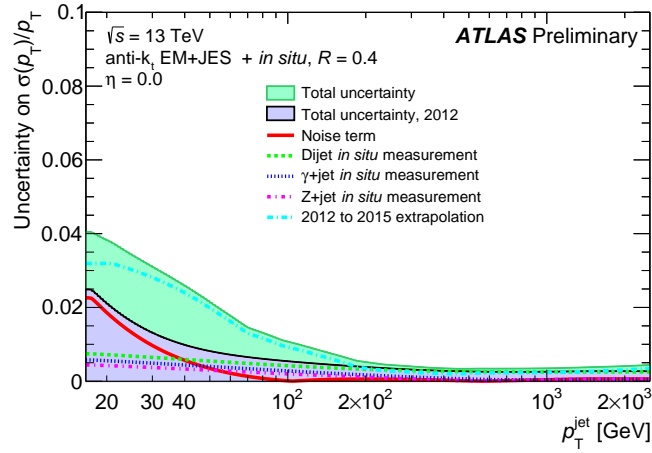


Figure 7.27: The fractional JER uncertainty as function of the jet p_T for $|\eta| = 0$ (relatively stable as function of $|\eta|$) estimated for the 2015 data. [182]

light-jet) are varied by $\pm 1\sigma$.

2. Efficiency Extrapolation: As the SFs have been extracted up to limited jet p_T (400 GeV for b-jets identification), an extrapolation process is taking place to higher momentum. This induce an extra uncertainty to the SFs. To assess its impact the SFs have been varied by $\pm 1\sigma$ of the extrapolation uncertainty.

Missing Energy

In general, the individual uncertainties of each reconstructed object are propagated to the E_T^{miss} calculation. The two uncertainties described below concern only the soft-term, reconstructed from tracks ($\mathbf{p}_T^{\text{miss,soft}}$), in the $\mathbf{p}_T^{\text{miss}}$ calculation (Eq. 5.4).

The uncertainty of the soft-term characterise how well it is modeled in simulations. In an event without real E_T^{miss} the $\mathbf{p}_T^{\text{miss,soft}}$ is expected to be perfectly balanced to the $\mathbf{p}_T^{\text{miss,hard}}$ ¹. Therefore, $Z(\rightarrow ee) + \text{jets}$ events are used and $\mathbf{p}_T^{\text{miss,soft}}$ -related quantities are compared to different simulations and the uncertainty of each one is defined as the envelope of the differences. These quantities are:

1. Soft-track Energy Scale: The mean value of the $\mathbf{p}_T^{\text{miss,soft}}$ parallel to the $\mathbf{p}_T^{\text{miss,hard}}$. Its uncertainty effect to the analysis is evaluated by varying the $\mathbf{p}_T^{\text{miss,soft}}$ by $\pm 1\sigma$.
2. Soft-track Energy Resolution: The root-mean-square of the parallel and perpendicular components of the $\mathbf{p}_T^{\text{miss,soft}}$ to the $\mathbf{p}_T^{\text{miss,hard}}$. Similarly to the JER, its uncertainty effect is evaluated by smearing the energy of simulated events with a Gaussian with mean value 1 and width the soft-track energy resolution uncertainty.

Leptons

The lepton related uncertainties have found to have minimal impact to the work of this dissertation. However, they are fully incorporated into all the results. Short description of the different components if following.

¹The $\mathbf{p}_T^{\text{miss}}$ without the $\mathbf{p}_T^{\text{miss,soft}}$ term.

1. **Energy Scale:** The electrons and muons are calibrated to the corresponding absolute energy scales, as described in Sections 5.2 and 5.3. For the case of electrons more than 60 systematic effects are considered but for the purpose of this work they are combined in a simplified model resulting one parameter. The impact of the energy scale uncertainty to the analysis is evaluated by individually varying each scale by $\pm 1\sigma$.
2. **Energy Resolution:** Similarly to the jets, the reconstructed electron and muon momentum is smeared independently based on Gaussians with mean value one and width the corresponding energy resolution uncertainty. For the muons case, two smearings are taking place, one regarding the ID and one the MS resolution. In this way the impact of the leptons energy resolution uncertainty to the analysis is estimated.
3. **Efficiency:** Different lepton efficiency SFs are mentioned in Sections 5.2 and 5.3. In general, these are correcting the response of simulations to the rates measured in data and have corresponding uncertainties. Independent variations of each SF withing its uncertainty assessing its effect to the analysis observables. For both leptons flavours, the trigger, reconstruction, identification and isolation SFs variation is considered.

Data-taking Conditions

1. **Luminosity:** The uncertainty on the luminosity of the 2015-16 Run 2 dataset used is 2.1%. This value is measured using the methods described in Section 3.1. This uncertainty impact is taken into account by scaling by $\pm 1\sigma$ the total integrated luminosity.

Mismodeling

1. m_{eff} Reweighting: As described in Section 7.4 a reweighting procedure is taking place, for events with at least one lepton, to correct the mismodeled m_{eff} shape. An uncertainty on this procedure is considered where the full size of the correction factors is applied as a one-sided variation.

7.7.2 Theoretical Uncertainties

Uncertainties are employed to account for different choices made regarding the simulation of physics processes, as described in Appendix B. These choices include the hard-scatter generation program and matching scheme, the parton shower/hadronisation model and the amount of initial/final-state radiation. Additional uncertainties accounting for the limited cross-section knowledge regarding some rare SM processes and the SUSY signal. All the theoretical uncertainties per physics process considered are described below.

$t\bar{t}$ Production

1. **Hard-Scatter & Matching:** An uncertainty is employed by evaluating the dif-

ference between the nominal generation program used (Powheg-Box) and the alternative MadGraph5_aMC@NLO.

2. PS & Hadronisation: Similarly, the alternative parton shower and hadronisation program Herwig++ v2.7.1 is used. The difference with the nominal (Pythia) is assigned as a systematic uncertainty.
3. ISR Radiation: The amount of initial- and final-state radiation is increased (decreased) by shifting the $h_{\text{damp}}^1 = 2 m_{\text{top}}$ ($h_{\text{damp}} = m_{\text{top}}$), multiplying the renormalisation and factorisation scales by 0.5 (2) and using a high-radiation (low-radiation) variation of the PERUGIA2012 tune. The differences to the nominal setup are interpreted as one uncertainty.
4. Heavy-Flavour: An additional uncertainty is applied to the fraction of $t\bar{t}$ events produced in association with jets originating from b- or c-quarks to account for the large theoretical uncertainties these processes suffer from. In particular, the production cross-section of these events is varied by 30% in accordance with the measurement of this cross-section by the ATLAS collaboration using $\sqrt{s} = 8$ TeV data [183].

Single-top Production

Uncertainties from different aspects of the Single-top production modeling are considered that overall account for up to 10% changes on the yields of the various regions.

1. Interference: The generation of Wt-channel of the single-top process in NLO accuracy gives rise to diagrams appearing in the LO $t\bar{t}$ production as well, leading to potential double counting and interference effects. An example is shown in Figure 7.28. To assess the sensitivity of the analysis phase space to these phenomena, inclusive WbWb events are generated in a coherent way such that diagrams from both $t\bar{t}$ and Wt and their interference are included. These are compared with the sum of the individual $t\bar{t}$ and Wt and the difference on the yields is imposed as an uncertainty. This is the major theoretical uncertainty on the modeling of the single-top production.
2. ISR Radiation: Similarly to the $t\bar{t}$ process the amount of radiation is varied by the use of alternative PERUGIA2012 tunings.
3. Cross-section: The production cross-section is varied by 5% according to relevant uncertainty estimates [184].

Z/W + jets Production

1. Scales: To estimate the effect of the renormalisation, factorisation, matching and resummation scale² choices, these are varied by factors of 0.5 and 2. The overall impact of these uncertainties on the total Z/W + jets yield can be up to 50%.

¹The h_{damp} parameter controls the transverse momentum of the first additional emission beyond the leading-order Feynman diagram in the parton shower and therefore regulates the emissions against which the $t\bar{t}$ system recoils.

²The equivalent of h_{damp} parameter.

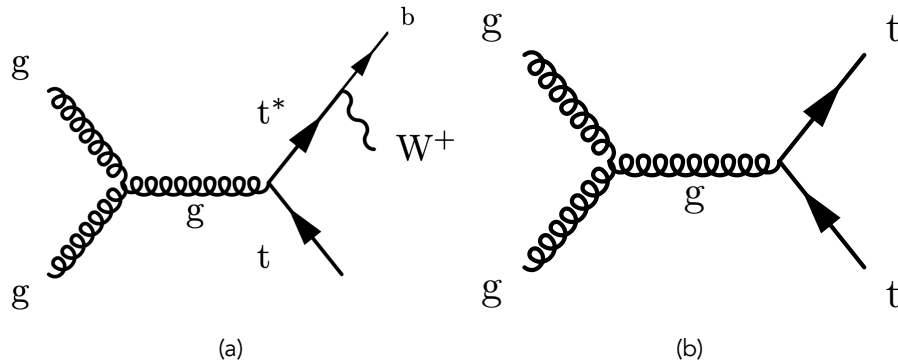


Figure 7.28: (a) NLO Wt production, (b) LO $t\bar{t}$ production (charge conjugate diagrams are implied). After the top quarks decay the final state of both diagrams is the same and the interference is large when the t^* is on-shell. The diagrams comprise an original work of the author.

$t\bar{t}X$ Production

1. Cross-section: The production cross-section is varied by 50%.

SUSY Production

1. Cross-section: The uncertainty on the cross-section of each signal model is determined as the envelope of predictions using different PDF sets and factorisation and renormalisation scales [84]. Exemplary, this uncertainty accounts for 20% for an 1.5 TeV \tilde{g} and rise to 30% for a 2 TeV \tilde{g} .

7.8 Results

The compatibility of the observed data with the estimated SM background in all the cut-and-count VRs, as presented in Figure 7.24, indicates that the background and systematic uncertainties model is reliable. Therefore, and using a relation similar to Eq. 7.6, the background estimation is extrapolated to the SRs and the corresponding data are unblinded. The resulted yields are detailed in Table 7.13 for the Gtt1L, Gtt0L and Gbb regions. The results are also summarised in Figure 7.29 where the bottom panel shows the observed significance (Eq. 6.6) in each region. No significant data deviation above the expected SM processes are seen. Additionally, two representative distributions of the E_T^{miss} are shown in Figure 7.30 after the data unblinding in the leptonic Gtt region targeting boosted topologies (Gtt-1L-B) and in the Gbb region targeting ISR topologies (Gbb-VC).

In general, the systematic uncertainties on the background estimate range from about 25% to 80% in the various cut-and-count SRs. The main source is the theoretical uncertainties govern the $t\bar{t}$ production modeling and can be up to 70%. This is expected in the extreme phase space explored, featuring multiple b-jets and large missing energy, where limited measurements have been performed to constrain it. Additionally, the alternative simulation samples used to estimate the different uncertainty compon-

Table 7.13: Background-only fits resulted yields extrapolated to the cut-and-count SRs. The uncertainties include both statistical and systematic components. The “Fitted background” (“MC-only background”) is the expected SM yield after (before) the fit. Tables published in [4].

(a)				
SR-Gtt-1L				
Targeted kinematics	B	M	C	
Observed events	0	1	2	
Fitted background	0.5 ± 0.4	0.7 ± 0.4	2.1 ± 1.0	
$t\bar{t}$	0.4 ± 0.4	0.5 ± 0.4	1.2 ± 0.8	
Single-top	0.04 ± 0.05	0.03 ± 0.06	0.35 ± 0.28	
$t\bar{t} + X$	0.08 ± 0.05	0.09 ± 0.06	0.50 ± 0.28	
Z+jets	0.049 ± 0.023	0.050 ± 0.023	< 0.01	
W+jets	< 0.01	< 0.01	0.024 ± 0.026	
Diboson	< 0.01	< 0.01	< 0.01	
MC-only background	0.43	0.45	1.9	

(b)				
SR-Gtt-0L				
Targeted kinematics	B	M	C	
Observed events	2	5	28	
Fitted background	1.5 ± 0.5	3.5 ± 1.3	38 ± 8	
$t\bar{t}$	0.9 ± 0.4	1.8 ± 0.7	31 ± 8	
Single-top	0.21 ± 0.14	0.6 ± 0.4	1.3 ± 1.1	
$t\bar{t} + X$	0.12 ± 0.07	0.45 ± 0.25	3.0 ± 1.6	
Z+jets	0.06 ± 0.10	0.3 ± 0.9	0.49 ± 0.31	
W+jets	0.07 ± 0.06	0.18 ± 0.15	0.67 ± 0.22	
Diboson	0.06 ± 0.07	0.12 ± 0.07	< 0.01	
Multijet	0.09 ± 0.11	0.04 ± 0.05	1.3 ± 2.1	
MC-only background	1.3	3.3	23	

(c)				
SR-Gbb				
Targeted kinematics	B	M	C	VC
Observed events	2	2	5	0
Fitted background	2.1 ± 0.7	3.0 ± 1.0	5.8 ± 1.9	4.7 ± 2.3
$t\bar{t}$	1.2 ± 0.6	1.9 ± 0.7	3.8 ± 1.3	3.1 ± 1.3
Single-top	0.31 ± 0.16	0.39 ± 0.16	0.46 ± 0.20	0.15 ± 0.18
$t\bar{t} + X$	0.12 ± 0.06	0.33 ± 0.19	0.6 ± 0.4	0.19 ± 0.11
Z+jets	0.15 ± 0.34	0.2 ± 0.6	0.6 ± 1.3	0.8 ± 1.9
W+jets	0.12 ± 0.09	0.13 ± 0.12	0.29 ± 0.19	0.37 ± 0.30
Diboson	0.06 ± 0.04	< 0.01	< 0.01	0.15 ± 0.08
Multijet	0.10 ± 0.12	0.022 ± 0.025	0.03 ± 0.04	0.016 ± 0.020
MC-only background	1.9	2.7	4.4	3.9

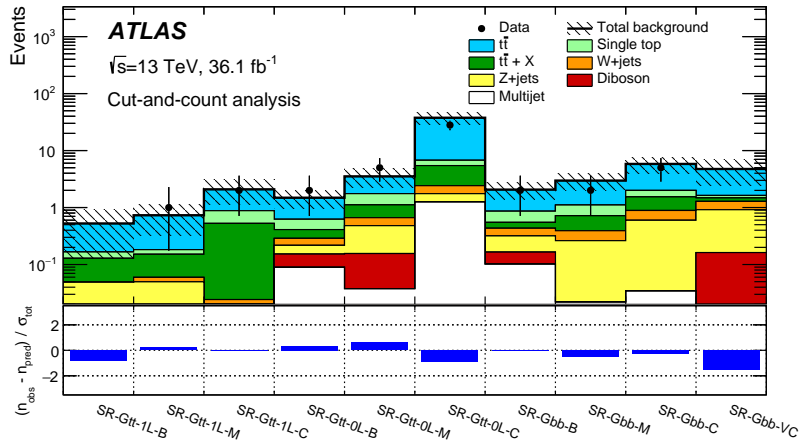


Figure 7.29: Background-only fit results extrapolated to the cut-and-count SRs. The top panel shows the observed number of events and the predicted background, the bottom panel shows the observed significance in each region. The uncertainty band on the total SM background includes both statistical and systematic components. Figure published in [4].

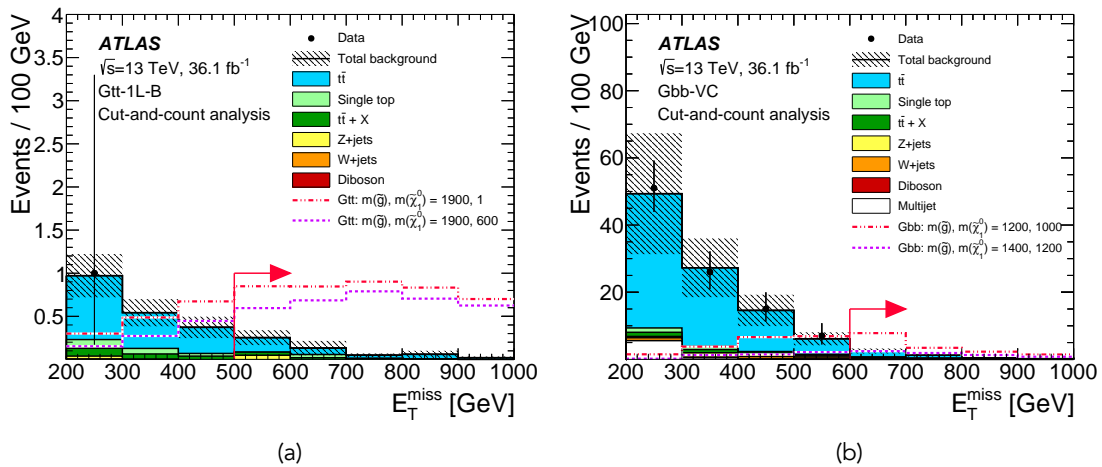


Figure 7.30: The E_T^{miss} distribution in (a) Gtt-1L-B and (b) Gbb-VC before the E_T^{miss} selection (the red arrow indicates the actual SR selection threshold). The uncertainty band includes both statistical and systematic components. Two signal model distributions are overlaid for comparison purposes (legend masses in GeV). Figures published in [4].

ents (hard-scatter, parton shower/hadronisation, radiation) are often limited in statistics in the high- p_T tails this analysis targets thus artificially these uncertainties increase.

The second largest uncertainty on the background estimate originates from the detector response modeling. Its major component is the JES which takes values up to about 5 to 35% in the various regions. The JER component is the next largest and has been found to contribute up to 26%. Flavour-tagging related uncertainties are sub-

leading in all the regions. The latter is an advantage of the constant b-jet multiplicity selection between corresponding control and signal regions such that the uncertainties cancel.

Finally, the statistical uncertainty of the various CRs used to extract the normalisation factors range from 10 to 30% while the residual uncertainty from the m_{eff} reweighting procedure from 10 to 15%. Figure 7.31a summarise the relative size of all the systematic uncertainties and their components for all the cut-and-count SRs.

As no significant deviation from the SM expectation is observed, the background estimation is extrapolated to the multi-bin regions too and the corresponding data were unblinded. The results are shown in Figure 7.32a where in general the observed data yield is consistent with the SM background estimation over the 14 bins. The largest deviation is found in the SR-OL-HH with local¹ significance of 2.3σ . In particular for this region, the $E_{\text{T}}^{\text{miss}}$ distribution is shown in Figure 7.32b along with two signal models overlaid. It can be seen that the data excess is not compatible with the expected signal distribution.

The size of the corresponding systematic uncertainties per region is shown in Figure 7.31b where similar conclusions as the cut-and-count regions are drawn. The multi-bin regions are especially used for the model-dependent result interpretation described Section 7.9.1.

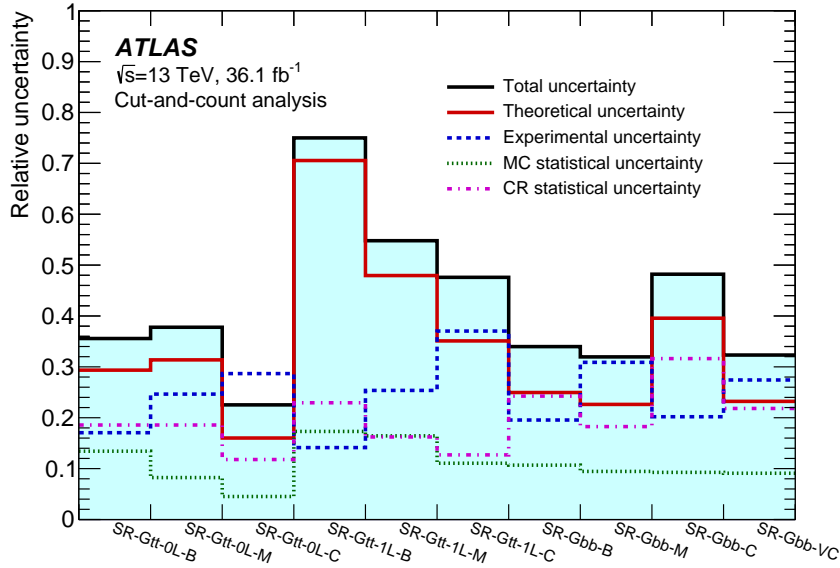
7.9 Interpretation

The cut-and-count SRs have been designed based on wide kinematic selections in order to assess the compatibility of the observed data with the expected SM background yield in the phase space where the SUSY signals under study are expected to appear. Since no significance excess of data above the SM background is seen in any SRs (Figure 7.29), the results are used to place limits on BSM scenarios. These are either the SUSY models that this search is motivated and optimised for – model-dependent exclusion limits – or a general BSM scenario with no particular model assumption – model-independent upper limits.

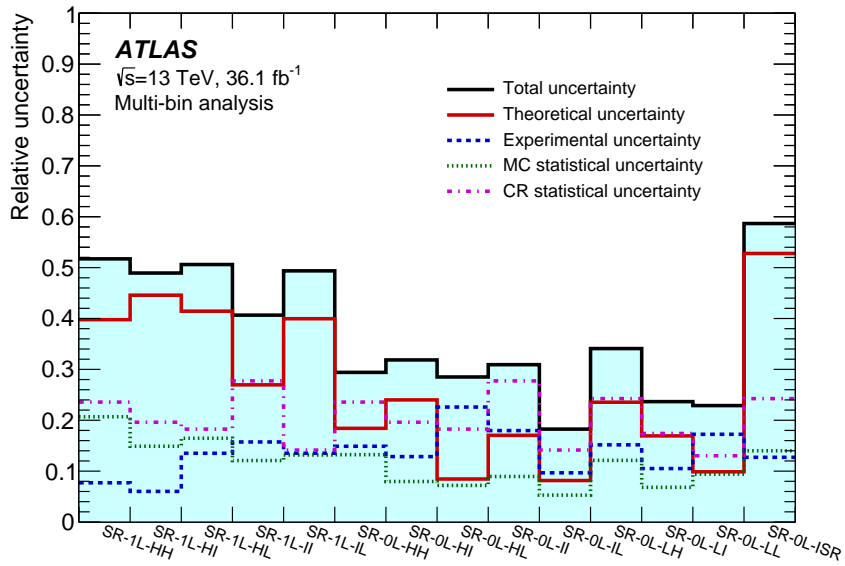
The model-dependent limits are placed via the exclusion fit, described in Section 6.2.3, while the model-independent via the discovery fit, described in Section 6.2.4. Both cases are two-step processes; first a likelihood maximisation procedure is extracting the signal strength of a BSM signal model (SUSY or general BSM) and second, the CL_s technique is used to place the limits at 95% CL by excluding different signal-plus-background hypotheses.

All the systematic uncertainties of the SM background, detailed in Section 7.7, are considered in both the exclusion and discovery fits. In the case of the exclusion fit only,

¹Calculated only by the SR-OL-HH yields without taking into account the look-elsewhere effect.

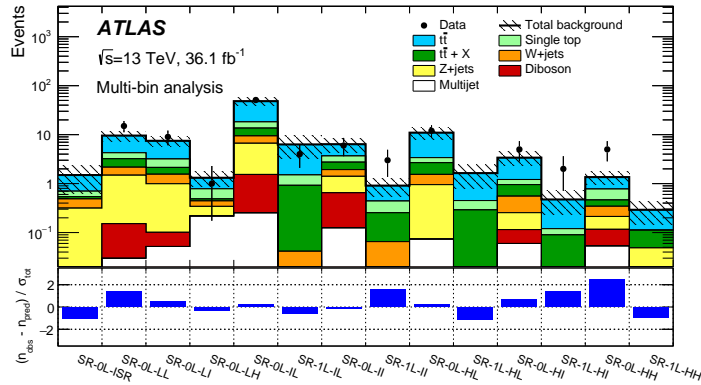


(a)

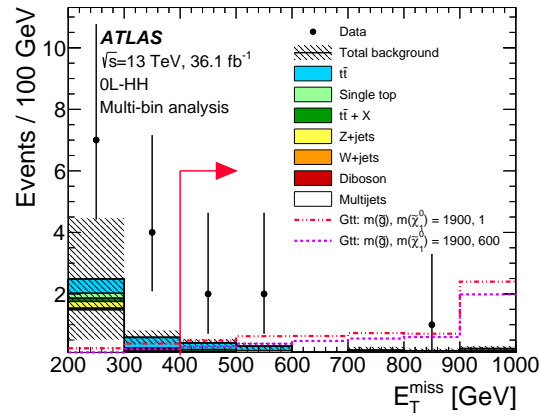


(b)

Figure 7.31: Relative systematic uncertainties for all the (a) cut-and-count and (b) multi-bin regions. The individual uncertainties can be correlated, such that the total background uncertainty is not necessarily their sum in quadrature. Figures published in [4].



(a)



(b)

Figure 7.32: (a) Background-only fit results extrapolated to the multi-bin SRs. The top panel shows the observed number of events and the predicted background, the bottom panel shows the observed significance in each region. (b) The E_T^{miss} distribution in SR-OL-HH before the E_T^{miss} selection (the red arrow indicates the actual SR selection threshold). All the uncertainties shown include both statistical and systematic components. Figures published in [4].

experimental and theoretical uncertainties on the SUSY signal yield are considered as well.

7.9.1 Model-dependent Limits

Model-dependent limits are placed on the simplified models under study; the Gtt, Gbb and the variables BR model incorporating Gtb decays as well, as described in Section 7.2. All the different mass scenarios shown in Figures 7.3a and 7.3b are considered for the Gtt and Gbb models, thus an exclusion contour in the $m(\tilde{g}) - m(\tilde{\chi}_1^0)$ plane can be drawn, while just few particular scenarios for the variables BR model in order to evaluate the behavior of the analysis into a mixed final state.

To achieve a stronger exclusion limit, all the multi-bin regions are statistically com-

bined, providing complementary sensitivity to wide range of final state object multiplicities and kinematic configurations. Independent exclusion fits are performed for each SUSY mass scenario so each signal-plus-background hypothesis is tested against the background-only via the CL_s technique. The results are shown in Figure 7.33 for both the Gtt and Gbb models. The expected limit is derived using the fitted – by the exclusion fit – SM background under the background-only hypothesis and the expected SUSY signal yields in each region. Its uncertainty band is derived varying the yields within 1σ of all the systematic uncertainties apart from the signal cross-section uncertainty. On the other hand, the observed limit is obtained by substituting the fitted background with the observed data yield and the uncertainty band by varying the signal yield within 1σ of the SUSY cross-section uncertainty.

Gluino masses up to 1.97 (1.92) TeV are excluded at 95% CL for neutralino masses lower than 300 GeV for the Gtt (Gbb) model. Compared to the previous results using only 2015 data (3.2 fb^{-1}) the sensitivity to gluino mass has been improved by 300 GeV for the Gtt model and by 450 GeV for the Gbb model [164]. The weaker observed limits for large mass-splitting scenarios, especially on the Gtt model, originates from the slight data excess seen in SR-0L-HH and SR-1L-HI (Figure 7.32).

For comparison purposes, the exclusion limits are also derived using the cut-and-count regions. At this time the regions cannot be statistically combined so independent fits are performed. The results however are combined for each SR type: Gtt-1L, Gtt-0L and Gbb by just selecting the sub-region (B, M, C or VC) with the best (lower) CL_s value per model-point. The exclusion limits for the three cases are shown in Figure 7.34. Few drawbacks compared to the multi-bin strategy are then apparent: 1) the expected limits are in general similar or weaker, 2) the contours are discontinuous over the parameter space as the sensitivity transition, in terms of object multiplicity and kinematic configuration, happening is coarser intervals and 3) for the Gtt model, the 1L regions provide in general better sensitivity than the 0L for any model-point, however by their statistical combination a significantly stronger limit can be derived compared to either of them alone.

The multi-bin SRs are also used to place exclusion limits for a variable BR model, explained in Section 7.2. In this case the gluino is allowed to decay via the three-body $\tilde{g} \rightarrow \bar{t}b\tilde{\chi}_1^+$ ($\tilde{\chi}_1^+ \rightarrow f\tilde{\chi}_1^0$) as well. The BRs of the Gtt, Gbb and Gtb decays are all add up to unity. The observed and expected limits for an almost massless neutralino and three gluino mass scenarios are shown in Figure 7.35a in the $\text{BR}(\tilde{g} \rightarrow \bar{t}t\tilde{\chi}_1^0) - \text{BR}(\tilde{g} \rightarrow \bar{b}b\tilde{\chi}_1^0)$ plane with the Gtb BR being equal to:

$$\text{BR}(\tilde{g} \rightarrow \bar{t}b\tilde{\chi}_1^+) = 1 - \text{BR}(\tilde{g} \rightarrow \bar{t}t\tilde{\chi}_1^0) - \text{BR}(\tilde{g} \rightarrow \bar{b}b\tilde{\chi}_1^0). \quad (7.8)$$

The exclusion limits are weaker around the bottom-left corner that corresponds to 100% Gtb decay as the analysis is optimised only for Gtt and Gbb decays. Furthermore, be-

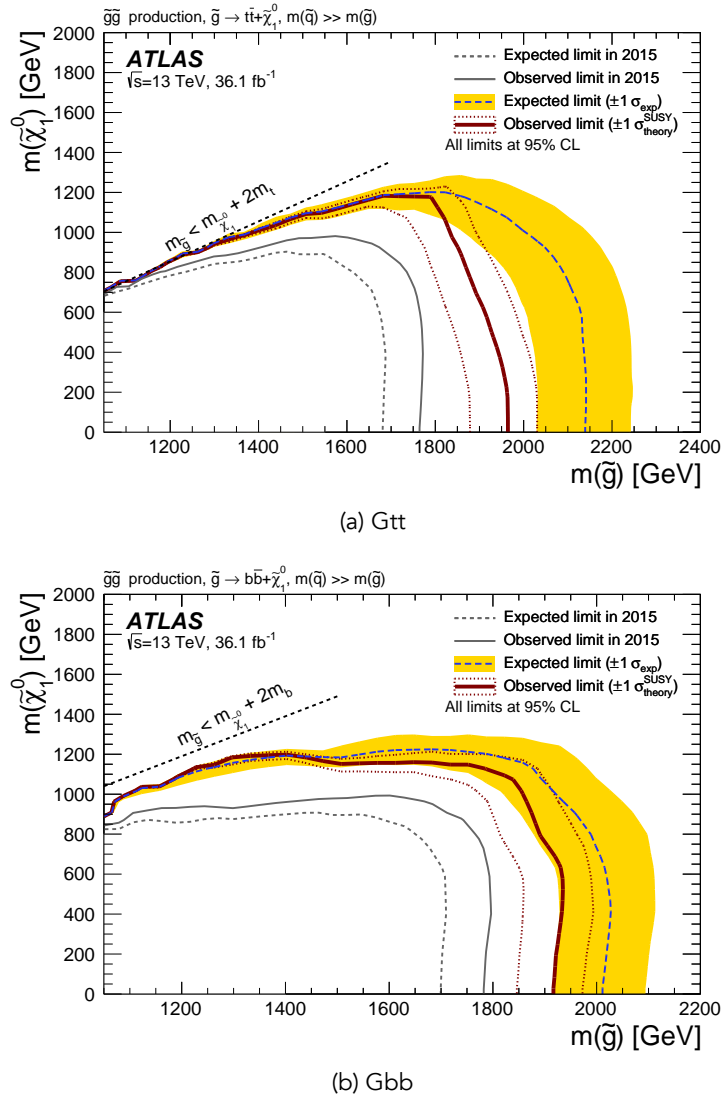


Figure 7.33: Exclusion limits for the (a) Gtt and (b) Gbb models derived using the statistical combination of all the multi-bin SRs. The dashed lines show the expected limits along with the impact of all the systematic uncertainties apart from the signal cross-section uncertainty. The solid lines show the observed limit along with the impact of the cross-section uncertainty of the SUSY signals. The expected and observed limits from the equivalent search using only 2015 data are also shown [164]. Figures published in [4].

sides the sensitivity on the whole plane for the 1.8 TeV \tilde{g} scenario, the data excess in the SR-0L-HH and SR-1L-HI bins suppresses the observed limit and models with high Gtb BR are surviving.

Similar results are shown in Figure 7.35b for a fixed \tilde{g} mass at 1.9 TeV and three $m(\tilde{\chi}_1^0)$ scenarios. For $\tilde{\chi}_1^0$ masses up to about 600 GeV there is exclusion sensitivity to almost all the plane, due to the data excess though a weaker observed limit is derived. For example, only decays with high Gtt and Gbb BRs are excluded for $m(\tilde{\chi}_1^0) = 600$ GeV.

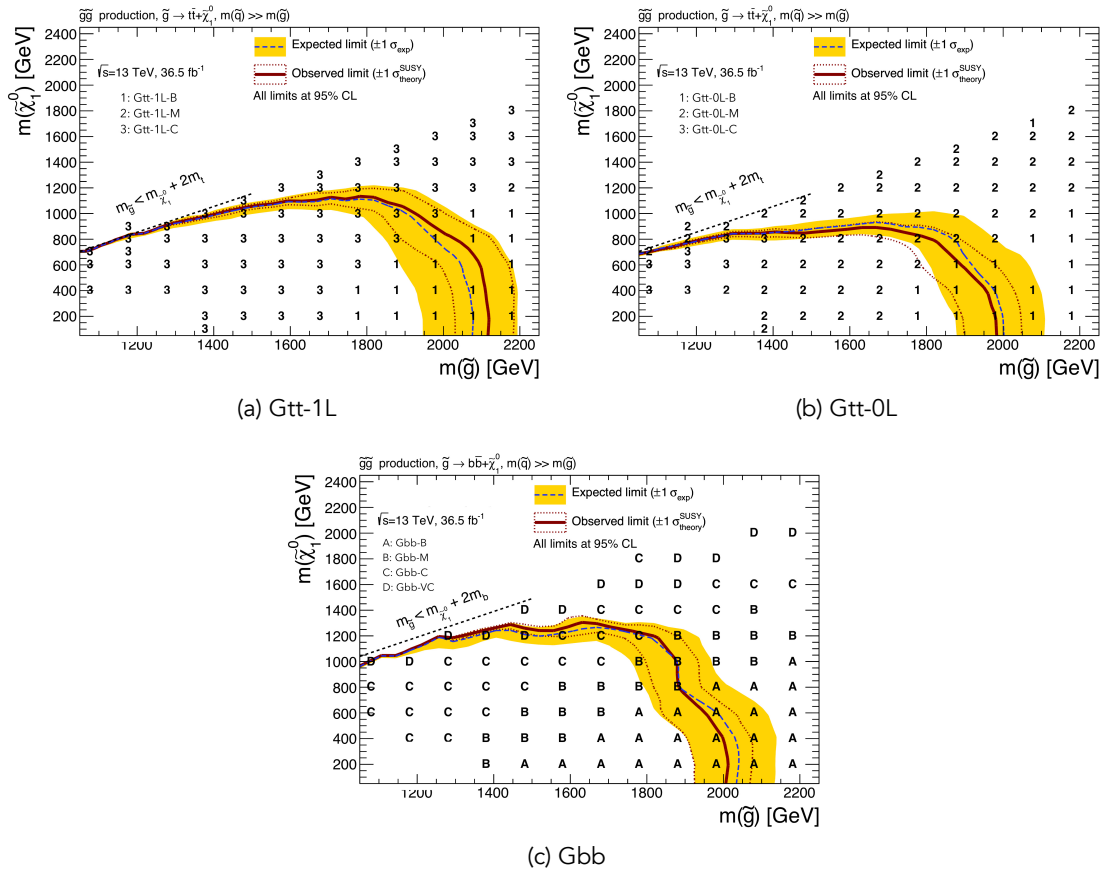


Figure 7.34: Exclusion limits for the (a) and (b) Gtt and (c) Gbb models derived using the cut-and-count SRs. The dashed lines show the expected limits along with the impact of all the systematic uncertainties apart from the signal cross-section uncertainty. The solid lines show the observed limit along with the impact of the cross-section uncertainty of the SUSY signals. Figures courtesy of the ATLAS Collaboration.

7.9.2 Model-independent Limits

Finally yet importantly, the results are used to place limits in BSM signals without any particular model assumption. In particular, a general BSM signal is considered and 95% CL upper limits are placed on its possible event yield. These can be translated in upper limits on the so-called *visible*¹ BSM cross-section by dividing them with the integrated luminosity. The limits presented in this section are placed by performing the discovery fit on the cut-and-count SRs only as any statistical combination assumes the the knowledge of the signal distribution over the corresponding bins in contrast to the model-independent concept. The limits are presented in Table 7.14.

¹The visible cross-section is defined as the product of the production cross-section, the acceptance and efficiency of a signal.

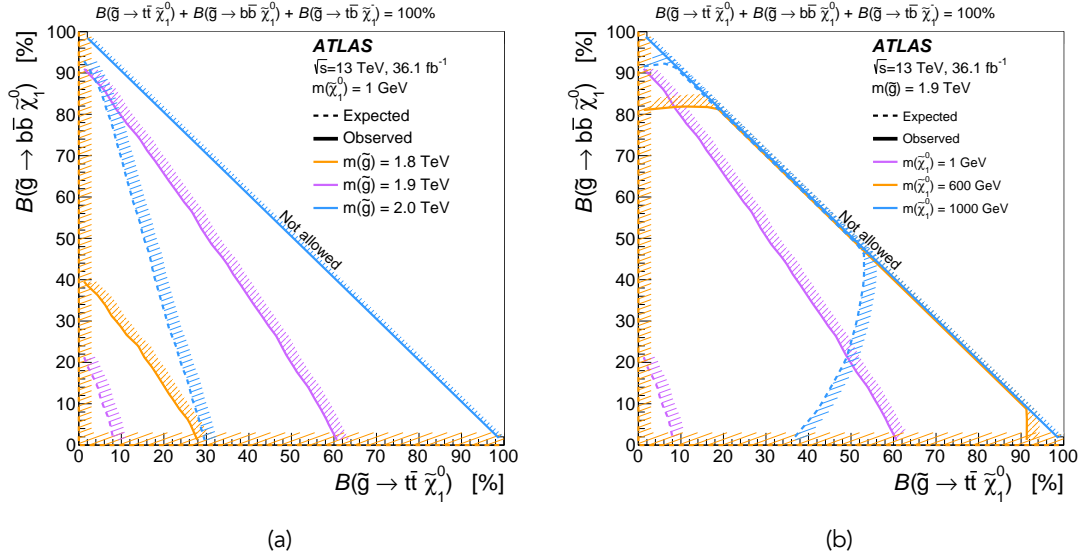


Figure 7.35: Exclusion limits for the variable BR model for (a) an almost massless $\tilde{\chi}_1^0$ and various \tilde{g} masses and (b) for 1.9 GeV \tilde{g} and various $\tilde{\chi}_1^0$ masses. The limits are derived using the multi-bin SRs. The dashed (solid) lines show the expected (observed) limits. The hashing indicates which side of the line is excluded. Figures published in [4].

Table 7.14: Model-independent limits at 95% CL: the discovery p-value (truncated at 0.5) and the equivalent significance ($p_0(Z)$), the upper-limit on the visible BSM cross-section (σ_{vis}^{95}) and the observed and expected number of BSM events for each cut-and-count SR ($S_{\text{obs/exp}}^{95}$). Table published in [4].

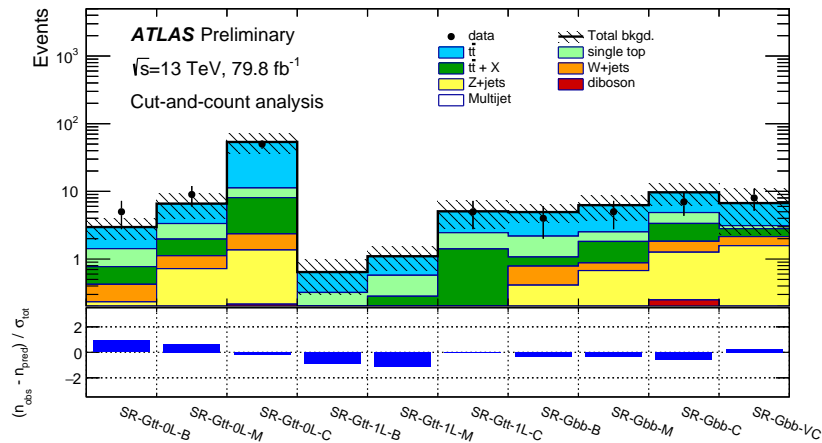
Signal channel	$p_0(Z)$	σ_{vis}^{95} [fb]	S_{obs}^{95}	S_{exp}^{95}
SR-Gtt-1L-B	0.50 (0.00)	0.08	3.0	$3.0_{-0.0}^{+1.0}$
SR-Gtt-1L-M	0.34 (0.42)	0.11	3.9	$3.6_{-0.4}^{+1.1}$
SR-Gtt-1L-C	0.50 (0.00)	0.13	4.8	$4.7_{-0.9}^{+1.8}$
SR-Gtt-0L-B	0.32 (0.48)	0.13	4.8	$4.1_{-0.6}^{+1.7}$
SR-Gtt-0L-M	0.25 (0.69)	0.21	7.5	$6.0_{-1.4}^{+2.3}$
SR-Gtt-0L-C	0.50 (0.00)	0.39	14.0	$17.8_{-4.5}^{+6.6}$
SR-Gbb-B	0.50 (0.00)	0.13	4.6	$4.6_{-1.0}^{+1.7}$
SR-Gbb-M	0.50 (0.00)	0.12	4.4	$5.0_{-1.1}^{+1.9}$
SR-Gbb-C	0.50 (0.00)	0.18	6.6	$6.9_{-1.8}^{+2.7}$
SR-Gbb-VC	0.50 (0.00)	0.08	3.0	$4.6_{-1.3}^{+2.0}$

7.10 Conclusion

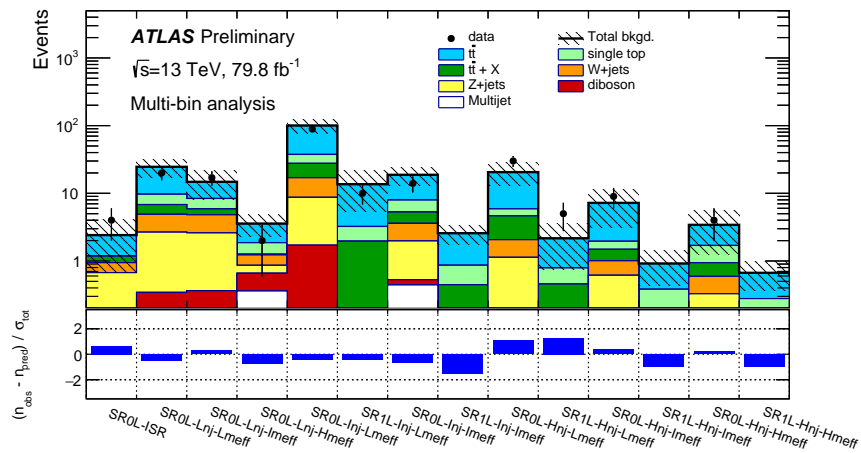
In this chapter a search for the production of gluinos decaying via third-generation squarks was presented. The dataset used was collected during 2015 and 2016 by the ATLAS detector and corresponds to 36.1 fb^{-1} of $\sqrt{s} = 13 \text{ TeV}$ pp collisions data produced by the LHC. The analysis was optimised based on the simplified Gtt and Gbb models and the final states explored are comprised of multiple jets, of which at least three should have been identified to originate from the hadronisation of a b-quark, large missing energy and potentially the presence of leptons. Two SR design strategies have been followed: overlapping cut-and-count SRs with wide kinematic selections are assessing the compatibility of the observed data with the SM background while orthogonal multi-bin regions are placing tight exclusion limits on the models under study. In all cases the dominant SM background is the $t\bar{t}$ production in association with extra jets and its normalisation has been extracted from data in dedicated control regions.

The data in all the SRs were kept out of the study until the background was estimated and validated. As no significant excess has been found in any cut-and-count SR after the unbinding, the multi-bin regions are used to place exclusion limits on the simplified SUSY models. In particular, for $\tilde{\chi}_1^0$ masses below 300 GeV \tilde{g} masses up to 1.97 (1.92) are excluded for the Gtt (Gbb) model. These results improve upon the exclusion limits obtained with the 2015 dataset alone. Finally, limits towards more realistic SUSY scenarios where the \tilde{g} undergoes a three-body decay to one, two or three top quarks, along with b-quarks and the LSP, are also placed.

Motivated by the mild data-excess observed in SR-0L-HH and SR-1L-HI the analysis was reiterated – using exactly the same selections described here in order not to introduce any bias – in 2018 including the 2017 LHC dataset as well [185]. The integrated luminosity was more than doubled (79.9 fb^{-1}) thus a much more reliable, in terms of statistics, dataset was used. The background-only fit results extrapolated to the various SRs are presented in Figures 7.36a and 7.36b for the cut-and-count and multi-bin regions respectively. No significant excess of data above the expected SM background is observed overall and especially in the SR-0L-HH and SR-1L-HI thus the excess seen previously in Figure 7.32a is regarded as a statistical fluctuation. Moreover, updated results using the full LHC Run 2 dataset (139 fb^{-1}) are expected to be published during 2020.



(a) Cut-and-count



(b) Multi-bin

Figure 7.36: Background-only fit results extrapolated to the (a) cut-and-count and (b) multi-bin SRs for the analysis using the 2015-17 dataset. The top panel shows the observed number of events and the predicted background, the bottom panel shows the observed significance in each region. [185]



8. Sbottom Search

Searching for sbottom quark pair production in final states containing Higgs bosons, b-jets and missing energy in the full LHC Run 2 dataset

8.1 Introduction

The motivation and potential for discovering sbottom squarks at the LHC has been highlighted in Section 2.3. The ATLAS collaboration has been searching for them since the start of the LHC Run 2 period in minimal decay chains and final states [186]. Currently, by exploiting the statistical power of the full Run 2 dataset, powerful searches beyond the direct decays (e.g. $\tilde{b}_1 \rightarrow b\tilde{\chi}_1^0$) are possible.

This chapter describes the search for the pair production of sbottom quarks decaying in a complex scenario via an intermediate $\tilde{\chi}_2^0$ state that gives rise to Higgs bosons ($\tilde{\chi}_2^0 \rightarrow h\tilde{\chi}_1^0$). Particularly, the dominant decay of this Higgs boson to b-quarks is considered, and a unique final state characterised by the presence of up to six b-jets, zero charged leptons and large missing energy is studied for SUSY signatures.

This chapter is organised as follows: in Section 8.2 the SUSY model in search is described and in Section 8.3 the data and simulation samples used are presented. In Section 8.4 the event selection applied in search of the signal is described and in Section 8.5

the background estimation procedures are summarised. The systematics uncertainties of the analysis are detailed in Section 8.6 while the results and interpretation can be found in Section 8.7 and Section 8.8 respectively. Eventually, concluding remarks are made in Section 8.9.

8.2 SUSY Model

8.2.1 Description

In general, the SUSY search program of the ATLAS collaboration is designed in a bottom-up fashion; the searches are categorised based on final states instead of SUSY models. With this approach, particular theoretical considerations can be omitted and a general discovery-oriented search is conducted. However, it is always useful to know in which MSSM scenarios the search model appears. This eventually helps on the systematic study of phenomenologically realistic models, such as the pMSSM [86, 187].

As discussed already in the context of Gtb model of Chapter 7, in MSSM cases with higgsino-like LSP (Table 2.2), the mass splitting between the gaugino mass eigenstates is at $\mathcal{O}(100 \text{ MeV} - 10 \text{ GeV})$. As a consequence, the decays of $\tilde{\chi}_2^0$ to $\tilde{\chi}_1^0$ are mediated via virtual Z bosons while the decay via the Higgs boson is heavily suppressed. On the other hand, in cases in which the mixing of the lightest neutralinos and charginos with the higgsino is small, there is no such mass degeneracy. In particular, in scenarios in which the LSP is a bino-like state and the Next-to-LSP (NLSP) a wino-like state, the decays of $\tilde{\chi}_2^0$ to the LSP are suppressed via the Z boson thus enhanced via the Higgs boson [188]. It's noteworthy that neutralino decays are the main source of Higgs boson within the MSSM [189].

This behavior is moreover seen in pMSSM scans after imposing the constraints implied by the LHC Run 1 searches. In Figure 8.1a, a sample of 300,000 pMSSM models, used by the ATLAS Run 1 SUSY summary paper [86], which provide high $\text{BR}(\tilde{\chi}_2^0 \rightarrow h\tilde{\chi}_1^0)$ are studied for the LSP type. It is found that all the models have indeed a bino-like LSP, while in Figure 8.1b the type of $\tilde{\chi}_2^0$ – a prevalent NLSP – is identified for the surviving models as a pure-higgsino, pure-wino or a mixture of them. Due to limited statistical power and specific tailored searches targeting decay chains involving Higgs bosons, there are models of bino-like LSP with high $\text{BR}(\tilde{\chi}_2^0 \rightarrow h\tilde{\chi}_1^0)$ that the experiments weren't sensitive to so far.

In this analysis therefore, an uncovered signature of pair produced sbottom quarks is targeted. The simplified model used assumes that the lightest sbottom quarks and the two lightest neutralino mass eigenstates are the only SUSY particles accessible at the LHC energy. The \tilde{b}_1 is assumed to decay with 100% BR to a b-quark and a $\tilde{\chi}_2^0$. Each of the $\tilde{\chi}_2^0$ consecutively decays with 100% BR to a Higgs boson and a $\tilde{\chi}_1^0$, the LSP. The Feynman diagram of the simplified modes is shown in Figure 8.2.

The Higgs bosons of the model are SM-like. The mass is set to 125 GeV and the

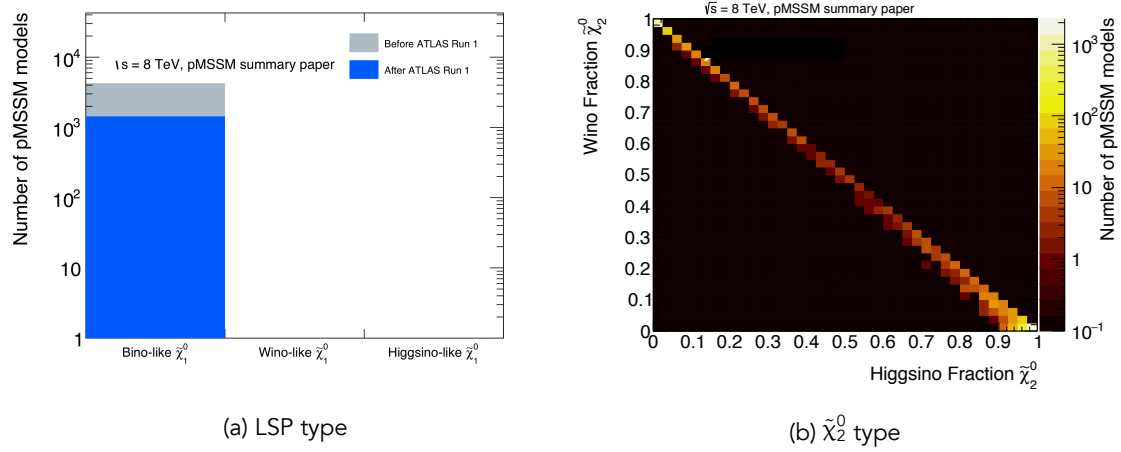


Figure 8.1: (a) The LSP ($\tilde{\chi}_1^0$) type of the pMSSM models offering $\text{BR}(\tilde{\chi}_2^0 \rightarrow h\tilde{\chi}_1^0) > 0.8$ before and after the ATLAS Run 1 constrains. (b) The $\tilde{\chi}_2^0$ type of the pMSSM models of (a) after the ATLAS Run 1 constrains. Both figures are made using the sample of 300,000 pMSSM models studied at [86].

decay BRs are the ones listed in Table 1.2. However, only the dominant and relevant decay channels are further considered: $b\bar{b}$, W^+W^- , $\tau^+\tau^-$, ZZ . The SM-like Higgs boson can be regarded as the lightest of the neutral Higgs bosons introduced in the MSSM.

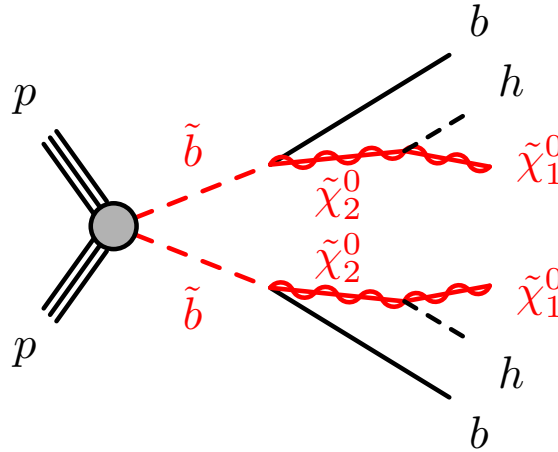


Figure 8.2: The Feynman diagram of the model targeted by the analysis. Sbottom quarks are produced in pairs and each one decays to $b\tilde{\chi}_2^0$. Each $\tilde{\chi}_2^0$ decays to $h\tilde{\chi}_1^0$. All BRs are set to 100%. Figure published in [5].

8.2.2 Signal Grids

The targeted SUSY model of Figure 8.2 has three free parameters: the masses of the \tilde{b}_1 , $\tilde{\chi}_2^0$ and $\tilde{\chi}_1^0$. To reduce its dimensionality and make the analysis feasible, two independent mass hierarchy assumptions have been considered thus two two-dimensional models

are studied for different $m(\tilde{b}_1)$ and $m(\tilde{\chi}_2^0)$ scenarios. These are described below:

1. **DM130 Grid:**

In the first set of models, a fixed mass difference between the neutralinos ($\tilde{\chi}_1^0$ and $\tilde{\chi}_2^0$) is considered and set to 130 GeV. This assumption ensures the production of an on-shell Higgs boson by the decay $\tilde{\chi}_2^0 \rightarrow h\tilde{\chi}_1^0$. The masses of the \tilde{b}_1 and $\tilde{\chi}_2^0$ vary in the range of 400 to 1500 GeV and 150 to 930 GeV, respectively, and all the model-points considered are shown in Figure 8.3a. $\tilde{\chi}_2^0$ mass scenarios below ~ 150 GeV fall out of the scope of this analysis as they result, due to the kinematic configuration, in a final state with little missing energy.

The same model of sbottom quark production with the same $\Delta m(\tilde{\chi}_2^0, \tilde{\chi}_1^0)$ has been also recently studied by the CMS collaboration using data collected in 2016 and 2017 (77.5 fb^{-1}) [190]. In that case though, the $h \rightarrow \gamma\gamma$ decay mode is exploited. This has the virtue of an additional particle in the final state that can be used for triggering, allowing the probe of lower $\tilde{\chi}_2^0$ masses. Yet, the small $\text{BR}(h \rightarrow \gamma\gamma)$ is limiting the analysis sensitivity to high \tilde{b}_1 masses. In particular, after no excess above the expected SM background has been found in data, \tilde{b}_1 masses up to 530 GeV have been excluded for an almost massless LSP.

2. **N60 Grid:**

In the second set of models, the mass of the $\tilde{\chi}_1^0$ has been fixed to 60 GeV motivated by DM relic density measurements. Generally, bino-like LSP scenarios tend to overproduce DM [191], and in order to keep its abundance within the current measured limits, an efficient annihilation mechanism is needed. An appealing case is the Higgs-pole annihilation where the LSP should have mass $m(\tilde{\chi}_1^0) \simeq m(h)/2 = 60$ GeV. The masses of the \tilde{b}_1 and $\tilde{\chi}_2^0$ considered vary in the range of 300 to 1600 GeV and 200 to 1595 GeV respectively, as shown in Figure 8.3b.

This model has been previously studied by the ATLAS collaboration using the Run 1 dataset [162]. The lower collision energy along with the limited statistics, that prevented selections with high b-jets multiplicities, resulted in much weaker sensitivity than the one presented in this work. In particular, exclusion limits were placed to \tilde{b}_1 masses up to 750 GeV.

8.3 Data, Triggers and Simulations

The dataset used in this analysis corresponds to the LHC Run 2 pp collision data collected by the ATLAS detector during the years 2015 to 2018. The integrated luminosity corresponds to $139 \pm 2.4 \text{ fb}^{-1}$.

The events used are mainly collected using E_T^{miss} triggers (see Section 3.2.5) with online thresholds varying from 70 to 110 GeV. The exact E_T^{miss} trigger chains used for this analysis are listed in Table 8.1. A procedure similar to the one described in Section 7.3 is employed to determine the offline E_T^{miss} threshold to ensure fully efficient

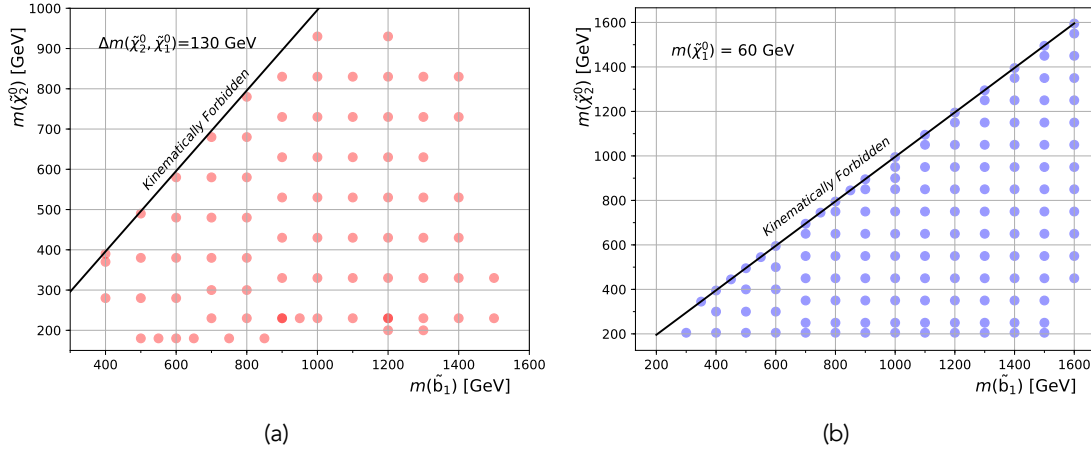


Figure 8.3: The model-points considered for the (a) DM130 and (b) N60 mass hierarchy assumptions. The figures comprise an original work of the author.

trigger decisions. The ratio of data events firing the $E_{\text{T}}^{\text{miss}}$ trigger as function of the offline calculated $E_{\text{T}}^{\text{miss}}$ is shown for the 2017 data in Figure 8.4 in the relevant phase space. The offline threshold is chosen at 250 GeV.

Data period	$E_{\text{T}}^{\text{miss}}$ Trigger
2015	HLT_xe70_mht_L1XE50
2016 A-D3	HLT_xe90_mht_L1XE50
2016 D4-F1	HLT_xe100_mht_L1XE50
2016 F2-	HLT_xe110_mht_L1XE50
2017 B1-D5	HLT_xe110_pufit_L1XE55
2017 D6-	HLT_xe110_pufit_L1XE50
2018 B-C5	HLT_xe110_pufit_xe70_L1XE50
2018 C6-	HLT_xe110_pufit_xe65_L1XE50

Table 8.1: The list of $E_{\text{T}}^{\text{miss}}$ triggers per data-taking period used for this analysis.

Additionally, in order to select the low- $E_{\text{T}}^{\text{miss}}$ two-lepton events required for the background estimation purposes described in Section 8.5.3, few single-lepton triggers are used. These are fully efficient after requiring the lepton p_{T} to be greater than 27 GeV.

MC simulated events are used to model both the SUSY signal and the SM background processes. These are generated and detector-simulated as described in Sections 1.4 and 3.2.6, and afterwards are reconstructed as described in Chapter 5. The background processes considered in this analysis comprise of:

1. top quark pair production ($t\bar{t}$),
2. single-top quark production,
3. Z and W bosons production in association with jets (Z/W + jets),

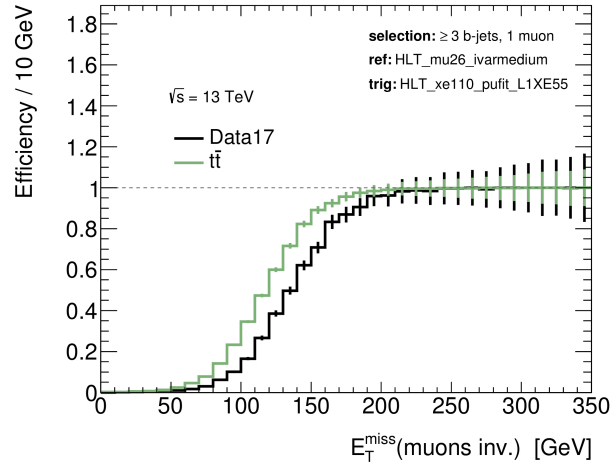


Figure 8.4: The trigger efficiency curve for the 2017 dataset and a $t\bar{t}$ simulated sample in the relevant phase space (≥ 4 jets and ≥ 3 b-jets). The E_T^{miss} shown on the horizontal axis is the offline reconstructed but considering the muons as invisible particles to compensate the bias introduced by the lack of MS information on the online E_T^{miss} calculation. Figure courtesy of the ATLAS Collaboration.

4. top quark pair production in association with vector bosons ($t\bar{t}V$) or Higgs bosons ($t\bar{t}H$) and
5. diboson production (ZZ, ZW, WW).

The contribution of other background sources such as multi-jet production, three/four top quark or three vector boson production have been found to be negligible and are not considered further. In Table 8.2 the programs used for the hard-scatter generation, parton showering, hadronisation and underlying event simulation are listed for the signal and each of the backgrounds considered. All the simulated processes are normalised to the best available theoretically calculated cross-section. Further technical details, along with references, on the production of the simulated samples can be found in Appendix B.

Table 8.2: List of the event generation, parton shower, hadronisation and underlying event programs used for the different physics processes. The tunes and the PDF set used are also listed. In the last column, the accuracy of the theoretical cross-section used to normalise each sample is quoted.

Process	Generator	PS + Hadronisation + UE	Tune	PDF Set	cross-section Order
SUSY signal	MadGraph5_aMC@NLO v2.2	Pythia v8.2			NNLO _{approx.} +NNLL [192–195]
$t\bar{t}$	Powheg-Box v2	Pythia v8.2	A14	NNPDF23LO	NNLO+NNLL [175, 176]
Single-top					
$t\bar{t}V$	MadGraph5_aMC@NLO v2.3	Pythia v8.2			NLO [59]
$t\bar{t}H$					
Z/W + jets	Sherpa v2.2.1		Default	NNPDF30NNLO	NNLO [178]
Diboson					NLO [196]

8.4 Signal Event Selection

In this section, first, the physics object used in this analysis are defined and the event selection criteria employed to target the SUSY signal are following. Similarly to the gluino search of Chapter 7, two levels of the physics objects quality are defined, the `baseline` and `signal` and their definitions are listed in Table 8.3.

Table 8.3: The selection criteria of the `baseline` and `signal` physics objects used for this analysis.

Physics Object	Baseline Definition	Signal Definition
Jets	$p_T > 20 \text{ GeV}, \eta < 2.8$	$p_T > 30 \text{ GeV}$, JVT selection
b-Jets	-	$p_T > 30 \text{ GeV}, \eta < 2.5$
Electrons	<i>Loose Id</i> , $p_T > 4.5 \text{ GeV}, \eta < 2.47, z_0 \sin(\theta) < 0.5 \text{ mm}$	<i>Tight Id</i> , $p_T > 20 \text{ GeV}$, Fixed Isolation, $ d_0 /\sigma(d_0) < 5$
Muons	<i>Medium Id</i> , $p_T > 4 \text{ GeV}, \eta < 2.7, z_0 \sin(\theta) < 0.5 \text{ mm}$	$p_T > 20 \text{ GeV}$, Fixed Isolation, $ d_0 /\sigma(d_0) < 3$

The capability to select events that potentially originate from the SUSY model described in Section 8.2 is of primary importance, thus defines the general phase space explored. This is characterised by multiple b-jets, that can originate from both the decay of the sbottom and the Higgs boson, and large missing energy from neutralinos escaping detection. As only the dominant decay of the Higgs boson to b-quarks is targeted, events with leptons or taus are suppressed. In particular, events containing `baseline` leptons are suppressed as the lower p_T threshold compared to the `signal` definition provides a stronger veto. However, this is not the case for the auxiliary measurements needed to estimate the background, as described in Section 8.5, where events with leptons or low missing energy are used.

To target the different kinematic configurations occurring as function of the SUSY masses hierarchy, on both the DM130 and N60 model assumptions, three SRs are defined and described in Sections 8.4.2–8.4.4. Their definitions are optimised to maximise the expected discovery significance, described in Section 6.2.4, similarly to the cut-and-count SRs of Section 7.5. As always, in the context of this dissertation, the data in the SRs are kept blinded until the background is estimated and validated as described in Section 8.5.

8.4.1 Discriminating Variables

Several discriminating variables are defined both on the basis of kinematic properties of the `signal` objects, defined in Table 8.3, and on the event as a whole. Since the final state of this search is similar to the gluino search of Chapter 7, few variables are common while others go beyond naive definitions and demonstrate the developments over the last years of the Run 2 period of the LHC (e.g \mathcal{S}). The full list of variables used along with a short description of each one is following¹

¹The variable notation might slightly differ from the one of Chapter 7 in order to correspond to what is used for the publication of this work in [5].

- N_{jets} ($N_{\text{b-jets}}$): The number of jets (b-jets) of an event. As described above, large number of jets is expected on events originating from the SUSY model, in particular up to six b-jets (2 from the SUSY decay, 4 from the two Higgs decays) could be found. On the other hand, there are only few SM processes that can lead to such large jet multiplicities so this variable is a powerful discriminant.
- $p_{\text{T}}(\text{b}_1)$: The p_{T} of the leading tagged b-jet of the event. The b-jets originating from the decay of a SUSY particle (b_1) are expected to be more energetic than the ones from SM process (e.g. $\text{t}\bar{\text{t}}$). This is dictated by the mass hierarchy that place the SUSY particles higher than the SM ones. The distribution of the $p_{\text{T}}(\text{b}_1)$ of a SUSY signal against the SM background can be seen in Figure 8.5a.
- $E_{\text{T}}^{\text{miss}}$: The missing energy of the event, reconstructed as described in Section 5.8. Events from the SUSY model are expected to have larger $E_{\text{T}}^{\text{miss}}$ compared to SM processes as it is apparent in Figure 8.5b.
- m_{eff} : The effective mass of an event, in the context of this analysis, is defined as the scalar sum of all the jets p_{T} and the $E_{\text{T}}^{\text{miss}}$ of the event:

$$m_{\text{eff}} = \sum p_{\text{T}}^{\text{jet}} + E_{\text{T}}^{\text{miss}} \quad (8.1)$$

The sbottom quarks are expected to be as heavy as $\mathcal{O}(1 \text{ TeV})$, their decays lead to energetic products thus the m_{eff} is expected to have large values for the SUSY model compared to the SM background. This is apparent in Figure 8.5c.

- \mathcal{S} : The *object-based $E_{\text{T}}^{\text{miss}}$ significance* has been originally developed to discriminate events with fake $E_{\text{T}}^{\text{miss}}$, arising from mismeasured particles, from events with genuine $E_{\text{T}}^{\text{miss}}$ from particles escaping detection (e.g. $\nu, \tilde{\chi}_1^0$) [197]. It is defined as:

$$\mathcal{S} = \sqrt{\frac{|\mathbf{p}_{\text{T}}^{\text{miss}}|^2}{\sigma_{\text{L}}^2(1 - \rho_{\text{LT}}^2)}}, \quad (8.2)$$

where σ_{L} is the momentum resolution of the detector, parallel to the $\mathbf{p}_{\text{T}}^{\text{miss}}$ (longitudinal) and for a given p_{T} and $|\eta|$, taking under consideration all the different particles contributing to the $\mathbf{p}_{\text{T}}^{\text{miss}}$ calculation (Eq. 5.4). The ρ_{LT} is a correlation factor between the σ_{L} and its transverse component. The momentum resolution of the detector is, in general, extracted from MC simulations that well reproduce the resolution measured in data. For jets however, which is the main contributing object of this analysis, it is defined as the maximum between the one extracted from the simulation and the one measured in data.

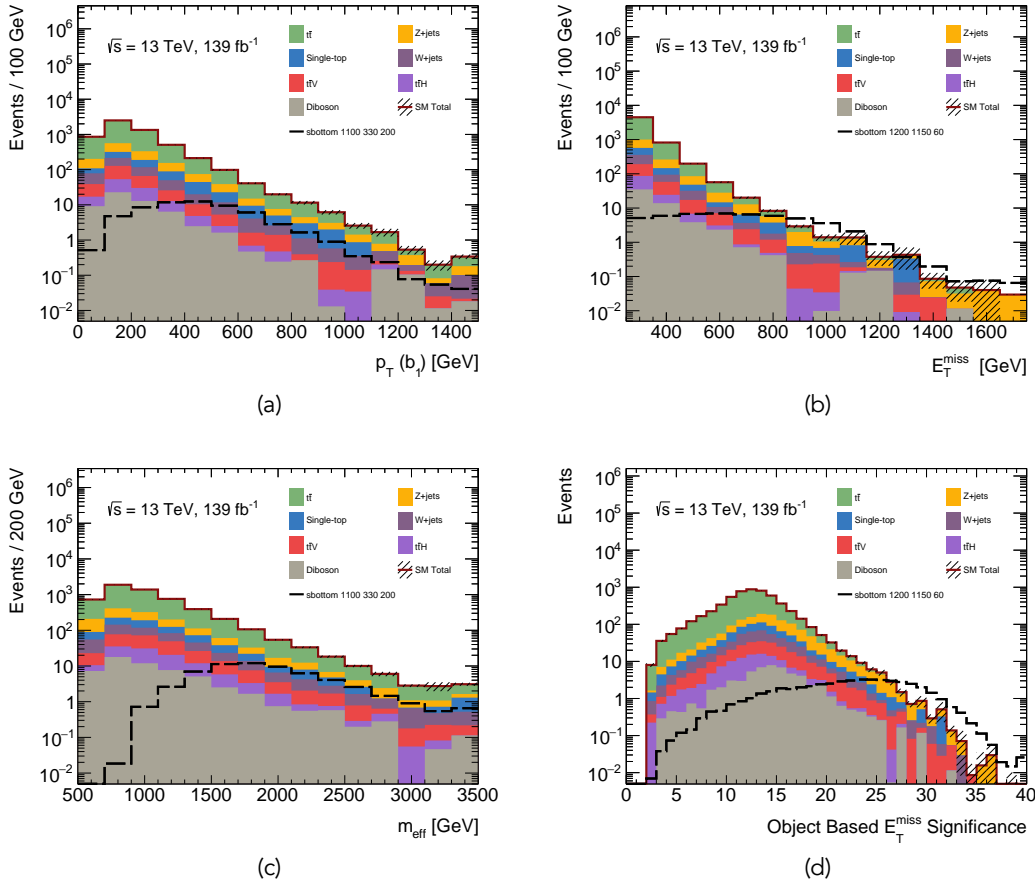


Figure 8.5: Distributions of $p_T(b_1)$, E_T^{miss} , m_{eff} and \mathcal{S} for simulated events of both the SM background and the SUSY signal in a loose selection relevant to the analysis ($N_{\text{leptons}}(\text{baseline}) = 0$, $N_{\text{jets}} > 4$, $N_{\text{b-jets}} \geq 3$, $E_T^{\text{miss}} > 250$ GeV). Only statistical uncertainties are shown. The figures comprise an original work of the author.

In an event-by-event basis, the \mathcal{S} quantifies the probability that the reconstructed E_T^{miss} is consistent with the zero real E_T^{miss} hypothesis, i.e. the reconstructed E_T^{miss} is consistent with the finite momentum resolution and particle identification inefficiencies of the detector. A high value of \mathcal{S} indicates that an event might contain a particle that escaped detection.

Beyond its original purpose, the \mathcal{S} is a powerful discriminant between processes with moderate and high E_T^{miss} . For instance, it can efficiently discriminate SUSY processes from irreducible SM backgrounds where moderate E_T^{miss} arise from neutrinos in the final state, as it can be seen in Figure 8.5d.

Previous SUSY searches of the ATLAS and CMS experiments [198, 199] have defined the E_T^{miss} significance as just the ratio of E_T^{miss} over the energy resolution:

$$\frac{E_T^{\text{miss}}}{\sigma_{\text{calo}}}, \quad (8.3)$$

based on the assumption that the E_T^{miss} is calculated by calorimeter signals only. The energy resolution then, following the stochastic nature of the measurement, can be approximated by:

$$\sigma_{\text{calo}} = \kappa \sqrt{\sum E_T}, \quad (8.4)$$

where κ has been measured to ~ 0.5 for the ATLAS detector during Run 1 [200]. However, the above definition is agnostic on any measurement beyond the calorimeter or directional correlations between them. The improvement introduced by \mathcal{S} against the naive definition of Eq. 8.3 or the bare E_T^{miss} has been demonstrated to provide increased significance to discover the complex sbottom SUSY signal under study in the SM background, as seen in Figure 8.6.

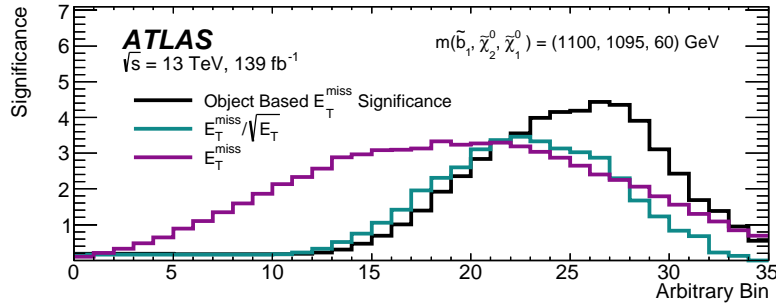


Figure 8.6: Integrated expected discovery significance calculated for a sbottom signal against all the SM background. The phase space shown is defined by the SRC (Section 8.4.4) before the \mathcal{S} selection. Figure published in [5].

- $\Delta\phi(j_1, E_T^{\text{miss}})$: The azimuthal angle between the leading (non-b-tagged) jet and the $\mathbf{p}_T^{\text{miss}}$. Similarly to the Gbb-VC SR of Chapter 7, this variable – along with a high p_T selection on the leading jet – is used to select events where the $\mathbf{p}_T^{\text{miss}}$ is back-to-back with the leading jet, effectively topologies where very energetic initial-state radiation is recoiling against the SUSY system.
- $\min[\Delta\phi(\text{jet}_{1-4}, \mathbf{p}_T^{\text{miss}})]$: The minimum azimuthal angle between the first four leading jets and the $\mathbf{p}_T^{\text{miss}}$. As in the gluino search case, this variable proves to be a powerful discriminating tool against multi-jet background events containing large amount of fake E_T^{miss} . Studies using data-driven multi-jet estimations, summarised in Appendix C, indicate that a selection of $\min[\Delta\phi(\text{jet}_{1-4}, \mathbf{p}_T^{\text{miss}})] > 0.4$ rad is sufficient to reduce the multi-jet background to negligible amounts and it applied to all the 0-lepton regions hereafter, unless it's explicitly stated.

8.4.2 Signal Region A

The *Signal Region A* (SRA) targets the *bulk* region of both signal grids (DM130 and N60). The term *bulk* refers to the moderate to high mass splitting cases between the \tilde{b}_1 and $\tilde{\chi}_2^0$ and includes the majority of the model-points shown in Figures 8.3a and 8.3b. In these cases the b-jets from both the decay of the \tilde{b}_1 and Higgs boson are highly energetic, leaving distinct signatures into the detector. This leads to final states with up to six b-jets (two from the \tilde{b}_1 and four from the two Higgs decays). Additionally, large missing energy is expected from the $\tilde{\chi}_1^0$ that escapes detection. The kinematic configuration of the SUSY model that the SRA targets is shown in Figure 8.7a.

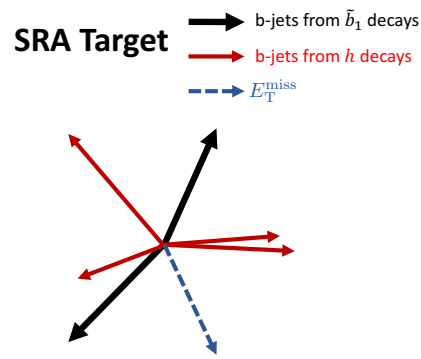
8.4.2.1 Max-Min Algorithm

In the six b-jets kinematic configuration the SRA targets, it is crucial to be able to identify the ones originating from the Higgs bosons decays. This will eventually allow the reconstruction of the Higgs candidate and the application of a selection on its invariant mass can further reduce the SM background. The identification of the Higgs candidate is performed by the *Max-Min* algorithm described in the following. It's important to be stressed that because of the limited statistics of the dataset only one of the two Higgs candidates is reconstructed. As it can be seen in Figure 8.8 the predicted number of events with more than four b-jets make any selection on them meaningless. The problem is mainly on the limited SM background that makes its trustful estimation, via the semi-data-driven techniques described in Section 8.5, impossible.

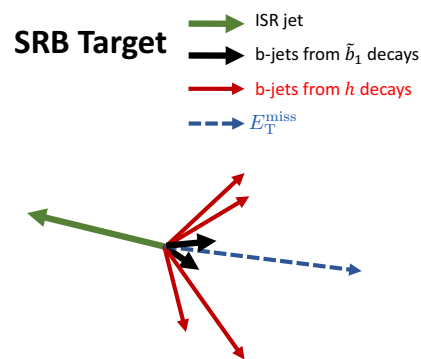
In order to select the Higgs decay products, the max-min algorithm is checking the spacial separation of the b-jets. In general, the two b-jets arising from the \tilde{b}_1 decay are expected to have larger spacial separation than the b-jets from the Higgs decay. The spacial separation in this context is defined as the distance in the $|\eta| - \phi$ plane, $\Delta R = \sqrt{\Delta|\eta|^2 + \Delta\phi^2}$. This has been identified in truth-level studies of the SUSY signals, as it can be seen in Figure 8.9.

The algorithm is executed in an event-by-event basis, by 1) iterating over all the available b-jets and identifies the pair with the maximum ΔR , this is regarded as originating from the \tilde{b}_1 decay. Afterwards, 2) among the remaining b-jets, it identifies the pair with the minimum ΔR , which is regarded as originating from the Higgs decay and its invariant mass can be calculated. Furthermore, 3) selection criteria are applied onto the two b-jet pairs identified from the iterating steps just described. These are two spacial separation and one invariant mass criteria and are described below:

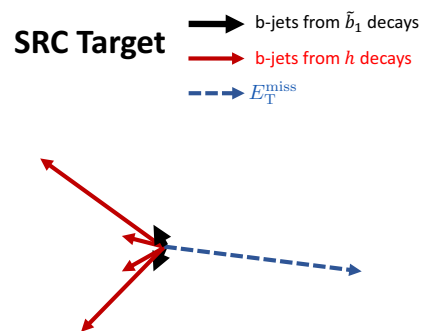
- $\Delta R_{\max}(b, b)$: The spatial separation of the two b-jets regarded as originating from the \tilde{b}_1 decay.
- $\Delta R_{\max-\min}(b, b)$: The spatial separation of the two b-jets regarded as originating from the Higgs decay.
- $m(h_{\text{cand}})$: The invariant mass of the two b-jets regarded as originating from the Higgs decay.



(a) bulk



(b) compressed DM130



(c) compressed N60

Figure 8.7: The different signal kinematic configurations targeted by the three Signal Regions. Figure published in [5].

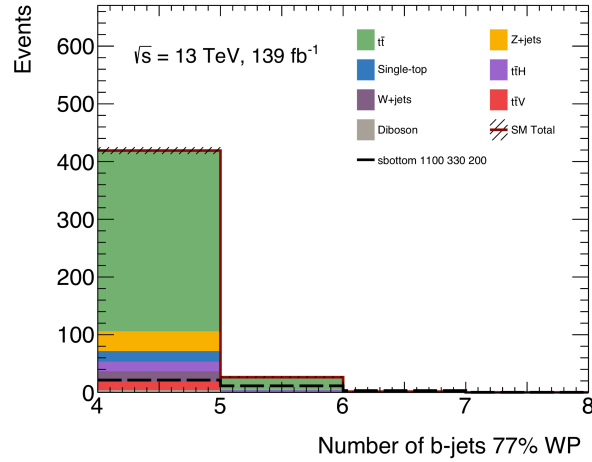


Figure 8.8: The distribution of $N_{b\text{-jets}}$ for simulated events of both the SM background and a signal model. It can be seen that the predicted number of events with higher than four b-jets is very limited. The loose 0-lepton selection applied is the same as in Figure 8.5 but the same conclusion is drawn for 1-lepton events that are used for background estimation purposes, as described in Section 8.5. Only statistical uncertainties are shown. The figure comprises an original work of the author.

After optimisation studies, it was found that increased sensitivity to the signal is provided by applying a selection on the $\Delta R_{\max}(b, b)$ and $\Delta R_{\max-\min}(b, b)$. In particular, events are discarded if the separation between the b-jets of the \tilde{b}_1 decay is less than 2.5 or between the b-jet pair of the Higgs decay is larger than 2.5. The effect for two signal models (one from the DM130, the other from the N60 scenario) in a relevant phase

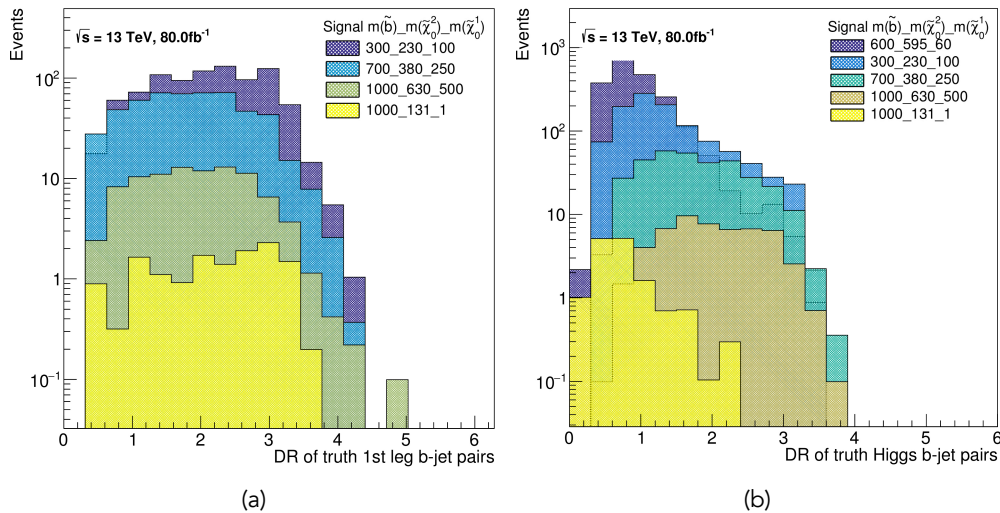


Figure 8.9: Truth-level distributions of the ΔR distance between the b-jets from (a) the \tilde{b}_1 decay and (b) the Higgs decay for few signal models. The two b-jets arising from the \tilde{b}_1 decay tend to have larger spacial separation than the b-jets from the Higgs decay. Figures courtesy of the ATLAS Collaboration.

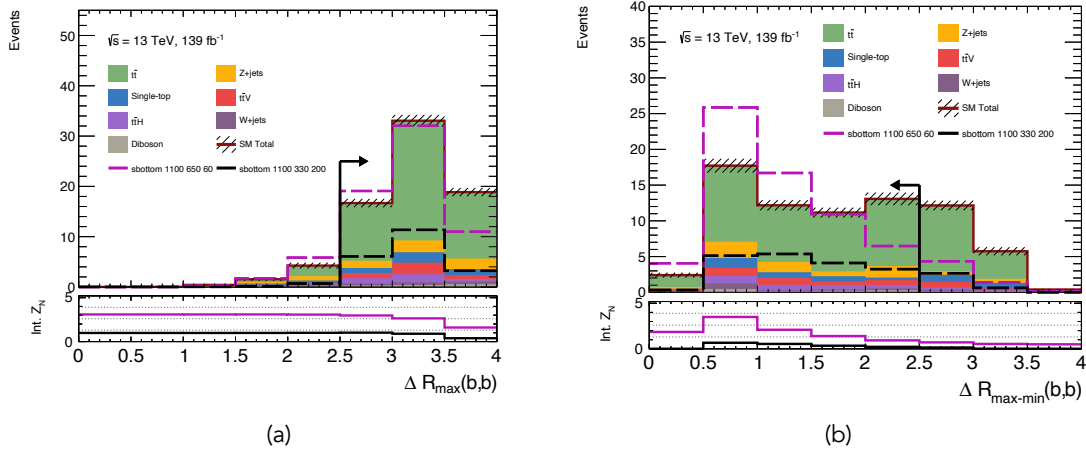


Figure 8.10: The distribution of (a) $\Delta R_{\max}(b, b)$ and (b) $\Delta R_{\max-\min}(b, b)$ variables for simulated events of the SM background and two signal cases. The increased significance provided by the ΔR selection of 2.5 is shown at the bottom panel of the plots. The selection applied is based on the one of Figure 8.5 but with $N_{\text{jets}} > 6$, $N_{b\text{-jets}} \geq 4$, $E_T^{\text{miss}} > 350$ GeV. Only statistical uncertainties are shown. The figures comprise an original work of the author.

space can be seen in Figure 8.10.

Finally, 4) an invariant mass selection on $m(h_{\text{cand}})$ is also applied to suppress SM background processes that mimic the signal but with b-jets that are not originating from a Higgs resonance. Even if the Higgs mass has been measured to 125 GeV, a selection just above 80 GeV is applied without upper bound. Detector resolution effects and incorrect identification by the max-min algorithm have found to deteriorate the $m(h_{\text{cand}})$ value thus a wide range is considered.

Overall, the max-min algorithm has been found to correctly select a $h \rightarrow b\bar{b}$ pairing, for a single Higgs decay, in about 20 to 40% of the cases. This value varies among the different signal models as the b-jet kinematics are dependent on the masses hierarchy.

8.4.2.2 Definition & Yields

Beyond the application of the max-min algorithm, distinct characteristics of the signal are used to discriminate from the SM background. As already mentioned, multiple highly energetic b-jets along with large missing energy are expected from the \tilde{b}_1 pair initiated decay chain. On the other hand, the SM processes are in general less energetic, so selections in high values of the above quantities can powerfully discriminate the signal. On event-level, these characteristics are all encapsulated in the m_{eff} definition thus this variable is the main discriminant of the SRA.

As the SRA targets the bulk of both the signal grids, a large parameter phase space with complex kinematics should be covered. It was observed that the various signal models can have quite different m_{eff} distributions, as it is shown in Figure 8.11. Therefore, three incremental and mutually exclusive sub-regions based on m_{eff} selections are defined. These are termed *low* (SRA-L) with values from 1 to 1.5 TeV, *moderate* (SRA-M) with values from 1.5 to 2 TeV and *high* (SRA-H) with values above 2.5 TeV. This *multi-bin* strategy – following the concept introduced for the gluino search in Section 7.5.2 – allows a smooth sensitivity gradient on the model parameter space and an eventually stronger model exclusion, in case of null-results, by statistical combination, as explained in Section 6.2.3.

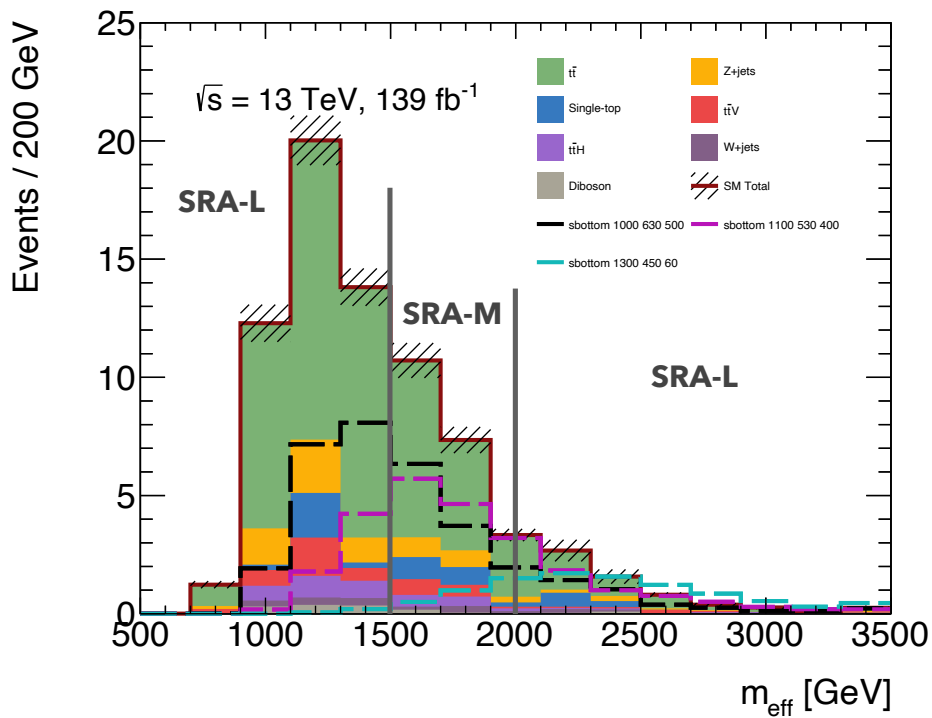


Figure 8.11: The distribution of the m_{eff} in simulated events for both the SM background and three signal models. The fact that the signal peaks are on different values led the design of the multi-bin regions. The selection applied is the same as in Figure 8.10. Only statistical uncertainties are shown. The figure comprises an original work of the author.

Additionally, a veto is applied to events containing taus, reconstructed as described in Section 5.6. This is beneficial as only about 2% of the Higgs decays will lead to taus¹ in contrast to the SM background where tau presence is not so rare. Indeed, it has been found, as presented in Figure 8.12, that larger fraction of the signal is passing the τ -veto compared to the background. This leads to further increased sensitivity.

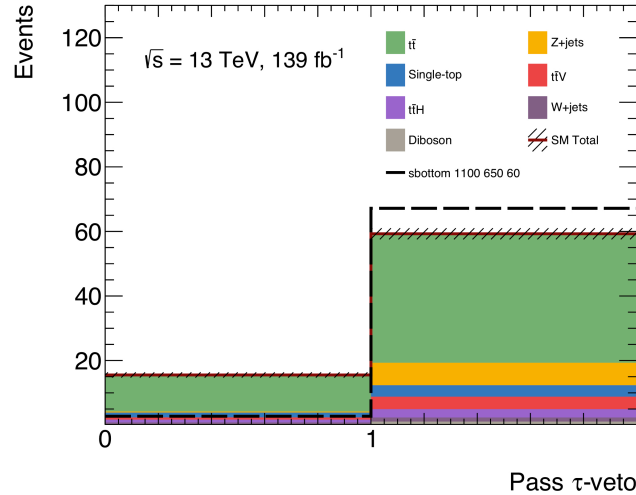
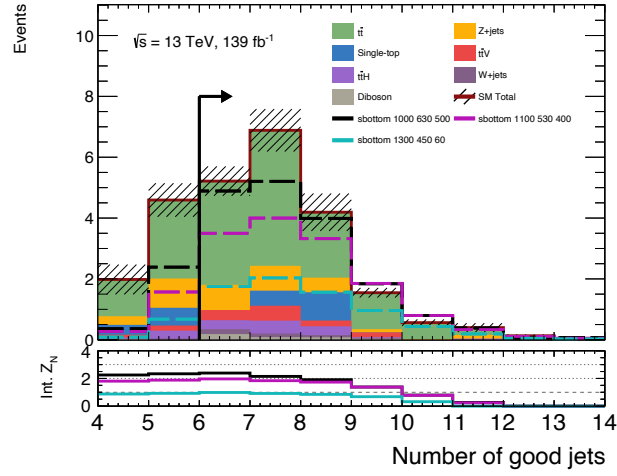


Figure 8.12: The number of events passing the tau-veto (1) versus the ones failing (0). The fraction of signal events failing the veto is negligible to all the models targeted by SRA. The selection applied is the same as in Figure 8.10. Only statistical uncertainties are shown. The figure comprises an original work of the author.

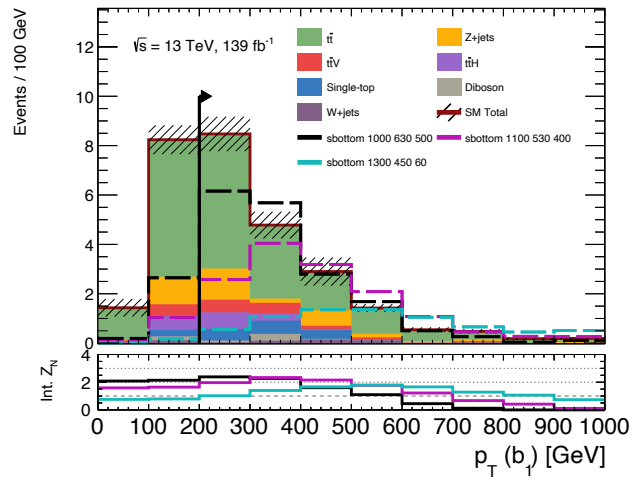
Signal benchmark models from the bulk of both the DM130 and N60 grids have been chosen to optimise the final selection of the SRA in order to maximise the expected discovery significance. The variables considered and the values chosen are presented in Table 8.4. In Figure 8.13 the selected values of the N_{jets} , $p_{\text{T}}(b_1)$ and $E_{\text{T}}^{\text{miss}}$ are justified by plotting the SRA selection before the application of each variable. At the bottom panel, the integrated expected discovery significance is shown.

Finally, Table 8.5 lists the expected background and signal benchmark yields. The acceptance of SRA to the signal benchmarks vary from about 4% to 14%.

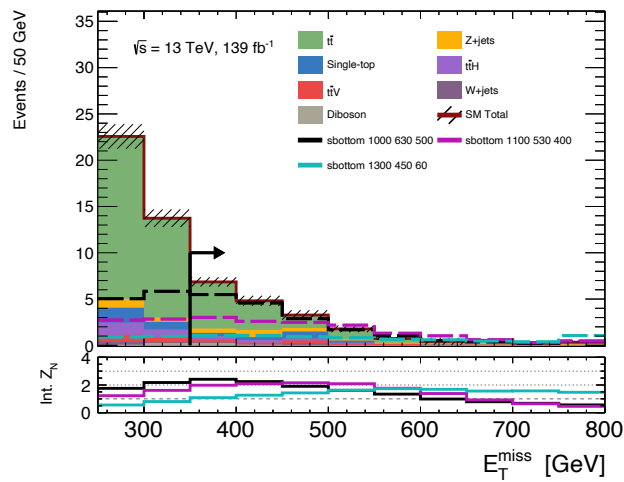
¹As a reminder to the reader, the term taus in the context of this dissertation refers to hadronically decaying taus only.



(a)



(b)



(c)

Figure 8.13: Distributions of the (a) N_{jets} , (b) $p_{\text{T}}(b_1)$ and (c) $E_{\text{T}}^{\text{miss}}$ justifying the SRA definition. The selection applied is the SRA before the corresponding variable of each plot. The bottom panel shows the integrated expected discovery significance. Only statistical uncertainties are shown. The figures comprise an original work of the author.

Table 8.4: The selection criteria defining the SRA regions.

Variable	SRA	SRA-L	SRA-M	SRA-H
N_{leptons} (baseline)		0		
N_{jets}		≥ 6		
$N_{\text{b-jets}}$		≥ 4		
$E_{\text{T}}^{\text{miss}}$ [GeV]		> 350		
$p_{\text{T}}(\mathbf{b}_1)$ [GeV]		> 200		
$\min[\Delta\phi(\text{jet}_{1-4}, \mathbf{p}_{\text{T}}^{\text{miss}})]$ [rad]		> 0.4		
τ -veto		✓		
$\Delta R_{\text{max}}(\mathbf{b}, \mathbf{b})$		> 2.5		
$\Delta R_{\text{max-min}}(\mathbf{b}, \mathbf{b})$		< 2.5		
$m(h_{\text{cand}})$ GeV		> 80		
m_{eff} TeV	> 1.0	$\in [1.0, 1.5]$	$\in [1.5, 2]$	> 2

Table 8.5: Expected background and signal benchmark yields for the SRA and the m_{eff} bins at 140.5 fb^{-1} . The brackets next to each signal yield present the expected discovery significance. The uncertainty includes only the statistical component.

Process	SRA	SRA-L	SRA-M	SRA-H
$\bar{t}t$	12.01 ± 0.61	6.26 ± 0.48	4.01 ± 0.36	1.74 ± 0.13
Z + jets	1.89 ± 0.52	1.16 ± 0.49	0.40 ± 0.10	0.32 ± 0.10
$\bar{t}tV$	1.12 ± 0.23	0.66 ± 0.16	0.28 ± 0.13	0.18 ± 0.10
Single-top	1.41 ± 0.75	0.46 ± 0.50	0.36 ± 0.36	0.59 ± 0.42
$\bar{t}tH$	0.43 ± 0.09	0.28 ± 0.07	0.11 ± 0.05	0.04 ± 0.04
W + jets	0.37 ± 0.15	0.23 ± 0.13	0.11 ± 0.07	0.04 ± 0.03
Diboson	0.40 ± 0.21	0.35 ± 0.21	0.00 ± 0.00	0.04 ± 0.04
SM	17.62 ± 1.15	9.40 ± 0.91	5.26 ± 0.54	2.96 ± 0.46
$m(\bar{\mathbf{b}}_1, \bar{\mathbf{x}}_2^0, \bar{\mathbf{x}}_1^0) = (1000, 630, 500)$ GeV	15.25 ± 0.81 (1.70)	7.91 ± 0.58 (1.42)	5.10 ± 0.46 (1.35)	2.24 ± 0.32 (0.79)
$m(\bar{\mathbf{b}}_1, \bar{\mathbf{x}}_2^0, \bar{\mathbf{x}}_1^0) = (1100, 530, 400)$ GeV	12.68 ± 0.35 (1.42)	2.94 ± 0.17 (0.45)	6.38 ± 0.24 (1.68)	3.36 ± 0.19 (1.24)
$m(\bar{\mathbf{b}}_1, \bar{\mathbf{x}}_2^0, \bar{\mathbf{x}}_1^0) = (1300, 450, 60)$ GeV	6.85 ± 0.20 (0.73)	0.13 ± 0.03 (0.00)	1.49 ± 0.09 (0.28)	5.23 ± 0.18 (1.91)

8.4.3 Signal Region B

The *Signal Region B* (SRB) targets the *compressed* scenarios of the DM130 grid. The term *compressed* refers to small mass splitting between the \tilde{b}_1 and $\tilde{\chi}_2^0$ ($\Delta m(\tilde{b}_1, \tilde{\chi}_2^0) \approx 20$ GeV). In these cases the decay chain products are not energetic enough to be reconstructed; the b-jets wouldn't pass the p_T threshold of Table 8.3 nor the E_T^{miss} would be enough to trigger the event. To tackle this, an ISR topology is exploited; events where a highly energetic jet, radiated from the initial-state partons, recoils against the SUSY system. This provides a momentum boost to the whole decay chain, leading eventually to an energetic enough final state. This is the same topology explored previously to target compressed Gbb scenarios in Chapter 7. Even after the ISR boost however, the b-jets from the \tilde{b}_1 decay have still low energy and do not leave an apparent signature to the detector. The kinematic configuration of the SUSY model that the SRB targets is shown in Figure 8.7b.

8.4.3.1 Alternative Max-Min Algorithm

As in this case the b-jets from the \tilde{b}_1 decay are not energetic enough to be reconstructed, the max-min algorithm of SRA is not applicable. Therefore, an alternative variant has been developed targeting the identification of the b-jets from the two Higgs decays instead. In general, the spatial separation of the b-jets from a Higgs decay depends on the transverse momentum of the Higgs boson, p_T^h :

$$\Delta R(\text{b}, \text{b}) \sim \frac{2m(h)}{p_T^h}. \quad (8.5)$$

As the \tilde{b}_1 masses targeted by this analysis are high ($\gtrsim 500$ GeV), the accessible ISR boost is not enough to provide sufficient momentum to the Higgs boson via the $\tilde{\chi}_2^0$. This observation led to an algorithm looking for b-jet pairings with maximum ΔR .

In an event-by-event basis, the algorithm iterates over all the available b-jets and identifies the pair with maximum ΔR , these are regarded as originating from one of the Higgs decays. From the remaining jets, the pair with the second-to-maximum ΔR is identified and regarded as originating from the second Higgs decay. Eventually, the invariant mass of each pair is calculated and a Higgs-like selection (75 - 175 GeV) is applied to their average, $m(h_{\text{cand1}}, h_{\text{cand2}})_{\text{avg}}$. As it can be seen in Figure 8.14, this selection helps to separate the signal from the SM background where b-jets are present but not originating from a Higgs resonance.

The efficiency of correctly selecting the b-jets from the Higgs decays using this algorithm estimated at the range of 15 to 30%.

8.4.3.2 Definition & Yields

As in the case of SRA, selections are also applied to the E_T^{miss} and m_{eff} in order to further discriminate the signal from the SM background. These have been optimised,

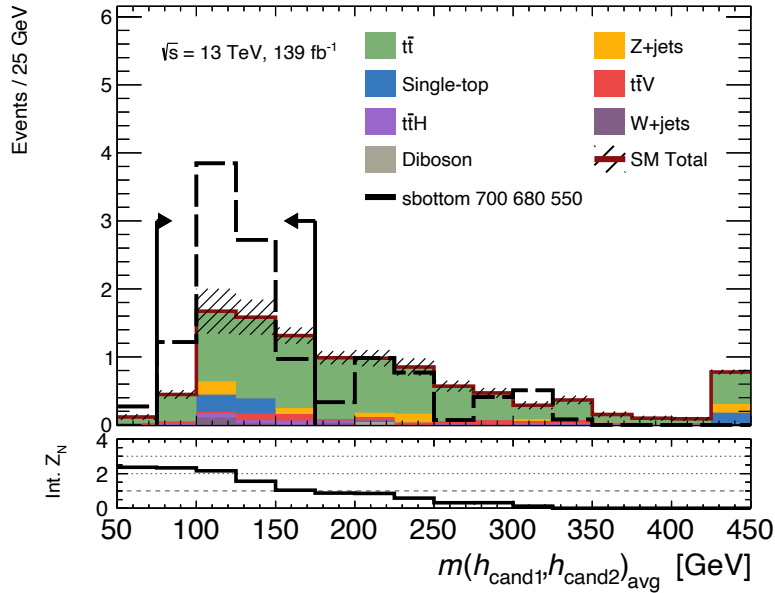


Figure 8.14: The distribution of $m(h_{\text{cand1}}, h_{\text{cand2}})_{\text{avg}}$ in a signal model against the SM background. A Higgs-like invariant mass selection increase the expected discovery significance (bottom panel). The selection applied is the same as in Figure 8.5 but with an additional high p_T ISR jet. Only statistical uncertainties are shown. The figure comprises an original work of the author.

as previously, to maximise the discovery significance of a benchmark signal. Additionally, the ISR topology is selected by requiring the leading (in p_T) jet of the event to be highly energetic, not-b-tagged and having large azimuthal separation from the E_T^{miss} . The τ -veto is also applied for the same reasons as in SRA.

The final SRB definition is presented in Table 8.6 while in Figure 8.15 the selected values of the $p_T(j_1)$ and E_T^{miss} are justified by plotting the SRB selection before the application of each variable.

Finally, Table 8.7 lists the expected background and signal benchmark yields. The acceptance of SRB to the signal benchmark at $\mathcal{O}(0.1\%)$ level but the limited statistical power of the simulated model in this extreme phase space prohibits an accurate estimation of this number. Because of the compressed mass hierarchy of the signal few events are able to pass the high E_T^{miss} and $N_{\text{b-jets}}$ selection. Similar level of acceptance has been previously measured for the ISR SR of Chapter 7 (Gbb-VC).

8.4.4 Signal Region C

The *Signal Region C* (SRC) targets the compressed ($\Delta m(\tilde{b}_1, \tilde{\chi}_2^0) \approx 50$ GeV) scenarios of the N60 grid. In these cases the ΔR based algorithms do not allow for significant discrimination between signal and background. This is because not many of the b-jets from the \tilde{b}_1 decay and/or the Higgs decays are energetic enough. Additionally, as the \tilde{b}_1 masses targeted by this region are much higher than before ($\gtrsim 1000$ GeV), the

Table 8.6: The selection criteria defining the SRB region.

Variable	SRB
N_{leptons} (baseline)	0
N_{jets}	≥ 5
$N_{\text{b-jets}}$	≥ 4
$E_{\text{T}}^{\text{miss}}$ [GeV]	> 350
$\min[\Delta\phi(\text{jet}_{1-4}, \mathbf{p}_{\text{T}}^{\text{miss}})]$ [rad]	> 0.4
τ -veto	✓
$p_{\text{T}}(j_1)$ [GeV]	> 350
leading jet non-b-jet	✓
$ \Delta\phi(j_1, E_{\text{T}}^{\text{miss}}) $ [rad]	> 2.8
$m(h_{\text{cand}1}, h_{\text{cand}2})_{\text{avg}}$ [GeV]	$\in [75, 175]$
m_{eff} [TeV]	> 1.0

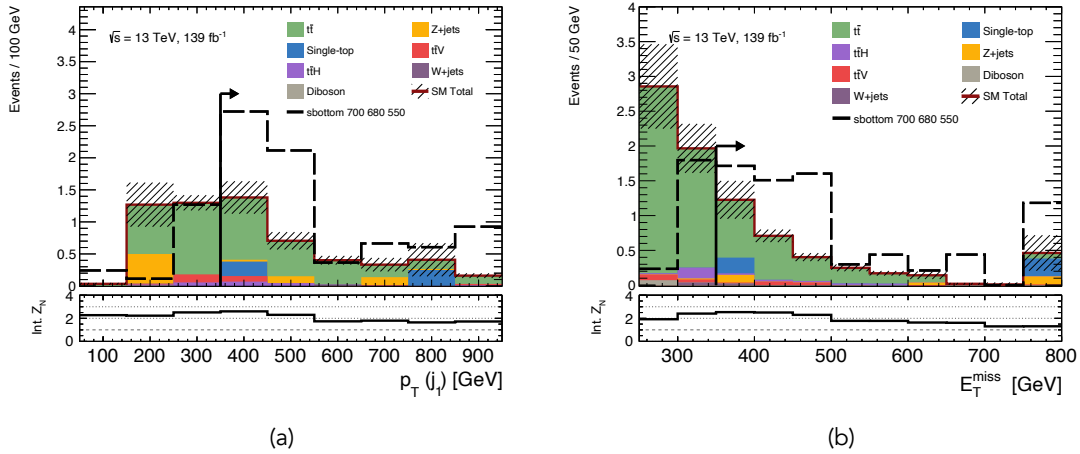


Figure 8.15: Distributions of the (a) $p_{\text{T}}(j_1)$ and (b) $E_{\text{T}}^{\text{miss}}$. The selection applied is the SRB before the corresponding variable of each plot. The limited statistics on the signal make it difficult to draw strong conclusions but these selections have found to provide the best sensitivity in a variety of compressed $\Delta m(\tilde{b}_1, \tilde{\chi}_2^0)$ signals. The bottom panel shows the integrated expected discovery significance. The figures comprise an original work of the author.

achievable ISR boost is not sufficient for all the decay products to reach the p_{T} thresholds of Table 8.3. However, these type of signals can be targeted when the b-jets from the Higgs decays are very energetic. As the remaining momentum is not enough to produce more energetic b-jets, the hadronic activity of the event is low compared to the $E_{\text{T}}^{\text{miss}}$. This configuration leads to very significant $E_{\text{T}}^{\text{miss}}$ and presented in Figure 8.7c.

The main discriminating variable of SRC is the object-based $E_{\text{T}}^{\text{miss}}$ significance. Following the multi-bin strategy of SRA, the phase space of SRC is further divided to mutually exclusive \mathcal{S} bins. This provides the same virtues as before, a sensitivity gradient to wide parameter space ($m(\tilde{b}_1)$) and, in case of null-results, stronger model exclusion by

Table 8.7: Expected background and signal benchmark yields for the SRB at 140.5 fb^{-1} . The brackets next to the signal yield present the expected discovery significance. The uncertainty includes only the statistical component.

Process	SRB
$t\bar{t}$	2.35 ± 0.15
Single-top	0.51 ± 0.36
$t\bar{t}V$	0.09 ± 0.08
$t\bar{t}H$	0.05 ± 0.03
Z + jets	0.05 ± 0.03
W + jets	0.01 ± 0.01
SM	3.06 ± 0.40
$m(\tilde{b}_1, \tilde{\chi}_2^0, \tilde{\chi}_1^0) = (700, 680, 550) \text{ GeV}$	$6.41 \pm 1.01 (2.26)$

statistical combination. No additional discriminating variables are used as the usage of just \mathcal{S} found sufficient.

The lower threshold of \mathcal{S} is chosen at 22 after optimisation based on a compressed signal benchmark. Then the four bins defined are incremented by 2 up to 28 and are shown in Figure 8.16. The full SRC selection can be found in Table 8.8 and the expected background and signal benchmark yields in Table 8.9. The acceptance of SRC to the signal benchmarks vary from about 9% to 18%. It is worth noting that the SRC has found to be sensitive to $\tilde{b}_1 - \tilde{\chi}_2^0$ mass splittings down to $\sim 5 \text{ GeV}$.

Table 8.8: The selection criteria defining the SRC and the four \mathcal{S} bins.

Variable	SRC	SRC22	SRC24	SRC26	SRC28
$N_{\text{leptons (baseline)}}$			0		
N_{jets}			≥ 4		
$N_{\text{b-jets}}$			≥ 3		
$E_{\text{T}}^{\text{miss}} [\text{GeV}]$			> 250		
$\min[\Delta\phi(\text{jet}_{1-4}, \mathbf{p}_{\text{T}}^{\text{miss}})] [\text{rad}]$			> 0.4		
\mathcal{S}	> 22	$\in [22, 24]$	$\in [24, 26]$	$\in [26, 28]$	> 28

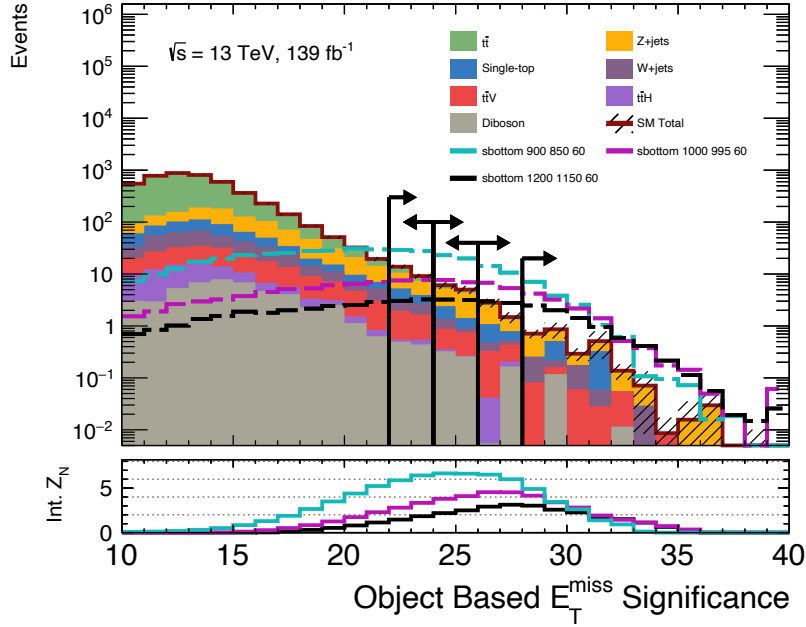


Figure 8.16: The distribution of S in simulated events for both the SM background and three signal benchmark models. The multi-bin strategy allows from sensitivity in a spectrum of signal models. The selection applied is the SRB (Table 8.8) before the S cut. Only statistical uncertainties are shown. The figure comprises an original work of the author.

Table 8.9: Expected background and signal benchmark yields for the SRC and the S bins at 139 fb^{-1} . The brackets next to each signal yield present the expected discovery significance. The uncertainty includes only the statistical component.

Process	SRC	SRC22	SRC24	SRC26	SRC28
Z + jets	17.77 ± 1.53	8.77 ± 1.06	5.91 ± 1.00	1.98 ± 0.41	1.12 ± 0.17
$t\bar{t}$	6.93 ± 0.23	4.96 ± 0.19	1.38 ± 0.11	0.43 ± 0.05	0.16 ± 0.03
Single-top	6.45 ± 1.28	3.46 ± 0.89	1.56 ± 0.72	0.87 ± 0.44	0.56 ± 0.37
$t\bar{t}V$	4.31 ± 0.33	2.52 ± 0.25	1.01 ± 0.17	0.52 ± 0.11	0.25 ± 0.10
W + jets	3.46 ± 0.59	2.16 ± 0.55	0.63 ± 0.17	0.24 ± 0.06	0.42 ± 0.10
Diboson	1.82 ± 0.39	0.94 ± 0.27	0.59 ± 0.23	0.17 ± 0.16	0.13 ± 0.09
$t\bar{t}H$	0.27 ± 0.08	0.16 ± 0.06	0.04 ± 0.03	0.08 ± 0.03	0.00 ± 0.00
SM	41.02 ± 2.15	22.97 ± 1.55	11.11 ± 1.28	4.29 ± 0.64	2.64 ± 0.44
$m(\tilde{b}_1, \tilde{\chi}_2^0, \tilde{\chi}_1^0) = (900, 850, 60) \text{ GeV}$	$140.21 \pm 2.21 (5.87)$	$56.90 \pm 1.40 (4.35)$	$42.97 \pm 1.22 (5.40)$	$24.89 \pm 0.94 (5.71)$	$15.45 \pm 0.75 (4.90)$
$m(\tilde{b}_1, \tilde{\chi}_2^0, \tilde{\chi}_1^0) = (1000, 995, 60) \text{ GeV}$	$54.32 \pm 0.95 (2.80)$	$15.21 \pm 0.50 (1.37)$	$14.63 \pm 0.48 (2.27)$	$12.14 \pm 0.44 (3.31)$	$12.34 \pm 0.46 (4.14)$
$m(\tilde{b}_1, \tilde{\chi}_2^0, \tilde{\chi}_1^0) = (1200, 1150, 60) \text{ GeV}$	$26.74 \pm 0.33 (1.46)$	$6.29 \pm 0.16 (0.50)$	$6.38 \pm 0.16 (1.00)$	$5.77 \pm 0.15 (1.72)$	$8.30 \pm 0.18 (3.02)$

8.5 Background Estimation

8.5.1 Processes and Strategy

Following the definition of the SRs, the expected SM background contributions to each region are presented in Figure 8.17. The main process contributing to SRA and SRB (65-70%) is $t\bar{t}$ production in association with b-jets, originating mainly from $g \rightarrow b\bar{b}$ splitting (Figure 8.18a). On the other hand, in SRC the dominant process is the Z + jets production with the Z decaying to neutrinos (Figure 8.18b). This difference led to two background estimation strategies, one for the SRA and SRB and one for the SRC.

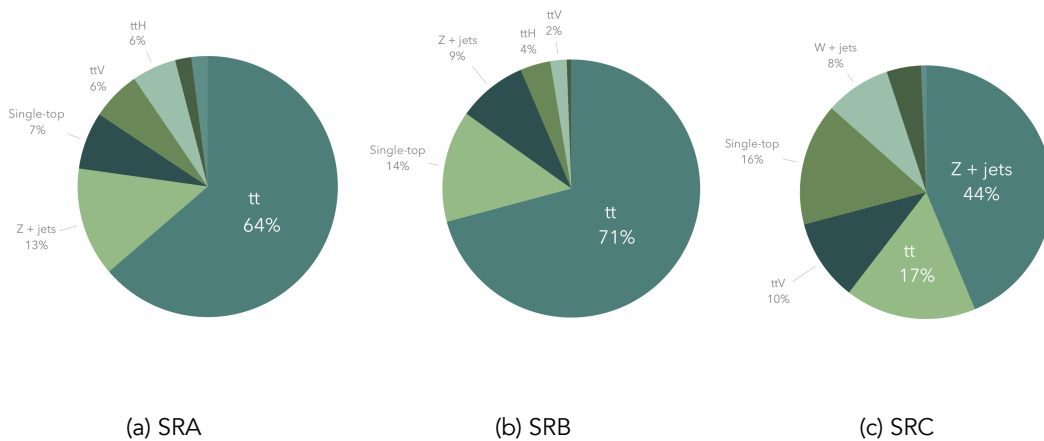


Figure 8.17: The relative SM background contribution expected from simulations for each SR. The figures comprise an original work of the author.

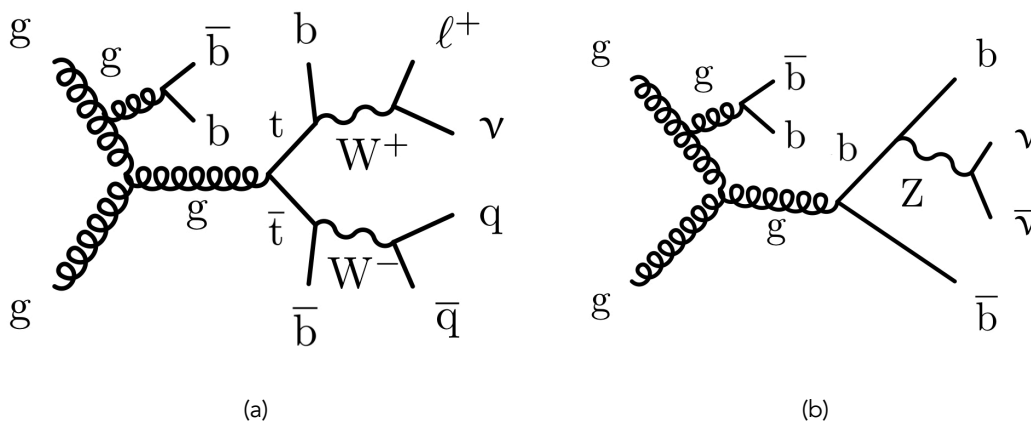


Figure 8.18: The two main SM backgrounds to this search: (a) production of a $t\bar{t}$ pair decaying semi-leptonically in association with a gluon splitting to a pair of b-jets, (b) production of a Z decaying to neutrinos in association with b-jets. The charged conjugate diagrams also implied. The diagrams comprise an original work of the author.

In general, the SM backgrounds are estimated in a semi-data-driven fashion, similar to the gluino search of Chapter 7. For the dominant processes ($t\bar{t}$, Z + jets and Single-top), the shape of the observables is taken from MC simulations, but the normalisation is extracted from data through a fit in dedicated CRs. For the sub-dominant background processes, both the shape and the normalisation are taken from MC simulations. The background-only fit, described in Section 6.2.1, is performed simultaneously into all the CRs corresponding to a single SR and determines the μ -factors by maximising a combined likelihood based on Eq. 6.1.

The major background processes are targeted in their leptonic decays. Thus the orthogonality of the CRs to the SRs is achieved by the presence of one or two `signal` leptons. Extra variables taking into account the presence of leptons are used for the CR definitions:

- m_T : For the 1-lepton regions, the transverse mass between the leading lepton and the E_T^{miss} defined as:

$$m_T = \sqrt{2p_T^\ell E_T^{\text{miss}}(1 - \cos \Delta\phi(\ell, \mathbf{p}_T^{\text{miss}}))}, \quad (8.6)$$

where $\Delta\phi(\ell, \mathbf{p}_T^{\text{miss}})$ is the azimuthal angle between the lepton and the $\mathbf{p}_T^{\text{miss}}$. This variable is used to suppress fake leptons originating from multi-jet processes; the real leptons from the $t\bar{t}$ background are coming from the heavy W resonance they have higher m_T

- $\tilde{E}_T^{\text{miss}}$: This variable is referred to as the *lepton-corrected missing energy* and is used exclusively in the 2-lepton region. As explained in Section 8.5.3, a 2-lepton selection is used to model the Z + jets background. In particular, $Z \rightarrow \ell\ell$ events are used as a proxy to the $Z \rightarrow \nu\nu$ process. Therefore, the two leptons in the event are removed from the $\mathbf{p}_T^{\text{miss}}$ calculation, effectively treating them as invisible particles. The E_T^{miss} in that region, after the lepton subtraction, is referred to as $\tilde{E}_T^{\text{miss}}$.
- $m_{\ell\ell}$: The invariant mass of the two leptons in the 2-lepton region. Similarly as the $\tilde{E}_T^{\text{miss}}$, this variable is only used in the 2-lepton region. As the $Z \rightarrow \ell\ell$ decay is targeted, the invariant mass of the lepton pair is used to select leptons from the on-shell decay of the Z .

A background validation process is also taking place in different VRs. They are defined per SR type (A, B, C) and with similar selection to the corresponding SR. Events without any `baseline` leptons are used and the orthogonality to the SRs is achieved by other selections, as described below.

8.5.2 Regions A & B

The main background process of the SRA and SRB is the $t\bar{t}$ production. When the $t\bar{t}$ pair decays semi-leptonically and the lepton is not identified – either mis-identified as jet or falls out of the detector acceptance – a zero lepton final state with E_T^{miss} , originating from the escape of the neutrino, is reconstructed. Additionally, if an initial or final state radiated gluon split to a b-quark pair, the b-jet multiplicity is as high as the signal. The stochastic nature of particle production and decay leads to $t\bar{t}$ events identified by the ΔR based algorithms and eventually contributing to the SR yield. These semi-leptonic $t\bar{t}$ events are normalised by a single-lepton CRs for both the SRA (CRA) and SRB (CRB) cases.

The need for proximity of the CRs to the SRs dictates a high m_{eff} selection. As this is the main discriminating variable in the SRA and SRB and encapsulates most of the event kinematics it is beneficial to retain the same threshold to the SRs ($m_{\text{eff}} > 1$ TeV). However, background modeling studies revealed a discrepancy between the data and MC prediction in the tail of the m_{eff} distribution. It was observed that more events are predicted by the $t\bar{t}$ simulation than found in data for $m_{\text{eff}} \gtrsim 1.5$ TeV. This discrepancy though is no larger than the (theoretical) uncertainties of the simulation, as it can be seen in Figure 8.19. This behavior motivated the sub-division of the CRA to three m_{eff} bins, in accordance with the SRA, allowing for the calculation of a single μ -factor for the $t\bar{t}$ process but with individual uncertainty constrains per bin. Effectively, the fit is allowed to correct the simulation, with respect to the data, within the uncertainties of each m_{eff} bin (C term in Eq. 6.1).

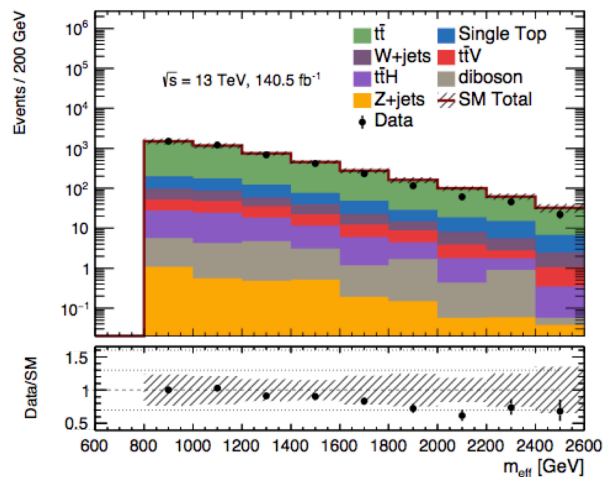


Figure 8.19: The distribution of m_{eff} in the data and simulation before the background-only fit. The discrepancy is apparent on the ratio of the bottom panel. The selection applied is the same as in Figure 8.5 but with one signal lepton instead. Both statistical and the systematic uncertainties described in Section 8.6 are shown. The figure comprises an original work of the author.

This mismodeling has been also observed by previous analyses studying multiple b-jet final states, as the work described in Chapter 7. In those cases ad hoc kinematic reweighing methods are employed to correct the simulation. With the multi-bin fit strategy presented in this work any reweighing or further correction is redundant as the uncertainties in the background prediction are allowed to vary over the m_{eff} spectrum (discussed in Section 8.6). The origin of the mismodeling hasn't been identified but recent calculations of higher order corrections (NNLO QCD and NLO EW) of the $t\bar{t}$ process have shown that the discrepancy can be reduced [201].

The validation of the $t\bar{t}$ background estimation happens in zero-lepton VRs. These are two independent and correspond to the two types of SRs: $\text{VRA}0\ell$ and $\text{VRB}0\ell$. The $\text{VRA}0\ell$ is further sub-division in m_{eff} bins, in accordance with the SRA and $\text{CRA}1\ell$. This ensures the validation of the background estimation in the same multi-bin approach the SRA is designed on.

The CRA and CRB are defined based on the requirements for minimal signal contamination and maximal proximity to the corresponding SRs. In general, they are characterised by one signal lepton and high m_{eff} selection (same as the SRs). Requirements on the $E_{\text{T}}^{\text{miss}}$, $p_{\text{T}}(\text{b}_1)$ and $|\Delta\phi(\text{j}_1, E_{\text{T}}^{\text{miss}})|$ are relaxed to increase the sample statistics. For the same reason the ΔR algorithms for the Higgs candidate identification are not used. Furthermore, the τ -veto and $\min[\Delta\phi(\text{jet}_{1-4}, \mathbf{p}_{\text{T}}^{\text{miss}})]$ requirements are also dropped but an m_{T} selection is added to reduce the fake lepton background. The complete selection criteria of CRA and CRB are presented in Table 8.10. Figure 8.20 show well modeling of important kinematic variables in $\text{CRA}1\ell$ and $\text{CRB}1\ell$ even before the fit, the fact that gives confidence to the background estimation strategy.

Table 8.10: The selection criteria defining the $\text{CRA}1\ell$ and $\text{CRB}1\ell$.

Variable	$\text{CRA}1\ell$	$\text{CRA}1\ell\text{-L}$	$\text{CRA}1\ell\text{-M}$	$\text{CRA}1\ell\text{-H}$	$\text{CRB}1\ell$
N_{leptons} (baseline)			1		
N_{leptons} (signal)			1		
N_{jets}		≥ 6			≥ 4
$N_{\text{b-jets}}$		≥ 4			
$E_{\text{T}}^{\text{miss}}$ [GeV]		> 250			> 300
$p_{\text{T}}(\text{b}_1)$ [GeV]		> 100			-
$p_{\text{T}}(\text{j}_1)$ [GeV]		-			> 350
leading jet non-b-jet		-			✓
$ \Delta\phi(\text{j}_1, E_{\text{T}}^{\text{miss}}) $ [rad]		-			> 2.2
m_{T} [GeV]			> 20		
m_{eff} TeV	> 1.0	$\in [1.0, 1.5]$	$\in [1.5, 2]$	> 2	> 1.0

Based on simulations before the fit, the purity of the $t\bar{t}$ process is 82% for the $\text{CRA}1\ell$ and 87% for the $\text{CRB}1\ell$. The signal contamination is at $\mathcal{O}(1\%)$ level for models surviving

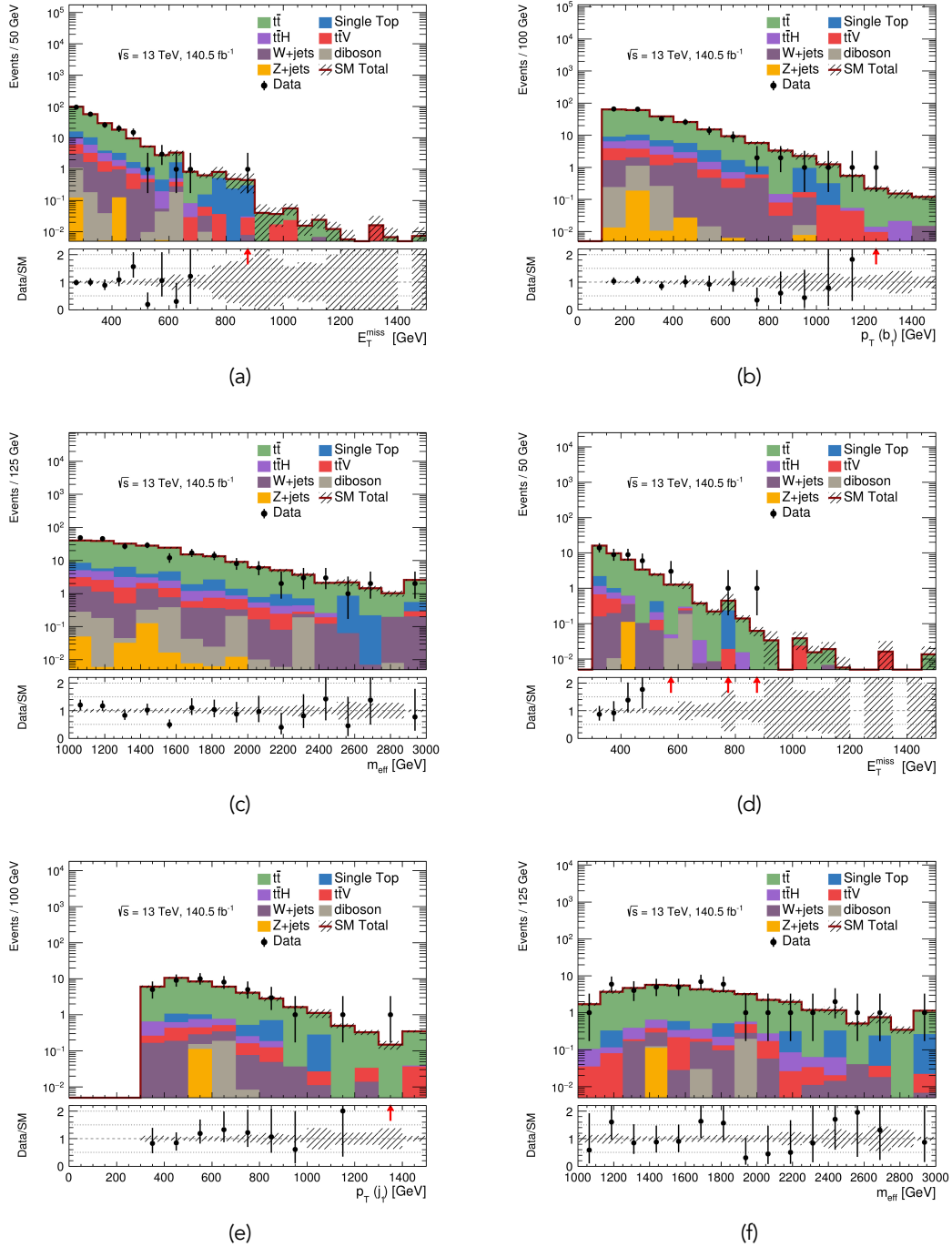


Figure 8.20: Distributions of (a) and (d) E_T^{miss} , (b) and (e) $p_T(b_1)$ and (c) and (f) m_{eff} show the modeling of each variable before the fit. The top plots correspond to the CRA1 l while the bottom to the CRB1 l . Only statistical uncertainties are shown. The figures comprise an original work of the author.

previous iteration of the analysis [160].

Regarding the VRs definitions, events with `baseline` leptons are vetoed, similarly to the SRs. The orthogonality in this case is achieved by lower b-jet multiplicity requirement. To increase the statistics of the sample the E_T^{miss} selection is relaxed in the $\text{VRA0}\ell$ case. An inverse \mathcal{S} selection is also applied for the both $\text{VRA0}\ell$ and $\text{VRB0}\ell$ to ensure they are mutually exclusive with the SRC. The complete selection criteria of $\text{VRA0}\ell$ and $\text{VRB0}\ell$ are presented in Table 8.11. Figure 8.21 show good modeling of the shape of two important kinematic variables in $\text{VRA0}\ell$ and $\text{VRB0}\ell$ respectively.

Based on simulations before the fit, the purity of the $t\bar{t}$ process is 67% for the $\text{VRA0}\ell$ and 73% for the $\text{VRB0}\ell$. The signal contamination has found 20% at maximum for models surviving previous iteration of the analysis [160].

Table 8.11: The selection criteria defining the $\text{VRA0}\ell$ and $\text{VRB0}\ell$.

Variable	$\text{VRA0}\ell\text{-L}$	$\text{VRA0}\ell\text{-M}$	$\text{VRA0}\ell\text{-H}$	$\text{VRB0}\ell$
N_{leptons} (<code>baseline</code>)		0		
N_{jets}		≥ 6		≥ 4
$N_{\text{b-jets}}$		3		
E_T^{miss} [GeV]		> 350		
$p_T(\text{b}_1)$ [GeV]		> 100		-
$p_T(\text{j}_1)$ [GeV]		-		> 350
leading jet non-b-jet		-		✓
$ \Delta\phi(\text{j}_1, E_T^{\text{miss}}) $ [rad]		-		> 2.8
τ -veto		✓		
$\min[\Delta\phi(\text{jet}_{1-4}, \mathbf{p}_T^{\text{miss}})]$ [rad]		> 0.4		
\mathcal{S}		< 22		
m_{eff} TeV	$\in [1.0, 1.5]$	$\in [1.5, 2]$	> 2	> 1.0

8.5.3 Region C

As shown already in Figure 8.17 the major contributing background in the SRC is the $Z + \text{jets}$ production in association with b-jets. When the Z boson decays to neutrinos it can generate significant E_T^{miss} with respect to the hadronic activity of the event, thus high \mathcal{S} . In order to estimate the $Z \rightarrow \nu\nu$ process, $Z \rightarrow \ell\ell$ decays are used as a proxy; a two lepton CR ($\text{CRC2}\ell$) resembling the kinematics of the SRC is used to extract the normalisation.

Furthermore, $t\bar{t}$ and Single-top events comprise about 33% of the SM background. As both of the processes originate from top quark production, a single CR and one μ -factor is used for their normalisation. Along the same lines to $\text{CRA1}\ell$ and $\text{CRB1}\ell$, a single lepton CR ($\text{CRC1}\ell$) is designed to be enriched in both processes and used to fit the μ_{Top} .

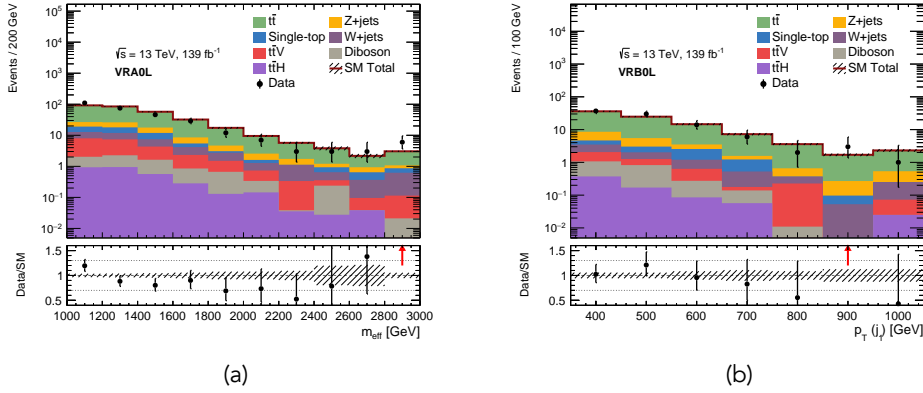


Figure 8.21: Distributions of (a) m_{eff} and (d) $p_T(j_1)$ show the modeling of each variable before the fit in VRA0 ℓ and VRB0 ℓ respectively. Only statistical uncertainties are shown. The figures comprise an original work of the author.

Following the normalisation of two SM processes, two VRs are also defined; one for the Z + jets process (VRC0 ℓ -Z) and one for the Top (VRC0 ℓ -T). Both are comprised of events without leptons in order to be close to the SR phase space.

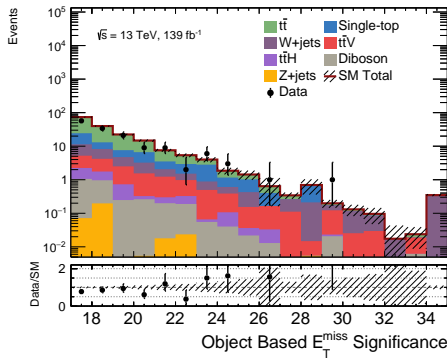
The CRC2 ℓ is defined by the selection of two Same-Flavour Opposite-Sign (SFOS) signal leptons with the purpose to reconstruct the $Z \rightarrow \ell\ell$ decay. An invariant mass constrain around the Z pole mass is also applied to enhance the selection of leptons that genuinely originating from the decay of the Z boson. As described previously, the missing energy is recalculated with the leptons treated as invisible particles and a selection on the $\tilde{E}_T^{\text{miss}}$ is substituting the E_T^{miss} requirement of SRC. To further increase the $Z \rightarrow \ell\ell$ purity, only events with low E_T^{miss} are selected. The \mathcal{S} requirement is dropped to increase the statistics of the sample.

The CRC1 ℓ is defined by the selection of one signal lepton. The definition closely resembles the SRC, with a relaxed requirement on \mathcal{S} and an extra requirements on m_T . The definitions of both CRC2 ℓ and CRC1 ℓ are presented in Table 8.12. In Figures 8.22 and 8.23 the modeling of important kinematic variables in the two CRs is shown. The very good agreement between data and simulations, even before the fit, gives confidence on the regions definition.

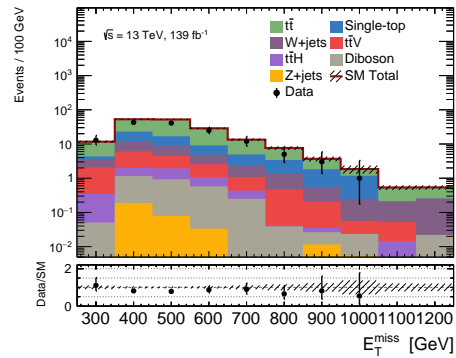
The purity of the top processes ($t\bar{t}$ & Single-top) in CRC1 ℓ is 80% while the Z + jets in CRC2 ℓ 70%.

Table 8.12: The selection criteria defining the CRC2 ℓ and CRC1 ℓ .

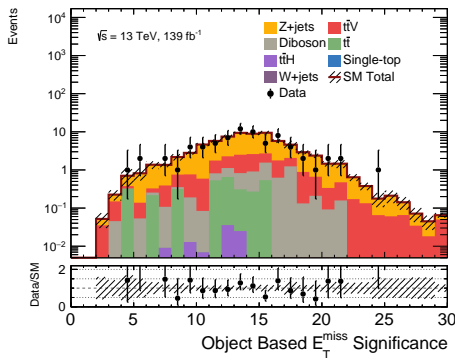
Variable	CRC2 ℓ	CRC1 ℓ
N_{leptons} (baseline)	2	1
N_{leptons} (signal)	2 (SFOS)	1
$p_{\text{T}}(\ell_1)$ [GeV]	> 27	-
N_{jets}	≥ 4	-
$N_{\text{b-jets}}$	≥ 3	-
$E_{\text{T}}^{\text{miss}}$ [GeV]	< 70	> 250
$\tilde{E}_{\text{T}}^{\text{miss}}$ [GeV]	> 250	-
$m_{\ell\ell}$ [GeV]	$\in [86, 106]$	-
m_{T} [GeV]	-	> 20
\mathcal{S}	-	> 17



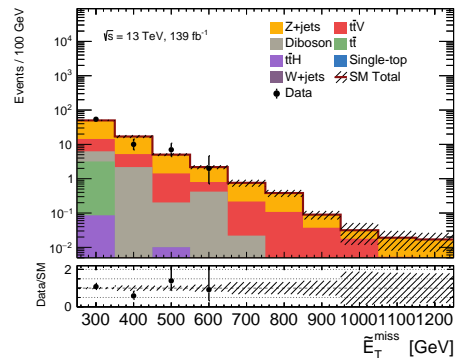
(a)



(b)

Figure 8.22: Distributions of (a) \mathcal{S} and (b) $E_{\text{T}}^{\text{miss}}$ show the modeling of each variable before the fit in the CRC1 ℓ . Only statistical uncertainties are shown. The figures comprise an original work of the author.

(a)



(b)

Figure 8.23: Distributions of (a) \mathcal{S} and (b) $E_{\text{T}}^{\text{miss}}$ show the modeling of each variable before the fit in the CRC2 ℓ . Only statistical uncertainties are shown. The figures comprise an original work of the author.

Regarding the VRs definitions, events with zero baseline leptons are selected, similarly to the SRs. In general, the definition of the VRs closely resembles the one of SRC, although they kept mutually exclusive. The orthogonality in the VRC0 l -Z case is achieved via lower selections on $N_{b\text{-jets}}$ and \mathcal{S} while in the VRC0 l -T case via lower $\min[\Delta\phi(\text{jet}_{1-4}, \mathbf{p}_T^{\text{miss}})]$ and \mathcal{S} selections. An upper limit on the E_T^{miss} for the VRC0 l -Z is placed to reduce the signal contamination. The complete selection criteria of VRC0 l -Z and VRC0 l -T are presented in Table 8.13. Figure 8.24 show good modeling of the shape of two important kinematic variables in VRC0 l -Z and VRC0 l -T respectively.

Based on simulations before the fit, the purity of the top processes in the VRC0 l -T is 79% while the Z + jets in VRC0 l -Z is 55%. The signal contamination has found negligible for models surviving previous iteration of the analysis [160].

Table 8.13: The selection criteria defining the VRC0 l -Z and VRC0 l -T .

Variable	VRC0 l -Z	VRC0 l -T
N_{leptons} (baseline)		0
N_{jets}		≥ 4
$N_{b\text{-jets}}$	2	≥ 3
$\min[\Delta\phi(\text{jet}_{1-4}, \mathbf{p}_T^{\text{miss}})]$	> 1.2	$\in [0.2, 0.4]$
E_T^{miss} [GeV]	$\in [250, 600]$	> 250
\mathcal{S}	$\in [20, 22]$	$\in [15, 22]$

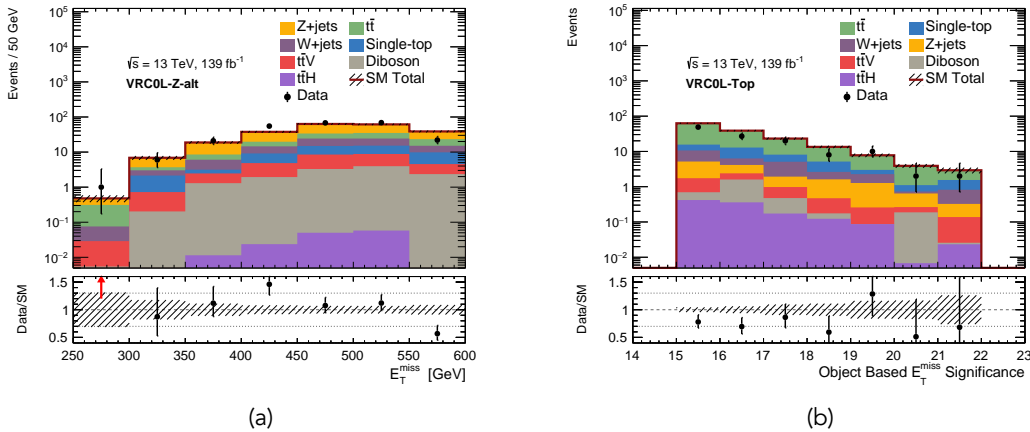


Figure 8.24: Distributions of (a) E_T^{miss} and (d) \mathcal{S} show the modeling of each variable before the fit in VRC0 l -Z and VRC0 l -T respectively. Only statistical uncertainties are shown. The figures comprise an original work of the author.

8.5.4 Background-only Fit Results

Summarising, the normalisation of two SM processes is extracted from data for this analysis. For the SRA and SRB the major background $t\bar{t}$ is normalised in the single-lepton $CRA1\ell$ and $CRB1\ell$ respectively. For the SRC the major backgrounds Z + jets and Top ($t\bar{t}$ & Single-top) are normalised in the two-lepton $CRC2\ell$ and the single-lepton $CRC1\ell$ respectively. Corresponding VRs are verifying each background prediction in a zero-lepton selection. Both the CRs and VRs are mutually exclusive to the SRs. The phase space of all the regions used is presented schematically in Figure 8.25.

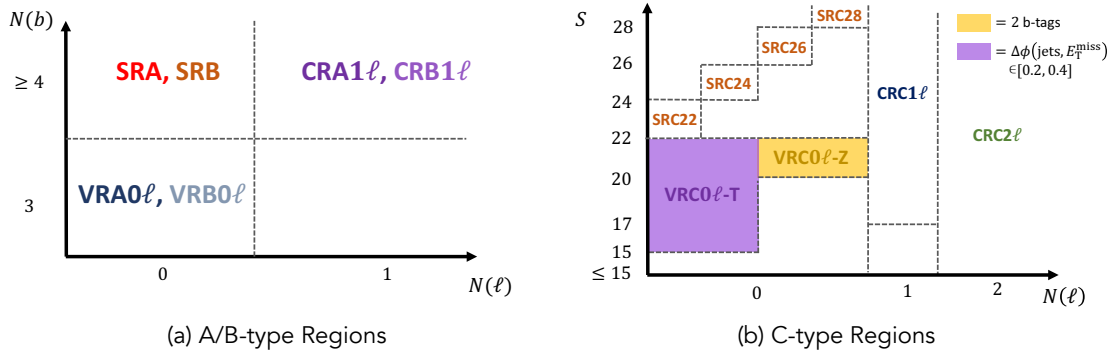


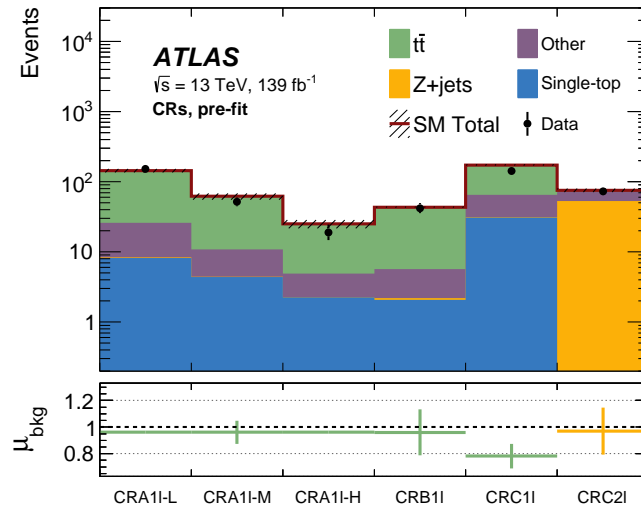
Figure 8.25: Schematic representation of the phase space determine the analysis regions. Figure published in [5]

After performing the three independent (one for each region type) background-only fits, four μ -factors are extracted. The result is presented in the bottom panel of Figure 8.26a, where it can be seen that all the μ -factors are compatible with unity within their (statistical) uncertainties. This is not the case for the μ_{Top} , extracted from the $CRC1\ell$. This behavior is explained by the fact that different b-jet multiplicity phase space (≥ 3) is targeted by this region compared to $CRA1\ell$ and $CRB1\ell$ (≥ 4). The top panel of the plot presents the data and simulated yield in each region before the fit.

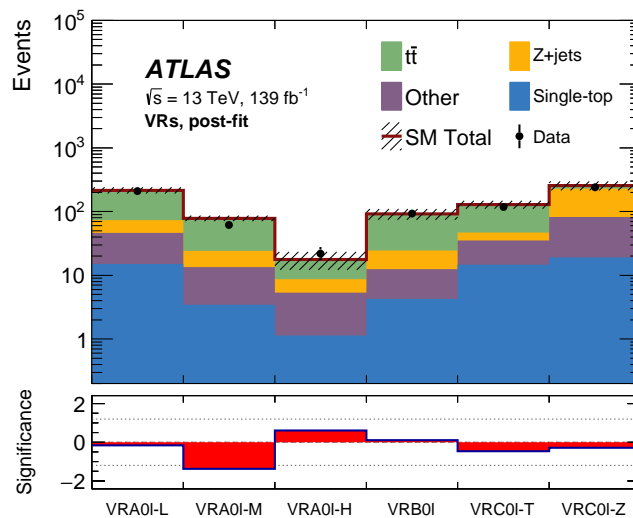
As already mentioned, the Higgs identification algorithms have been dropped by the $CRA1\ell$ and $CRB1\ell$ definitions in order to enhance their statistics. Therefore, the modeling of the invariant mass variables calculated by them ($m(h_{\text{cand}})$ and $m(h_{\text{cand}1}, h_{\text{cand}2})_{\text{avg}}$) is important to be verified so the fitted background can be confidently extrapolated to the corresponding SR. The Figure 8.27 shows excellent modeling of the shape of both invariant masses after the fit.

Along the lines of the Eq. 7.6, the expected background in the bin i of a VR can be estimated by extrapolating the μ -factors from the CRs:

$$N_{\text{bkg}}(\text{VR}-i) = \sum_p \underbrace{\mu_p}_{\text{CR}_p} \times \theta_i N_p^{\text{MC}}(\text{VR}-i) + N_{\text{Other}}^{\text{MC}}(\text{VR}-i), \quad (8.7)$$



(a)



(b)

Figure 8.26: (a) The data and simulated yield in each CR (top) and the extracted μ -factors for each SM process normalised (bottom). For the $\text{CRA}1\ell$ the fit is performed in all the m_{eff} bins but a single μ_{tt} -factor is extracted. (b) Results of the background estimation extrapolated in the VRs. The top panel shows the predicted and observed yields and the bottom the significance [157] of their difference. Backgrounds with minor contribution (ttV , ttH , $W + \text{jets}$, Diboson) are grouped and labelled as "Other". The uncertainties include both statistical and the systematic components described in Section 8.6. Figures published in [5].

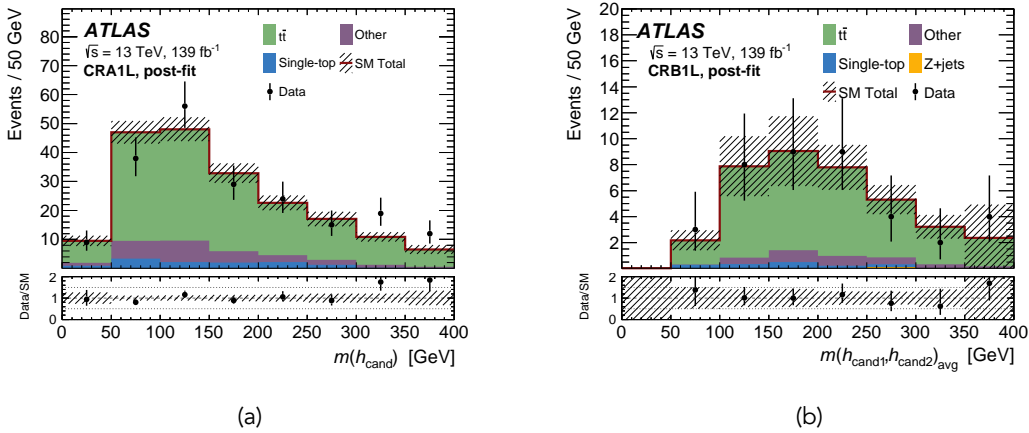


Figure 8.27: Distributions of (a) $m(h_{\text{cand}})$ and (b) $m(h_{\text{cand1}}, h_{\text{cand2}})_{\text{avg}}$ in CRA1 ℓ and CRB1 ℓ respectively after the fit. Both statistical and the systematic uncertainties described in Section 8.6 of the background estimate are shown. Figures published in [5].

where p is a particular SM process normalised by the fit and “Other” the rest of the processes taken directly from simulations. The results are presented in Figure 8.26b where it can be seen that there is overall good agreement between the data and the estimated SM yield. The largest discrepancy is found in the VRA0 ℓ -M but accounts only for 1.4 standard deviations. As a reminder to the reader, the significance definition used in this analysis stems from the p-value definition of Eq. 6.7.

In the fit described above and all the results presented in the last section the full set of the systematics uncertainties considered for this analysis is included. The next section is dedicated to detail each one of them.

8.6 Systematic Uncertainties

The systematic uncertainties treatment follows closely the concepts presented for the gluino search in Section 7.7. The uncertainties are categorised into (1) experimental, (2) theoretical and (3) statistical components and their effect on the final observables is estimated by varying specific parameters, within their uncertainties (1σ), on the simulated events only. This section is dedicated to describe each one of these parameters.

The discussion on the uncertainties cancellation is relevant to this analysis as well, with residual only uncertainties to affect the estimated yield of major background processes that are normalised in CRs. Finally, the systematic uncertainties on the signal model are included only during the result interpretation via the exclusion fit described in Section 6.2.3 and do not canceled at all.

8.6.1 Experimental Uncertainties

As the same experimental techniques are used for both the sbottom and the gluino searches presented in this dissertation the uncertainties related to the objects reconstruction and the data-taking conditions originate from the same component and have the same treatment. For the reader, all the experimental uncertainties presented in Section 7.7 should be considered as a base and only the differences regarding this search are presented below.

Jets

1. Energy Scale: A difference with the JES uncertainty described previously is the application of a more sophisticated reduction scheme that preserves higher level of correlation among the different component: the roughly 100 parameters are combined in a reduced set of six for this search. In any case, studies have shown that the the final observables are insensitive to the correlation of the different JES components. The JES uncertainty for the dataset used here, as function of a jet p_T , can be seen in Figure 8.28 and it's overall below 5%.
2. Energy Resolution: Similarly to the JES, the reduction scheme of the JER has been developed for the uncertainty to be described by eight components. Additionally, for the full Run 2 dataset the JER and its uncertainty are estimated from data and shown in Figure 5.6a.
3. JVT Efficiency: The usage of the JVT for PU suppression purposes has been described in Section 5.4. Its efficiency has been measured in data using $Z(\rightarrow \mu\mu) + \text{jets}$ events and uncertainties originating from the $Z + \text{jets}$ process modeling are propagated to the SF correcting the simulation. To estimate these uncertainties impact to the analysis, the SFs are varied by $\pm 1\sigma$.

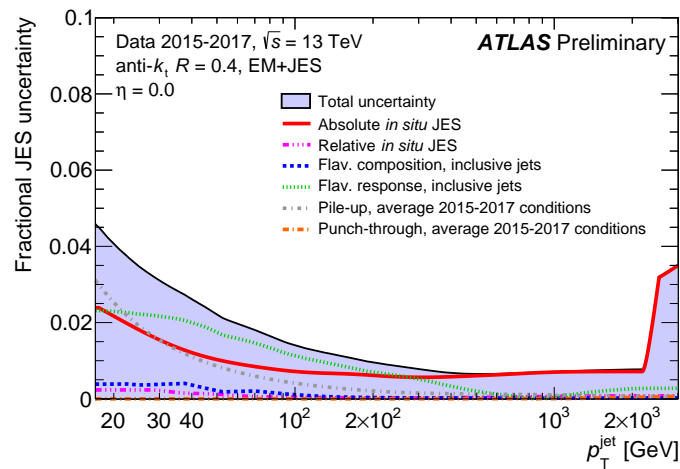


Figure 8.28: The fractional JES uncertainty as function of the jet p_T for $|\eta| = 0$ (relatively stable as function of $|\eta|$) as estimated in the 2015-2017 dataset but used for the 2018 data as well. [141]

Flavour-tagging

The same uncertainty components described previously are used. The difference relies on the values of the mis-identification efficiencies correspond to the full Run 2 dataset (Table 5.4). Thus different SFs with different uncertainties are used.

Missing Energy

In general, the individual uncertainties of each reconstructed object are propagated to both the E_T^{miss} and S calculations while the two additional uncertainties considered (soft-track energy scale & resolution) follow the previous description.

Leptons

As previously, the lepton related uncertainties have minimal impact the results. However, the same components described previously are fully incorporated into the fits. The only difference regarding the full Run 2 dataset is the application of an additional correction to the reconstructed muon momentum accounting for MS tube misalignment. To estimate the effect of the uncertainty of this correction an additional $\pm 1\sigma$ energy scale variation is performed.

Data-taking Conditions

1. Luminosity: The uncertainty on the luminosity of the full Run 2 dataset is 1.7%. This value is using the methods described in Section 3.1. This uncertainty impact is taken into account by scaling by $\pm 1\sigma$ the total integrated luminosity.

8.6.2 Theoretical Uncertainties

The theoretical uncertainties considered on this search might significantly differ to the ones presented in Section 7.7. Thus all the components are explicitly detailed below.

 $t\bar{t}$ Production

1. Hard-Scatter & Matching: An uncertainty is employed by evaluating the difference between the nominal generation program used (Powheg-Box) and the alternative MadGraph5_aMC@NLO.
2. PS & Hadronisation: Similarly, the alternative parton shower and hadronisation program Herwig 7 [202] is used. The difference with the nominal (Pythia) is assigned as a systematic uncertainty.
3. I/FSR Radiation: The amount of initial- and final-state radiation is increased (decreased) by shifting the $h_{\text{damp}} = 3 m_{\text{top}}$ ($h_{\text{damp}} = 1.5 m_{\text{top}}$), multiplying the renormalisation and factorisation scales by 0.5 (2) and using a high-radiation (low-radiation) variation of the A14 tune [203]. The differences to the nominal setup are interpreted as two uncertainties (ISR and FSR).

 $t\bar{t}$ Associated Production

1. $t\bar{t}Z$: A constant over kinematic observables 12% uncertainty is employed to account for inaccuracy on the calculated cross-section.
2. $t\bar{t}H$: Similarly, a 30% uncertainty is employed for the top processes involving a

Higgs boson.

Z + jets Production

1. Scales: To estimate the effect of the renormalisation, factorisation, matching and resummation scale¹ choices, a parametrisation based on the truth number of jets is used. These relative uncertainties have all merged to one parameter since the analysis has found insensitive to their correlation.

SUSY Production

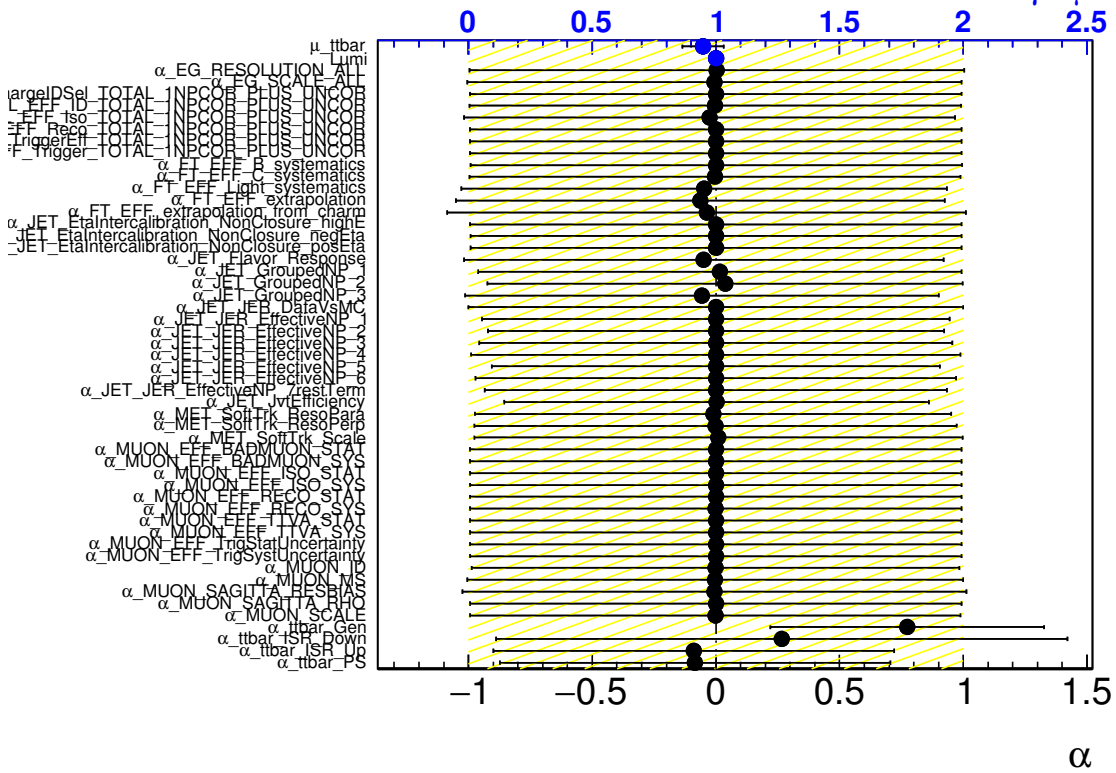
1. cross-section: The cross-section of each signal model is varied by $\pm 1\sigma$ around the it's nominal value [192–195]. The difference on the final observable (CLs) is regarded as the cross-section uncertainty and accounts between 7% and 17% for \tilde{b} masses in the range of 400 to 1500 GeV.
2. ISR Radiation: An additional uncertainty to account for the ISR radiation modeling has been calculated by applying alternative radiation tunes to the hadronisation model (Pythia), similarly to the $t\bar{t}$ case described above. This uncertainty can contribute up to 10%, especially for models targeted by SRB where an ISR jet is selected.

In cases when a single parameter is constrained in more than one regions (e.g. $\mu_{t\bar{t}}$ in CRA1 ℓ m_{eff} bins) it is not unexpected that the nuisance parameters of the fit (i.e. systematic uncertainties) are shifted from their initial values (*pulling*) or constrained. It is generally accepted that pulls within 1σ of the initial uncertainty are adequate and imply that alternative models better describe the data. The Figure 8.29a shows the pulls of the nuisance parameters of the background-only fit in CRA1 ℓ . No deviation more than 1σ from the initial value is observed. The largest pull found on the uncertainty originating from the hard-scatter simulation and parton shower to hadronisation matching choices made on the modeling of the $t\bar{t}$ process. This behavior is explained by the fact that the alternative program (MadGraph5_aMC@NLO) predicts the shape of m_{eff} better than the nominal (Powheg-Box) in CRA1 ℓ , as shown in Figure 8.29b. This is effectively fixing the mismodeling shown in Figure 8.19. Detailed studies have shown that this is not a general characteristic over many observables and the Powheg-Box is still used as the nominal program [180].

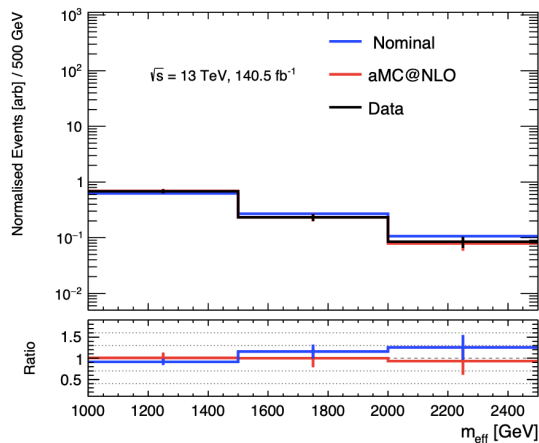
8.7 Results

The good agreement between the estimated SM yield and observed data events in the various VRs, presented in Figure 8.26b, gives confidence that the background model is robust. This is further supported by the good modeling of important variables in the CRs (Figure 8.27) and the minimal post-fit pulls of the different systematic uncertainties (Figure 8.29a). Following these observations, the background estimation is extrapolated to the SRs and the corresponding data are unblinded. The results are detailed in

¹The equivalent of h_{damp} parameter.



(a)



(b)

Figure 8.29: (a) The pulls of the nuisance parameters of the background-only fit performed in CRA1 l . The yellow band shows 1σ uncertainty on the initial value of the parameters and the black dot its fitted value. (b) Distribution of the m_{eff} of the $t\bar{t}$ processes for the nominal (Powheg-Box) and the MadGraph5_aMC@NLO programs in CRA1 l . The bottom panel compares distributions shapes with the observed data. Both figures comprise an original work of the author.

Tables 8.14 and 8.15 and summarised in Figure 8.30. The bottom panel of Figure 8.30 presents the significance of the difference between the estimated background and data yield in terms of standard deviations for each SR. No significant excess of data over the expected SM background is observed in any SR. The largest deviation found in SRC22 and has a local significance of 1.1.

Table 8.14: The background-only fit results extrapolated to the SRA and SRB along with the observed data yield. The uncertainty includes both the statistical and systematic components. Table published in [5].

	SRA	SRA-L	SRA-M	SRA-H	SRB
Observed events	17	12	3	2	3
Fitted SM bkg events	17.1 ± 2.8	8.4 ± 1.7	5.7 ± 0.8	3.0 ± 1.5	3.3 ± 0.9
$t\bar{t}$	10.1 ± 2.5	4.7 ± 1.5	3.7 ± 0.6	1.7 ± 1.4	2.3 ± 0.8
Z +jets	2.6 ± 0.4	1.3 ± 0.2	0.9 ± 0.2	0.4 ± 0.1	0.3 ± 0.1
Single-top	1.4 ± 0.3	0.4 ± 0.1	0.3 ± 0.1	0.6 ± 0.2	0.5 ± 0.1
$t\bar{t} + W/Z$	1.2 ± 0.3	0.7 ± 0.1	0.3 ± 0.1	0.1 ± 0.0	0.07 ± 0.02
$t\bar{t} + h$	1.1 ± 0.2	0.7 ± 0.1	0.3 ± 0.1	0.1 ± 0.0	0.13 ± 0.02
W +jets	0.4 ± 0.1	0.2 ± 0.1	0.1 ± 0.0	–	0.02 ± 0.01
Diboson	0.4 ± 0.1	0.3 ± 0.1	–	–	–
$m(\tilde{b}_1, \tilde{\chi}_2^0, \tilde{\chi}_1^0) = (1100, 330, 200)$ GeV	13.7 ± 0.3	0.7 ± 0.1	6.3 ± 0.2	6.6 ± 0.2	0.3 ± 0.1
$m(\tilde{b}_1, \tilde{\chi}_2^0, \tilde{\chi}_1^0) = (700, 680, 550)$ GeV	1.3 ± 0.6	0.2 ± 0.1	0.5 ± 0.4	0.6 ± 0.4	7.4 ± 1.2
$m(\tilde{b}_1, \tilde{\chi}_2^0, \tilde{\chi}_1^0) = (1200, 1150, 60)$ GeV	8.7 ± 0.2	1.4 ± 0.1	3.4 ± 0.1	3.8 ± 0.1	0.6 ± 0.1

Table 8.15: The background-only fit results extrapolated to the SRC along with the observed data yield. The uncertainty includes both the statistical and systematic components. Table published in [5].

	SRC	SRC22	SRC24	SRC26	SRC28
Observed events	47	28	12	4	3
Fitted SM bkg events	37.9 ± 6.2	21.2 ± 4.1	10.6 ± 2.3	3.7 ± 0.9	2.4 ± 0.6
$t\bar{t}$	5.4 ± 2.6	3.9 ± 2.3	1.1 ± 0.6	0.3 ± 0.3	0.1 ± 0.1
Z +jets	17.6 ± 4.7	8.8 ± 2.5	6.0 ± 1.8	1.7 ± 0.7	1.1 ± 0.4
Single-top	5.0 ± 1.5	2.7 ± 1.0	1.2 ± 0.3	0.7 ± 0.2	0.4 ± 0.1
$t\bar{t} + W/Z$	4.3 ± 0.6	2.5 ± 0.4	1.1 ± 0.2	0.5 ± 0.1	0.2 ± 0.1
$t\bar{t} + h$	0.2 ± 0.0	0.2 ± 0.0	–	0.1 ± 0.0	0.0 ± 0.0
W +jets	3.5 ± 0.8	2.2 ± 0.5	0.6 ± 0.2	0.2 ± 0.1	0.4 ± 0.1
Diboson	1.8 ± 0.3	0.9 ± 0.2	0.6 ± 0.1	0.2 ± 0.0	0.1 ± 0.1
$m(\tilde{b}_1, \tilde{\chi}_2^0, \tilde{\chi}_1^0) = (1100, 330, 200)$ GeV	0.4 ± 0.1	0.3 ± 0.1	0.1 ± 0.0	0.03 ± 0.02	0.03 ± 0.01
$m(\tilde{b}_1, \tilde{\chi}_2^0, \tilde{\chi}_1^0) = (700, 680, 550)$ GeV	1.2 ± 0.5	0.5 ± 0.2	0.7 ± 0.4	–	–
$m(\tilde{b}_1, \tilde{\chi}_2^0, \tilde{\chi}_1^0) = (1200, 1150, 60)$ GeV	26.7 ± 0.3	6.3 ± 0.2	6.4 ± 0.2	5.8 ± 0.2	8.3 ± 0.2

The total systematic uncertainty on the background estimate of SRA and SRB is 16% and 27% respectively. The higher uncertainty for SRB is regarded to the more extreme phase space explored (ISR plus 4 b-jets). The major uncertainties for the SRA and SRB are the theoretical uncertainties of the $t\bar{t}$ production. In particular, the ones related to the parton shower/hadronisation model and FSR radiation. This is expected from the

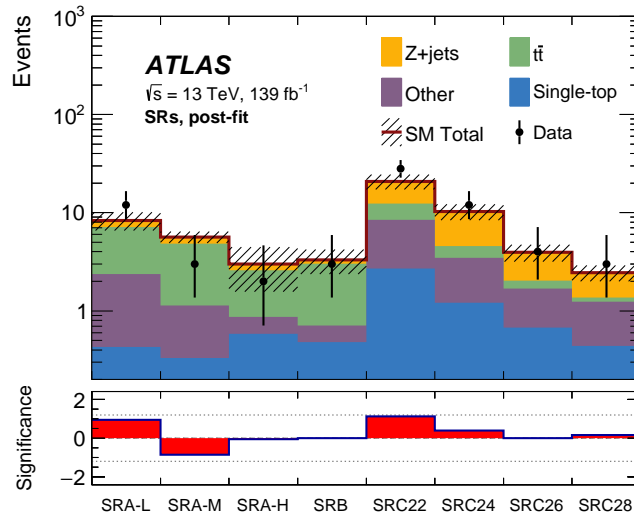


Figure 8.30: Unblinded results for all the SRs considered. The top panel shows the predicted and observed yields and the bottom the significance [157] of their difference. Both the statistical and systematic uncertainties of the background estimate are shown. Figure published in [5].

high b-jet multiplicity (and the ISR for the SRB) phase space selection. The b-jets beyond the ones from the $t\bar{t}$ decay originating from gluon splitting ($g \rightarrow b\bar{b}$) that is modeled at the showering and not at the matrix element calculation. The larger experimental component arise from the uncertainty of the c-quark mis-identification SF but it only accounts to about 4% (9%) for the SRA (SRB).

Regarding the SRC, the total systematic uncertainty is 16% with the experimental and theoretical components to have similar contributions. The dominant theoretical uncertainty originates from the scales considered on the modeling of the Z + jets process followed by uncertainties originating from the hard-scatter and matching scheme choices for the $t\bar{t}$ process modeling. The major experimental uncertainty originates from the JES variations described above followed by the uncertainty of the c-quark mis-identification SF, as previously.

A summary of the different uncertainty contributions described above is presented in Table 8.16 for all the SRs.

Table 8.16: The relative systematic uncertainty of the background estimate of all the SRs considered. Different components are listed but can be correlated, such that they do not necessarily add up in quadrature to the total uncertainty. Table published in [5].

Region	SRA		SRB		SRC	
Total background expectation	17.1		3.3		37.9	
Total background uncertainty	2.8	(16%)	0.9	(27%)	6.2	(16%)
Systematic, experimental	1.4	(8%)	0.3	(10%)	3.0	(8%)
Systematic, theoretical	2.3	(13%)	0.6	(18%)	3.2	(8%)
Statistical, MC samples	0.7	(4%)	0.4	(12%)	2.0	(5%)

Finally, Figure 8.31 shows distributions of important kinematic variables in SRA, SRB and SRC before the specific selection is applied. The plots compare the expected SM background, the observed data distributions. Relevant benchmark signal models are also overlaid.

8.8 Interpretation

Since no significant excess of data above the expected SM background is observed in any of the SRs (Figure 8.30), the results are used to place one-sided upper limits at 95% CL on possible BSM scenarios. These scenarios include both the SUSY model motivated and optimised this search and a general BSM scenario with no particular model assumption; the so-called model-dependent and model-independent limits respectively. These are derived by the exclusion and discovery fits respectively (Sections 6.2.3 and Section 6.2.4).

All the systematic uncertainties of the SM background, listed in Section 8.6, are considered in both the exclusion and discovery fits. In the case of the exclusion fit only, experimental and theoretical uncertainties on the SUSY signal yield are considered as well. The size of the former is found to be between 6% and 36% for the signal scenarios targeted by SRA, between 11% and 37% for scenarios targeted by SRB and between 4% and 40% for scenarios targeted by SRC. In general, these are largely dominated by the uncertainty on the b-tagging efficiency.

8.8.1 Model-dependent Limits

The limits are placed on the simplified sbottom model (Figure 8.2) used to optimise this search. All the different $m(\tilde{b}_1), m(\tilde{\chi}_2^0), m(\tilde{\chi}_1^0)$ model-points presented in Figures 8.3a and 8.3b are considered independently in exclusion fits and via the the CL_s prescription the signal-plus-background hypothesis is tested against the background-only hypothesis.

Each SR type (A, B, C) is considered independently. However, for the SRA and SRC cases, the corresponding m_{eff} and \mathcal{S} bins are statistically combined giving a better exclusion sensitivity in a wide range of the parameter-space. The exclusion contours are presented in Figures 8.32 and 8.33. Following each region target, the SRA results are interpreted for both the DM130 and N60 grids while the SRB and SRC only for the DM130 and N60 respectively. The expected limit is derived using the fitted – by the exclusion fit under the background-only hypothesis – SM background and the simulated SUSY signal yields in each SR. The uncertainty band indicates the 1σ variation of the limit while varying the yields within the total uncertainty apart from the theoretical uncertainties of the signal. On the other hand, the observed limit is obtained by substituting the fitted background with the observed data yield and the uncertainty band by varying the signal yield within 1σ of its theoretical uncertainty.

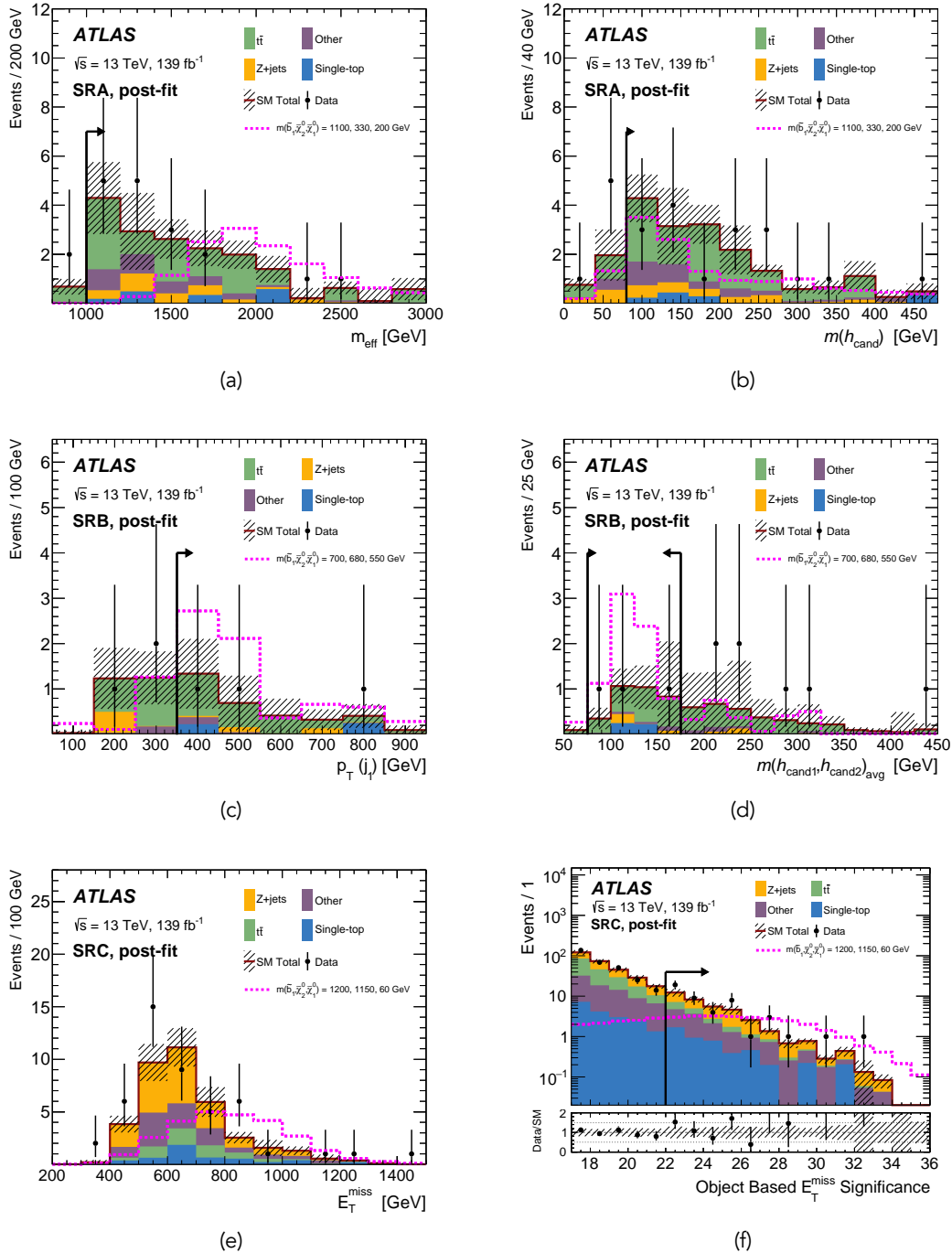
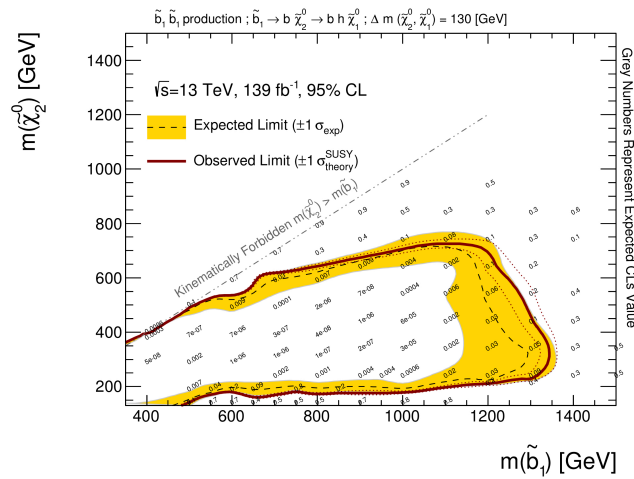


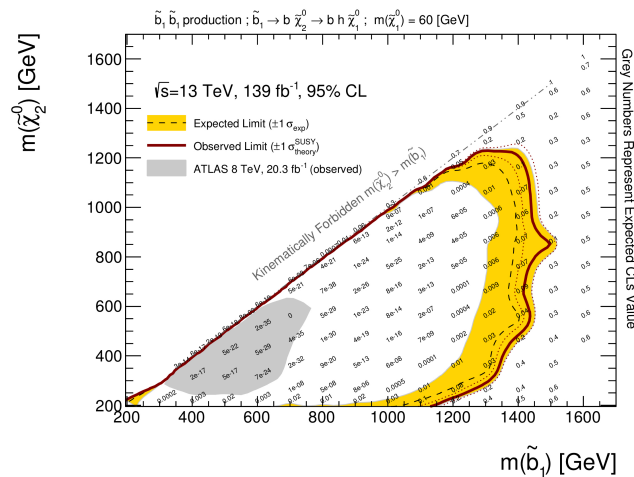
Figure 8.31: Distributions of (a) m_{eff} , (b) $m(h_{\text{cand}})$, (c) $p_{\text{T}}(j_1)$, (d) $m(h_{\text{cand}1}, h_{\text{cand}2})_{\text{avg}}$, (e) $\tilde{E}_{\text{T}}^{\text{miss}}$ and (d) \mathcal{S} . The selection applied is the relevant SR, before the corresponding variable selection, except of (e) where the full SRC selection is applied. Backgrounds with minor contribution ($t\bar{t}V$, $t\bar{t}H$, $W + \text{jets}$, Diboson) are grouped and labelled as "Other". Both the statistical and systematic uncertainties of the background estimate are shown. Figures published in [5].

Furthermore, the limits of each region are combined to derive two final ones; one for the DM130 and one for the N60 scenario. Similarly to the methodology followed in the gluino search, the region that provides the best expected CL_s (grey numbers of Figures 8.32 and 8.33) is used per model-point while no statistical combination is taking place. The combined limits are presented in Figure 8.34.

Sbottom masses up to 1.3 TeV (1.45 TeV) have been excluded for models based on the DM130 (N60) mass assumption. The largest $\tilde{\chi}_2^0$ mass excluded is 1.25 TeV for \tilde{b}_1 mass of 1.3 TeV and $\tilde{\chi}_1^0$ 60 GeV.

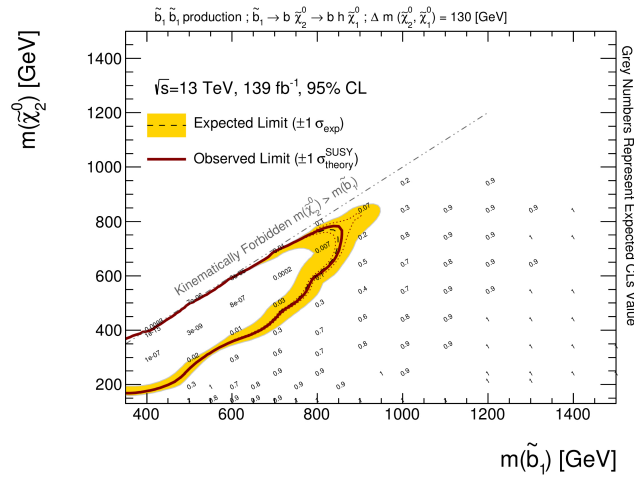


(a) SRA at DM130

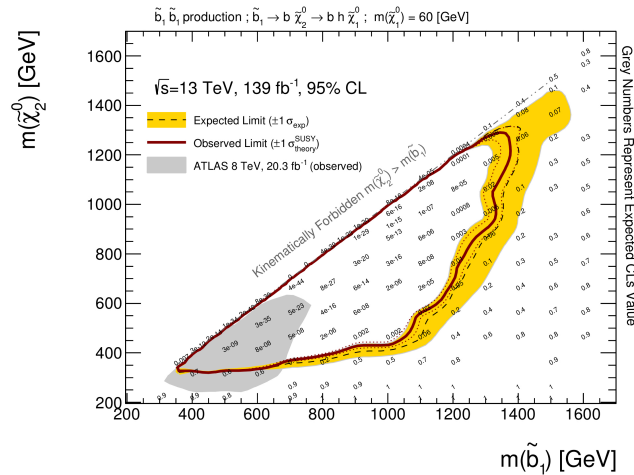


(b) SRA at N60

Figure 8.32: Exclusion contours at 95% CL based on the results of the SRA. Models following the DM130 (N60) mass assumption are shown on the left column (right). The ATLAS Run 1 (8 TeV) limit is taken from [162]. Figure courtesy of the ATLAS Collaboration.



(a) SRB at DM130



(b) SRC at N60

Figure 8.33: Exclusion contours at 95% CL based on the results of the SRB and SRC. Models following the DM130 (N60) mass assumption are shown on the left column (right). The ATLAS Run 1 (8 TeV) limit is taken from [162]. Figure courtesy of the ATLAS Collaboration.

8.8.2 Model-independent Limits

Last but not least, model-independent limits are also placed using the analysis results, in the same way as presented in Section 7.9.2. In particular, a general BSM signal is considered and 95% CL upper limits are placed on its possible event yield. The limits presented in this section are placed by performing the discovery fit only in the inclusive SRs – no m_{eff} or \mathcal{S} bins are considered as this assumes the knowledge of the signal distribution over the corresponding variable.

Table 8.17 lists the upper limits on the number of possible BSM events, the visible cross-section and the background-only hypothesis p-value. The weakest limits that correspond to SRC originate from the slight excess of data observed in SRC22 (Figure 8.30).

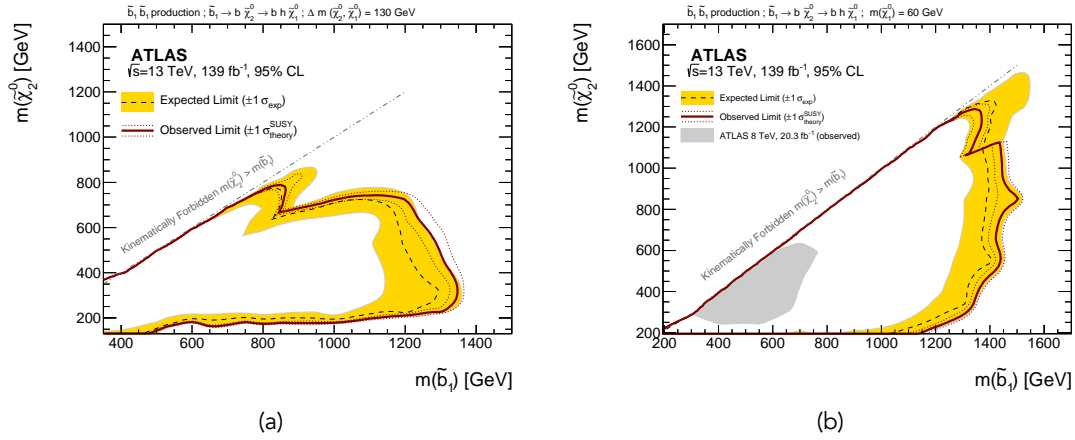


Figure 8.34: Combined exclusion contours at 95% CL based on the results of all the SRs for (a) models following the DM130 and (b) the N60 mass assumptions. The ATLAS Run 1 (8 TeV) limit is taken from [162]. Figures published in [5]

Table 8.17: The model-independent limits derived for each SR. The first (second) column lists the expected (observed) 95% CL upper limit on a BSM process yield and the third one on the visible cross-section. The last column lists the discovery p-value, i.e. the probability of a background-only fluctuation resulting at least as extreme results as observed. The latter is truncated at 0.50.

Signal Region	S_{exp}^{95}	S_{obs}^{95}	σ_{vis} [fb]	p_0
SRA	$10.1^{+4.7}_{-3.1}$	9.0	0.06	0.50
SRB	$5.1^{+2.8}_{-1.7}$	4.9	0.04	0.50
SRC	$20.8^{+7.0}_{-5.5}$	26.0	0.19	0.17

8.9 Conclusion

A search for the pair production of sbottom quarks decaying in a complex scenario was presented in this chapter. The full Run 2 dataset, collected from 2015 to 2018 by the ATLAS detector, was used and corresponds to 139 fb^{-1} of $\sqrt{s} = 13 \text{ TeV}$ pp collisions. The particular SUSY scenario searched for consists of sbottom quarks that decay to b-quarks and the second-to-lightest neutralinos ($\tilde{\chi}_2^0$), with the subsequent decay of the $\tilde{\chi}_2^0$ to a Higgs boson and the LSP ($\tilde{\chi}_1^0$). As the dominant decay of the Higgs boson to b-quarks is considered, the resulting final state has a unique, for BSM physics searches, configuration of zero leptons, up to six b-jets and large missing energy. To probe such extreme phase space was only recently feasible due to the large statistical power of the full Run 2 dataset. On the drawback, the SM processes with such high energetic b-jets are poorly constrained by measurements so novel data analysis techniques are employed to cope with the kinematic discriminant mismodeling observed.

As no significant excess of data above the expected SM background is observed, the simplified model investigated is constrained. In particular, sbottom quark masses

up to 1.5 (1.3) TeV are excluded for $\tilde{\chi}_2^0$ masses up to 1100 (750) GeV in models with fixed $m(\tilde{\chi}_1^0) = 60$ GeV ($\Delta m(\tilde{\chi}_2^0, \tilde{\chi}_1^0) = 130$ GeV). This is the first constrain of the model with fixed $\Delta m(\tilde{\chi}_2^0, \tilde{\chi}_1^0)$ placed by the ATLAS collaboration and, in general, the results of this work are the strongest constrains of the third generation SUSY squark sector placed by accelerator-based experiments.

Such a high sensitivity is a virtue of the extreme phase space explored. Only few SM processes can generate such many and high energetic b-jets thus the reduced background offers higher search reach. This is apparent in Figure 8.35 where the analysis of this work (green) place the tightest exclusion limit on the sbottom quark mass compared to other analysis that look into simpler final states. This behavior showcases the power of a larger dataset, complex topologies can be studied and more BSM scenarios can be searched for.

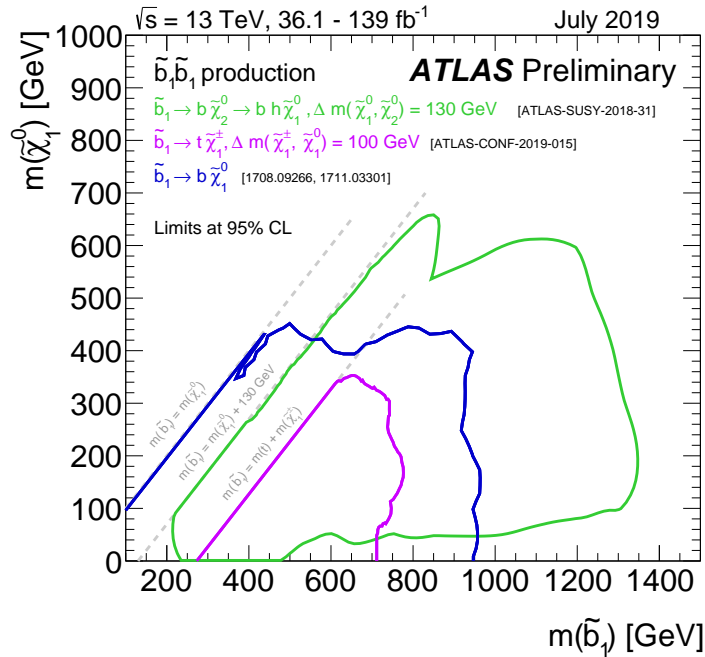


Figure 8.35: Combined exclusion limit on the $m(\tilde{b}_1) - m(\tilde{\chi}_1^0)$ mass plane of three independent SUSY analysis exploring different final states. The limit derived by the analysis of this work is indicated by green. The blue limit is placed by an analysis studying a final state with two b-jets and potentially a lepton, and the purple by an analysis studying a final state with jets and either two leptons with the same charge or at least three leptons. [89]



9. Conclusions and Outlook

The (HL-)LHC is going to probe no more or no less of what exactly nature has created

Given multiple observations, such as the presence of DM, there is scientific consensus that the SM is far from a complete model to describe all of the phenomena that occur in the Universe. SUSY is an extension of the SM that has the potential to explain several phenomena by introducing an extended space-time symmetry where fermion partners are associated to the SM bosons and vice versa. The new partners introduced not only act as DM candidates, but also alleviate theoretical gaps in the model, as the stabilisation the Higgs mass from higher-order radiative corrections. SUSY is an appealing hypothesised feature of nature that motivated the new physics phenomena searched in this work. In particular, data from the LHC Run 2 $\sqrt{s} = 13$ TeV pp collisions, collected with the ATLAS detector, were used to investigate the production of SUSY particles.

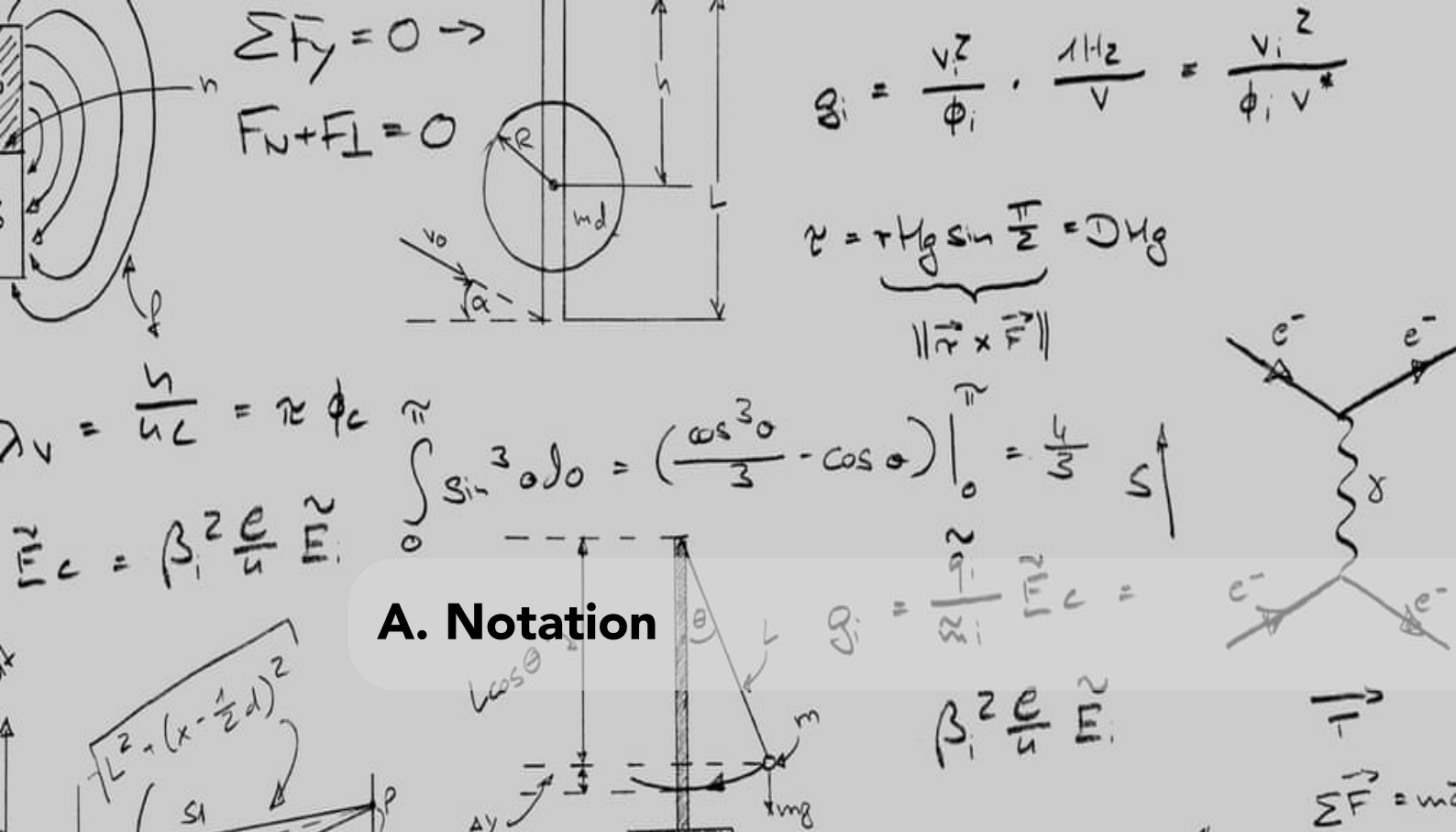
Two SUSY searches are presented throughout this dissertation exploring an extreme phase space with the main characteristic being the presence of multiple b-jets and large missing energy. This is only recently feasible because of the large statistical power of the LHC Run 2 dataset. However, in such cases it is hard to achieve a trustful estimate of the SM background and besides superior detector understanding and performance, novel data analysis techniques, such as multi-bin fits, have been employed.

No significant excess of events above the predicted SM background is observed

in both searches conducted in this dissertation. First, a search for the pair production of gluinos via third generation squarks is detailed. Using this analysis, gluino masses up to 1.97 (1.92) TeV have been excluded, at 95% CL, in cases where the gluinos are assumed to decay via top (bottom) squarks and for $\tilde{\chi}_1^0$ masses below 300 GeV. The results are also interpreted as function of the gluino branching ratio to the various third generation squark configurations. For instance, gluino masses up to 1.9 TeV, for almost massless $\tilde{\chi}_1^0$, have been excluded only if $\text{BR}(\tilde{g} \rightarrow t\bar{b}\tilde{\chi}_1^-) < 10\%$. Second, a search for the pair production of sbottom quarks in scenarios where the sbottom decays via an intermediate $\tilde{\chi}_2^0$ state and lead to final states with Higgs bosons is detailed. The results of this work have excluded sbottom masses up to 1.5 (1.3) TeV, for $\tilde{\chi}_2^0$ masses up to 1100 (750) GeV, in models with fixed $m(\tilde{\chi}_1^0) = 60$ GeV ($\Delta m(\tilde{\chi}_2^0, \tilde{\chi}_1^0) = 130$ GeV). Both analyses results significantly improve upon the exclusion limits obtained with the Run 1 dataset.

This work is not a unique example of absence of new physics signals in the datasets produced at the LHC is not a unique characteristic of this work (or even of the SUSY searches). Only the recent years the unprecedented collision energy allows to probe higher mass scale phenomena and to explore a new physics energy regime at the multi-TeV energy scale where BSM physics are theoretically expected. As an example, currently the SUSY mass scale reach of the LHC is at about 1-2 TeV (see Figure 2.7) while theoretical calculations expect the M_S to be at few TeV to explain the Higgs mass at the MSSM (see Figure 2.3a). Last but by no means least, all the derived sparticle mass limits referred above are based on models usually conceiving a phenomenologically oversimplified view of nature.

Looking towards the future, the HL-LHC is expected to start data-taking data in 2026 with an increased collision energy. The true virtue, though, comes from the much greater in size dataset to be collected. The higher luminosity – that comes with higher radiation tolerance demands in detector technology, a topic studied in the context of this dissertation – will allow the investigation of more realistic, thus complex, and rare BSM physics scenarios. These BSM searches should not only focus on the heavy mass scale regime but in corners of the currently explored scale as well. This would be only achieved with advances in analysis techniques and detector performance.



A. Notation

This appendix summarise all the undefined notation (Table A.1), excluding the SI units, and the abbreviations (Table A.2) used in the main text of this dissertation. The values of the CKM matrix elements are also explicitly given (Table A.3).

It should be also stressed that the so-called *natural* unit system is generally used – unless explicit \hbar or c symbols are present in equations or the discussion is related to macroscopic sizes, e.g. the detector dimensions. In this system the speed of light (c) is equal to the reduced Planck constant ($\hbar = h/2\pi$) and are both one:

$$c = \hbar = 1. \tag{A.1}$$

In this system the mass has the same units as the energy (e.g. GeV) and the time and leng units of inverse energy (e.g. GeV⁻¹).

Table A.1: Summary of the undefined symbols used in the main text.

Symbol	Definition
c	Speed of light: 299,792,458 m s ⁻¹
h	Planck's constant: 6.63×10^{-34} m ² kg s ⁻¹
eV	Electronvolt: 1 eV \simeq 1.6 J
h	Normalised Hubble constant: $h = H_0/100 \simeq 0.67$ km s ⁻¹ Mpc ⁻¹ = 0.22×10^{-10} s ⁻¹ [204]

∂_μ	Covariant four-gradient: $\partial_\mu = \left(\frac{\partial}{\partial t}, \frac{\partial}{\partial x}, \frac{\partial}{\partial y}, \frac{\partial}{\partial z} \right)$
$F_{\mu\nu}$	Covariant field-strength tensor: $F_{\mu\nu} = \partial_\mu A_\nu - \partial_\nu A_\mu$, where A a vector field four-potential.
Ψ^\dagger	Wavefunction Hermitian conjugate: $\Psi^\dagger = (\Psi^*)^T$
$U(n)$	Unitary group: group of $n \times n$ unitary matrices.
$SU(n)$	Special unitary group: group of $n \times n$ unitary matrices with determinant one.
γ	Lorentz factor: $1/\sqrt{1 - \frac{v^2}{c^2}}$, where v the relative velocity of an object.
β	Ratio of v to c : v/c
σ^k	Pauli matrices: $\sigma^1 = \begin{pmatrix} 0 & 1 \\ 1 & 0 \end{pmatrix}$, $\sigma^2 = \begin{pmatrix} 0 & -i \\ i & 0 \end{pmatrix}$, $\sigma^3 = \begin{pmatrix} 1 & 0 \\ 0 & -1 \end{pmatrix}$
γ^μ	γ -matrices: $\gamma^0 = \begin{pmatrix} 1 & 0 & 0 & 0 \\ 0 & 1 & 0 & 0 \\ 0 & 0 & -1 & 0 \\ 0 & 0 & 0 & -1 \end{pmatrix}$, $\gamma^1 = \begin{pmatrix} 0 & 0 & 0 & 1 \\ 0 & 0 & 1 & 0 \\ 0 & -1 & 0 & 0 \\ -1 & 0 & 0 & 0 \end{pmatrix}$, $\gamma^2 = \begin{pmatrix} 0 & 0 & 0 & -i \\ 0 & 0 & i & 0 \\ 0 & i & 0 & 0 \\ -i & 0 & 0 & 0 \end{pmatrix}$, $\gamma^3 = \begin{pmatrix} 0 & 0 & 1 & 0 \\ 0 & 0 & 0 & -1 \\ -1 & 0 & 0 & 0 \\ 0 & 1 & 0 & 0 \end{pmatrix}$, $\gamma^5 = \begin{pmatrix} 0 & 0 & 1 & 0 \\ 0 & 0 & 0 & 1 \\ 1 & 0 & 0 & 0 \\ 0 & 1 & 0 & 0 \end{pmatrix}$
λ^α	Gell-Mann matrices: $\lambda^1 = \begin{pmatrix} 0 & 1 & 0 \\ 1 & 0 & 0 \\ 0 & 0 & 0 \end{pmatrix}$, $\lambda^2 = \begin{pmatrix} 0 & -i & 0 \\ i & 0 & 0 \\ 0 & 0 & 0 \end{pmatrix}$, $\lambda^3 = \begin{pmatrix} 1 & 0 & 0 \\ 0 & -1 & 0 \\ 0 & 0 & 0 \end{pmatrix}$, $\lambda^4 = \begin{pmatrix} 0 & 0 & 1 \\ 0 & 0 & 0 \\ 1 & 0 & 0 \end{pmatrix}$, $\lambda^5 = \begin{pmatrix} 0 & 0 & -i \\ 0 & 0 & 0 \\ i & 0 & 0 \end{pmatrix}$, $\lambda^6 = \begin{pmatrix} 0 & 0 & 0 \\ 0 & 0 & 1 \\ 0 & 1 & 0 \end{pmatrix}$, $\lambda^7 = \begin{pmatrix} 0 & 0 & 0 \\ 0 & 0 & -i \\ 0 & i & 0 \end{pmatrix}$, $\lambda^8 = \frac{1}{\sqrt{3}} \begin{pmatrix} 1 & 0 & 0 \\ 0 & 1 & 0 \\ 0 & 0 & -2 \end{pmatrix}$

Table A.2: Summary of all the abbreviations used in the main text.

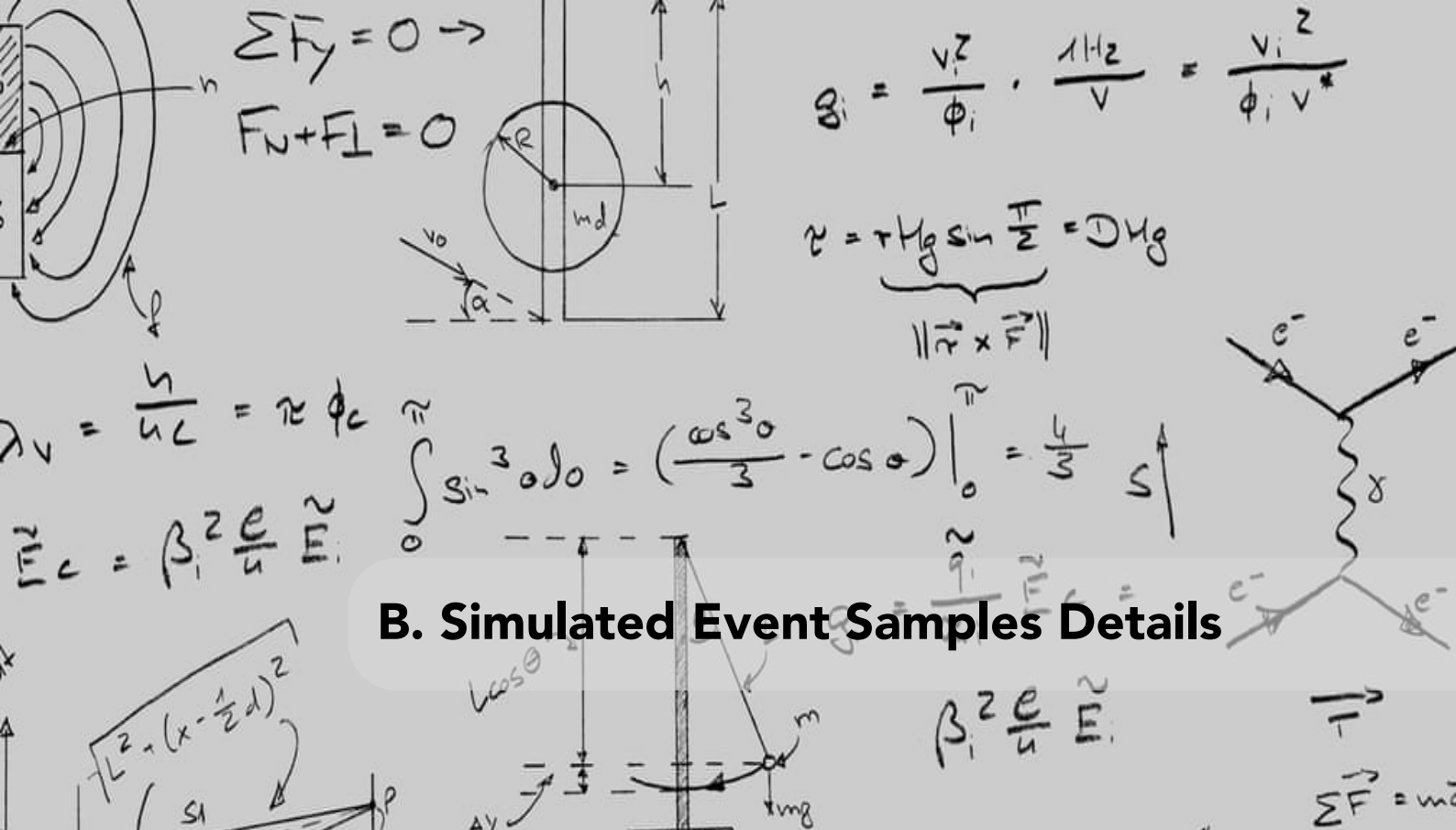
Abbreviation	Definition
ADC	Analogue to Digital Converted
ATLAS	A Toroidal LHC Apparatus
BDT	Boosted Decision Tree

BEH	Brout-Englert-Higgs
BR	Branching Ratio
BSM	Beyond Standard Model
CCE	Charge Collection Efficiency
CL	Confidence Level
CKM	Caribbo-Kobayashi-Maskawa
CR	Control Region
DM	Dark Matter
EMCal	Electromagnetic Calorimeter
FCal	Forward Calorimeter
FSR	Final State Radiation
HCal	Hadronic Calorimeter
HLT	High Level Trigger
HV	High Voltage
IBL	Insertable B-Layer
Id	Identification Class
ID	Inner Detector
IP	Interaction Point
ISR	Initial State Radiation
ITk	Inner Tracker
JER	Jet Energy Resolution
JES	Jet Energy Scale
JVT	Jet Vertex Tagger
LH-LHC	High-Luminosity Large Hadron Collider
LHC	Large Hadron Collider
LSP	Lightest Supersymmetric Particle
MC	Monte Carlo
MDT	Monitored Drift Tubes
MIP	Minimum-Ionising Particle
MS	Muon Spectrometer
MSSM	Minimal Supersymmetric Standard Model
NLSP	Next-to-Lightest Supersymmetric Particle
PDF	Parton Distribution Function
<i>pdf</i>	Probability Density Function
PMNS	Pontecorvo–Maki–Nakagawa–Sakata
pMSSM	Phenomenological Minimal Supersymmetric Standard Model
PS	Parton Shower
PU	Pile-Up
PV	Primary Vertex

QCD	Quantum Chromodynamics
QED	Quantum Electrodynamics
QFT	Quantum Field Theory
S/N	Signal-to-Noise Ratio
SCT	SemiConductor Tracker
SFOS	Same Flavour Opposite-Sign
SM	Standard Model
SR	Signal Region
SSB	Spontaneous Symmetry Breaking
SUSY	Supersymmetry
SV	Secondary Vertex
TRT	Transition Radiation Tracker
TV	Tertiary Vertex
UE	Underlying Event
VEV	Vacuum Expectation Value
VR	Validation Region
VSM	Vector Supermultiplet
xSM	Chiral Supermultiplet

Table A.3: The values of the CKM matrix elements rounded to the second decimal digit. [35]

Element	Value
ud	0.97
us	0.22
ub	0.00
cd	0.22
cs	0.97
cb	0.04
td	0.01
ts	0.04
tb	1.00



B. Simulated Event Samples Details

The purpose of this appendix is to provide technical description regarding the production of the Monte Carlo simulated event samples used for the work described in Chapters 7 and 8. First, the description of the SUSY processes is provided while the SM processes are following.

B.1 SUSY Processes

B.1.1 Gluino model

The sample of the gluino model, described in Section 7.2, is generated using MadGraph5_aMC@NLO v2.2.2 [205] at leading order (LO) in the strong coupling constant including the emission of up to two additional partons. The PDF set used is the NNPDF23-LO [206]. Afterwards, the sample is interfaced with Pythia 8.186 [207] tuned with the A14 [66] set of parameters in order to model the parton showering, hadronisation and underlying event effects. The matching of the matrix element with the parton shower is performed following the CKKW-L prescription [208]. Finally, the samples are normalised to the theoretically calculated cross-sections at next-to-leading order (NLO) in the strong coupling constant adding the resummation of soft gluon emissions at next-to-leading-logarithmic accuracy (NLL) [84, 170–174].

B.1.2 Sbottom model

The sample of the sbottom model, described in Section 8.2, is produced similarly with the gluino model described above. The version of the MadGraph5_aMC@NLO used is 2.2.3 while the Pythia version is 8.210 [209]. The samples are normalised to the theoretically calculated cross-sections at approximate next-to-next-to-leading order (NNLO_{approx.})

in the strong coupling constant adding the resummation of soft gluon emissions at next-to-next-to-leading-logarithmic accuracy (NNLL) [192–195]. The nominal cross-section is derived using the PDF4LHC15_mc PDF set, following the recommendations of Ref. [210].

B.2 SM Processes

B.2.1 Top Pair Production

The production of top quark pairs ($t\bar{t}$) is modeled using the Powheg-Box v2 [211–214] generator at NLO in the strong coupling constant. The PDF set used is the NNPDF23LO. Top quarks are decayed at LO using MadSpin [215, 216] preserving all spin correlations. Afterwards, the events are interfaced with Pythia v8.230 [209], tuned with the A14 set of parameters, in order to model the parton showering, hadronisation and underlying event effects. The h_{damp} parameter set to $1.5 m_{\text{top}}$ [203] while the renormalisation and factorisation scales are set to $\sqrt{m_{\text{top}}^2 + p_{\text{T}}^2}$. The decays of bottom and charm hadrons are simulated using the EvtGen v1.2.0 program [217]. Finally, the samples is normalised to the theoretically calculated cross-section at next-to-next-to-leading order (NNLO) in the strong coupling constant including the resummation of NNLL soft-gluon emissions calculated using Top++2.0 [175, 218–223].

A slightly older configuration of the programs is used for the generation of the $t\bar{t}$ events used at the work described in Chapter 7. For the matrix element calculation, the PDF set used on the Powheg-Box program is the CT10 [224]. The version of the Pythia used is the 6.428 [60] with CTEQ6L1 PDF set [62] and the PERUGIA2012 [225] set of parameters while the h_{damp} parameter was set to the mass of the top quark (172.5 GeV).

For proton–proton collisions at a centre-of-mass energy of $\sqrt{s} = 13$ TeV, this cross-section corresponds to 832 ± 51 fb using a top-quark mass of 172.5 GeV.

B.2.2 Single-Top Production

In general, the production of single-top quark processes (Wt-channel, s-channel and t-channel) is modeled similarly to the $t\bar{t}$ events described above. The main difference concerns the t-channel production modeling, where the four flavour scheme on the PDF set is employed, i.e. b-quarks are not considered part of the proton and can only appear in the final state thus the t-channel single-top production is initiated by gluon splitting, as shown at the diagram of Figure B.1. Regarding the Wt-channel, the diagram removal scheme [226] was employed to handle the interference with the $t\bar{t}$ production [203].

All the single-top processes are normalised to the best available theoretically calculated production cross-section. For proton–proton collisions at a centre-of-mass energy of $\sqrt{s} = 13$ TeV and using a top-quark mass of 172.5 GeV these cross-section values for the production modes considered are summarised in Table B.1 along with their level of accuracy.

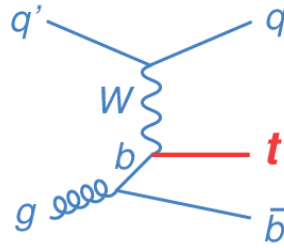


Figure B.1: The t-channel production of single-top quarks considered via the four flavour scheme. Diagram taken from [227].

Table B.1: The cross-sections for the three single-top production modes considered. The values in the parentheses correspond to anti-top quark production.

Production Mode	cross-section [pb]	Accuracy
Wt-channel	71.7 ± 3.8	NLO+NNLL [184, 228]
t-channel	$54.9^{+2.3}_{-1.9}$ ($29.7^{+1.7}_{-1.5}$)	NLO [184, 228]
s-channel	$6.35^{+0.23}_{-0.20}$ ($3.97^{+0.19}_{-0.17}$)	

B.2.3 Associated Top Production

B.2.3.1 $t\bar{t}V$

The production of pair of top quarks in association with a vector boson (Z or W) is modeled using the MadGraph5_aMC@NLO v2.2.3 generator which provides matrix elements at NLO in the strong coupling constant. The PDF set used is the NNPDF23LO. Top quarks are decayed at LO using MadSpin preserving all spin correlations. Afterwards, the events are interfaced with Pythia v8.210, tuned with the A14 set of parameters, in order to model the parton showering, hadronisation and underlying event effects while the renormalisation and factorisation scales are set to $0.5 \times \sum_i \sqrt{m_i^2 + p_{T,i}^2}$, where the sum runs over all the particles generated from the matrix element calculation. The decays of bottom and charm hadrons are simulated using the EvtGen v1.2.0 program.

An older version of Pythia, in particular v8.186, is used for the generation of the $t\bar{t}V$ events used for the work described in Chapter 7.

The cross-sections used to normalise the samples are calculated at NLO QCD and NLO EW accuracies [59]. The $t\bar{t}Z$ cross-section is further supplemented with an off-shell correction. The predicted values at $\sqrt{s} = 13$ TeV are $0.88^{+0.09}_{-0.11}$ pb and $0.60^{+0.08}_{-0.07}$ pb for $t\bar{t}Z$ and $t\bar{t}W$ respectively.

B.2.3.2 $t\bar{t}H$

The production of pair of top quarks in association with a Higgs boson is modeled similarly to the $t\bar{t}V$ processes described above. The only difference regards the work described in Chapter 7; the PDF set used is the CT10 while the program used to model the parton showering, hadronisation and underlying event effects is the Herwig++ v2.7.1

tuned with the UEEE5 [229] set of parameters.

The cross-sections used to normalise the samples are calculated at NLO QCD and NLO EW accuracies [59]. The predicted values at $\sqrt{s} = 13$ TeV are 507^{+35}_{-50} fb.

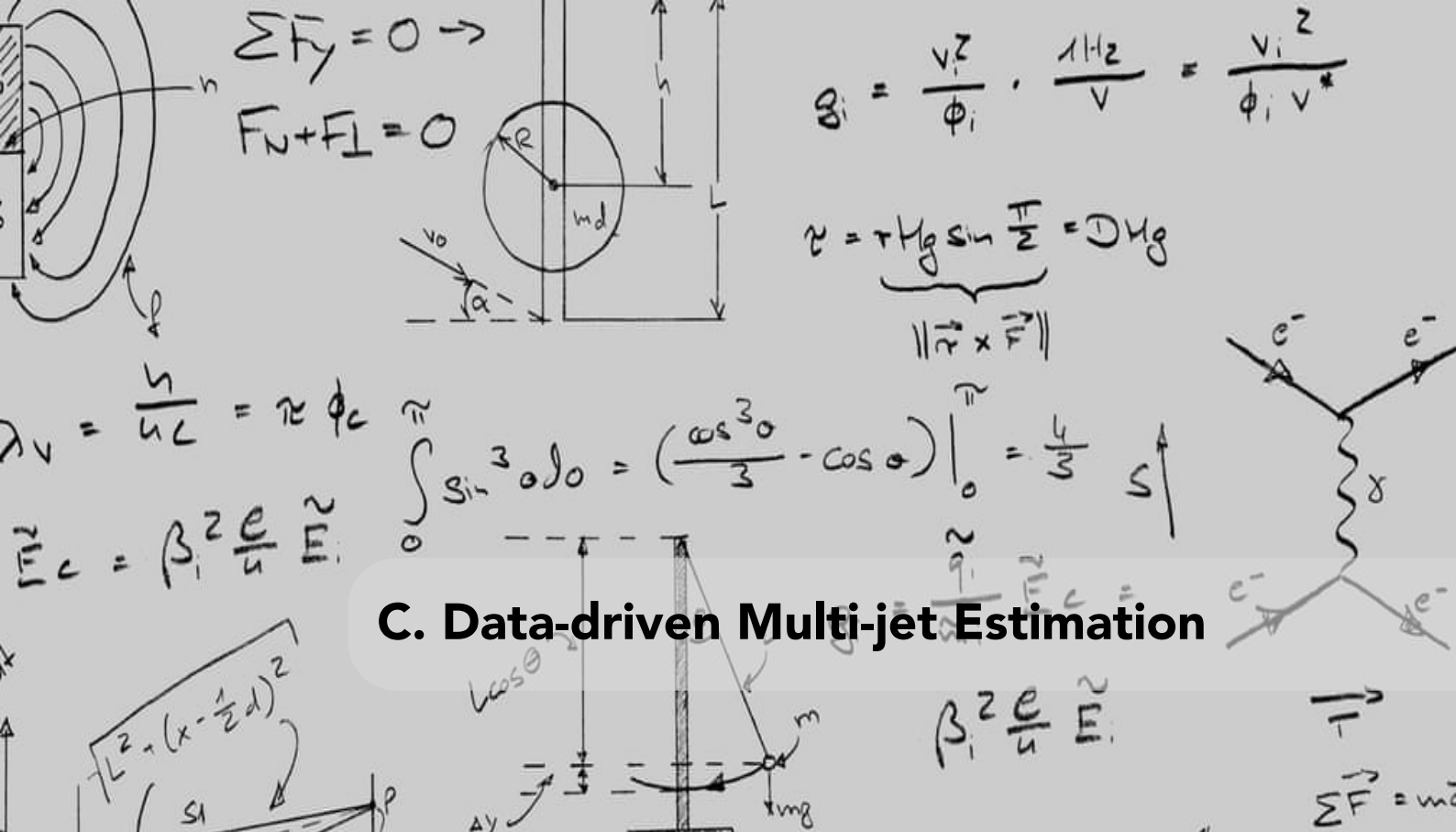
B.2.4 Vector Boson Production

The production of vector bosons (Z and W) in association with jets is modeled using the Sherpa v2.2.1 [61] program. The matrix elements are calculated for up to additional two partons at NLO accuracy and up to four partons at LO accuracy in the strong coupling constant using the Comix [230] and OpenLoops [231, 232] generators. The matrix elements are merged to the parton shower generated by Sherpa [233] using the ME+PS@NLO prescription [234–237]. The PDF set used is the NNPDF30NNLO [238] along with a dedicated set of parton-shower parameters developed by the Sherpa authors while the renormalisation and factorisation scales are set to m_V . For the work described in Chapter 7, the version 2.2.0 of the Sherpa program is used. Further details on the configuration can be found in [239].

The best available cross-sections used to normalise the samples are calculated at NNLO accuracy [178] and the value correspond to 2.089 ± 0.003 nb for the Z + jets process.

B.2.5 Diboson Production

The production of diboson processes (ZZ,ZW,WW) is modeled similarly to the Z/W + jets processes described above. Matrix elements are calculated up to additional one (zero) parton for the ZZ (ZW,WW) processes with the OpenLoops generator and the parton showering, hadronisation and underlying event are generated by Sherpa. For the work described in Chapter 7, the version of the Sherpa program used is the v2.1.1 with the CT10 PDF. Further details on the configuration along with the NLO cross-sections used to normalise the samples can be found in [196].



C. Data-driven Multi-jet Estimation

A brief overview of the data-driven technique used to estimate the multi-jet SM background against the searches of this work, along with material supporting the arguments of the main text are presented in this appendix. A detailed description of the technique can be found in [240].

C.1 Jet Smearing Technique

Mismeasurement of jets originating from QCD multi-jet production can lead to significant amounts of fake E_T^{miss} , as described already in Section 5.8. For instance, multi-jet simulations have shown that events with $\sum E_T \gtrsim 1$ TeV can lead to hundreds of GeV of fake E_T^{miss} (see Figure 5.6b) and m_{eff} . Considering also the enormous cross-section of the multi-jet processes (10^{5-7} times larger than the SUSY cross-sections) the amount of events with fake E_T^{miss} ending in the SRs of this work might be considerable.

The large multi-jet cross-section – that drives the amount of simulated events generated – along with the inaccurate description of the detector in simulations (JER and PU effects) make the simulation of multi-jet events with fake E_T^{miss} unfeasible. Therefore, a data-driven technique known as *Jet Smearing* is used to derive these events estimation and is used in both searches presented in this dissertation. The concept of the technique is to alter, or *smear*, as sample of well-measured data events (*seed data*), based on a function that describes the detector response, in order to produce a larger sample of “mismeasured” *pseudo-data* with fake E_T^{miss} . The latter sample is used to estimate the multi-jet event yield in each of the kinematic regions of interest. The concept is illustrated in Figure C.1.

The Jet Smearing estimate is derived as described on the following steps:

1. **Well-measured Events:** First, well-measured data events are collected to seed

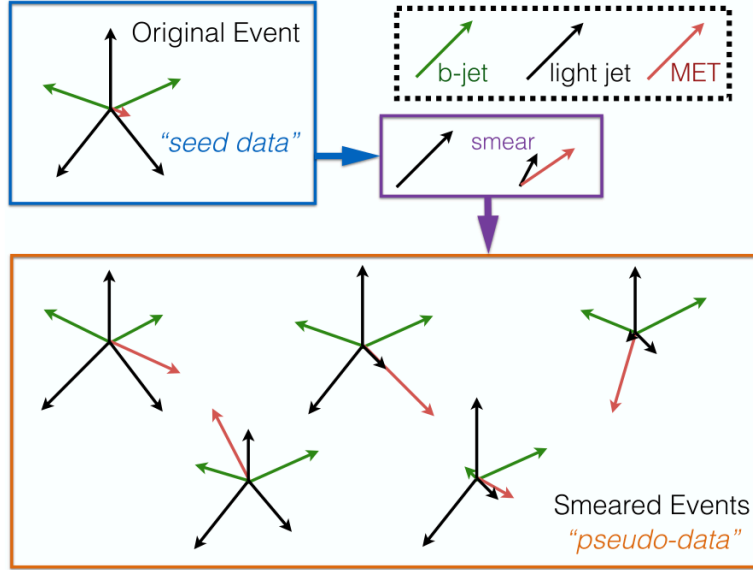


Figure C.1: Illustration of the Jet Smearing technique. First, seed data are collected, second they are smeared by a function inducing an imbalance thus fake E_T^{miss} is generated. The process repeated multiple times and a large sample of pseudo-data is obtained to be used to derive the multi-jet event yield estimate. [240]

the smearing process. Main characteristic of these events is the small values of the so-called E_T^{miss} Significance (E_T^{miss} Sig.) defined as:

$$E_T^{\text{miss}} \text{ Sig.} = \frac{E_T^{\text{miss}} - M}{\sqrt{\sum E_T}}, \quad (\text{C.1})$$

where M is a tunable to each particular analysis needs numerical parameter to compensate any residual bias. The seeds events collected should have values of E_T^{miss} Sig. less than $0.5 + 0.1 N_{\text{b-jets}} \text{ GeV}^{1/2}$ ($N_{\text{b-jets}} = 3$ for the analysis of this work), where the $N_{\text{b-jets}}$ dependence accounts for the real E_T^{miss} induced by the neutrinos originating from the B-hadrons decay. As the fake E_T^{miss} multi-jet background heavily depends on the PU conditions, different samples of seed data are collected for the gluino and sbottom analyses, either from the partial 2015-16 or the full Run 2 dataset respectively.

2. **Response Map:** The response map is the function that describes the detector jet response (i.e. how well the energy of a jet energy is reconstructed) and is used to smear the seed events. The map is derived by simulated multi-jet events [207], as function of the reconstructed jet p_T , and is defined as the ratio of reconstructed over the truth jet energy:

$$R_{\text{MC}} = \frac{E_{\text{Reco}}}{E_{\text{Truth}}}. \quad (\text{C.2})$$

An example of a response map for events containing b-jets is shown in Figure C.2.

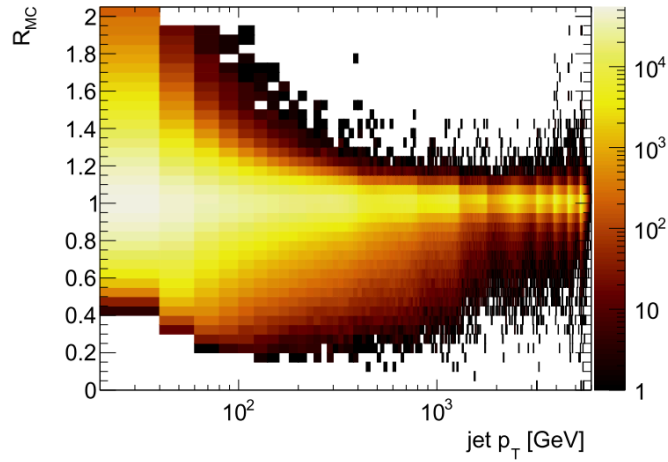


Figure C.2: Jet response map derived from multi-jet simulations. [240]

3. **Smearing:** Each jet of each seed event is smeared by a random number sampled by the R_{MC} distribution as function of its p_T . The process is repeated at $\mathcal{O}(1000)$ times thus a significantly larger sample of pseudo-data is generated. These pseudo-data resemble the properties of truly mismeasured multi-jet data events.
4. **Corrections:** Additional corrections are applied to the pseudo-data sample to account for the ambiguities on the R_{MC} construction – as it is derived solely from simulations – and to biases regarding the seed selection. These corrections are derived by well-balanced events of photons (or Z bosons) against a b-jet where the genuine E_T^{miss} is expected to be zero.
5. **Normalisation & Validation:** After the pseudo-data are generated, the sample normalisation is derived in analysis-specific multi-jet enriched control regions, referred as *CRQCD*, after subtracting from the data yield the rest of the expected SM processes. The various *CRQCD* are typically defined by placing an inverse $\min[\Delta\phi(\text{jet}_{1-4}, \mathbf{p}_T^{miss})]$ selection (< 0.1). After the normalisation, the full multi-jet estimate is verified in multi-jet enriched validation regions (*VRQCD*) by checking the data modeling of important kinematic variables. The *VRQCD* are defined in an intermediate phase space between the *CRQCD* and the analysis regions ($0.1 < \min[\Delta\phi(\text{jet}_{1-4}, \mathbf{p}_T^{miss})] < 0.4$). For the two analyses of in this dissertation, *CRQCD* and *VRQCD* distributions are presented in Section C.2.
6. **Systematic Uncertainties:** Finally, systematic uncertainties are applied to the method. Primary, an uncertainty is calculated by variation of the seed selection (E_T^{miss} Sig.) to account for any bias on the criteria applied. Additionally, a fixed 30% uncertainty is applied to cover any misestimate of the R_{MC} shape. Statistical uncertainties of the pseudo-data sample are also calculated.

C.2 Analyses Control Samples

After the seed data were collected and smeared as described above, they are normalised to CRQCDs for each of the two analyses of this work. For both cases, the normalisation is derived in a phase space closely related to each analysis and the details are given in Table C.1.

Table C.1: The selection criteria of the CRQCDs for the two analyses of this work.

Variable	Units	Glucino CRQCD (Chapter 7)	Sbottom CRQCD (Chapter 8)
N_{leptons}			0
N_{jets}			≥ 4
$N_{\text{b-jets}}$			≥ 3
$E_{\text{T}}^{\text{miss}}$	GeV	> 200	> 250
m_{eff}	GeV		> 1000
$\min[\Delta\phi(\text{jet}_{1-4}, \mathbf{p}_{\text{T}}^{\text{miss}})]$			< 0.1

In Figures C.4 and C.5 couple of the main discriminating variables of the gluino and sbottom analysis in the corresponding CRQCDs are presented respectively. The ratio of data events, after all the expected non-multi-jet processes have been subtracted, over the Jet Smearing estimation defines the extracted normalisation factor. Furthermore, it can be seen that all the distributions shape is adequately modeled.

After the successful closure of the method in the various VRQCDs for both the analysis, the multi-jet background is estimated in all the regions of interest (CRs, VRs, SRs). As described in the main text as well, the contribution in all the regions has been found negligible for both the analyses. Most importantly, this is explicitly shown for the SRs in Figure 7.297.32a for the gluino analysis and in Figure C.3 for the sbottom analysis.

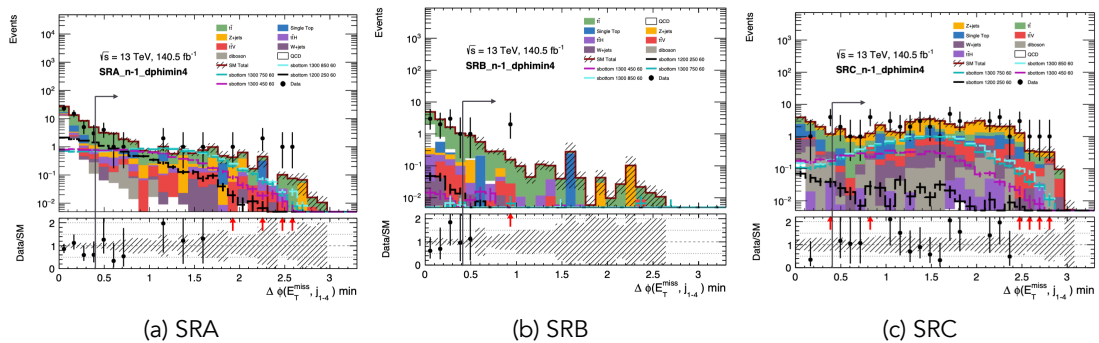


Figure C.3: Distributions of the $\min[\Delta\phi(\text{jet}_{1-4}, \mathbf{p}_{\text{T}}^{\text{miss}})]$ variable on each of the sbottom analysis SRs before the application of its selection. It can be seen that above values of 0.4, negligible amount of multi-jet contribution to the total SM background remains. Figures courtesy of the ATLAS Collaboration.

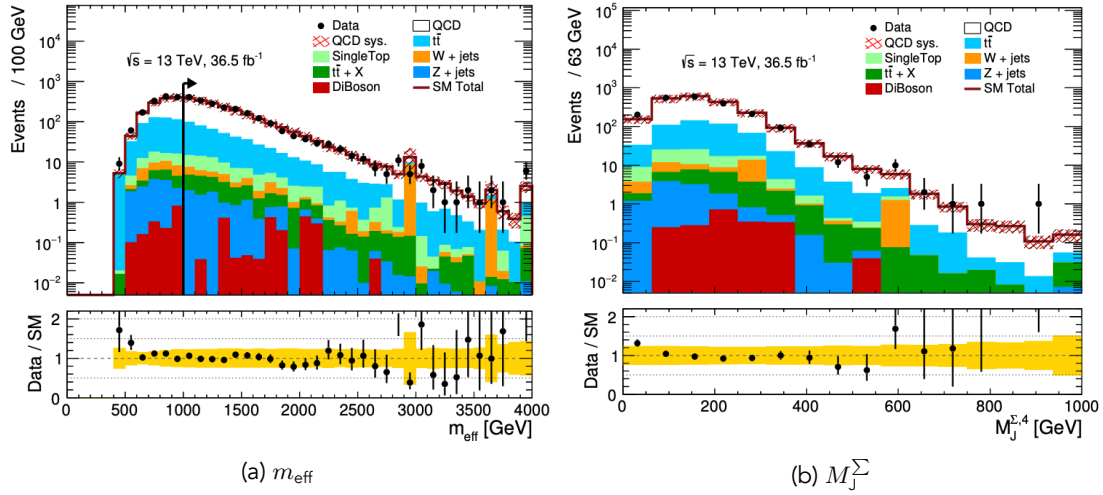


Figure C.4: Main discriminating variables distributions in CRQCD of the gluino analysis of Chapter 7 before the Jet Smearing estimate is scaled. The figures comprise an original work of the author.

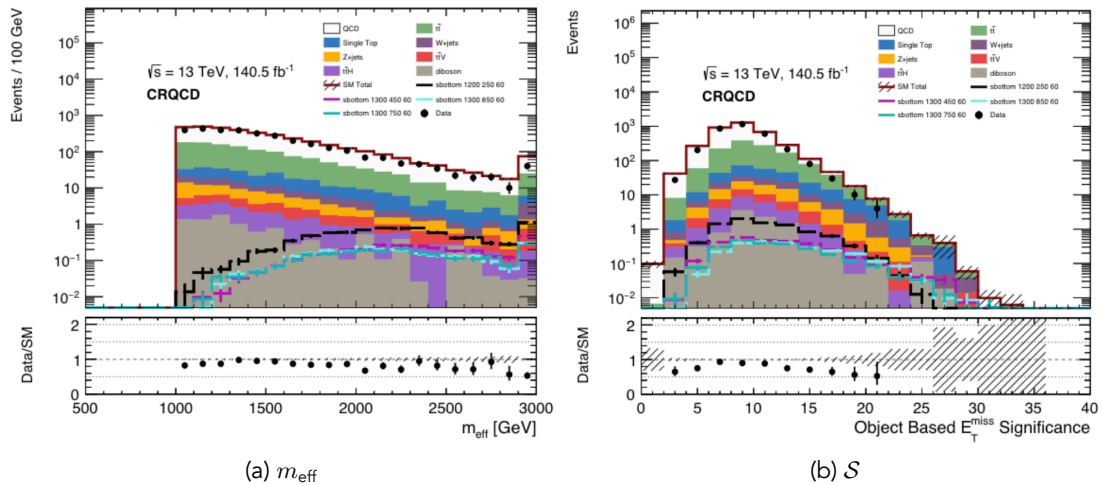


Figure C.5: Main discriminating variables distributions in CRQCD of the sbottom analysis of Chapter 8 before the Jet Smearing estimate is scaled. The figures comprise an original work of the author.



References

- [1] O. S. Brüning et al. “LHC Design Report”. CERN Yellow Reports: Monographs (2004). doi: [10.5170/CERN-2004-003-V-1](https://doi.org/10.5170/CERN-2004-003-V-1) (cit. on p. 17).
- [2] The ATLAS Collaboration. “The ATLAS Experiment at the CERN Large Hadron Collider”. *Journal of Instrumentation* 3 (2008), p. 8003. doi: [10.1088/1748-0221/3/08/S08003](https://doi.org/10.1088/1748-0221/3/08/S08003) (cit. on p. 18).
- [3] E. Kourlitis et al. “The Upgraded Microstrip Silicon Sensor Characterisation Facility of the University of Sheffield”. *PoS TWEPP2018* (2019), p. 28. doi: [10.22323/1.343.0028](https://doi.org/10.22323/1.343.0028) (cit. on pp. 18, 81, 83, 84, 86–89).
- [4] The ATLAS Collaboration. “Search for Supersymmetry in Final States with Missing Transverse Momentum and Multiple b-Jets in Proton-proton Collisions at $\sqrt{s} = 13$ TeV with the ATLAS Detector”. *J. High Energ. Phys.* 06 (2018), p. 107. doi: [10.1007/JHEP06\(2018\)107](https://doi.org/10.1007/JHEP06(2018)107) (cit. on pp. 18, 112, 116, 125, 128, 133, 134, 137, 141–143, 148, 150, 151, 157, 158, 160, 161, 163, 165, 252).
- [5] The ATLAS Collaboration. “Search for Bottom-squark Pair Production with the ATLAS Detector in Final States Containing Higgs Bosons, b-Jets and Missing Transverse Momentum”. *J. High Energ. Phys.* 12 (2019), p. 60. doi: [10.1007/JHEP12\(2019\)060](https://doi.org/10.1007/JHEP12(2019)060) (cit. on pp. 18, 171, 175, 178, 180, 201–203, 208, 209, 211, 214).
- [6] The HL-LHC project. *LHC / HL-LHC Plan*. <http://hilumilhc.web.cern.ch>. May 2018 (cit. on p. 19).
- [7] M. Thomson. “*Modern Particle Physics*”. New York: Cambridge University Press, 2013. isbn: 9781107034266 (cit. on pp. 24, 25, 30, 37).

- [8] S. Weinberg. "A Model of Leptons". *Phys. Rev. Lett.* 19 (1967), p. 1264. doi: [10.1103/PhysRevLett.19.1264](https://doi.org/10.1103/PhysRevLett.19.1264) (cit. on pp. 24, 33).
- [9] J. Goldstone. "Field Theories with « Superconductor » Solutions". *Il Nuovo Cimento* 19 (1961), p. 154. doi: [10.1007/BF02812722](https://doi.org/10.1007/BF02812722) (cit. on p. 24).
- [10] J. Goldstone, A. Salam, and S. Weinberg. "Broken Symmetries". *Phys. Rev.* 127 (1962), p. 965. doi: [10.1103/PhysRev.127.965](https://doi.org/10.1103/PhysRev.127.965) (cit. on p. 24).
- [11] F. Englert and R. Brout. "Broken Symmetry and the Mass of Gauge Vector Mesons". *Phys. Rev. Lett.* 13 (9 1964), p. 321. doi: [10.1103/PhysRevLett.13.321](https://doi.org/10.1103/PhysRevLett.13.321) (cit. on p. 24).
- [12] P. W. Higgs. "Broken Symmetries, Massless Particles and Gauge Fields". *Phys. Lett.* 12 (1964), p. 132. doi: [10.1016/0031-9163\(64\)91136-9](https://doi.org/10.1016/0031-9163(64)91136-9) (cit. on p. 24).
- [13] G. S. Guralnik, C. R. Hagen, and T. W. B. Kibble. "Global Conservation Laws and Massless Particles". *Phys. Rev. Lett.* 13 (1964), p. 585. doi: [10.1103/PhysRevLett.13.585](https://doi.org/10.1103/PhysRevLett.13.585) (cit. on p. 24).
- [14] G. 't Hooft and M. J. G. Veltman. "Regularization and Renormalization of Gauge Fields". *Nucl. Phys.* B44 (1972), p. 189. doi: [10.1016/0550-3213\(72\)90279-9](https://doi.org/10.1016/0550-3213(72)90279-9) (cit. on p. 24).
- [15] M. Gell-Mann. "The Eightfold Way: A Theory of Strong Interaction Symmetry" (1961). doi: [10.2172/4008239](https://doi.org/10.2172/4008239) (cit. on p. 24).
- [16] G. Zweig. "An SU_3 Model for Strong Interaction Symmetry and Its Breaking". Tech. rep. CERN-TH-401. 1964 (cit. on p. 24).
- [17] O. W. Greenberg. "Spin and Unitary Spin Independence in a Paraquark Model of Baryons and Mesons". *Phys. Rev. Lett.* 13 (1964), p. 598. doi: [10.1103/PhysRevLett.13.598](https://doi.org/10.1103/PhysRevLett.13.598) (cit. on p. 24).
- [18] M. Y. Han and Y. Nambu. "Three-Triplet Model with Double $SU(3)$ Symmetry". *Phys. Rev.* 139 (1965), B1006–B1010. doi: [10.1103/PhysRev.139.B1006](https://doi.org/10.1103/PhysRev.139.B1006) (cit. on p. 24).
- [19] H. Fritzsch, M. Gell-Mann, and H. Leutwyler. "Advantages of the Color Octet Gluon Picture". *Phys. Lett.* 47B (1973), p. 365. doi: [10.1016/0370-2693\(73\)90625-4](https://doi.org/10.1016/0370-2693(73)90625-4) (cit. on p. 24).
- [20] D. J. Gross and F. Wilczek. "Ultraviolet Behavior of Non-Abelian Gauge Theories". *Phys. Rev. Lett.* 30 (1973), p. 1343. doi: [10.1103/PhysRevLett.30.1343](https://doi.org/10.1103/PhysRevLett.30.1343) (cit. on p. 25).
- [21] H. D. Politzer. "Reliable Perturbative Results for Strong Interactions?" *Phys. Rev. Lett.* 30 (1973), p. 1346. doi: [10.1103/PhysRevLett.30.1346](https://doi.org/10.1103/PhysRevLett.30.1346) (cit. on p. 25).

-
- [22] Y. A. Golfand and E. P. Likhtman. "Extension of the Algebra of Poincare Group Generators and Violation of p Invariance". *JETP Lett.* 13 (1971), p. 323 (cit. on p. 25).
- [23] D. V. Volkov and V. P. Akulov. "Is the Neutrino a Goldstone Particle?" *Phys. Lett. B* 46 (1973), p. 109. doi: [10.1016/0370-2693\(73\)90490-5](https://doi.org/10.1016/0370-2693(73)90490-5) (cit. on p. 25).
- [24] J. Wess and B. Zumino. "Supergauge Transformations in Four-Dimensions". *Nucl. Phys. B* 70 (1974), p. 39. doi: [10.1016/0550-3213\(74\)90355-1](https://doi.org/10.1016/0550-3213(74)90355-1) (cit. on p. 25).
- [25] J. Wess and B. Zumino. "Supergauge Invariant Extension of Quantum Electrodynamics". *Nucl. Phys. B* 78 (1974), p. 1. doi: [10.1016/0550-3213\(74\)90112-6](https://doi.org/10.1016/0550-3213(74)90112-6) (cit. on p. 25).
- [26] S. Ferrara and B. Zumino. "Supergauge Invariant Yang-Mills Theories". *Nucl. Phys. B* 79 (1974), p. 413. doi: [10.1016/0550-3213\(74\)90559-8](https://doi.org/10.1016/0550-3213(74)90559-8) (cit. on p. 25).
- [27] A. Salam and J. A. Strathdee. "Supersymmetry and Nonabelian Gauges". *Phys. Lett. B* 51 (1974), p. 353. doi: [10.1016/0370-2693\(74\)90226-3](https://doi.org/10.1016/0370-2693(74)90226-3) (cit. on p. 25).
- [28] The ATLAS Collaboration. "Standard Model Physics" (Mar. 2019). <https://twiki.cern.ch/twiki/bin/view/AtlasPublic/StandardModelPublicResults> (cit. on p. 26).
- [29] W. Pauli. "Über den Zusammenhang des Abschlusses der Elektronengruppen im Atom mit der Komplexstruktur der Spektren". *Zeitschrift für Physik* 31 (1925), p. 765. doi: [10.1007/BF02980631](https://doi.org/10.1007/BF02980631) (cit. on p. 25).
- [30] E. Fermi. "Sulla Quantizzazione del Gas Perfetto Monoatomico". *Rend. Lincei* 3 (1926), p. 145. doi: [10.1103/PhysRevLett.30.1346](https://doi.org/10.1103/PhysRevLett.30.1346) (cit. on p. 25).
- [31] P. A. M. Dirac and R. H. Fowler. "On the Theory of Quantum Mechanics". *Proc. R. Soc. Lond. A* 112 (1926). doi: [10.1098/rspa.1926.0133](https://doi.org/10.1098/rspa.1926.0133) (cit. on p. 25).
- [32] J. J. Thomson. "XL. Cathode Rays". *The London, Edinburgh, and Dublin Philosophical Magazine and Journal of Science* 44 (1897), p. 293. doi: [10.1080/14786449708621070](https://doi.org/10.1080/14786449708621070) (cit. on p. 27).
- [33] C. D. Anderson and S. H. Neddermeyer. "Cloud Chamber Observations of Cosmic Rays at 4300 Meters Elevation and Near Sea-Level". *Phys. Rev.* 50 (1936), p. 263. doi: [10.1103/PhysRev.50.263](https://doi.org/10.1103/PhysRev.50.263) (cit. on p. 27).
- [34] M. L. Perl et al. "Evidence for Anomalous Lepton Production in $e^+ - e^-$ Annihilation". *Phys. Rev. Lett.* 35 (1975), p. 1489. doi: [10.1103/PhysRevLett.35.1489](https://doi.org/10.1103/PhysRevLett.35.1489) (cit. on p. 27).
- [35] M. Tanabashi et al. "Review of Particle Physics". *Phys. Rev. D* 98 (2018), p. 30001. doi: [10.1103/PhysRevD.98.030001](https://doi.org/10.1103/PhysRevD.98.030001) (cit. on pp. 27, 31–33, 44, 80, 222).

- [36] Fermat's Library. "The Proposal of the Neutrino (Translated)" (1930). <https://fermatslibrary.com/s/the-proposal-of-the-neutrino> (cit. on p. 27).
- [37] C. L. Cowan et al. "Detection of the Free Neutrino: a Confirmation". *Science* 124 (1956), p. 103. doi: [10.1126/science.124.3212.103](https://doi.org/10.1126/science.124.3212.103) (cit. on p. 28).
- [38] Y. Fukuda et al. "Evidence for Oscillation of Atmospheric Neutrinos". *Phys. Rev. Lett.* 81 (Aug. 1998), p. 1562. doi: [10.1103/PhysRevLett.81.1562](https://doi.org/10.1103/PhysRevLett.81.1562) (cit. on p. 28).
- [39] Q. R. Ahmad et al. "Direct Evidence for Neutrino Flavor Transformation from Neutral-Current Interactions in the Sudbury Neutrino Observatory". *Phys. Rev. Lett.* 89 (2002), p. 11301. doi: [10.1103/PhysRevLett.89.011301](https://doi.org/10.1103/PhysRevLett.89.011301) (cit. on p. 28).
- [40] M. Aker et al. "Improved Upper Limit on the Neutrino Mass from a Direct Kinematic Method by KATRIN". *Phys. Rev. Lett.* 123 (2019), p. 221802. doi: [10.1103/PhysRevLett.123.221802](https://doi.org/10.1103/PhysRevLett.123.221802) (cit. on p. 28).
- [41] David Galbraith. "Standard Model Infographic" (2012). <http://davidgalbraith.org/portfolio/ux-standard-model-of-the-standard-model/> (cit. on p. 28).
- [42] R. A. Serway, C. J. Moses, and C. A. Moyer. *Modern Physics*. Cengage Learning, 2004. isbn: 9781111794378 (cit. on p. 28).
- [43] J. I. Friedman and H. W. Kendall. "Deep Inelastic Electron Scattering". *Annual Review of Nuclear Science* 22 (1972), p. 203. doi: [10.1146/annurev.ns.22.120172.001223](https://doi.org/10.1146/annurev.ns.22.120172.001223) (cit. on p. 28).
- [44] H. L. Anderson et al. "Total Cross Sections of Positive Pions in Hydrogen". *Phys. Rev.* 85 (1952), p. 936. doi: [10.1103/PhysRev.85.936](https://doi.org/10.1103/PhysRev.85.936) (cit. on p. 29).
- [45] V. E. Barnes et al. "Observation of a Hyperon with Strangeness Minus Three". *Phys. Rev. Lett.* 12 (8 Feb. 1964), pp. 204–206. doi: [10.1103/PhysRevLett.12.204](https://doi.org/10.1103/PhysRevLett.12.204) (cit. on p. 29).
- [46] M. Kobayashi and T. Maskawa. "CP-Violation in the Renormalizable Theory of Weak Interaction". *Progress of Theoretical Physics* 49 (1973), pp. 652–657. doi: [10.1143/PTP.49.652](https://doi.org/10.1143/PTP.49.652) (cit. on p. 29).
- [47] S. W. Herb et al. "Observation of a Dimuon Resonance at 9.5-GeV in 400-GeV Proton-Nucleus Collisions". *Phys. Rev. Lett.* 39 (1977), p. 252. doi: [10.1103/PhysRevLett.39.252](https://doi.org/10.1103/PhysRevLett.39.252) (cit. on p. 29).
- [48] CDF Collaboration. "Observation of Top Quark Production in $p\bar{p}$ Collisions". *Phys. Rev. Lett.* 74 (1995), p. 2626. doi: [10.1103/PhysRevLett.74.2626](https://doi.org/10.1103/PhysRevLett.74.2626) (cit. on p. 29).
- [49] D0 Collaboration. "Search for High Mass Top Quark Production in $p\bar{p}$ Collisions at $\sqrt{s} = 1.8$ TeV". *Phys. Rev. Lett.* 74 (1995), p. 2422. doi: [10.1103/PhysRevLett.74.2422](https://doi.org/10.1103/PhysRevLett.74.2422) (cit. on p. 29).

-
- [50] N. Cabibbo. "Unitary Symmetry and Leptonic Decays". *Phys. Rev. Lett.* 10 (1963), p. 531. doi: [10.1103/PhysRevLett.10.531](https://doi.org/10.1103/PhysRevLett.10.531) (cit. on p. 29).
- [51] CKMfitter Group. "CP Violation and the CKM Matrix: Assessing the Impact of the Asymmetric B Factories". *Eur. Phys. J. C* 41 (2005), p. 1. doi: [10.1140/epjc/s2005-02169-1](https://doi.org/10.1140/epjc/s2005-02169-1) (cit. on p. 29).
- [52] E. Noether. "Invariant Variation Problems". *Transport Theory and Statistical Physics* 1 (1971), p. 186. doi: [10.1080/00411457108231446](https://doi.org/10.1080/00411457108231446) (cit. on p. 30).
- [53] The ALEPH Collaboration et al. "Precision Electroweak Measurements on the Z Resonance". *Physics Reports* 427 (2006), p. 257. doi: [10.1016/j.physrep.2005.12.006](https://doi.org/10.1016/j.physrep.2005.12.006) (cit. on p. 32).
- [54] J. Ellis. "Higgs Physics". *Proceedings, 2013 European School of High-Energy Physics (ESHEP 2013): Paradfurdo, Hungary, June 5-18, 2013*. 2015, p. 117. doi: [10.5170/CERN-2015-004.117](https://doi.org/10.5170/CERN-2015-004.117) (cit. on p. 33).
- [55] L. Cardani. "Neutrinoless Double Beta Decay Overview". *SciPost Phys. Proc.* 1 (2019), p. 24. doi: [10.21468/SciPostPhysProc.1.024](https://doi.org/10.21468/SciPostPhysProc.1.024) (cit. on p. 34).
- [56] The ATLAS Collaboration. "Observation of a New Particle in the Search for the Standard Model Higgs Boson with the ATLAS Detector at the LHC". *Physics Letters B* 716 (2012), p. 1. doi: [10.1016/j.physletb.2012.08.020](https://doi.org/10.1016/j.physletb.2012.08.020) (cit. on p. 34).
- [57] CMS Collaboration. "Observation of a New Boson at a Mass of 125 GeV with the CMS experiment at the LHC". *Physics Letters B* 716 (2012), p. 30. doi: [10.1016/j.physletb.2012.08.021](https://doi.org/10.1016/j.physletb.2012.08.021) (cit. on p. 34).
- [58] CMS Collaboration. "Measurements of Properties of the Higgs Boson Decaying into the Four-lepton Final State in pp Collisions at $\sqrt{s} = 13$ TeV". *J. High Energy Phys.* 11 (2017), p. 47. doi: [10.1007/JHEP11\(2017\)047](https://doi.org/10.1007/JHEP11(2017)047) (cit. on p. 35).
- [59] D. de Florian et al. "Handbook of LHC Higgs Cross Sections: 4. Deciphering the Nature of the Higgs Sector" (2016). doi: [10.23731/CYRM-2017-002](https://doi.org/10.23731/CYRM-2017-002) (cit. on pp. 35, 120, 174, 225, 226).
- [60] T. Sjöstrand, S. Mrenna, and P. Z. Skands. "PYTHIA 6.4 Physics and Manual". *J. High Energy Phys.* 05 (2006), p. 26. doi: [10.1088/1126-6708/2006/05/026](https://doi.org/10.1088/1126-6708/2006/05/026) (cit. on pp. 39, 224).
- [61] T. Gleisberg et al. "Event generation with SHERPA 1.1". *J. High Energy Phys.* 02 (2009), p. 7. doi: [10.1088/1126-6708/2009/02/007](https://doi.org/10.1088/1126-6708/2009/02/007) (cit. on pp. 39, 226).
- [62] J. Pumplin et al. "New Generation of Parton Distributions with Uncertainties From Global QCD Analysis". *J. High Energy Phys.* 07 (2002), p. 12. doi: [10.1088/1126-6708/2002/07/012](https://doi.org/10.1088/1126-6708/2002/07/012) (cit. on pp. 40, 224).

- [63] S. Höche. "Introduction to Parton-shower Event Generators". *Proceedings, Theoretical Advanced Study Institute in Elementary Particle Physics: Journeys Through the Precision Frontier: Amplitudes for Colliders (TASI 2014): Boulder, Colorado, June 2-27, 2014*. 2015, p. 235. doi: [10.1142/9789814678766_0005](https://doi.org/10.1142/9789814678766_0005) (cit. on p. 41).
- [64] S. Frixione and B. R. Webber. "Matching NLO QCD computations and parton shower simulations". *J. High Energ. Phys.* 06 (2002), p. 29. doi: [10.1088/1126-6708/2002/06/029](https://doi.org/10.1088/1126-6708/2002/06/029) (cit. on p. 41).
- [65] P. Nason. "A New method for combining NLO QCD with shower Monte Carlo algorithms". *J. High Energ. Phys.* 11 (2004), p. 40. doi: [10.1088/1126-6708/2004/11/040](https://doi.org/10.1088/1126-6708/2004/11/040) (cit. on p. 41).
- [66] The ATLAS Collaboration. "ATLAS Run 1 Pythia8 tunes". Tech. rep. ATL-PHYS-PUB-2014-021. <https://cds.cern.ch/record/1966419>. 2014 (cit. on pp. 41, 223).
- [67] R. H. Parker et al. "Measurement of the Fine-structure Constant as a Test of the Standard Model". *Science* 360 (2018), p. 191. doi: [10.1126/science.aap7706](https://doi.org/10.1126/science.aap7706) (cit. on p. 42).
- [68] C. J. Conselice et al. "The Evolution of Galaxy Number Density at $z < 8$ and Its Implications". *The Astrophysical Journal* 830 (2016), p. 83. doi: [10.3847/0004-637x/830/2/83](https://doi.org/10.3847/0004-637x/830/2/83) (cit. on p. 42).
- [69] The ATLAS Collaboration. "Measurement of Dijet Azimuthal Decorrelations in pp Collisions at $\sqrt{s} = 8$ TeV with the ATLAS Detector and Determination of the Strong Coupling". *Phys. Rev. D* 98 (2018), p. 92004. doi: [10.1103/PhysRevD.98.092004](https://doi.org/10.1103/PhysRevD.98.092004) (cit. on p. 42).
- [70] The ATLAS Collaboration. "Combined Measurements of Higgs Boson Production and Decay Using up to 80 fb^{-1} of Proton-Proton Collision Data at $\sqrt{s} = 13$ TeV Collected with the ATLAS Experiment". *Phys. Rev. D* 101 (2020), p. 12002. doi: [10.1103/PhysRevD.101.012002](https://doi.org/10.1103/PhysRevD.101.012002) (cit. on p. 42).
- [71] A.N. Schellekens. "Beyond the Standard Model" (2017). <https://www.nikhef.nl/~t58/BSM.pdf> (cit. on p. 43).
- [72] A. V. Zasov et al. "Dark matter in galaxies". *Physics-Usppekhi* 60 (2017), p. 3. doi: [10.3367/ufne.2016.03.037751](https://doi.org/10.3367/ufne.2016.03.037751) (cit. on pp. 43, 44).
- [73] J. P. Dietrich et al. "A Filament of Dark Matter Between Two Clusters of Galaxies". *Nature* 487 (2012), p. 202. doi: [10.1038/nature11224](https://doi.org/10.1038/nature11224) (cit. on pp. 43, 44).
- [74] G. Jungman, M. Kamionkowski, and K. Griest. "Supersymmetric Dark Matter". *Phys. Rept.* 267 (1996), p. 195. doi: [10.1016/0370-1573\(95\)00058-5](https://doi.org/10.1016/0370-1573(95)00058-5) (cit. on p. 44).

-
- [75] S. Coleman and J. Mandula. "All Possible Symmetries of the S Matrix". *Phys. Rev.* 159 (), p. 1251. doi: [10.1103/PhysRev.159.1251](https://doi.org/10.1103/PhysRev.159.1251) (cit. on p. 48).
- [76] R. Haag, J. T. Lopuszanski, and M. Sohnius. "All Possible Generators of Supersymmetries of the S Matrix". *Nucl. Phys.* B88 (1975), p. 257. doi: [10.1016/0550-3213\(75\)90279-5](https://doi.org/10.1016/0550-3213(75)90279-5) (cit. on p. 48).
- [77] S. P. Martin. "A Supersymmetry Primer" (1997), p. 1. doi: [10.1142/9789812839657_0001](https://doi.org/10.1142/9789812839657_0001), [10.1142/9789814307505_0001](https://doi.org/10.1142/9789814307505_0001) (cit. on pp. 48, 50–53, 56).
- [78] A. Signer. "ABC of SUSY". *J. Phys.* G36 (2009), p. 73002. doi: [10.1088/0954-3899/36/7/073002](https://doi.org/10.1088/0954-3899/36/7/073002) (cit. on p. 49).
- [79] I. Aitchison. *Supersymmetry in Particle Physics: An Elementary Introduction*. Cambridge University Press, 2007. doi: [10.1017/CB09780511619250](https://doi.org/10.1017/CB09780511619250) (cit. on p. 51).
- [80] D. J. H. Chung et al. "The Soft Supersymmetry Breaking Lagrangian: Theory and Applications". *Phys. Rept.* 407 (2005), p. 1. doi: [10.1016/j.physrep.2004.08.032](https://doi.org/10.1016/j.physrep.2004.08.032) (cit. on p. 51).
- [81] K. Abe et al. "Search for Proton Decay via $p \rightarrow e^+\pi^0$ and $p \rightarrow \mu^+\pi^0$ in 0.31 Megaton-Years Exposure of the Super-Kamiokande Water Cherenkov Detector". *Phys. Rev. D* 95 (2017), p. 12004. doi: [10.1103/PhysRevD.95.012004](https://doi.org/10.1103/PhysRevD.95.012004) (cit. on p. 53).
- [82] E. Bagnaschi et al. "Likelihood Analysis of the pMSSM11 in Light of LHC 13-TeV Data". *European Physical Journal C* 78 (2018), p. 256. doi: [10.1140/epjc/s10052-018-5697-0](https://doi.org/10.1140/epjc/s10052-018-5697-0) (cit. on p. 54).
- [83] P. Draper, G. Lee, and C. E. M. Wagner. "Precise Estimates of the Higgs Mass in Heavy Supersymmetry". *Phys. Rev. D* 89 (2014), p. 55023. doi: [10.1103/PhysRevD.89.055023](https://doi.org/10.1103/PhysRevD.89.055023) (cit. on p. 55).
- [84] C. Borschensky et al. "Squark and Gluino Production Cross Sections in pp Collisions at $\sqrt{s} = 13, 14, 33$ and 100 TeV". *Eur. Phys. J.* C74 (2014), p. 3174. doi: [10.1140/epjc/s10052-014-3174-y](https://doi.org/10.1140/epjc/s10052-014-3174-y) (cit. on pp. 55, 73, 120, 156, 223).
- [85] C. F. Berger et al. "Supersymmetry Without Prejudice". *J. High Energ. Phys.* 02 (2009), p. 23. doi: [10.1088/1126-6708/2009/02/023](https://doi.org/10.1088/1126-6708/2009/02/023) (cit. on p. 56).
- [86] The ATLAS Collaboration. "Summary of the ATLAS Experiment's Sensitivity To Supersymmetry after LHC Run 1 — Interpreted in the Phenomenological MSSM". *J. High Energ. Phys.* 10 (2015), p. 134. doi: [10.1007/JHEP10\(2015\)134](https://doi.org/10.1007/JHEP10(2015)134) (cit. on pp. 56, 57, 170, 171).
- [87] J. Alwall, P. C. Schuster, and N. Toro. "Simplified Models for a First Characterization of New Physics at the LHC". *Phys. Rev. D* 79 (2009), p. 75020. doi: [10.1103/PhysRevD.79.075020](https://doi.org/10.1103/PhysRevD.79.075020) (cit. on p. 56).

- [88] The ATLAS Collaboration. "Search for Supersymmetry in Events with b -Tagged Jets and Missing Transverse Momentum in pp Collisions at $\sqrt{s} = 13$ TeV with the ATLAS Detector". *J. High Energ. Phys.* 11 (2017), p. 195. doi: [10.1007/JHEP11\(2017\)195](https://doi.org/10.1007/JHEP11(2017)195) (cit. on p. 58).
- [89] The ATLAS Collaboration. "SUSY July 2019 Summary Plot Update". Tech. rep. ATL-PHYS-PUB-2019-022. July 2019 (cit. on pp. 59, 215).
- [90] De Broglie, L. "Recherches Sur la Théorie des Quanta". *Ann. Phys.* 10 (1925), p. 22. doi: [10.1051/anphys/192510030022](https://doi.org/10.1051/anphys/192510030022) (cit. on p. 63).
- [91] C. E. Hill et al. "Present Performance of the CERN Proton Linac". CERN-PS-98-045-HP (1998), p. 4 (cit. on p. 64).
- [92] "The Proton Synchrotron Booster" (2012). <https://cds.cern.ch/record/1997372> (cit. on p. 64).
- [93] "Proton Synchrotron" (1959). <https://cds.cern.ch/record/1479637> (cit. on p. 64).
- [94] M. Zinser. "Search for New Heavy Charged Bosons and Measurement of High-Mass Drell-Yan Production in Proton—Proton Collisions". Springer International Publishing, 2018, p. 47. isbn: 978-3-030-00650-1. doi: [10.1007/978-3-030-00650-1_4](https://doi.org/10.1007/978-3-030-00650-1_4) (cit. on p. 64).
- [95] CMS Collaboration. "The CMS Experiment at the CERN LHC". *Journal of Instrumentation* 3 (2008), p. 8004. doi: [10.1088/1748-0221/3/08/S08004](https://doi.org/10.1088/1748-0221/3/08/S08004) (cit. on p. 65).
- [96] LHCb Collaboration. "The LHCb Detector at the LHC". *Journal of Instrumentation* 3 (2008), p. 8005. doi: [10.1088/1748-0221/3/08/S08005](https://doi.org/10.1088/1748-0221/3/08/S08005) (cit. on p. 65).
- [97] ALICE Collaboration. "The ALICE experiment at the CERN LHC". *Journal of Instrumentation* 3 (2008), p. 8002. doi: [10.1088/1748-0221/3/08/S08002](https://doi.org/10.1088/1748-0221/3/08/S08002) (cit. on p. 65).
- [98] TOTEM Collaboration. "The TOTEM Experiment at the CERN Large Hadron Collider". *Journal of Instrumentation* 3 (2008), p. 8007. doi: [10.1088/1748-0221/3/08/S08007](https://doi.org/10.1088/1748-0221/3/08/S08007) (cit. on p. 65).
- [99] LHCf Collaboration. "Forward Physics with the LHCf Experiment". *PoS LHCP2018* (2018), p. 207. doi: [10.22323/1.321.0207](https://doi.org/10.22323/1.321.0207) (cit. on p. 65).
- [100] A. De Roeck and J. L. Pinfold. "The MoEDAL experiment at the LHC". *PoS LHCP2016* (2016), p. 99. doi: [10.22323/1.276.0099](https://doi.org/10.22323/1.276.0099) (cit. on p. 65).
- [101] The ATLAS Collaboration. "Delivered Luminosity Versus Time for 2011-2018 (pp Data Only)" (Feb. 2019). <https://twiki.cern.ch/twiki/bin/view/AtlasPublic/LuminosityPublicResultsRun2> (cit. on p. 66).

-
- [102] G. Avoni et al. "The New LUCID-2 Detector for Luminosity Measurement and Monitoring in ATLAS". *Journal of Instrumentation* 13 (2018), p. 7017. doi: [10.1088/1748-0221/13/07/P07017](https://doi.org/10.1088/1748-0221/13/07/P07017) (cit. on p. 66).
- [103] The ATLAS collaboration. "Luminosity Determination in pp Collisions at $\sqrt{s} = 13$ TeV Using the ATLAS Detector at the LHC". ATLAS-CONF-2019-021 (2019) (cit. on p. 66).
- [104] J. Pequeno. "Computer Generated Image of the Whole ATLAS Detector". "<https://cds.cern.ch/record/1095924>". Mar. 2008 (cit. on p. 67).
- [105] B. Nachman. "Investigating the Quantum Properties of Jets and the Search for a Supersymmetric Top Quark Partner with the ATLAS Detector". <https://cds.cern.ch/record/2204912>. PhD thesis. 2016 (cit. on p. 69).
- [106] K. Potamianos. "The Upgraded Pixel Detector and the Commissioning of the Inner Detector Tracking of the Atlas Experiment for Run-2 At the Large Hadron Collider". *PoS EPS-HEP2015* (2015), p. 261 (cit. on p. 70).
- [107] The ATLAS Collaboration. "Expected performance of the ATLAS b -tagging algorithms in Run-2". Tech. rep. ATL-PHYS-PUB-2015-022. 2015 (cit. on pp. 70, 100).
- [108] A.-L. Poley. "Studies of Adhesives and Metal Contacts on Silicon Strip Sensors for the ATLAS Inner Tracker". <https://cds.cern.ch/record/2320823>. PhD thesis. 2018 (cit. on pp. 71, 80, 81).
- [109] E. Segrè. "Nuclei and particles: an introduction to nuclear and subnuclear physics". New York: Benjamin, 1964. isbn: 9780486478845 (cit. on p. 72).
- [110] The ATLAS Collaboration. "Performance of the ATLAS Trigger System in 2015". *Eur. Phys. J. C77* (2017), p. 317. doi: [10.1140/epjc/s10052-017-4852-3](https://doi.org/10.1140/epjc/s10052-017-4852-3) (cit. on p. 74).
- [111] The ATLAS Collaboration. "The ATLAS Simulation Infrastructure". *Eur. Phys. J. C70* (2010), p. 823. doi: [10.1140/epjc/s10052-010-1429-9](https://doi.org/10.1140/epjc/s10052-010-1429-9) (cit. on p. 74).
- [112] S. Agostinelli et al. "GEANT4: A Simulation Toolkit". *Nucl. Instrum. Meth. A506* (2003), p. 250. doi: [10.1016/S0168-9002\(03\)01368-8](https://doi.org/10.1016/S0168-9002(03)01368-8) (cit. on p. 74).
- [113] The ATLAS Collaboration. "The Simulation Principle and Performance of the ATLAS Fast Calorimeter Simulation FastCaloSim". Tech. rep. ATL-PHYS-PUB-2010-013. 2010 (cit. on p. 74).
- [114] G. Apollinari et al. "High-Luminosity Large Hadron Collider (HL-LHC)". *CERN Yellow Rep. Monogr. 4* (2017), p. 1. doi: [10.23731/CYRM-2017-004](https://doi.org/10.23731/CYRM-2017-004) (cit. on p. 75).
- [115] The ATLAS Collaboration. "Letter of Intent for the Phase-II Upgrade of the ATLAS Experiment". Tech. rep. CERN-LHCC-2012-022. 2012 (cit. on p. 76).

- [116] The ATLAS Collaboration. *Technical Design Report for the ATLAS Inner Tracker Strip Detector*. Tech. rep. CERN-LHCC-2017-005. 2017 (cit. on pp. 76, 77, 79, 80).
- [117] Y. Unno et al. "Development of n^+ -in-p Large-area Silicon Microstrip Sensors for Very High Radiation Environments – ATLAS12 Design and Initial Results". *Nucl. Instrum. Meth.* A765 (2014), p. 80. doi: [10.1016/j.nima.2014.06.086](https://doi.org/10.1016/j.nima.2014.06.086) (cit. on p. 77).
- [118] L. B. A. Hommels et al. "Detailed Studies of Full-size ATLAS12 Sensors". *Nucl. Instrum. Meth.* A831 (2016), p. 167. doi: [10.1016/j.nima.2016.03.042](https://doi.org/10.1016/j.nima.2016.03.042) (cit. on pp. 78, 80).
- [119] M. Moll. "Radiation Damage in Silicon Particle Detectors: Microscopic Defects and Macroscopic Properties". <http://www-library.desy.de/cgi-bin/showprep.pl?desy-thesis99-040>. PhD thesis. 1999 (cit. on pp. 78, 79).
- [120] F. Hartmann. "Evolution of Silicon Sensor Technology in Particle Physics". *Springer Tracts Mod. Phys.* 275 (2017), p. 1. doi: [10.1007/978-3-319-64436-3](https://doi.org/10.1007/978-3-319-64436-3) (cit. on pp. 78–81, 86).
- [121] M. S. Lazo, D. M. Woodall, and P. J. McDaniel. "Silicon and Silicon dioxide neutron damage functions". *Sandia National Laboratories* 87 (1987), p. 98 (cit. on p. 78).
- [122] S. M. Sze and K. K. Ng. *Physics of Semiconductor Devices*. Wiley, 2006. isbn: 9780470068304 (cit. on p. 80).
- [123] High Technology Sources Limited. "Sr-90 Product Information" (2008). <http://hightechsource.co.uk/sr-90/> (cit. on p. 81).
- [124] Saint-Gobain Ceramics and Inc. Plastics. "BC-400 Product Information" (2018). <https://www.crystals.saint-gobain.com/products/bc400-bc404/> (cit. on p. 82).
- [125] Hamamatsu Photonics K.K. "Photosensor Modules H10720/H10721 Serier Information" (2016). https://www.hamamatsu.com/resources/pdf/etd/H10720_H10721_TPM01062E.pdf (cit. on p. 82).
- [126] R. Marco-Hernandez. "A Portable Readout System for Microstrip Silicon Sensors (ALIBAVA)". *IEEE Transactions on Nuclear Science* 56 (2009), p. 1642. doi: [10.1109/TNS.2009.2017261](https://doi.org/10.1109/TNS.2009.2017261) (cit. on p. 82).
- [127] S. Löchner and M. Schmelling. *The Beetle Reference Manual*. Tech. rep. LHCb-2005-105. Geneva: CERN, 2006 (cit. on p. 82).
- [128] P. Allport et al. "Recent Results and Experience with the Birmingham MC40 Irradiation Facility". *Journal of Instrumentation* 12 (Mar. 2017), p. 3075. doi: [10.1088/1748-0221/12/03/c03075](https://doi.org/10.1088/1748-0221/12/03/c03075) (cit. on pp. 85, 89).

-
- [129] T. Cornelissen et al. "The new ATLAS track reconstruction (NEWT)". *J. Phys. Conf. Ser.* 119 (2008), p. 032014. doi: [10.1088/1742-6596/119/3/032014](https://doi.org/10.1088/1742-6596/119/3/032014) (cit. on p. 91).
- [130] M. Aaboud et al. "Performance of the ATLAS Track Reconstruction Algorithms in Dense Environments in LHC Run 2". *Eur. Phys. J. C* 77 (2017), p. 673. doi: [10.1140/epjc/s10052-017-5225-7](https://doi.org/10.1140/epjc/s10052-017-5225-7) (cit. on p. 91).
- [131] R. Fruhwirth. "Application of Kalman Filtering to Track and Vertex Fitting". *Nucl. Instrum. Meth.* A262 (1987), p. 444. doi: [10.1016/0168-9002\(87\)90887-4](https://doi.org/10.1016/0168-9002(87)90887-4) (cit. on p. 92).
- [132] The ATLAS Collaboration. "Reconstruction of Primary Vertices at the ATLAS Experiment in Run 1 Proton-Proton Collisions at the LHC". *Eur. Phys. J. C* 77 (2017), p. 332. doi: [10.1140/epjc/s10052-017-4887-5](https://doi.org/10.1140/epjc/s10052-017-4887-5) (cit. on p. 92).
- [133] The ATLAS Collaboration. "Vertex performance in 2018 data" (2018). <https://atlas.web.cern.ch/Atlas/GROUPS/PHYSICS/PLOTS/IDTR-2018-006/> (cit. on p. 93).
- [134] The ATLAS Collaboration. "Electron and Photon Energy Calibration with the ATLAS Detector Using 2015–2016 LHC Proton-Proton Collision Data". *Journal of Instrumentation* 14 (2019), p. 3017. doi: [10.1088/1748-0221/14/03/P03017](https://doi.org/10.1088/1748-0221/14/03/P03017) (cit. on p. 93).
- [135] The ATLAS Collaboration. "Electron Reconstruction and Identification in the ATLAS Experiment Using the 2015 and 2016 LHC Proton-Proton Collision Data at $\sqrt{s} = 13$ TeV". *Eur. Phys. J. C* 79 (2019), p. 639. doi: [10.1140/epjc/s10052-019-7140-6](https://doi.org/10.1140/epjc/s10052-019-7140-6) (cit. on pp. 94, 95).
- [136] The ATLAS Collaboration. "Measurement of the Photon Identification Efficiencies with the ATLAS Detector Using LHC Run 2 Data Collected In 2015 and 2016". *Eur. Phys. J. C* 79 (2019), p. 205. doi: [10.1140/epjc/s10052-019-6650-6](https://doi.org/10.1140/epjc/s10052-019-6650-6) (cit. on p. 95).
- [137] The ATLAS Collaboration. "Muon Reconstruction Performance of the ATLAS Detector in Proton-Proton Collision Data at $\sqrt{s} = 13$ TeV". *Eur. Phys. J. C* 76 (2016), p. 292. doi: [10.1140/epjc/s10052-016-4120-y](https://doi.org/10.1140/epjc/s10052-016-4120-y) (cit. on p. 96).
- [138] The ATLAS Collaboration. "Topological Cell Clustering in the ATLAS Calorimeters and Its Performance in LHC Run 1". *Eur. Phys. J. C* 77 (2017), p. 490. doi: [10.1140/epjc/s10052-017-5004-5](https://doi.org/10.1140/epjc/s10052-017-5004-5) (cit. on p. 96).
- [139] M. Cacciari, G. P. Salam, and G. Soyez. "The Anti- k_t Jet Clustering Algorithm". *J. High Energ. Phys.* 04 (2008), p. 63. doi: [10.1088/1126-6708/2008/04/063](https://doi.org/10.1088/1126-6708/2008/04/063) (cit. on pp. 96, 98).

- [140] The ATLAS Collaboration. "Jet Energy Scale Measurements and Their Systematic Uncertainties in Proton-Proton Collisions at $\sqrt{s} = 13$ TeV with the ATLAS Detector". *Phys. Rev. D* 96 (2017), p. 72002. doi: [10.1103/PhysRevD.96.072002](https://doi.org/10.1103/PhysRevD.96.072002) (cit. on p. 97).
- [141] The ATLAS Collaboration. "Jet energy scale and uncertainties in 2015-2017 data and simulation" (2018). <https://atlas.web.cern.ch/Atlas/GROUPS/PHYSICS/PLOTS/JETM-2018-006/> (cit. on pp. 98, 204).
- [142] The ATLAS Collaboration. "Plots of Njets vs Pile-Up in 2017 data" (2017). <https://atlas.web.cern.ch/Atlas/GROUPS/PHYSICS/PLOTS/JETM-2017-009/> (cit. on p. 98).
- [143] M. Cacciari, G. P. Salam, and G. Soyez. "The Catchment Area of Jets". *J. High Energ. Phys.* 04 (2008), p. 5. doi: [10.1088/1126-6708/2008/04/005](https://doi.org/10.1088/1126-6708/2008/04/005) (cit. on p. 97).
- [144] The ATLAS collaboration. "Tagging and suppression of pileup jets". ATLAS-CONF-2014-018 (2014) (cit. on p. 97).
- [145] The ATLAS collaboration. "Selection of Jets Produced in 13TeV Proton-Proton Collisions with the ATLAS Detector". ATLAS-CONF-2015-029 (2015) (cit. on p. 98).
- [146] Benjamin Nachman et al. "Jets from Jets: Re-clustering as a Tool for Large Radius Jet Reconstruction and Grooming at the LHC". *J. High Energ. Phys.* 02 (2015), p. 75. doi: [10.1007/JHEP02\(2015\)075](https://doi.org/10.1007/JHEP02(2015)075) (cit. on p. 99).
- [147] The ATLAS Collaboration. "Performance of b -Jet Identification in the ATLAS Experiment". *Journal of Instrumentation* 11.04 (2016), p. 4008. doi: [10.1088/1748-0221/11/04/P04008](https://doi.org/10.1088/1748-0221/11/04/P04008) (cit. on p. 99).
- [148] The ATLAS Collaboration. "ATLAS b -Jet Identification Performance and Efficiency Measurement with $t\bar{t}$ events in pp Collisions at $\sqrt{s} = 13$ TeV". *Eur. Phys. J.* C79 (2019), p. 970. doi: [10.1140/epjc/s10052-019-7450-8](https://doi.org/10.1140/epjc/s10052-019-7450-8) (cit. on pp. 99–101).
- [149] The ATLAS Collaboration. "Calibration of the b -Tagging Efficiency on Charm Jets Using a Sample of $W+c$ Events with $\sqrt{s} = 13$ TeV ATLAS data". ATLAS-CONF-2018-055 (2018) (cit. on p. 100).
- [150] The ATLAS Collaboration. "Measurement of b -Tagging Efficiency of c -Jets in $t\bar{t}$ Events Using a Likelihood Approach with the ATLAS Detector". ATLAS-CONF-2018-001 (2018) (cit. on p. 100).
- [151] The ATLAS Collaboration. "Calibration of Light-flavour Jet b -Tagging Rates on ATLAS Proton-Proton Collision Data at $\sqrt{s} = 13$ TeV". ATLAS-CONF-2018-006 (2018) (cit. on p. 100).

-
- [152] The ATLAS Collaboration. *Optimisation of the ATLAS b-Tagging Performance for the 2016 LHC Run*. Tech. rep. ATL-PHYS-PUB-2016-012. Geneva: CERN, 2016 (cit. on p. 101).
- [153] The ATLAS Collaboration. "Reconstruction of Hadronic Decay Products of Tau Leptons with the ATLAS Experiment". *Eur. Phys. J. C* 76 (2016), p. 295. doi: [10.1140/epjc/s10052-016-4110-0](https://doi.org/10.1140/epjc/s10052-016-4110-0) (cit. on p. 101).
- [154] The ATLAS Collaboration. " E_T^{miss} Performance in the ATLAS Detector Using 2015-2016 LHC pp Collisions". ATLAS-CONF-2018-023 (2018) (cit. on p. 103).
- [155] The ATLAS Collaboration. "Jet Energy Resolution in 2017 Data and Simulation" (2018). <https://atlas.web.cern.ch/Atlas/GROUPS/PHYSICS/PLOTS/JETM-2018-005/> (cit. on p. 104).
- [156] M. Baak et al. "HistFitter Software Framework for Statistical Data Analysis". *The European Physical Journal C* 75 (2015), p. 153. doi: [10.1140/epjc/s10052-015-3327-7](https://doi.org/10.1140/epjc/s10052-015-3327-7) (cit. on pp. 109, 151).
- [157] G. Choudalakis and D. Casadei. "Plotting the Differences Between Data and Expectation". *Eur. Phys. J. Plus* 127 (2012), p. 25. doi: [10.1140/epjp/i2012-12025-y](https://doi.org/10.1140/epjp/i2012-12025-y) (cit. on pp. 111, 202, 209).
- [158] G. Cowan et al. "Asymptotic Formulae for Likelihood-based Tests of New Physics". *The European Physical Journal C* 71 (2011), p. 1554. doi: [10.1140/epjc/s10052-011-1554-0](https://doi.org/10.1140/epjc/s10052-011-1554-0) (cit. on pp. 112, 113).
- [159] A. L. Read. "Presentation of Search Results: The CL(s) Technique". *J. Phys.* G28 (2002), p. 2693. doi: [10.1088/0954-3899/28/10/313](https://doi.org/10.1088/0954-3899/28/10/313) (cit. on p. 112).
- [160] The ATLAS Collaboration. "Search for Bottom-squark Pair Production with the ATLAS Detector in Final States Containing Higgs Bosons, b-jets and Missing Transverse Momentum in pp Collisions at $\sqrt{s} = 13\text{ TeV}$ ". ATLAS-CONF-2018-040 (2018) (cit. on pp. 113, 197, 200).
- [161] R. Barbieri and G. F. Giudice. "Upper Bounds on Supersymmetric Particle Masses". *Nuclear Physics B* 306 (1988), p. 63. doi: [https://doi.org/10.1016/0550-3213\(88\)90171-X](https://doi.org/10.1016/0550-3213(88)90171-X) (cit. on p. 115).
- [162] The ATLAS Collaboration. "Search for Strong Production of Supersymmetric Particles in Final States with Missing Transverse Momentum and at Least Three b-Jets at $\sqrt{s} = 8\text{ TeV}$ Proton-Proton Collisions with the ATLAS Detector". *J. High Energy Phys.* 10 (2014), p. 24. doi: [10.1007/JHEP10\(2014\)024](https://doi.org/10.1007/JHEP10(2014)024) (cit. on pp. 116, 172, 212–214).
- [163] Z. Han et al. "Hunting Quasidegenerate Higgsinos". *Phys. Rev. D* 89 (2014), p. 75007. doi: [10.1103/PhysRevD.89.075007](https://doi.org/10.1103/PhysRevD.89.075007) (cit. on p. 117).

- [164] The ATLAS Collaboration. "Search for Pair Production of Gluinos Decaying via Stop and Sbottom in Events with b-Jets and Large Missing Transverse Momentum in pp Collisions at $\sqrt{s} = 13$ TeV with the ATLAS Detector". *Phys. Rev. D* 94 (2016), p. 32003. doi: [10.1103/PhysRevD.94.032003](https://doi.org/10.1103/PhysRevD.94.032003) (cit. on pp. 117, 147, 162, 163).
- [165] The ATLAS Collaboration. "Search for Supersymmetry in Final States with Two Same-sign or Three Leptons and Jets Using 36 fb^{-1} of $\sqrt{s} = 13$ TeV pp Collision Data with the ATLAS Detector". *J. High Energ. Phys.* 09 (2017), p. 84. doi: [10.1007/JHEP09\(2017\)084](https://doi.org/10.1007/JHEP09(2017)084) (cit. on p. 118).
- [166] CMS Collaboration. "Search for New Phenomena with the M_{T2} Variable in the All-hadronic Final State Produced in Proton-Proton Collisions at $\sqrt{s} = 13$ TeV". *Eur. Phys. J. C* 77 (2017), p. 710. doi: [10.1140/epjc/s10052-017-5267-x](https://doi.org/10.1140/epjc/s10052-017-5267-x) (cit. on p. 118).
- [167] CMS Collaboration. "Search for Supersymmetry in Multijet Events with Missing Transverse Momentum in Proton-Proton Collisions at 13 TeV". *Phys. Rev. D* 96 (2017), p. 32003. doi: [10.1103/PhysRevD.96.032003](https://doi.org/10.1103/PhysRevD.96.032003) (cit. on p. 118).
- [168] CMS Collaboration. "Search for Supersymmetry in pp Collisions at $\sqrt{s} = 13$ TeV in the Single-Lepton Final State Using the Sum of Masses of Large-Radius Jets". *Phys. Rev. Lett.* 119 (2017), p. 151802. doi: [10.1103/PhysRevLett.119.151802](https://doi.org/10.1103/PhysRevLett.119.151802) (cit. on p. 118).
- [169] CMS Collaboration. "Search for Physics Beyond the Standard Model in Events with Two Leptons of Same Sign, Missing Transverse Momentum, and Jets in Proton-Proton Collisions at $\sqrt{s} = 13$ TeV". *Eur. Phys. J. C* 77 (2017), p. 578. doi: [10.1140/epjc/s10052-017-5079-z](https://doi.org/10.1140/epjc/s10052-017-5079-z) (cit. on p. 118).
- [170] W. Beenakker et al. "Squark and Gluino Production at Hadron Colliders". *Nucl. Phys. B* 492 (1997), p. 51. doi: [10.1016/S0550-3213\(97\)80027-2](https://doi.org/10.1016/S0550-3213(97)80027-2) (cit. on pp. 120, 223).
- [171] A. Kulesza and L. Motyka. "Threshold Resummation for Squark-antisquark and Gluino-pair Production at the LHC". *Phys. Rev. Lett.* 102 (2009), p. 111802. doi: [10.1103/PhysRevLett.102.111802](https://doi.org/10.1103/PhysRevLett.102.111802) (cit. on pp. 120, 223).
- [172] A. Kulesza and L. Motyka. "Soft Gluon Resummation for the Production Of Gluino-gluino and Squark-antisquark Pairs at The LHC". *Phys. Rev. D* 80 (2009), p. 95004. doi: [10.1103/PhysRevD.80.095004](https://doi.org/10.1103/PhysRevD.80.095004) (cit. on pp. 120, 223).
- [173] W. Beenakker et al. "Soft-gluon Resummation for Squark and Gluino Hadroproduction". *J. High Energ. Phys.* 12 (2009), p. 41. doi: [10.1088/1126-6708/2009/12/041](https://doi.org/10.1088/1126-6708/2009/12/041) (cit. on pp. 120, 223).
- [174] W. Beenakker et al. "Squark and Gluino Hadroproduction". *Int. J. Mod. Phys. A* 26 (2011), p. 2637. doi: [10.1142/S0217751X11053560](https://doi.org/10.1142/S0217751X11053560) (cit. on pp. 120, 223).

-
- [175] M. Czakon and A. Mitov. "Top++: A Program for the Calculation of the Top-pair Cross-Section at Hadron Colliders". *Comput. Phys. Commun.* 185 (2014), p. 2930. doi: [10.1016/j.cpc.2014.06.021](https://doi.org/10.1016/j.cpc.2014.06.021) (cit. on pp. [120](#), [174](#), [224](#)).
- [176] N. Kidonakis. "Top Quark Production". *Proceedings, Helmholtz International Summer School on Physics of Heavy Quarks and Hadrons (HQ 2013): JINR, Dubna, Russia, July 15-28, 2013*. 2014, p. 139. doi: [10.3204/DESY-PROC-2013-03/Kidonakis](https://doi.org/10.3204/DESY-PROC-2013-03/Kidonakis) (cit. on pp. [120](#), [174](#)).
- [177] J. R. Andersen et al. "Handbook of LHC Higgs Cross Sections: 3. Higgs Properties". CERN Yellow Reports: Monographs (2013). doi: [10.5170/CERN-2013-004](https://doi.org/10.5170/CERN-2013-004) (cit. on p. [120](#)).
- [178] S. Catani et al. "Vector Boson Production at Hadron Colliders: a Fully Exclusive QCD Calculation at NNLO". *Phys. Rev. Lett.* 103 (2009), p. 82001. doi: [10.1103/PhysRevLett.103.082001](https://doi.org/10.1103/PhysRevLett.103.082001) (cit. on pp. [120](#), [174](#), [226](#)).
- [179] The ATLAS Collaboration. *Multi-Boson Simulation for 13 TeV ATLAS Analyses*. Tech. rep. ATL-PHYS-PUB-2016-002. 2016 (cit. on p. [120](#)).
- [180] The ATLAS Collaboration. "Measurements of Inclusive and Differential Fiducial Cross-sections of $t\bar{t}$ Production with Additional Heavy-flavour Jets in Proton-Proton Collisions at $\sqrt{s} = 13$ TeV with the ATLAS Detector". *J. High Energy Phys.* 04 (2019), p. 46. doi: [10.1007/JHEP04\(2019\)046](https://doi.org/10.1007/JHEP04(2019)046) (cit. on pp. [147](#), [206](#)).
- [181] CMS Collaboration. "Measurement of the $t\bar{t}b\bar{b}$ Production Cross Section in the All-jet Final State in pp Collisions at $\sqrt{s} = 13$ TeV". Tech. rep. CMS-PAS-TOP-18-011. 2019 (cit. on p. [147](#)).
- [182] The ATLAS Collaboration. "Jet Calibration and Systematic Uncertainties for Jets Reconstructed in the ATLAS Detector at $\sqrt{s} = 13$ TeV". Tech. rep. ATL-PHYS-PUB-2015-015. July 2015 (cit. on p. [153](#)).
- [183] The ATLAS Collaboration. "Measurements of Fiducial Cross-sections for $t\bar{t}$ Production with One or Two Additional b -Jets in pp Collisions at $\sqrt{s} = 8$ TeV Using the ATLAS Detector". *Eur. Phys. J. C* 76 (2016), p. 11. doi: [10.1140/epjc/s10052-015-3852-4](https://doi.org/10.1140/epjc/s10052-015-3852-4) (cit. on p. [155](#)).
- [184] P. Kant et al. "HatHor for Single Top-quark Production: Updated Predictions and Uncertainty Estimates for Single Top-quark Production in Hadronic Collisions". *Comput. Phys. Commun.* 191 (2015), p. 74. doi: [10.1016/j.cpc.2015.02.001](https://doi.org/10.1016/j.cpc.2015.02.001) (cit. on pp. [155](#), [225](#)).
- [185] The ATLAS Collaboration. "Search for Supersymmetry in Final States with Missing Transverse Momentum and Multiple b -jets in Proton-Proton Collisions at $\sqrt{s} = 13$ TeV with the ATLAS Detector". ATLAS-CONF-2018-041 (2018) (cit. on pp. [166](#), [167](#)).

- [186] The ATLAS collaboration. "Search for Supersymmetry in events with b-tagged jets and missing transverse energy in pp collisions at $\sqrt{s} = 13$ TeV with the ATLAS detector". ATLAS-CONF-2017-038 (2017) (cit. on p. 169).
- [187] V. Khachatryan et al. "Phenomenological MSSM Interpretation of CMS Searches in pp Collisions at $\sqrt{s} = 7$ and 8 TeV". *J. High Energy Phys.* 10 (2016), p. 129. doi: [10.1007/JHEP10\(2016\)129](https://doi.org/10.1007/JHEP10(2016)129) (cit. on p. 170).
- [188] K. Howe and P. Saraswat. "Excess Higgs Production in Neutralino Decays". *J. High Energy Phys.* 10 (2012), p. 65. doi: [10.1007/JHEP10\(2012\)065](https://doi.org/10.1007/JHEP10(2012)065) (cit. on p. 170).
- [189] A. Arbey, M. Battaglia, and F. Mahmoudi. "Higgs Production in Neutralino Decays in the MSSM". *The European Physical Journal C* 75 (2015), p. 108. doi: [10.1140/epjc/s10052-015-3316-x](https://doi.org/10.1140/epjc/s10052-015-3316-x) (cit. on p. 170).
- [190] CMS Collaboration. "Search for supersymmetry using Higgs boson to diphoton decays at $\sqrt{s} = 13$ TeV with the CMS detector". Tech. rep. CMS-PAS-SUS-18-007. 2019 (cit. on p. 172).
- [191] H. Baer et al. "Natural SUSY with a Bino- or Wino-like LSP". *Phys. Rev. D* 91 (2015), p. 75005. doi: [10.1103/PhysRevD.91.075005](https://doi.org/10.1103/PhysRevD.91.075005) (cit. on p. 172).
- [192] W. Beenakker et al. "NNLL-fast: Predictions for Coloured Supersymmetric Particle Production at the Lhc with Threshold and Coulomb Resummation". *J. High Energy Phys.* 12 (2016), p. 133. doi: [10.1007/JHEP12\(2016\)133](https://doi.org/10.1007/JHEP12(2016)133) (cit. on pp. 174, 206, 224).
- [193] W. Beenakker et al. "Stop Production at Hadron Colliders". *Nucl. Phys. B* 515 (1998), p. 3 (cit. on pp. 174, 206, 224).
- [194] Wim Beenakker et al. "Supersymmetric Top and Bottom Squark Production at Hadron Colliders". *J. High Energy Phys.* 8 (2010), p. 98. doi: [10.1007/JHEP08\(2010\)098](https://doi.org/10.1007/JHEP08(2010)098) (cit. on pp. 174, 206, 224).
- [195] Wim Beenakker et al. "NNLL Resummation for Stop Pair-production at the LHC". *J. High Energy Phys.* 05 (2016), p. 153. doi: [10.1007/JHEP05\(2016\)153](https://doi.org/10.1007/JHEP05(2016)153) (cit. on pp. 174, 206, 224).
- [196] The ATLAS Collaboration. "Multi-Boson Simulation for 13 TeV ATLAS Analyses". Tech. rep. ATL-PHYS-PUB-2017-005. 2017 (cit. on pp. 174, 226).
- [197] The ATLAS Collaboration. "Object-based Missing Transverse Momentum Significance in the ATLAS Detector". ATLAS-CONF-2018-038 (2018) (cit. on p. 176).
- [198] The ATLAS Collaboration. "Search for New Phenomena with Large Jet Multiplicities and Missing Transverse Momentum Using Large-radius Jets and Flavour-tagging at Atlas in 13 TeV pp Collisions". *J. High Energy Phys.* 12 (2017), p. 34. doi: [10.1007/JHEP12\(2017\)034](https://doi.org/10.1007/JHEP12(2017)034) (cit. on p. 177).

-
- [199] CMS Collaboration. "Search for Direct Production of Supersymmetric Partners of the Top Quark in the All-jets Final State In Proton-Proton Collisions at $\sqrt{S} = 13$ TeV". *J. High Energ. Phys.* 10 (2017), p. 5. doi: [10.1007/JHEP10\(2017\)005](https://doi.org/10.1007/JHEP10(2017)005) (cit. on p. 177).
- [200] The ATLAS Collaboration. "Performance of Missing Transverse Momentum Reconstruction in Proton-Proton Collisions at 7 TeV with ATLAS". *Eur. Phys. J. C* 72 (2012), p. 1844. doi: [10.1140/epjc/s10052-011-1844-6](https://doi.org/10.1140/epjc/s10052-011-1844-6) (cit. on p. 178).
- [201] M. Czakon et al. "Top-pair Production at the LHC Through NNLO QCD and NLO EW". *J. High Energ. Phys.* 10 (2017), p. 186. doi: [10.1007/JHEP10\(2017\)186](https://doi.org/10.1007/JHEP10(2017)186) (cit. on p. 195).
- [202] Johannes Bellm et al. "Herwig 7.0/Herwig++ 3.0 Release Note". *The European Physical Journal C* 76 (2016), p. 196. doi: [10.1140/epjc/s10052-016-4018-8](https://doi.org/10.1140/epjc/s10052-016-4018-8) (cit. on p. 205).
- [203] The ATLAS Collaboration. "Studies on Top-quark Monte Carlo Modelling for Top2016". Tech. rep. ATL-PHYS-PUB-2016-020. Sept. 2016 (cit. on pp. 205, 224).
- [204] N. Aghanim et al. "Planck 2018 Results. VI. Cosmological Parameters" (2018). <https://arxiv.org/abs/1807.06209> (cit. on p. 219).
- [205] J. Alwall et al. "The Automated Computation of Tree-level and Next-to-leading Order Differential Cross Sections, and Their Matching to Parton Shower Simulations". *J. High Energ. Phys.* 1407 (2014), p. 79. doi: [10.1007/JHEP07\(2014\)079](https://doi.org/10.1007/JHEP07(2014)079) (cit. on p. 223).
- [206] R. D. Ball et al. "Parton Distributions with LHC Data". *Nucl. Phys. B* 867 (2013), p. 244. doi: [10.1016/j.nuclphysb.2012.10.003](https://doi.org/10.1016/j.nuclphysb.2012.10.003) (cit. on p. 223).
- [207] T. Sjostrand, S. Mrenna, and P. Skands. "A Brief Introduction to PYTHIA 8.1". *Comput. Phys. Commun.* 178 (2008), p. 852. doi: [10.1016/j.cpc.2008.01.036](https://doi.org/10.1016/j.cpc.2008.01.036) (cit. on pp. 223, 228).
- [208] L. Lönnblad and S. Prestel. "Merging Multi-leg NLO Matrix Elements with Parton Showers". *J. High Energ. Phys.* 03 (2013), p. 166. doi: [10.1007/JHEP03\(2013\)166](https://doi.org/10.1007/JHEP03(2013)166) (cit. on p. 223).
- [209] Torbjörn Sjöstrand et al. "An Introduction to PYTHIA 8.2". *Comput. Phys. Commun.* 191 (2015), pp. 159–177. doi: [10.1016/j.cpc.2015.01.024](https://doi.org/10.1016/j.cpc.2015.01.024) (cit. on pp. 223, 224).
- [210] J. Butterworth et al. "PDF4LHC Recommendations for LHC Run II". *J. Phys.* G43 (2016), p. 23001. doi: [10.1088/0954-3899/43/2/023001](https://doi.org/10.1088/0954-3899/43/2/023001) (cit. on p. 224).
- [211] S. Frixione et al. "A Positive-weight Next-to-leading-order Monte Carlo for Heavy Flavour Hadroproduction". *J. High Energ. Phys.* 09 (2007), p. 126. doi: [10.1088/1126-6708/2007/09/126](https://doi.org/10.1088/1126-6708/2007/09/126) (cit. on p. 224).

- [212] P. Nason. "A New Method for Combining NLO QCD with Shower Monte Carlo Algorithms". *J. High Energ. Phys.* 0411 (2004), p. 40. doi: [10.1088/1126-6708/2004/11/040](https://doi.org/10.1088/1126-6708/2004/11/040) (cit. on p. 224).
- [213] S. Frixione, P. Nason, and C. Oleari. "Matching NLO QCD Computations with Parton Shower Simulations: the POWHEG Method". *J. High Energ. Phys.* 11 (2007), p. 70. doi: [10.1088/1126-6708/2007/11/070](https://doi.org/10.1088/1126-6708/2007/11/070) (cit. on p. 224).
- [214] S. Alioli et al. "A General Framework for Implementing NLO Calculations in Shower Monte Carlo Programs: the POWHEG BOX". *J. High Energ. Phys.* 1006 (2010), p. 43. doi: [10.1007/JHEP06\(2010\)043](https://doi.org/10.1007/JHEP06(2010)043) (cit. on p. 224).
- [215] S. Frixione et al. "Angular Correlations of Lepton Pairs from Vector Boson and Top Quark Decays in Monte Carlo Simulations". *J. High Energ. Phys.* 0704 (2007), p. 81. doi: [10.1088/1126-6708/2007/04/081](https://doi.org/10.1088/1126-6708/2007/04/081) (cit. on p. 224).
- [216] P. Artoisenet et al. "Automatic Spin-entangled Decays of Heavy Resonances In Monte Carlo Simulations". *J. High Energ. Phys.* 1303 (2013), p. 15. doi: [10.1007/JHEP03\(2013\)015](https://doi.org/10.1007/JHEP03(2013)015) (cit. on p. 224).
- [217] D. J. Lange. "The EvtGen Particle Decay Simulation Package". *Nucl. Instrum. Meth. A* 462 (2001), p. 152. doi: [10.1016/S0168-9002\(01\)00089-4](https://doi.org/10.1016/S0168-9002(01)00089-4) (cit. on p. 224).
- [218] M. Beneke et al. "Hadronic Top-quark Pair Production with NNLL Threshold Resummation". *Nucl. Phys. B* 855 (2012), p. 695. doi: [10.1016/j.nuclphysb.2011.10.021](https://doi.org/10.1016/j.nuclphysb.2011.10.021) (cit. on p. 224).
- [219] M. Cacciari et al. "Top-pair Production at Hadron Colliders with Next-to-next-to-leading Logarithmic Soft-gluon Resummation". *Phys. Lett. B* 710 (2012), p. 612. doi: [10.1016/j.physletb.2012.03.013](https://doi.org/10.1016/j.physletb.2012.03.013) (cit. on p. 224).
- [220] P. Bärnreuther, M. Czakon, and A. Mitov. "Percent Level Precision Physics at the Tevatron: First Genuine NNLO QCD Corrections to $q\bar{q} \rightarrow t\bar{t} + X$ ". *Phys. Rev. Lett.* 109 (2012), p. 132001. doi: [10.1103/PhysRevLett.109.132001](https://doi.org/10.1103/PhysRevLett.109.132001) (cit. on p. 224).
- [221] M. Czakon and A. Mitov. "NNLO Corrections to Top-pair Production at Hadron Colliders: the All-fermionic Scattering Channels". *J. High Energ. Phys.* 12 (2012), p. 54. doi: [10.1007/JHEP12\(2012\)054](https://doi.org/10.1007/JHEP12(2012)054) (cit. on p. 224).
- [222] M. Czakon and A. Mitov. "NNLO Corrections to Top Pair Production at Hadron Colliders: the Quark-Gluon Reaction". *J. High Energ. Phys.* 1301 (2013), p. 80. doi: [10.1007/JHEP01\(2013\)080](https://doi.org/10.1007/JHEP01(2013)080) (cit. on p. 224).
- [223] M. Czakon, P. Fiedler, and A. Mitov. "The Total Top Quark Pair Production Cross-section at Hadron Colliders Through $O(\alpha_S^4)$ ". *Phys. Rev. Lett.* 110 (2013), p. 252004. doi: [10.1103/PhysRevLett.110.252004](https://doi.org/10.1103/PhysRevLett.110.252004) (cit. on p. 224).

-
- [224] H.-L. Lai et al. "New Parton Distributions for Collider Physics". *Phys. Rev. D* 82 (2010), p. 74024. doi: [10.1103/PhysRevD.82.074024](https://doi.org/10.1103/PhysRevD.82.074024) (cit. on p. 224).
- [225] P. Z. Skands. "Tuning Monte Carlo Generators: The Perugia Tunes". *Phys. Rev. D* 82 (2010), p. 74018. doi: [10.1103/PhysRevD.82.074018](https://doi.org/10.1103/PhysRevD.82.074018) (cit. on p. 224).
- [226] S. Frixione et al. "Single-top Hadroproduction in Association with a W Boson". *J. High Energ. Phys.* 0807 (2008), p. 29. doi: [10.1088/1126-6708/2008/07/029](https://doi.org/10.1088/1126-6708/2008/07/029) (cit. on p. 224).
- [227] T Aaltonen et al. "Observation of s-Channel Production of Single Top Quarks at the Tevatron". *Physical review letters* 112 (2014), p. 231803. doi: [10.1103/PhysRevLett.112.231803](https://doi.org/10.1103/PhysRevLett.112.231803) (cit. on p. 225).
- [228] M. Aliev et al. "HATHOR: HAdronic Top and Heavy quarks crOss section calculator". *Comput. Phys. Commun.* 182 (2011), p. 1034. doi: [10.1016/j.cpc.2010.12.040](https://doi.org/10.1016/j.cpc.2010.12.040) (cit. on p. 225).
- [229] S. Gieseke, C. Rohr, and A. Siodmok. "Colour Reconnections in Herwig++". *Eur. Phys. J. C* 72 (2012), p. 2225. doi: [10.1140/epjc/s10052-012-2225-5](https://doi.org/10.1140/epjc/s10052-012-2225-5) (cit. on p. 226).
- [230] T. Gleisberg and S. Höche. "Comix, a New Matrix Element Generator". *J. High Energ. Phys.* 12 (2008), p. 39. doi: [10.1088/1126-6708/2008/12/039](https://doi.org/10.1088/1126-6708/2008/12/039) (cit. on p. 226).
- [231] F. Cascioli, P. Maierhofer, and S. Pozzorini. "Scattering Amplitudes with Open Loops". *Phys. Rev. Lett.* 108 (2012), p. 111601. doi: [10.1103/PhysRevLett.108.111601](https://doi.org/10.1103/PhysRevLett.108.111601) (cit. on p. 226).
- [232] A. Denner, S. Dittmaier, and L. Hofer. "Collier: a Fortran-based Complex One-Loop Library in Extended Regularizations". *Comput. Phys. Commun.* 212 (2017), p. 220. doi: [10.1016/j.cpc.2016.10.013](https://doi.org/10.1016/j.cpc.2016.10.013) (cit. on p. 226).
- [233] S. Schumann and F. Krauss. "A Parton Shower Algorithm Based on Catani-Seymour Dipole Factorisation". *J. High Energ. Phys.* 03 (2008), p. 38. doi: [10.1088/1126-6708/2008/03/038](https://doi.org/10.1088/1126-6708/2008/03/038) (cit. on p. 226).
- [234] S. Höche et al. "A Critical Appraisal of NLO+PS Matching Methods". *J. High Energ. Phys.* 09 (2012), p. 49. doi: [10.1007/JHEP09\(2012\)049](https://doi.org/10.1007/JHEP09(2012)049) (cit. on p. 226).
- [235] S. Höche et al. "QCD Matrix Elements + Parton Showers: The NLO Case". *J. High Energ. Phys.* 04 (2013), p. 27. doi: [10.1007/JHEP04\(2013\)027](https://doi.org/10.1007/JHEP04(2013)027) (cit. on p. 226).
- [236] S. Catani et al. "QCD Matrix Elements + Parton Showers". *J. High Energ. Phys.* 11 (2001), p. 63. doi: [10.1088/1126-6708/2001/11/063](https://doi.org/10.1088/1126-6708/2001/11/063) (cit. on p. 226).
- [237] S. Höche et al. "QCD Matrix Elements and Truncated Showers". *J. High Energ. Phys.* 05 (2009), p. 53. doi: [10.1088/1126-6708/2009/05/053](https://doi.org/10.1088/1126-6708/2009/05/053) (cit. on p. 226).

- [238] NNPDF Collaboration. "Parton Distributions for the LHC Run II". *J. High Energ. Phys.* 04 (2015), p. 40. doi: [10.1007/JHEP04\(2015\)040](https://doi.org/10.1007/JHEP04(2015)040) (cit. on p. 226).
- [239] The ATLAS Collaboration. "ATLAS Simulation of Boson Plus Jets Processes in Run 2". Tech. rep. ATL-PHYS-PUB-2017-006. 2017 (cit. on p. 226).
- [240] Macdonald C. "Searches for Supersymmetry in Final States Containing b-Tagged Jets with the ATLAS Detector". <http://etheses.whiterose.ac.uk/id/eprint/17990>. PhD thesis. 2017 (cit. on pp. 227–229).

Front cover and content cover pictures courtesy of Sergio Cittolin "Drawings of the elements of CMS detector, in the style of Leonardo da Vinci". Chapter 1, 2 and 3 cover pictures courtesy of Ouchhh "AVA_V2 / Particle Physics_Scientific_Installation", Barbara Hepworth "Genesis" and Michael Najjar "Supersymmetric Particles" respectively. Chapter 4 cover picture is an original work of the author. Chapter 6 cover picture courtesy of Andrew Ostrovsky "When Numbers Dream". Chapter 7 and 8 cover pictures courtesy of the ATLAS Collaboration [4]. Chapter 9 cover picture courtesy of Future Circular Collider Study. Appendices cover picture courtesy of OktalStudio "Quantum Physics On A Blackboard".